Government of Western Australia

Department of
Mines and Petroleum

REPORT
117

MINERAL SYSTEMS ANALYSIS OF THE WEST MUSGRAVE PROVINCE: REGIONAL STRUCTURE AND PROSPECTIVITY MODELLING

by A Joly, ARA Aitken, MC Dentith, A Porwal, RH Smithies, and IM Tyler

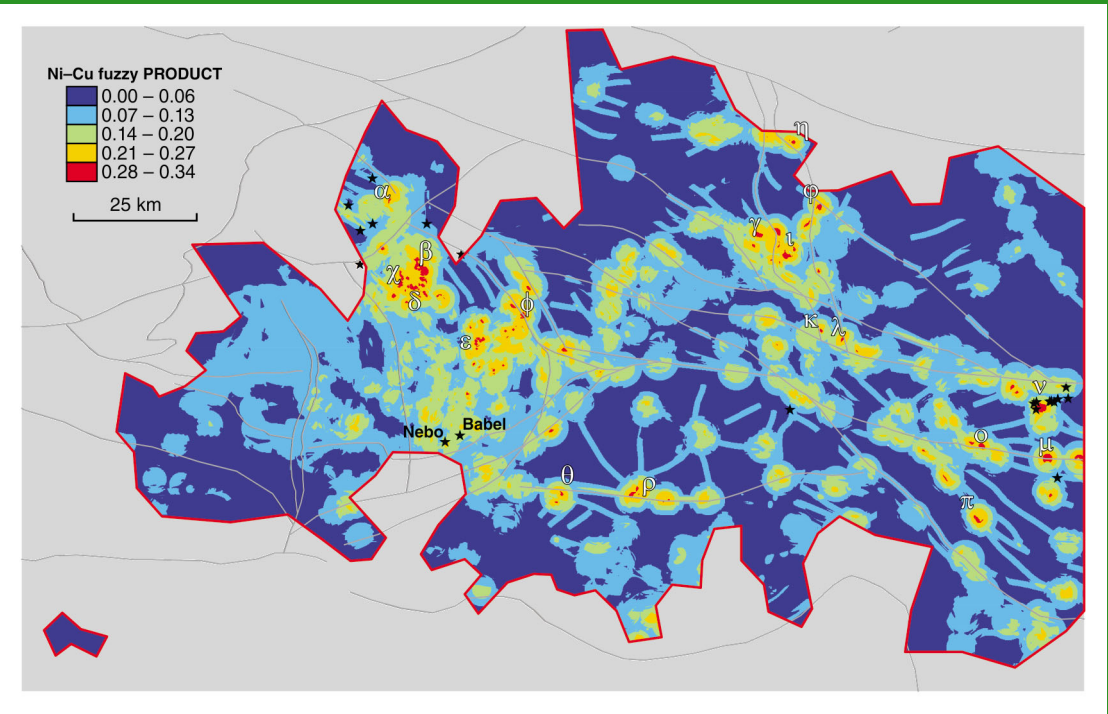

Centre for EXPLORATION TARGETING

ROYALTIES FOR REGIONS
EXPLORATION INCENTIVE SCHEME

Geological Survey of Western Australia

Government of **Western Australia**
Department of **Mines and Petroleum**

REPORT 117

MINERAL SYSTEMS ANALYSIS OF THE WEST MUSGRAVE PROVINCE: REGIONAL STRUCTURE AND PROSPECTIVITY MODELLING

by
A Joly[1], ARA Aitken[1], MC Dentith[1], A Porwal[1,2], RH Smithies, and IM Tyler

1 Centre for Exploration Targeting, The University of Western Australia, 35 Stirling Highway, Crawley, WA 6009, Australia

2 Indian Institute of Technology Bombay, Powai, Mumbai 400076, India

Perth 2014

Geological Survey of Western Australia

MINISTER FOR MINES AND PETROLEUM
Hon. Bill Marmion MLA

DIRECTOR GENERAL, DEPARTMENT OF MINES AND PETROLEUM
Richard Sellers

EXECUTIVE DIRECTOR, GEOLOGICAL SURVEY OF WESTERN AUSTRALIA
Rick Rogerson

REFERENCE
The recommended reference for this publication is:
Joly, A, Aitken, ARA, Dentith, MC, Porwal, A, Smithies, RH and Tyler, IM 2014, Mineral systems analysis of the west Musgrave Province: regional structure and prospectivity modelling: Geological Survey of Western Australia, Report 117, 99p.

National Library of Australia Cataloguing-in-Publication entry

Author:	Author: Joly, A., author.
Title:	Mineral systems analysis of the West Musgrave Province: regional structure and prospectivity modelling / A Joly, ARA Aitken, MC Dentith, A Porwal, RH Smithies, IM Tyler.
ISBN:	9781741685275 (ebook)
Subjects:	Mineralogy, Determinative--Western Australia—Musgrave Province. Prospecting--Western Australia--Musgrave Province. Geology, Structural--Western Australia--Musgrave Province
Other Authors/Contributors:	Aitken, A. R. A., author. Dentith, M.C., author. Porwal, A., author. Smithies, R. H., author. Tyler, I. M., author. Geological Survey of Western Australia.
Dewey Decimal Classification:	549.109941
ISSN 0508–4741	

Grid references in this publication refer to the Geocentric Datum of Australia 1994 (GDA94). Locations mentioned in the text are referenced using Map Grid Australia (MGA) coordinates, Zone 51. All locations are quoted to at least the nearest 100 m.

NGAANYATJARRA COUNCIL (Aboriginal Corporation)

Copy editor: SR White
Cartography: M Prause
Desktop publishing: RL Hitchings
Printed by Images on Paper, Perth, Western Australia

Published 2014 by Geological Survey of Western Australia
This Report is published in digital format (PDF) as part of a digital dataset on USB, and is available online at <www.dmp.wa.gov.au/GSWApublications>.

Further details of geological publications and maps produced by the Geological Survey of Western Australia are available from:
Information Centre
Department of Mines and Petroleum
100 Plain Street
EAST PERTH WESTERN AUSTRALIA 6004
Telephone: +61 8 9222 3459 Facsimile: +61 8 9222 3444
www.dmp.wa.gov.au/GSWApublications

Cover image: Fuzzy prospectivity model for the magmatic Ni–Cu mineral system over the west Musgrave Province

Contents

Appendix

Figures

Tables

---

* The Appendix, including tables (PDF), predictor and prospectivity maps (GeoTIFF), and selected ESRI ArcGIS data, are also provided separately on a USB. The Report may be accessed directly on our website independent of the USB.

Mineral systems analysis of the west Musgrave Province: regional structure and prospectivity modelling

by

A Joly , ARA Aitken[1], MC Dentith[1], A Porwal[1,2], RH Smithies, and IM Tyler

Abstract

This Report presents a multi-commodity prospectivity analysis of the west Musgrave Province, based on modelling by the Centre for Exploration Targeting (CET) at The University of Western Australia, of geological, geophysical and geochemical data collected by the Geological Survey of Western Australia (GSWA) during GSWA mapping programs. The datasets are used to create an interpretation of the 3D geometry and timing of major structures and architecture of subsurface stratigraphy. This is a critical component of the prospectivity analysis because major structures are believed to focus the flow of metal-bearing magmas and hydrothermal fluids. The majority of preserved major structures in the west Musgrave Province appear to have originated during the c. 1085–1040 Ma Giles Event, although many of these were subsequently reactivated during the Petermann and Alice Springs Orogenies. All primary and derived datasets are combined in a mineral system analysis which produces models that can be interrogated in a probabilistic framework. We then apply knowledge-based, or 'fuzzy', logic models in a GIS framework to assess prospectivity. This GIS-based 'fuzzy' analysis is an attempt to translate the expert knowledge of the geology of a given region and mineral systems into an automated approach where datasets can be systematically queried. It is the most suitable method of prospectivity analysis in regions with few or no known mineral occurrences. The analyses reported here are specifically relevant to the west Musgrave Province, but the approach to mineral prospectivity analysis is potentially applicable to any greenfields area and can be tailored to suit specific commodities and geological parameters.

The mineral prospectivity analysis was carried out for a range of commodities. The choice of commodities was based on the known prospectivity or endowment (i.e. known mineral deposits) of the west Musgrave Province and on perceived prospectivity based on interpreted geological and tectonic setting. The commodities and commodity styles include magmatic nickel–copper, magmatic platinum group elements (PGE), orogenic and intrusion-related gold, iron oxide–copper–gold (IOCG), tin–tungsten, and surficial uranium mineral systems. The results suggest that the west Musgrave Province is particularly prospective for magmatic nickel–copper and PGE deposits. The most favourable areas for magmatic Ni–Cu deposits are on the FINLAYSON and HOLT 1:100 000 geological map sheets, whereas for the magmatic PGE deposits the most favourable area is on the BELL ROCK map sheet. Favourable areas for intrusion-related gold mineralization occur mainly in the southern part of the BENTLEY map sheet and northern part of the MOUNT EVELINE map sheet. The COOPER map sheet is most prospective for orogenic gold deposits, whereas the greatest potential for IOCG deposits lies in the FINLAYSON, HOLT and BELL ROCK map sheet areas. Greatest potential for tin and tungsten deposits is in the BLACKSTONE and BELL ROCK map sheet areas and surficial uranium targets are identified in the BLACKSTONE map sheet area.

KEYWORDS: mineral deposits, mineralization, GIS, fuzzy logic, structural terranes, nickel–copper, platinum group elements, gold, tin–tungsten, uranium

1 Centre for Exploration Targeting, The University of Western Australia, 35 Stirling Highway, Crawley WA 6009, Australia

2 Indian Institute of Technology Bombay, Powai, Mumbai 400076 India

Introduction

The Centre for Exploration Targeting at The University of Western Australia is working with the Geological Survey of Western Australia (GSWA) to quantitatively assess the prospectivity of selected regions of Western Australia. These studies are funded by the Exploration Incentive Scheme (EIS), a Western Australia State Government initiative that aims to encourage exploration for the long-term sustainability of the State's resources sector. Thus, the focus of the studies is in underexplored regions of Western Australia, including the West Arunta Orogen, the Gascoyne Province and the Kimberley Craton margins. The current Report concerns the portion of the central Australian Musgrave Province that lies within Western Australia, here referred to as the 'west Musgrave Province'(WMP).

The Musgrave Province (Fig. 1) straddles the borders between Western Australia, South Australia and the Northern Territory. It is an east-trending belt of dominantly Mesoproterozoic rocks with a long and complex tectonic history involving multiple tectonic and magmatic events that collectively span the period from at least 1400 to 350 Ma. It remains one of the least explored Proterozoic terranes in Australia.

From 2004 to 2012, GSWA has conducted extensive geological investigations within the west Musgrave Province that have resulted in a dramatic increase in geological knowledge (GSWA 2010a,b, 2012 and references therein). To aid in the prospectivity analysis, a structural analysis of the region, based primarily on aeromagnetic data, was carried out to determine which of the structures in the WMP were active during each of the tectono-thermal events that have affected the region.

We use this interpretation, along with other geological and geochemical datasets, to generate conceptual mineral system models and prospectivity analyses for several commodities. The selected mineral systems are: 1) orthomagmatic nickel–copper; 2) magmatic platinum group elements (PGE); 3) orogenic and intrusion-related gold; 4) iron oxide–copper–gold (IOCG); 5) tin–tungsten (Sn–W); 6) surficial uranium. The first three of these commodities were selected predominantly on the basis of known prospects and deposits within the region. However, IOCG, Sn–W, and uranium systems, for which there are no known prospects, were included on the basis of conceptual favourability.

The GIS-based prospectivity analyses described here were implemented using a knowledge-based 'fuzzy' logic framework, which is the most suitable method of prospectivity analysis in regions with few or no known mineral occurrences. This requires several steps (McCuaig et al., 2010), foremost of which is the definition of reliably mappable proxies for the key components of the mineral system. The basic results are a series of predictor maps for each mineral system, which are combined to estimate overall mineral potential across a region. The results indicate the relative geological favourability for ore genesis within the applied mineral system model. These models may diverge from reality to varying degrees, due to uncertainties in the quality of the datasets used as proxies, the fidelity of each proxy to its conceptual partner, oversimplifications of the mineral system due to lack of reliable proxies, and user-induced biases in the implementation of the analysis. Users are encouraged to critically assess the predictor maps for individual proxies, and their influence on the final model.

Prospectivity analysis: rationale and methodology

The mineral systems approach

The mineral systems approach (MSA) to understanding mineral deposits has gained increasing acceptance over the past 20 years (Wyborn et al., 1994; Knox-Robinson and Wyborn, 1997; Hronsky, 2004; Blewett et al., 2009). The underpinning premise is that ore deposits are small expressions of much larger Earth process systems that operate on a variety of scales to focus mass and energy flux (McCuaig et al., 2010). The MSA aims to provide a holistic view of the entire process of mineralization including geodynamic setting, architecture, metal source, fluid flow drivers and pathways, and depositional mechanisms (Wyborn et al., 1994). It provides a generalized process-based framework; hence, it can be easily adapted to different geological environments and deposit types. The MSA is focused on processes that are often common across different mineral systems, rather than geological characteristics specific to one style of deposit. Therefore, it is flexible enough to allow for the discovery of a new style of deposit, rather than just analogues of those already discovered (Knox-Robinson and Wyborn, 1997; Mishra and Panigrahi, 1999; Hagemann and Cassidy, 2000; Porwal, 2006; Kreuzer et al., 2008; Joly et al., 2013). By breaking down the critical processes of mineralization and assuming that the probability of each of these processes is independent, mineral systems models can be integrated into a probabilistic framework and a probability of success can be calculated for discovery of potentially economic mineralization in a particular area. This concept has been applied to project evaluation (Lord et al., 2001), development of targeting decision tools (Kreuzer et al., 2008), and prospectivity analysis (Porwal et al., 2010, Joly et al., 2012).

A major advantage of the mineral systems approach is that it allows identification and prioritization of critical components for prospectivity analysis at a variety of scales ranging from the craton scale to deposit scale (McCuaig et al., 2010). Moreover, because the MSA comprises a series of components that can be theoretically considered conditionally independent, the approach can be readily integrated into a spatial statistical framework for estimating the probability of mineral deposits at any scale. For example, the overall probability of a deposit of the targeted type at a specific scale can be estimated from the individual probabilities of the components that are considered critical at that scale. The probabilities for the

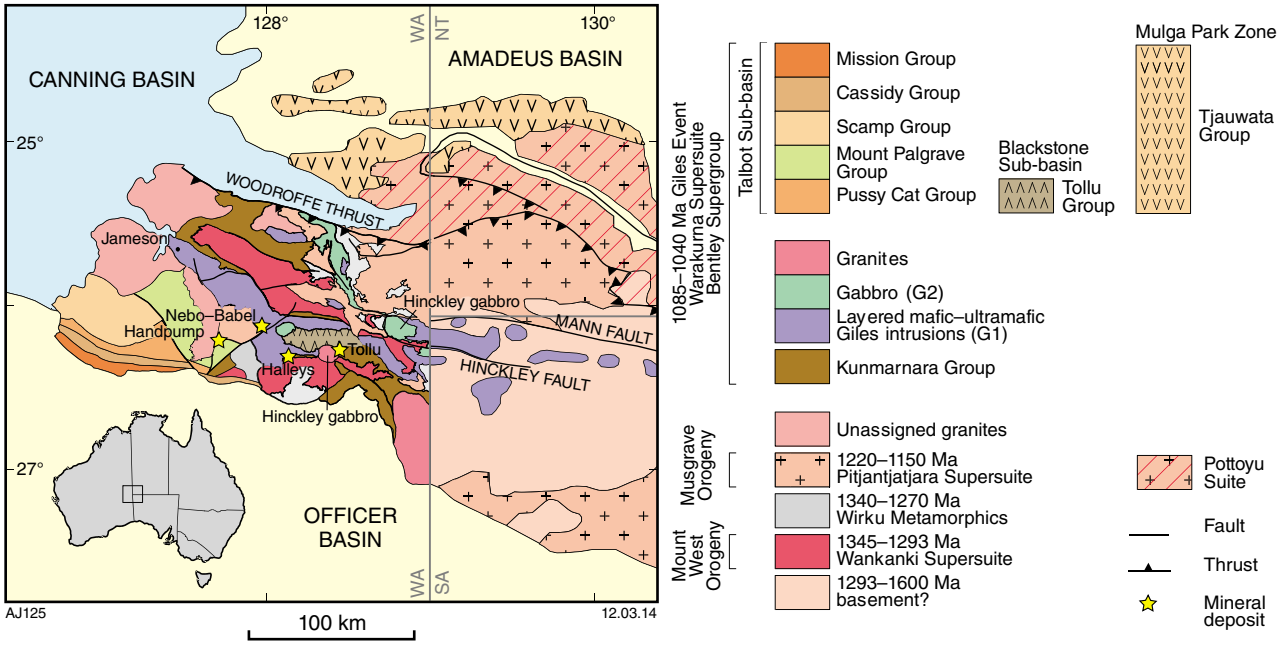

Figure 1. Regional geological sketch of the Musgrave Province within western central Australia (modified after Smithies et al., 2008; Glikson et al., 1996; Edgoose et al., 2004)

mineral systems components can be assigned subjectively based on expert knowledge, or estimated empirically from the distribution of known mineral deposits.

GIS-based automated prospectivity analysis

A mineral prospectivity model can be defined as a simplified mathematical function representing the relationship between targeting criteria (represented by predictor maps) and the targeted mineral deposits (Porwal, 2006). A variety of linear and non-linear functions are used to approximate the relationship between exploration criteria and mineral deposits. Based on the type of function used, mineral prospectivity models are classified as linear (e.g. weights-of-evidence) or non-linear (e.g. fuzzy, logistic regression, neural networks, neuro-fuzzy, or Bayesian network classifiers). They have also been alternatively classified into data driven and knowledge driven, based on whether the model parameters are estimated using conceptual knowledge or empirical data. Weights-of-evidence modelling is a data-driven approach that uses the theory of conditional probability to quantify spatial association between a set of predictor maps and a set of known mineral deposits (Agterberg, 1989; Agterberg and Bonham-Carter, 1990; Bonham-Carter and Agterberg, 1990).

The fuzzy model at a glance

Knowledge-driven mineral prospectivity mapping is appropriate in frontier or less-explored (or so-called 'greenfields') areas where no or very few mineral deposits of the type sought are known. Fuzzy logic is a knowledge-driven approach for prospectivity mapping that relies on subjective input for choosing the input predictor maps and their associated weights.

Fuzzy logic (knowledge-based GIS-driven prospectivity) analyses establish the relationship between the spatial exploration datasets and the exploration model, and are often employed in regions where there are few or no known mineral occurrences with which to 'train' the exploration datasets. Knowledge-driven techniques, such as fuzzy logic analysis, are subjective in that the 'explorer' determines the relative significance of the exploration datasets and assigns a significance weighting based on the exploration model. Knowledge-based prospectivity mapping is achieved by extracting the spatial relationships from exploration datasets on the basis of the exploration model, quantifying these spatial relationships and integrating them using mathematical operators chosen by the user. Fuzzy logic is a form of many-valued logic that deals with reasoning that is approximate rather than fixed and exact. Fuzzy logic variables may have a truth value that ranges in degree between 0 and 1, contrasting with traditional logic theory, where binary sets are either true or false.

The fuzzy-logic overlay method has been used widely in mineral potential assessments. For instance, An et al. (1991) used fuzzy logic to combine geophysical and geological maps for prospectivity analysis of base metal and iron deposits using expert knowledge to define the relative importance of a proxy (fuzzy-membership value or map weight). Bonham-Carter (1994) described examples of using fuzzy-logic overlay for assessing gold potential and landfill suitability. D'Ercole et al. (2000) used a fuzzy-logic approach to make a prospectivity analysis

of Mississippi Valley-type deposits using geochemical, stratigraphic, geophysical, and structural criteria. Knox-Robinson (2000) applied vector algebra in fuzzy modelling, where favourability was expressed as a vector whose direction is defined by 'fuzzy-membership value', and magnitude is defined by 'fuzzified confidence value', which represents a measure of the modeller's confidence in a prospectivity value (e.g. accuracy with which it has been mapped). Carranza and Hale (2000) applied fuzzy logic to map gold potential using derivatives of geological maps as inputs. Porwal et al. (2003) incorporated a data-driven approach in fuzzy modelling. A data-driven model uses a piece-wise linear function based on quantified spatial associations between predictor patterns and known mineral deposits for deriving fuzzy-membership values of input predictor maps. In other words, this data-driven approach simulates human reasoning for deriving fuzzy-membership values.

Of the many spatial modelling techniques, the knowledge-driven fuzzy logic model (Bonham-Carter, 1994) provides a convenient way to interpret and transfer expert knowledge into a quantitative spatial analysis using a GIS platform.

A generalized fuzzy model for mineral prospectivity mapping can be defined as follows: If X is a set of n predictor maps X_i (i =1 to n) with r patterns (or classes) denoted generically by x_{ij} (j =1 to r), then n fuzzy sets $\tilde{A}_i$ in X, containing favourable indicators for the targeted mineral deposit type, can be defined as follows (Porwal et al., 2003):

$$\tilde{A}_i = \left(x_{ij}, \mu_{\tilde{A}_i}\right) \mid x_{ij} \in X_i \qquad \text{Equation 1}$$

where μ_A is the membership function for estimating the fuzzy membership value of x_{ij} in the fuzzy set $\tilde{A}_i$. The fuzzy membership value defines how each point in the input space is mapped to a given set. Membership value (or degree of membership) is usually a real number between 0 (non-membership) and 1 (full membership). The fuzzy membership function can be linear, Gaussian, or any other appropriate function. Here we used the following linear function:

$$\mu_{\tilde{A}_i} = \frac{m_i \times w_j \times cf_i}{1000} \qquad \text{Equation 2}$$

where m_i is the map weight, w_j is the class weight and cf_i is the confidence factor.

Assigning map weights, class weights and confidence factors

An understanding of the different mineral systems, and the geological characteristics and history of a region are used to assign the map weights and class weights to the different fuzzy predictor map. The fuzzy membership values for the predictor maps are estimated from the map weights, class weights, and confidence factor using Equation 2.

Map weights correspond to the importance of the predictor map in the fuzzy analysis, i.e. the importance of that component in the mineral system, and are subjectively assigned a value between 1 and 10 (10 being the most prospective), based on expert knowledge. For example, faults of a particular age or style may be weighted higher than others, based either on empirical observations or conceptual understanding. Class weights indicate the spatial variations in each prospective feature, and these are in most cases assigned values based on a spatial distribution model, such as the distance to a fault or the density of features within a certain area. The confidence factor relates to the interpreters confidence in the precision with which the predictor map describes the desired component of the mineral system; for example, maps based on poorly distributed data may receive a low confidence factor. Maps that use proxies that are a poor descriptor of the desired mineral system component may also receive low confidence factors. Zero values or dummies are not assigned because these values generate instabilities in the fuzzy inference network.

Fuzzy modelling is implemented in the following two steps: 1) assigning map weights, class weights and confidence factors, and estimating fuzzy membership values for the fuzzy predictor maps; and 2) combining the fuzzy predictor maps using an appropriate fuzzy inference network to derive the fuzzy prospectivity map (Joly et al., 2012).

The use of subjectively derived fuzzy membership layers is a useful way of incorporating geological knowledge in an automated GIS-based method but does have three main drawbacks. First, there is a loss of information when translating raw data values to fuzzy membership values because a whole class or range of raw data values must be mapped to a single fuzzy membership value. Second, the fuzzy membership values are usually applied according to the degree to which parameter values conform to a deposit model, which itself may be flawed. Third, the assignment of fuzzy membership values is subjective (e.g. D'Ercole et al., 2000). Spatial analysis can provide a basis for estimating the fuzzy membership values; for example, the use by Knox-Robinson and Wyborn (1997) of statistically determined fuzzy membership values. However, for poorly known regions like the WMP, where known mineral deposits and occurrences are not necessarily representative of the spatial properties of their mineral systems, subjective judgement is less prone to error. We used this approach to determine the structure of the fuzzy inference net and to select the fuzzy operators used to combine the GIS layers.

Combining fuzzy membership values

The combination of different predictor maps in a fuzzy system is carried out by operators. Bonham-Carter (1994) described five operators that are commonly used for combining mineral exploration-related datasets. These are fuzzy AND, fuzzy OR, fuzzy algebraic PRODUCT, fuzzy algebraic SUM, and fuzzy GAMMA operators (see Joly et al., 2011 for more details). For example, if several prospectivity factors are all requirements of the mineral system then the fuzzy AND is used, which will return the lowest fuzzy value of all factors. In contrast, if the

requirement is that at least one of several prospectivity factors is present, then the fuzzy OR is used, which will return the highest fuzzy value. Fuzzy PRODUCT is a penalty function that returns the product of several fuzzy values (which are all less than one). Therefore, fuzzy PRODUCT provides a way to combine values without just returning the value of a single set, and yet strongly penalizing areas with low fuzzy value in any of the input factors.

Application to the west Musgrave Province

In greenfields exploration areas like the WMP, where there are few known prospects and deposits, knowledge-driven fuzzy models are the most appropriate models for prospectivity analysis. This is because the factors affecting different mineral systems are similar. Hence, many of the predictor maps created for one commodity may be applicable to another commodity. For example, in identifying potential physical traps, only physical characteristics such as rheology, permeability, proximity to fault, and spatial density of faults are considered. Likewise, chemical traps are identified based on whole-rock geochemistry.

All information relevant to prospectivity analysis of the WMP was extracted from public-domain sources. The extent of mapped geological entities was taken from the GSWA interpreted bedrock geological map (GSWA, 2010a). Whole-rock chemical data used in this study were extracted from the GSWA state geochemistry database (GSWA, 2010b) and GA OZCHEM database (Geoscience Australia, 2007). These data were analysed in their logarithm form (Singer and Kouda, 1999). Subsequently, threshold values Z_{log} — which, for an element concentration [X], corresponds to log [X] – mean(log [X])/2σ(log [X]) — were used to generate related predictor maps (see Cheng, 2007 for details). Element ratios and concentrations are interpolated using the inverse distance weighted (IDW) algorithm, a spatial autocorrelation technique that defines objects that are close to the model cell as more influential than those that are more distant. It is especially suitable if geochemistry sampling is unevenly distributed, as is the case in the WMP. ArcGIS software was used to carry out the analysis using a 100 m unit cell size. An understanding of the different mineral systems and the geological characteristics and history of the WMP (Table 1) was used to assign the map weights and class weights of these geochemical data to the fuzzy predictor maps.

The prospectivity analysis was undertaken on only part of the WMP because of uneven data coverage (i.e. the final prospectivity analysis covers only areas with reasonably high geochemical sample density). This is necessary because many of the mineral targeting elements, such as the chemical traps and pathways, are best represented by geochemical proxies. It also reduces the influence of boundary effects related to the lack of data at map edges and minimizes interpolation problems.

Overview of the geology of the west Musgrave Province

The Musgrave Province (Fig. 1) is a Mesoproterozoic belt bounded by Neoproterozoic to Paleozoic basins. It is expressed on geophysical images as a series of east-trending anomalies covering an area up to 800 km long and 350 km wide that straddles the borders between the Northern Territory, Western Australia, and South Australia. It lies at the convergence of Australia's main Proterozoic structural trends that reflect the amalgamation of the North, West, and South Australian Cratons.

The composition and structure of the basement to the province is cryptic. However, the Nd-isotopic and Hf-isotopic evolution of nearly all rocks in the province requires the presence of a Paleoproterozoic to early Mesoproterozoic juvenile basement, along with a minor Archean component (Smithies et al., 2010; Wade et al., 2005). Kirkland et al. (2012) recently showed that a major crust-forming event at c. 1900 Ma may have been the dominant contributor to the basement of the Musgrave Province.

Outcrop in the WMP includes rocks formed during several Mesoproterozoic events: a c. 1400 Ma unnamed event, the 1345–1293 Ma Mount West Orogeny, and the 1220–1150 Ma Musgrave Orogeny. The oldest, and least exposed, of these is a recently identified, and unnamed, event that involved intrusion and possible extrusion of felsic calc-alkaline magmas of the Papulankutja Supersuite and contemporaneous redistribution of this material into localized sedimentary basins at c. 1400 Ma (Howard et al., 2011; Kirkland et al., 2013). The oldest widespread exposed rocks in the WMP are paragneisses of the Wirku Metamorphics (Table 1). The protoliths to these were deposited between c. 1360 and 1307 Ma (Wade et al., 2005; Smithies et al., 2010; Evins et al., 2010; Howard et al., 2011), then metamorphosed at granulite facies, contemporaneously with the emplacement of the felsic magmas of the 1336–1293 Ma Wankanki Supersuite during the 1345–1293 Ma Mount West Orogeny (Fig. 1; Howard et al., 2007; Smithies et al., 2009; Smithies et al., 2010). The c. 1220–1150 Ma Pitjanjatjara Supersuite (Fig. 1) was subsequently emplaced during the 1220–1150 Ma Musgrave Orogeny, contemporaneously with widespread granulite facies metamorphism.

The Mount West and Musgrave Orogenies are both probably related to convergence of the South Australian Craton with the combined West and North Australian Cratons to produce a larger tectonic belt that included the Albany–Fraser Orogen (e.g. Myers et al., 1996; Aitken and Betts, 2008). The tectonic setting of these events is somewhat uncertain, but it is likely that the Mount West Orogeny reflects tectonics dominated by subduction and then subsequent collision, whereas the Musgrave Orogeny reflects the intraplate aftermath of this event (Smithies et al., 2011). The interpretation that orogenesis is associated with colliding cratonic blocks is important for assessing mineral prospectivity because magmatic metal-sulfide and iron oxide–copper–gold deposits both have a well-defined spatial association with the margins of the cratons (Begg et al., 2010; Maier and Groves, 2011).

Table 1. Structural evolution of the West Musgrave Province

Age (Ma)	*Event*	*Specified event* [e,f]	*Age (Ma)*	*Fabric description*	*Magmatic event*	*Tectonic event*	*Metamorphic event*
1345–1270	Mount West Orogeny: all basement lithologies are characterized by the scarcity of sulfur-bearing minerals, and whole-rock S concentrations are generally <100 ppm (Glikson et al.,1996)	MWO1	c. 1300	Earliest fabric (bedding?) in Wirku Metamorphics, and foliation in Wankanki Supersuite	Wankanki Supersuite	Convergent plate margin	Amphibolite to granulite facies metamorphism of paragneiss and orthogneiss
		MWO2		Tight to isoclinal folding of MWO1, reasonably widespread throughout area, but not pervasive			
1220–1150	Musgrave Orogeny	EMO	c. 1220	Foliation and folds in Wankanki/Wirku Basement and Pitjantjatjara Supersuite. Folded by MMO	Pitjantjatjara Supersuite	Intraplate orogen, kinematics poorly constrained	Amphibolite to granulite facies ultra-high temperature metamorphism (T >750°C; P = 5 ± 1 kb)
		MMO	1220–1180	Between early and late Pitjantjatjara Supersuite suites. Widespread ~NE oriented close folding of Wankanki/Wirku basement and parallel shear zones	Kulgera suite granites (including charnokites) 1185 ± 5 Ma[b, c]		
		LMO_MP	<1165	Fabric in Pitjantjatjara Supersuite N of Woodroffe Thrust			
		LMO	<1145	E–W trending fabric in Umutju granite – could be much younger			
			1155–1135	Fabric in Wirku Metamorphics and of Pitjantjatjara Supersuite at Cohn Hill			
1085–1040	Giles Event	S_K	1085–1078	Bedding in Kunmarnara Group	~1\100 Ma Type A dolerite dyke suite[c]	Intraplate rift event	Emplacement $P = 6 \pm 1$ kb; lower pressures in the western part of the block; local recrystallization of the intrusive lithologies
		S_G1	1078–1075	Igneous layering or contact in Giles 1 intrusions	Giles Suite Intrusions 1078 ± 3 Ma[c]	Warakurna LIP[d]	Emplacement of Bushveld-scale layered Giles Complex at c. 1080 Ma and 33–16 km depth: most abundant rock types are olivine gabbronorite to gabbronorite and troctolite
		S_G2	1078–1074	Igneous layering or contact in Giles 2 intrusions			Subsequent emplacement of smaller, more fractionated, shallow-level mafic intrusions: no published ages
		EGE	1078–1075	Early fabrics and folding in Giles Complex intrusions. Synmagmatic deformation			

Age (Ma)	Event	Specified event [e,f]	Age (Ma)	Fabric description	Magmatic event	Tectonic event	Metamorphic event
		EGE2	~1075	N–S oriented tight to isoclinal folding and shear zones in Murray Range and Hinckley Gabbro. Syn Giles 2			
		S_T	1073–1068	Bedding in Tollu Group	Smoke Hill Volcanics 1078±3 Ma[c]		
		S_TW	1090 – 1040	Bedding in Tjauwata Group			
		S_WK	1085–1040	Deformation surrounding Warakurna Supersuite granitoids	Tollu Granitoid 1076 ± 9 Ma, Winburn Granite 1077 ± 7 Ma		Later emplacement of A-type granites: roughly same age as Giles Complex, probably c. 1078 Ma
		MGE1	1076–1072	~E–W oriented tight folding of stratigraphy up to Tollu Group. Syn-Tollu granitoid			
		MGE1_MP		Tight N-trending folding of LMO_MP			
		S_PC	1071–1065	Bedding/contact in the Pussy Cat Group	Kathleen Ignimbrite 1071 ± 5 Ma		
		LGE1	1071–1065	NE oriented normal faults, some associated with large magnetic lows. Includes proto-Cavenagh fault. Post-dates Kathleen ignimbrite (1071 ± 5 Ma), pre-dates Warakurna Supersuite granite (1065 ± 9 Ma). Nebo–Babel intruded into this fabric?	Nebo–Babel 1068.0 ± 4.3 Ma[a]		
		LGE2	1071–1065	ESE-oriented shear zones with relatively minor folding			
		LGE2_MP		ESE-oriented shear zones and close folding of prior fabrics			
		S_P	1077–1064	Bedding in the Palgrave Group	Granitic dyke suites 1068±6 Ma; 1052±11 Ma		
		LGE3	1068–1067	N–S oriented shear zones and dykes and fault–related folding. Includes Jameson Fault of Seat et al. (2007), which cuts Nebo–Babel, and prospective Harcus intrusion in South Australia			
		S_S	1072 ± 8	Saturn intrusion emplaced, with associated deformation			
		S_C	1065–1057	Bedding in the Cassidy Group			

Table 1. continued

Age (Ma)	*Event*	*Specified event* [e,f]	*Age (Ma)*	*Fabric description*	*Magmatic event*	*Tectonic event*	*Metamorphic event*
1050–800	Post-Giles Events						
		S_M	<1055	Bedding in the Mission Group			
~1000		PGE1	?	NNE–SSW oriented dykes. May be Kullal Dolerite (undated)	NE-trending Type C olivine dolerite dyke suite[c]		
~800		S_DQ	1040–800	Bedding in Dean Quartzite (sediment)	NW-trending Type B quartz dolerite dykes[c]	Rifting of Rodinia	
600–520	Petermann Orogeny	EPO		Shear zones of variable but dominantly E–W orientation. Minor folding		Intraplate orogenesis linked to Gondwana assembly	Locally high pressure conditions (T~650°C, P=12 kb)
		EPO_MP		Earlier generation of E–W oriented shear zones			
		EPO_MP2		Petermann Nappe and westward extension			
		MPO		ESE-oriented anastomosing network of shear zones, with subordinate SW oriented shear zones. Minor folding			
		MPO_MP		N-directed thrusting			
		LPO		Late activity on the Woodroffe Thrust and associated splays			
		LPO_MP		Late activity on the Woodroffe Thrust and associated splays			
450–350	Alice Springs Orogeny	ASO	Permian	S-directed thrusting at southern margin of province, and reactivation of N-trending LGE3 shear zones		Intraplate orogenesis linked to Gondwana Assembly	
		ASO_MP		North trending shear zones			

NOTES: (a) U–Pb SHRIMP zircon crystallization age by Seat (2008)
(b) U–Pb on zircons by Mabuko et al. (1996)
(c) U–Pb on zircons by Sun et al. (1996)
(d) U–Pb on zircons by Wingate et al. (2004)
(e) MP modifier indicates that the deformation is observed in the Mulga Park Domain
(f) E, P or S are used to indicate whether deformation predates this unit (e.g. Early-Musgarve Orogeny 1 is EMO), is synchronous with the unit (e.g. syn-Tollu group is S_T), or post-dates the unit (e.g. Late-Petermann Orogeny is LPO)

The next major tectonic event to affect the WMP was the c. 1085–1040 Ma Giles Event. This was characterized by voluminous intraplate mafic and felsic magmatism of the Warakurna Supersuite (Fig. 1, Daniels, 1974; Ballhaus and Glikson, 1989, 1995; Ballhaus and Berry, 1991; Glikson et al., 1996). The Giles Event began with deposition of rocks of the Kurnmarnara Group onto exposed basement. These rocks form the earliest component of the Bentley Supergroup, consisting of a typical early-rift sequence of basalts and conglomerates (Fig. 1; Evins et al., 2010). The Kurnmarnara Group was then intruded by layered Giles 'G1' intrusions (e.g. Jameson intrusion, Fig. 1) and shortly after by the massive Giles 'G2' gabbro intrusions (e.g. Hinckley gabbro, Fig. 1). Rapid uplift and erosion brought these intrusions to the surface, followed by deposition of the remainder of the Bentley Supergroup, a c. 10 km-thick sequence of bimodal volcanics and associated sedimentary units (Fig. 1). Deformation continued throughout the Giles Event (Evins et al., 2010) and granitic plutons of the Warakurna Supersuite (e.g. Tollu granite, Fig. 1) were emplaced throughout the area over a wide time span from c. 1078 to 1060 Ma.

The Warakurna Supersuite was first recognized as a large igneous province by Wingate et al. (2004). Morris and Pirajno (2005) interpreted it to result from a mantle plume between 1078 and 1070 Ma, although Evins et al. (2010) argued that prolonged duration of the Giles Event and the rift-like architecture of the crust are incompatible with a simple mantle plume.

Magmatism in the WMP after the Giles Event is limited to mafic dykes and rare pegmatites emplaced at c. 1000 Ma (Kullal dykes and a garnet-bearing aplite dyke, Table 1), and mafic dykes emplaced at c. 825 Ma (Gairdner Dolerite) and 750 Ma (Howard et al., 2011). However, these intrusions are volumetrically minor.

Inferred broad crustal subsidence at c. 800 Ma initiated deposition in the Centralian Superbasin over two million square kilometres of Australia (Walter et al., 1995). This basin was disrupted at 540–600 Ma by a central uplift, and then dismembered by later Paleozoic tectonism into numerous smaller depocentres such as the Amadeus and Officer Basins (Fig. 1). There may have been an extensive carapace of sedimentary rocks over the Musgrave Province at this time (Walter et al., 1995). The Late Neoproterozoic Petermann Orogeny near the margins of the province, was caused by north-directed thrusting on shallow-dipping faults (e.g. Woodroffe Thrust, Piltardi Detachment Zone; Flöttmann et al., 2004; Raimondo et al., 2010), and burial of the northeastern parts of the WMP to subeclogite facies, then its exhumation to its previous crustal level (Scrimgeour and Close, 1999). This event is characterized in the central part of the WMP by north–south shortening and transpressional motion on pre-existing east-southeast (dextral) and northeast (sinistral) trending structures (e.g. Mann Fault, Hinckley Fault, Fig. 1; Aitken et al., 2009a). Major shear zones may preserve large Moho offsets, indicating the uplift of the central part of the WMP as a 'pop-up' structure (Lambeck and Burgess, 1992; Aitken et al., 2009b). The Petermann Orogeny has had relatively little influence on the southwestern parts of the WMP (Fig. 2; Smithies et al., 2008).

The 450–300 Ma Alice Springs Orogeny is represented in the Musgrave Province by south-directed thrusting at the southern margin and a monoclinal upturning of Ordovician sedimentary strata within the Officer Basin (Lindsay and Leven, 1996). The north-trending Lasseter–Mundrabilla Shear Zone probably formed initially during the Giles Event or earlier (Fig. 9), and was likely active during the Alice Springs Orogeny, separating shortening in the east from extension in the west (Braun et al., 1991).

The WMP can be subdivided internally into several fault-bounded tectonic zones, based on differences in lithology and metamorphic grade (Fig. 2). The southernmost Mamutjarra Zone is characterized by a mixture of high-grade gneisses and low-grade Warakurna Supersuite rocks. The central Tjuni Purlka Zone is characterized by high-grade gneiss and granites (Wirku Metamorphics, Wankanki and Pitjantjatjara Supersuites), with limited exposures of the Warakurna Supersuite. The Walpa Pulka Zone lies north and east of the Tjuni Purlka Zone, and is characterized by very high grade metamorphic rocks (dominantly Pitjantjatjara Supersuite and Wirku Metamorphics), and the virtual absence of Warakurna Supersuite rocks. Importantly, contacts between the Tjuni Purlka Zone and both the Mamutjarra and Walpa Pulka Zones were major channels for magmas of the Warakurna Supersuite, and major G1 and G2 intrusions are preserved along these contacts. The amphibolite facies Mulga Park Zone lies unexposed to the north of the Woodroffe Thrust, as the continuation of a terrane mapped to the east in the Northern Territory, and mainly consists of granite with a few screens of amphibolite and metasedimentary rocks (Camacho and Fanning, 1995). The Mitika Zone lies at the western end of the WMP, bounded by the Mulga Park Zone to the north, the Tjuni Purlka Zone to the east, and the Mamutjarra Zone to the south.

Structural analysis of aeromagnetic data

Methods and constraints

To assist with the prospectivity analysis of the WMP, a comprehensive structural analysis was undertaken using aeromagnetic (and gravity) data and the geological framework provided by GSWA (GSWA, 2010a, and references therein). These kinds of structural analyses have proved useful in studies of the Musgrave Province in South Australia and the Northern Territory (Aitken et al., 2008; Aitken and Betts, 2009a,b). The specific aims of the new aeromagnetic interpretation are to: 1) better understand the structural history and architecture of the area; 2) identify the most important structures in the region; and 3) assign ages of formation and movement to individual structures. The results constitute a new dataset created specifically for the prospectivity analysis.

Geology was constrained by 1:100 000-scale mapping since 2004 over the central eastern part of the WMP.

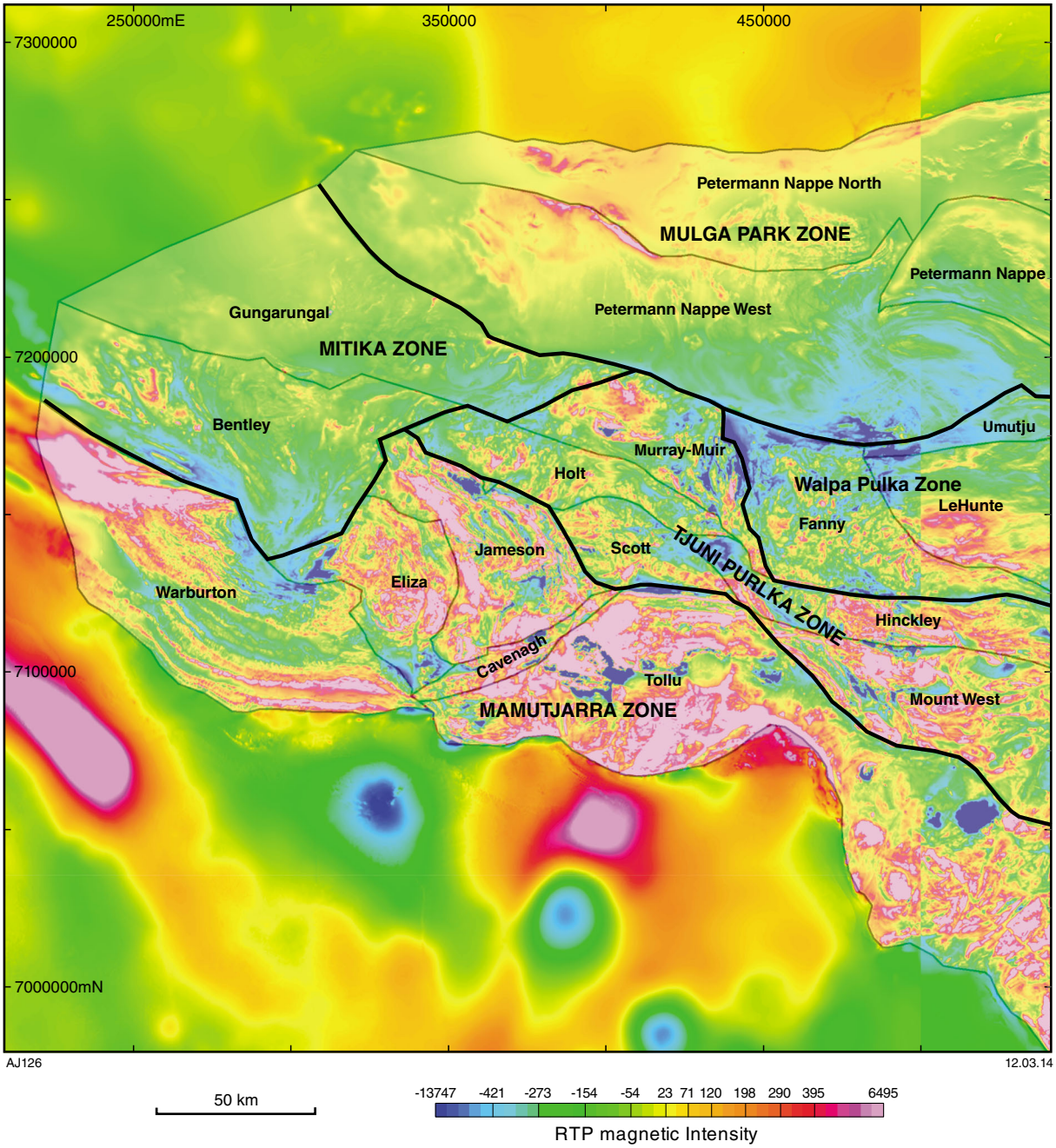

Figure 2. **Map showing the magnetic domains defined for the aeromagnetic interpretation, overlain on a reduced-to-pole magnetic intensity image. Heavy black lines are major tectonic zone boundaries.**

This mapping includes interpreted solid geology in areas lacking outcrop, and structural measurements from the GSWA's WAROX database (strike, dip and type of foliations, trend and plunge of fold axes). Elsewhere, 1:250 000-scale surface mapping dating from the 1960s was the best constraint available. The interpretation recognized 18 structurally distinct domains, each with a different magnetic character and evolution from its neighbours (Fig. 2, Table 2). Most domains are bounded by major shear zones, which typically show activity late in the evolution of the Musgrave Province, but have probable earlier histories. These domains are essentially subdivisions of the major tectonic zones identified in previous work (Table 2, Fig. 2).

Each domain was interpreted individually by defining magnetic form lines for early structures, then inferring later generations of structures from the deformation of these, and from relative timing with respect to intrusive and sedimentary events.

The magnetic interpretation identified a local sequence of deformation events within each domain and integrated these with the stratigraphy on the basis of local overprinting relationships with mapped geology. The stratigraphic position of deformation is poorly constrained in many places, leading to uncertainty arising from:

- a lack of local outcrop to constrain the geological interpretation of subsurface units
- a lack of radiometric dating, especially in the regions not recently mapped, to constrain the age of geological units
- the rapid evolution of tectonic events relative to the sensitivity of geochronological age estimates; this is particularly a problem for the Giles Event (see Evins et al., 2010)
- difficulty in correlating stratigraphy in newly mapped regions with that in regions of older, less detailed mapping.

Individual domain interpretations were integrated into a regional-scale analysis by correlating structural elements in terms of stratigraphic position, shared overprinting relationships with earlier events, structural style and orientation. These correlations are not unique, and so consideration is given to how readily the deformation in each domain can be correlated to deformation in other domains (Fig. 3).

Table 2. Magnetic character of the defined zones

Domain	*Zone*	*Magnetic character*
Tollu	Mamutjarra	Highly varied magnetic structure with high to very high amplitude magnetic fabrics in several orientations
Cavenagh	Mamutjarra	High amplitude SW–NE fabric associated with Cavenagh Fault
Jamieson	Mamutjarra	Very high amplitude NW–SE magnetic fabric in north, associated with Jamieson layered intrusion. Magnetic texture becomes less directional in south, but anomalies are still high amplitude
Eliza	Mamutjarra	Complex and varied structuring, including distinct circular feature. Moderate to high amplitude anomalies dominate
Warburton	Mamutjarra	High amplitude east trending magnetic fabric
Bentley	Mitika	Low to moderate amplitude magnetic amplitudes of varied orientations
Gungarungal	Mitika	Low amplitude, highly complex magnetic fabric
Mt West	Tjuni Purlka	SE trending very high amplitude magnetic fabric
Hinckley	Tjuni Purlka	Low to very high amplitude fabrics of multiple orientations
Scott	Tjuni Purlka	Moderate amplitude magnetic anomalies. SE and NE orientations dominate
Holt	Tjuni Purlka	Moderate amplitude magnetic fabrics of varied orientation
Murray-Muir	Tjuni Purlka	Moderate to very high amplitude intensity. Fairly high amplitude fabrics of ESE and NNW orientation
Fanny	Walpa Pulka	Moderate to high intensity, with high amplitude stippled texture
LeHunte	Walpa Pulka	Low to high intensity, E–W oriented streaky texture
Umutju	Walpa Pulka	Low intensity, smooth texture
Petermann Nappe West	Mulga Park	Moderate intensity. Smooth overall, but with low amplitude magnetic fabrics
Petermann Nappe	Mulga Park	Low to moderate intensity, with moderate amplitude SE oriented fabric
Petermann Nappe North	Mulga Park	Low to high intensity, with moderate amplitude fabrics of variable orientation

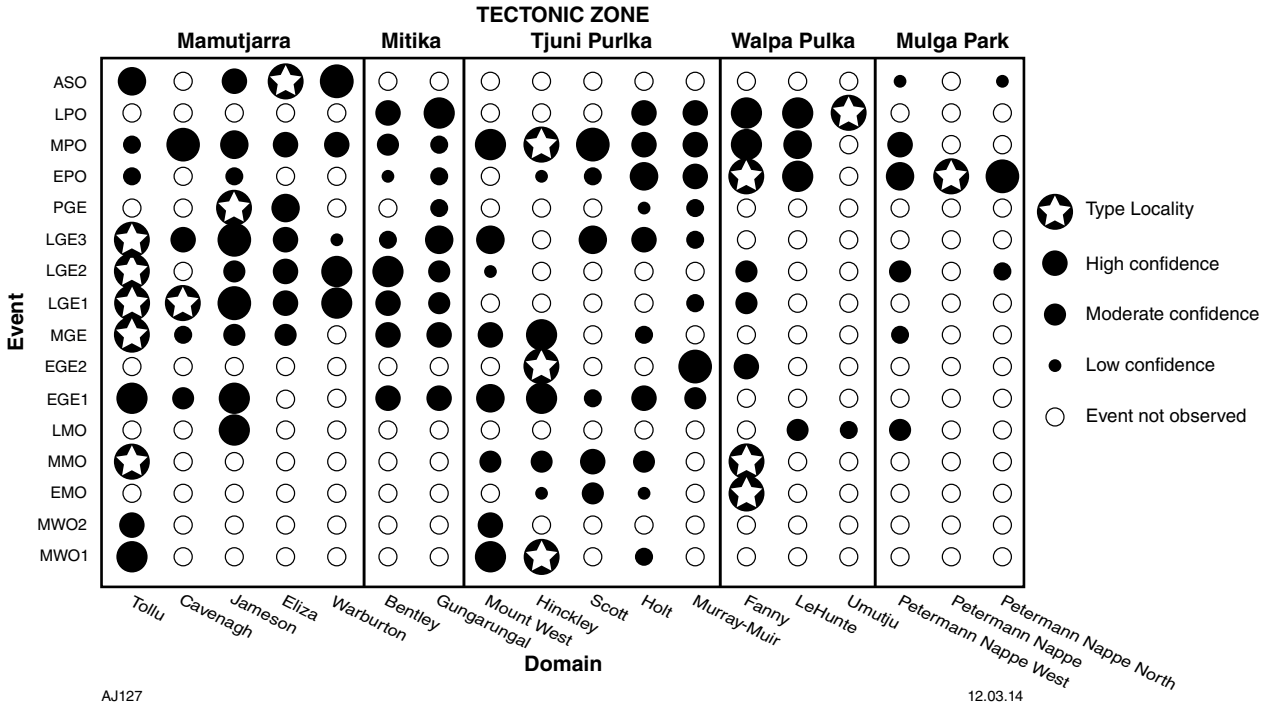

Figure 3. Domain-event confidence: degree to which the deformation imaged for each event, in each domain, is matched to the overall character of that event. Small circles indicate areas where the interpreted event is poorly constrained, isolated, and where it has conflicting character to other domains. Large circles indicate a high level of confidence in the interpretation of that event in that domain, and good correlation with the overall character of that event. MWO1 – Mount West Orogeny, first deformation; MWO2 – Mount West Orogeny, second deformation; EMO – Early Musgrave Orogeny; MMO – mid-Musgrave Orogeny; LMO; late Musgrave Orogeny; EGE1 – early Giles Event, first deformation; EGE2 – early Giles Event, second deformation; MGE – mid-Giles Event deformation; LGE1 – late Giles Event, first deformation; LGE2 – late Giles Event, second deformation; LGE3 – late Giles Event, third deformation; PGE1 – post-Giles Event deformation event; EPO – early Petermann Orogeny; MPO – mid-Petermann Orogeny; LPO – late Petermann Orogeny; ASO – Alice Springs Orogeny

Magnetic data sources

Aeromagnetic data from the WMP were compiled from nine separate surveys of differing ages (1996–2006) and flight-line spacings (200–400 m), and with either east–west or north–south flight-line orientations. To produce a consistent regional grid, levelled line data from each of these surveys were gridded into individual grids with 100 m cell size, and these were merged together using the 4th edition of the Australian continent-scale magnetic grid (Milligan and Franklin, 2004) as a datum. The long-wavelength variations removed from individual grids during merging were recovered and used to correct individual survey readings. This process generated a database of magnetic observations with a common base level. The corrected data were gridded with a 100 m cell size using a kriging algorithm and then reduced to pole to produce the regional total magnetic intensity grid (Fig. 2).

Results

The aeromagnetic interpretation identifies eight key periods in the evolution of the structural architecture of the WMP (Fig. 4): the Mount West Orogeny, the Musgrave Orogeny, the early, middle and late periods of the Giles Event, post-Giles deformation, the Petermann Orogeny, and the Alice Springs Orogeny (Tables 1 and 2). These are discussed individually below.

Mount West Orogeny (1345–1293 Ma)

This event is preserved in several early fabrics that overprint the Wankanki Supersuite and Wirku Metamorphics in the Tollu, Mount West, Hinckley, and Holt Domains, (Fig. 2), and that are in turn overprinted by the Pitjantjatjara Supersuite. The first event is defined by a relatively strong magnetic fabric (MWO1), which, at Mount Aloysius (Fig. 5b), correlates with layer-parallel gneissic banding in the Wirku Metamorphics and Wankanki Supersuite (Stewart, 1995). A similar fabric with a dominant west-northwest orientation is observed at Mount West, tightly folded and faulted about west-oriented structures (MWO2) that perhaps indicate a shear zone (Fig. 5c). The MWO1 magnetic fabric is isoclinally folded in the vicinity of Borrows Hill about structures also attributed to the Mount West Orogeny (MWO2), although this folding is not necessarily the same event as that observed at Mount West (A in Fig. 6b).

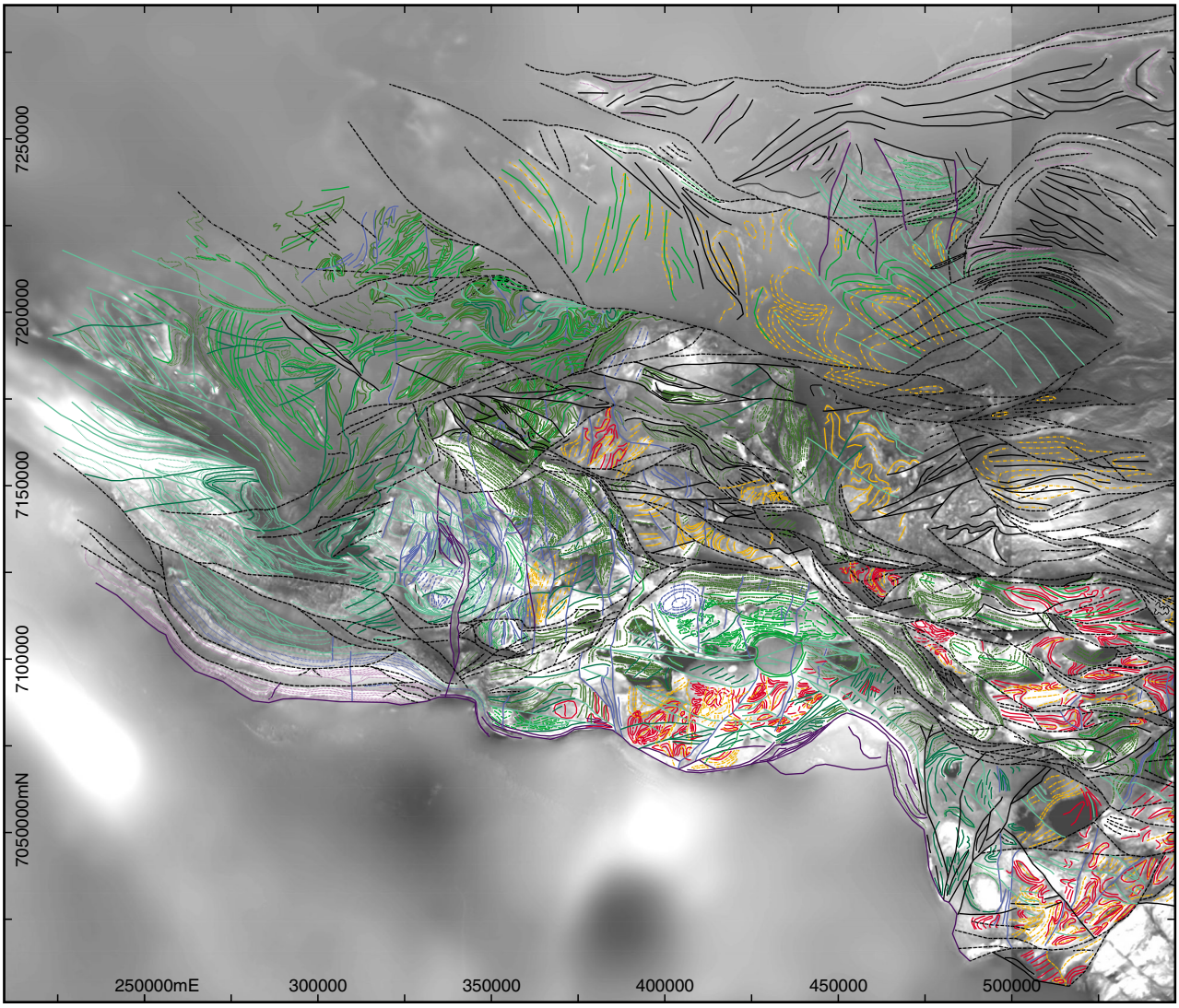

Mount West Orogeny

- MWO1 Earliest Fabric (bedding?) in Wirku Metamorphics, and foliation in Wankanki Supersuite
- MWO2 Tight to Isoclinal folding of MWO1.

Musgrave Orogeny

- EMO Foliation and folds in Wankanki/Wirku Basement and Pitjantjatjara Supersuite. Folded by MMO
- MMO Between early and late Pitjantjatjara Supersuite suites. Widespread ~ NE oriented close folding of Wankanki/Wirku basement and parallel shear zones.
- LMO E-W trending fabric in Umutju granite – could be much younger. Fabric in Wirku Metamorphics and of Pitjantjatjara Supersuite at Cohn Hill
- LMO_MP ?Musgravian? fabric in Pitjantjatjara Supersuite N of Woodroffe Thrust.

Giles Event

- S_K Bedding in Kunmarnara Group
- EGE Early fabrics and deformation in Giles Suite intrusions. Syn-G1 deformation.
- S_G1 Igneous Layering or contact in Giles Suite 1 intrusions
- EGE2 N-S oriented tight to isoclinal folding and shear zones in Murray Range and Hinckley Gabbro. Syn Giles 2
- S_G2 Igneous Layering or contact in Giles Suite 2 intrusions
- S_T Bedding in Tollu Group
- MGE1 ~ E-W oriented tight folding of stratigraphy up to Tollu Group. Syn Tollu Granitoid.
- MGE1_MP Tight N-trending folding of LMO_MP
- S_TW Bedding in Tjauwata Group
- S_WK Deformation surrounding Warakurna Supersuite granitoids
- S_PC Bedding/contact in the Pussy Cat Group
- LGE1 NE oriented shear zones
- S_P Bedding in the Mount Palgrave Group
- LGE2 E-SE oriented shear zones with minor folding
- LGE2_MP ESE oriented shear zones and close folding of prior fabrics
- LGE3 N-S oriented shear zones and dykes and fault-related folding. Syn Alcurra Dolerite Suite.
- S_S Deformation associated with the Saturn gabbro
- LGE4 NNE trending network of shear zones and folds, co-located dykes along some shear zones.
- S_C Bedding in the Cassidy Group

Post-Giles Event

- S_M Bedding in the Mission Group
- S_DQ Bedding in Dean Quartzite

Petermann Orogeny

- EPO Shear zones of variable but dominantly E-W orientation. Minor folding
- EPO_MP E-W oriented shear zones
- EPO_MP2 Petermann Nappe and westward extension.
- MPO ESE oriented anastomosing network of shear zones, with subordinate SW oriented shear zones. Minor folding
- MPO_MP N-directed Thrusting
- LPO Late activity on the Woodroffe Thrust and associated splays
- LPO_MP Late activity on the Woodroffe Thrust and associated splays

Alice Springs Orogeny

- ASO S-directed thrusting at southern margin of province, and reactivation of N trending LGE3 shear zones
- ASO_MP North trending shear zones

- All other values

Figure 4. Structural aeromagnetic interpretation of the West Musgrave Province. Structures are classified into the major province-wide tectonic events that were interpreted. Local overprinting relationships are largely robust; however, the overall classification is limited by the cross-domain correlations (Fig. 3). (Large-format PDF version of this figure is included on the USB accompanying this publication.)

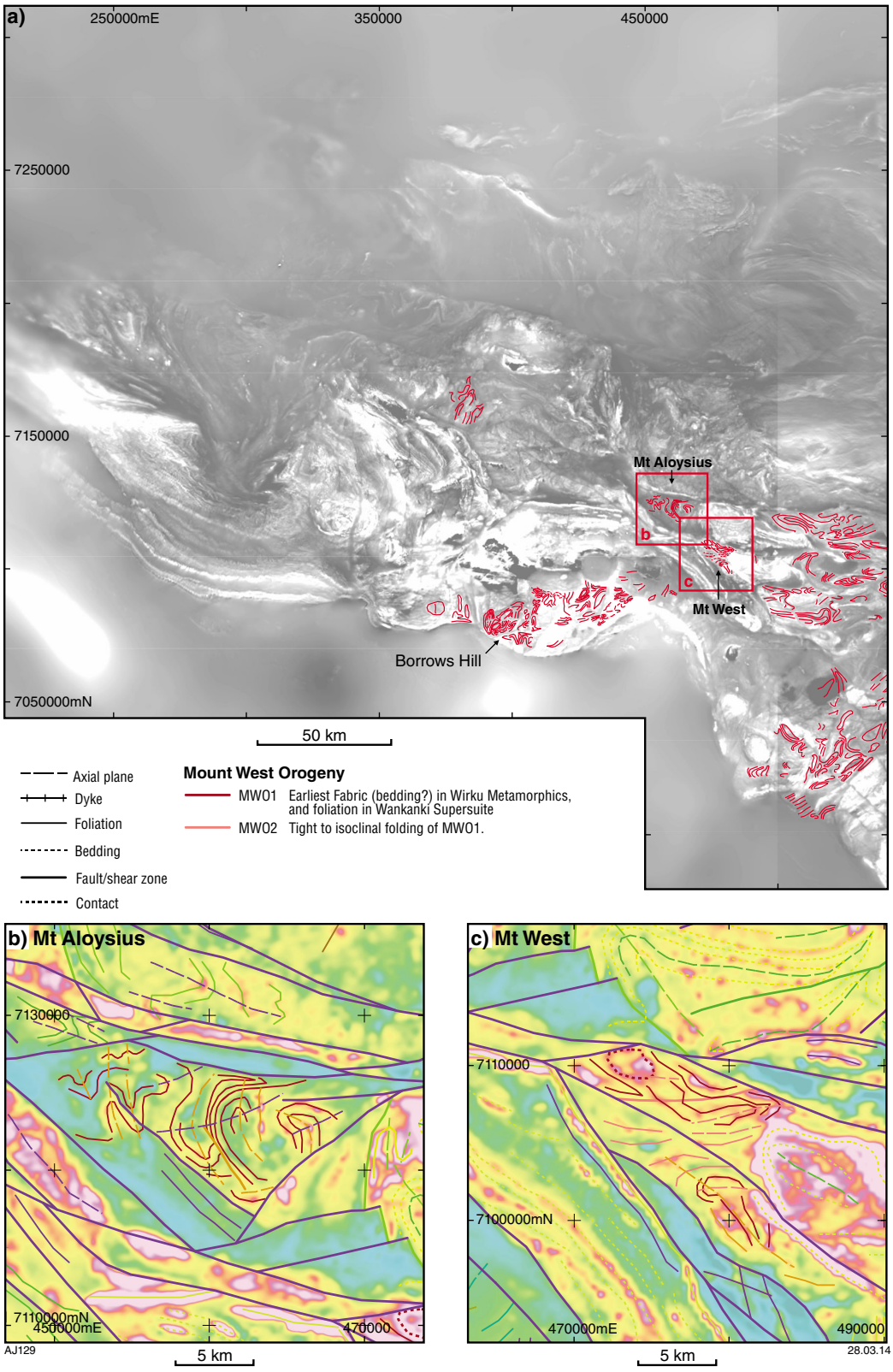

Figure 5. **Structures of the Mount West Orogeny: a) the distribution of structures attributed to the Mount West Orogeny, and two key localities; b) Mount Aloysius; and c) Mount West. At Mount Aloysius, complexly folded magnetic fabrics are defined that correlate well to the gneissosity identified in the Wankanki Supersuite and Wirku Metamorphics. See Stewart (1995) for a detailed structural analysis of this area. At Mount West, MWO1 has a dominant NW orientation, but is interrupted by an east-trending zone of deformation (MWO2). Another key locality, Borrows Hill (Fig. 6.) shows the same well-defined magnetic fabric in the Wirku Metamorphics, but also shows that this fabric is isoclinally folded in a second pre-Musgrave event (A). Other colours in the insets indicate structures from other events. See Figs 4, 6–12, and Table 1 for legends.**

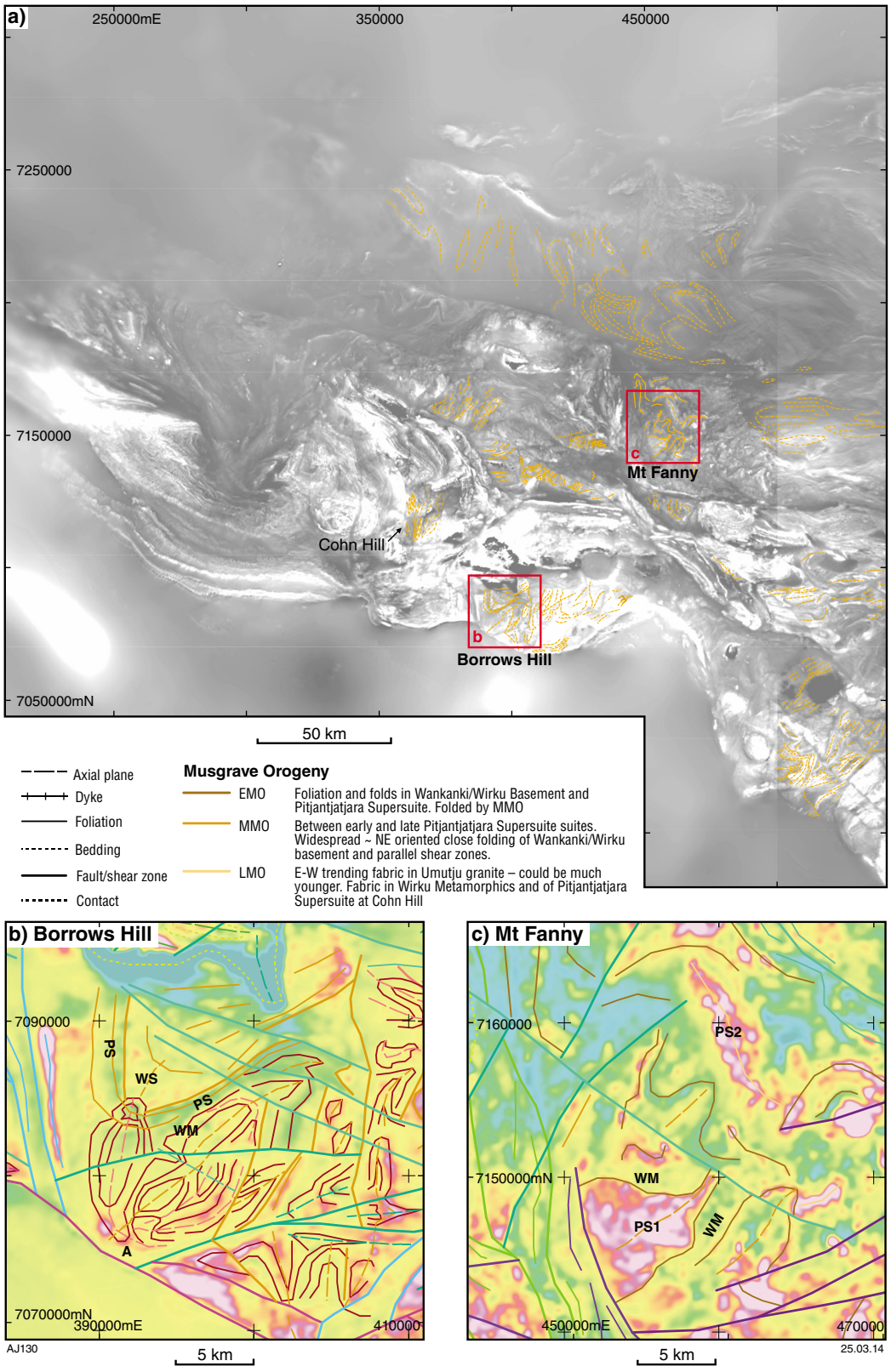

Figure 6. **Structures of the Musgrave Orogeny: a) the distribution of structures attributed to the Musgrave Orogeny, and two key localities; b) Borrows Hill; and c) Mt Fanny. At Borrows Hill, Pitjantjatjara Supersuite rocks (PS) have intruded into the contact between the Wankanki Supersuite (WS) and the Wirku Metamorphics (WM). Folding is interpreted to be synmagmatic. At Mt Fanny, the contact between magnetic Pitjantjatjara Supersuite (PS1), and non-magnetic Wirku Metamorphics (WM) is folded around a northeasterly plunging axis. Note the non-folded late Pitjantjatjara Supersuite pluton (PS2). Other colours in the insets indicate structures from other events. See Figs 4, 5, 7–12, and Table 1 for legends.**

Musgrave Orogeny (1220–1150 Ma)

Structures assigned to the Musgrave Orogeny (MO) have a close relationship with c. 1220–1150 Ma Pitjantjatjara Supersuite granites, reflecting pre-, syn- and post-magmatic deformation. Interpreted Musgravian structures are present throughout the eastern two-thirds of the region, though are best developed in the Tollu and Fanny Domains (Fig. 2). Key localities include Borrows Hill, Cohn Hill, and Mount Fanny (Fig. 6).

Early Musgrave Orogeny (EMO) structures are typically seen around contacts between early Pitjantjatjara Supersuite rocks and basement gneiss. At Mount Fanny, the contact between magnetic, migmatitic Pitjantjatjara Supersuite (PS1, 1219 ± 12 Ma, GSWA 174737, Bodorkos et al., 2008) and the non-magnetic Wirku Metamorphics (WM, 1272 ± 15 Ma, GSWA 183596, Kirkland et al., 2009a) is observed in both outcrop and aeromagnetic data (Fig. 6c).

The earliest Musgrave Orogeny structures are deformed around northeast-trending close folds inferred to have formed late during the Musgrave Orogeny event. The folds are commonly intruded by late-stage plutons of the Pitjantjatjara Supersuite. An example at Borrows Hill shows a shallowly northeast-plunging synform–antiform pair that affects the Pitjantjatjara Supersuite (PS), emplaced between Wankanki Supersuite (WS) above and Wirku Metamorphics (WM) below (Fig. 6b). Northeast-oriented, upright, tight folds also deform Pitjantjatjara Supersuite, Wirku Metamorphics, and early Musgrave structures at Mount Fanny (Fig. 6c), but are cut by later Pitjantjatjara Supersuite intrusions (PS2, c. 1180 Ma), which are not folded. This event is widespread in the Musgrave Province in South Australia; however, it has previously been interpreted as Musgrave in age due to relationships with largely undated Pitjantjatjara Supersuite intrusions (Aitken et al., 2008; Aitken and Betts, 2009b). Synmagmatic timing for this folding is preferred because the Pitjantjatjara Supersuite lacks an axial planar foliation, whereas an axial planar foliation is developed in both the Wankanki Supersuite and the Wirku Metamorphics. The Pitjantjatjara Supersuite intrusions may have been emplaced into the surfaces of flexural slip at the competency contrast between paragneiss and orthogneiss.

Late Musgrave deformation is indicated at Cohn Hill by north-northeasterly oriented tight folding of the EMO fabric in late Pitjantjatjara Supersuite (1160 ± 15 Ma; GSWA 191751.1, Sen et al., 2010a) and Wirku Metamorphics rocks, and by a north-northeasterly trending shear zone which truncates these folds at a slight angle. The minimum age of this deformation is constrained by a post-deformation pegmatite dyke, dated at 1134 ± 9 Ma (GSWA 191763, Sen et al., 2010b). Other late Musgrave structures may be seen in the LeHunte Domain, where there is a strong magnetic fabric in the c. 1175–1140 Ma Umutju Granite (Fig. 2; date derived from Edgoose et al., 2004), and in the Petermann Nappe West Domain, where a similar fabric is developed in rocks interpreted to be similar to the c. 1192–1144 Ma Pottoyu Suite granites (Edgoose et al., 2004). The minimum ages of these fabrics are poorly constrained and they could be as young as the earliest Petermann Orogeny.

Early Giles Event (1078–1074 Ma)

Deformation assigned to the early Giles Event (EGE) pre-dated deposition of the Tollu Group at c. 1073–1068 Ma (Fig. 1) and was broadly synchronous with the emplacement of the Giles 'G1' mafic intrusions at c. 1078–1074 Ma (Howard et al., 2011). Therefore, this deformation is related to pluton emplacement rather than regional tectonics. This event is poorly defined and heterogeneous. The earliest stages (EGE1) are characterized in the Holt, Gungarungal, and Bentley Domains by a magnetic fabric that corresponds to a metamorphic foliation developed in the Kunmarnara Group and basement rocks (Fig. 2). The orientation of this foliation is variable but it typically strikes northeast, and interpreted bedding (S_K) in the Kunmarnara Group is folded around this trend in several locations (Fig. 7a). EGE1 is characterized elsewhere by near-bedding-parallel layers, probably representing synmagmatic deformation within Giles G1 plutons (Fig. 7a). Examples include the Jameson and Blackstone intrusions, where synmagmatic deformation is common and igneous contacts (S_G1) commonly truncate earlier igneous fabrics (A – Fig. 7b). The G2 Hinckley gabbro (B – Fig. 7c) in the Hinckley Domain is overprinted by east-trending isoclinal folding and a parallel shear zone. These structures are interpreted as deformation of an earlier phase of the intrusion by a later phase during the growth of the intrusion, possibly corresponding with the oval-shaped area to the north (H_G2 – Fig. 7c).

EGE1 structures are locally overprinted by north-northwesterly trending shear zones and folds assigned to an EGE2 event. Key examples are in the Hinckley gabbro (Fig. 7a), where EGE1 axial plane and igneous layering (S_G2), are both folded, and in the adjacent Murray Ranges, where it is the dominant influence on structure (C – Fig. 7c). The absolute age of this event is constrained to 1075 ± 7 Ma from a porphyritic granite dyke that intrudes the axial plane of this fold (GSWA 174761, Kirkland et al., 2008).

Mid-Giles Event (1085–1064 Ma)

The early Giles Event was followed first by a period of exhumation and erosion (Evins et al., 2010), then by the deposition of the Tollu Group (Smoke Hill Volcanics and the Hogarth Formation) within the Blackstone Sub-basin, which exists within the Tollu Domain. These units were subsequently folded around a north-inclined syncline oriented east–west, assigned to the mid-Giles Event (MGE, Fig. 8). Deformation of inferred similar age and orientation affects the G2 Hinckley gabbro and basement gneiss in the Hinckley Domain, and the G1 Michael Hills and Latitude Hills intrusions in the Mount West Domain (Fig. 2).

Mid-Giles Event deformation is characterized in the Bentley, Gungarungal, and Holt Domains (Fig. 2) by tight folding of interpreted Kunmarnara Group bedding and early Giles Event fabrics (B, C – Fig. 8c). The orientations of related structures appear to vary from northwest in the south to northeast in the north. North-trending folding of interpreted Musgrave fabrics in the Petermann Nappe West Domain may also be of MGE age, although the age is very poorly constrained.

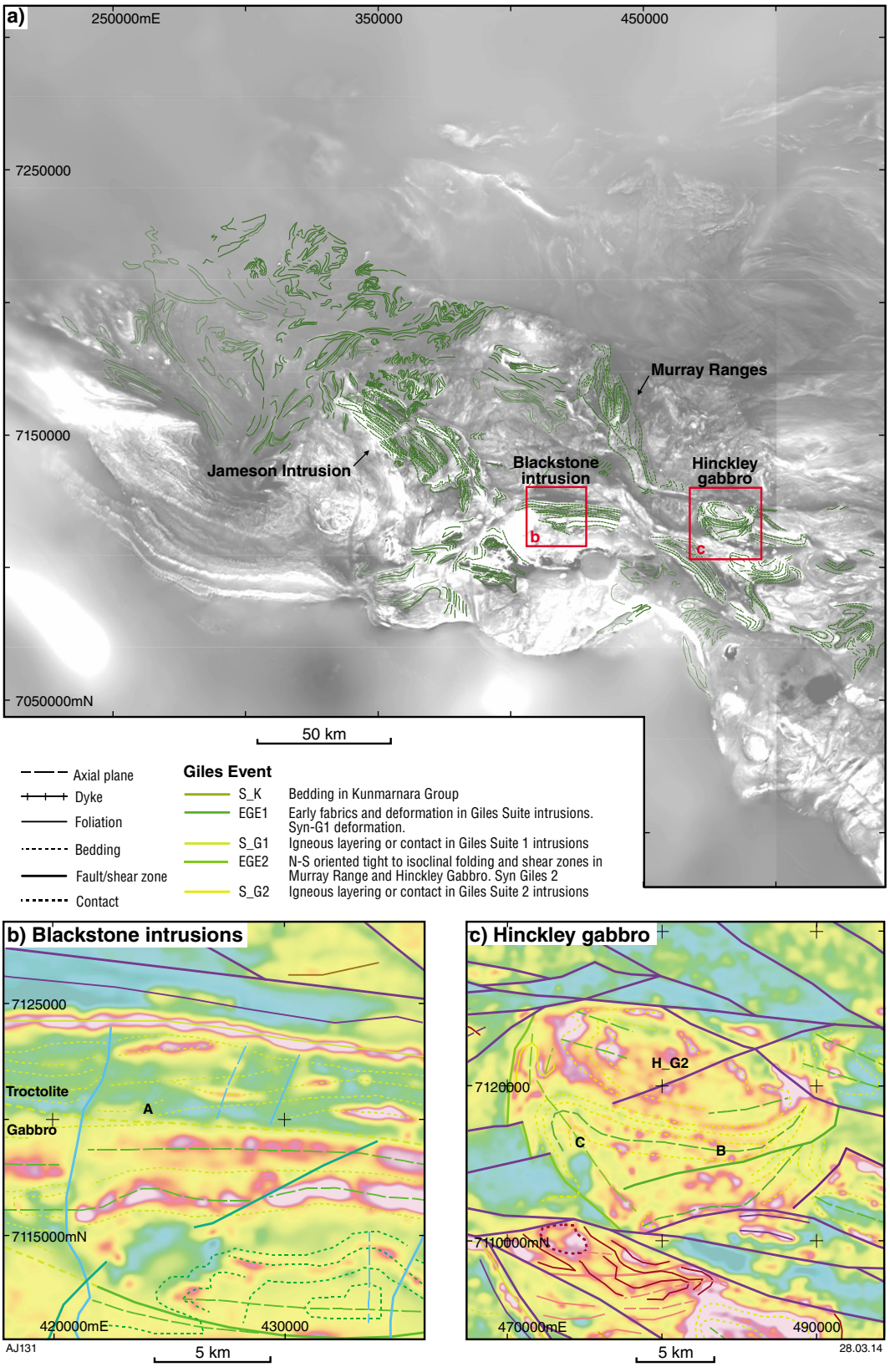

Figure 7. **Structures of the early Giles Event: a) the distribution of structures attributed to the early Giles Event, and two key localities; b) the Blackstone intrusion; and c) the Hinckley gabbro. In the Blackstone intrusion, magnetic layering within the basal troctolite unit is truncated by the contact with the overlying gabbroic unit (e.g. A). The pluton is steeply south dipping here. At the Hinckley gabbro, the intrusion of the oval intrusion to the northwest (HG2) has caused deformation of older material to the southeast (B) . Also imaged is the re-folding of this axial plane around a second NNW trending axis (C). Other colours in the insets indicate structures from other events. See Figs 4–6, 8–12, and Table 1 for legends.**

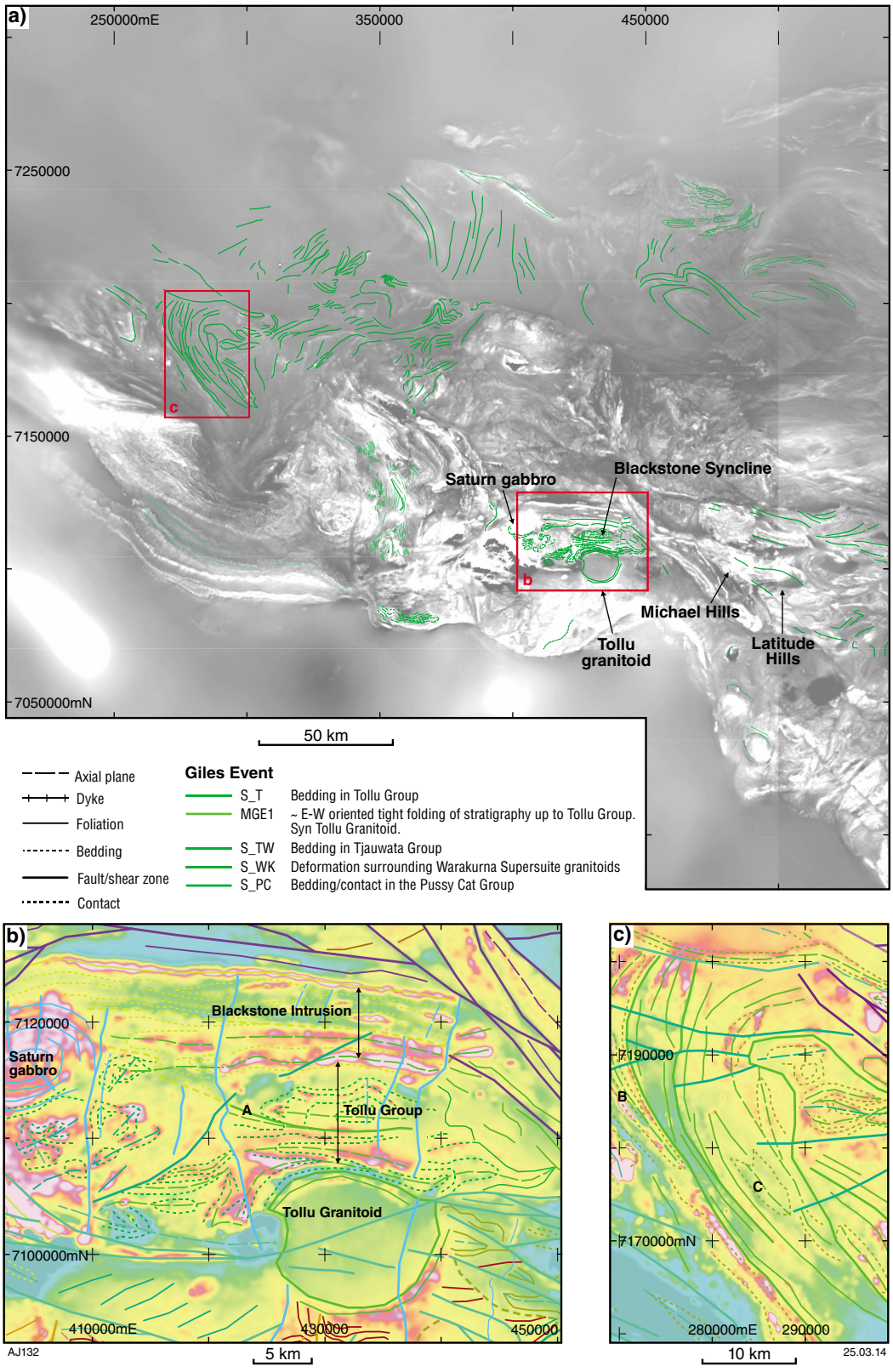

Figure 8. **Structures of the mid-Giles Event: a) the distribution of structures attributed to the mid-Giles Event, and two key localities; b) the Blackstone Syncline region; and c) the north Bentley Domain. In the Blackstone Syncline, the Blackstone intrusion and the Tollu Group are folded around an east-plunging axis. This folding is likely synchronous with the non-magnetic Tollu granite, which warps the axial planes, and pre-dates the Saturn gabbro (top left with distinctive rings), which truncates the folding. In the north Bentley Domain, a NW-trending fabric defined by the folding of interpreted Kunmarnara Group bedding is observed, although this is itself folded by a later event. Other colours in the insets indicate structures from other events. See Figs 4–7, 9–12, and Table 1 for legends.**

The Blackstone Syncline (Fig. 8b) is characterized by shallowly east-plunging, north-inclined close folding of volcanic rocks of the Tollu Group, and the underlying Blackstone intrusion. A fault on the southern limb of the syncline truncates layering, but does not repeat stratigraphy, suggesting some reverse faulting of limited throw within the synform (A – Fig. 8b). A moderately (30–50º) north-dipping cleavage observed in the Tollu Group may correlate with this event. The Tollu granite is interpreted to be synchronous with this event: the strain aureole surrounding this intrusion causes curvature of the MGE fold axial planes. The absolute age of this event is constrained by the crystallization age of the Smoke Hill Volcanics (1073 ± 7 Ma, GSWA 191728, Coleman et al., 2010), the syndeformational Tollu granite (1076 ± 9 Ma, GSWA 185583, Kirkland et al., 2009b) and the undeformed Saturn gabbro intrusion (1072 ± 8 Ma, Redstone Resources Ltd, 2008). The MGE event correlates with the macroscopic folding event identified by Evins et al. (2010).

Late Giles Event (1071–1040? Ma)

The late Giles Event (LGE) does not correlate especially well with any particular phases of the Ngaanyatjarra Rift suggested by Evins et al. (2010), but spans phases 5 through 7. These are interpreted to represent a continuous period of deformation and magmatism during which time the present crustal structure of the WMP, in particular the Mamutjarra Zone, was derived.

Three major episodes of deformation are recognized overprinting all but the uppermost Bentley Supergroup (Fig. 9). LGE deformation is widespread throughout the south and west of the area, and is well developed in the Warburton, Bentley, Eliza, and Tollu Domains (Fig. 2).

LGE1 is characterized by an array of northeast-oriented shear zones and foliations, and is associated with two major domain-bounding shear zones: the Cavenagh Fault, and the unnamed boundary between the Bentley Domain and the Eliza, Jameson, and Holt Domains (Fig. 2). Key localities are in the Cavenagh Range, the southern Jameson Range, and the Whitby Ranges (Fig. 9). Rocks of the Cavenagh Range (B – Fig. 9b) lie in the footwall of the northwest-dipping Cavenagh Fault, and record this event as a fairly subtle northeast-trending magnetic fabric that correlates with a prominent fracture pattern in outcrop, which is probably related to movement along the Cavenagh Fault at this time. A northeast-trending shear zone assigned to LGE1 also cuts the Blackstone intrusion and the Tollu Group to the northeast of the Cavenagh intrusion, but is in turn cut by a Warakurna Supersuite granite (A – Fig. 9b) dated at 1065 ± 9 Ma (GSWA 189563, Kirkland et al., 2014).

The LGE1 event in the southern Jameson Range is associated with two faults that juxtapose the Jameson intrusion against Pitjantjatjara Supersuite basement. There is a related, near-vertical cleavage in outcrop, but magnetic and gravity modelling (Aitken et al., 2013) indicates a north-dipping structure; hence, a normal shear sense. The amount of strike-slip is unknown, but the Jameson intrusion is c. 8 km thick to the north of the shear zone and absent to the south, indicating either significant offset or accommodation of the intrusion during emplacement. Many LGE1 structures inhabit the region between this shear zone and the Cavenagh Fault (Fig. 9a).

The Whitby Ranges contain a northeast-trending block of 1071 ± 5 Ma Kathleen Ignimbrite (GSWA 195723, Kirkland et al, 2011) that has apparently been uplifted into the probably younger Mount Palgrave Group (c. 1067–1063 Ma). The relative and absolute timing, orientation, and structural style of this block are consistent with uplift during the LGE1 event.

LGE2 deformation is very widespread and characterized by easterly to southeasterly trending shear zones and associated local folding. This event extends well into South Australia and correlates directly with Giles-age structures inferred by Aitken and Betts (2009a). LGE2 structures are observed in almost all domains, but are best developed in the Tollu, Warburton, and Bentley Domains. LGE2 in the Tollu Domain is characterized by an anastomosing array of east-trending shear zones that cut LGE1 structures, the Cavenagh intrusion, and the Tollu granite (Fig. 9b). In the Cavenagh Ranges, LGE2 is marked by: 1) an east-southeasterly trending shear zone, along which there has been an apparent dextral offset of the southern margin of the Cavenagh intrusion; 2) reactivation of the northeast margin of the Cavenagh intrusion; 3) development of open folds in existing fabrics; and 4) intrusion of two conjugate dykes between these shear zones (B – Fig. 9b). These structures collectively indicate a probable northwest–southeast directed maximum horizontal stress. Gravity and magnetic modelling (Aitken et al., 2013) indicate that the major shear zone is north dipping, and may accommodate up to 6 km of normal dip-slip displacement of the Cavenagh intrusion, indicating significant transtension when allied with the apparent dextral offset. LGE2 in the Warburton and Bentley Domains is marked by a series of easterly to southeasterly trending folds and shear zones that define the large-scale structural architecture of this region.

LGE3 is characterized by a parallel array of north-trending shear zones and localized folds. These are commonly intruded by mafic dykes, such as the well-exposed, though not yet mapped at 1:100 000 scale, example at Diorite Hill (Fig. 9a). The age of these dykes is interpreted to overlap the latest stages of Alcurra Dolerite suite magmatism (though the earliest Alcurra dolerites significantly pre-date this event; for example, those folded with the Tollu Group during MGE1). One of these shear zones (the Jameson Fault) is interpreted to cut the 1068 ± 4 Ma (Seat et al, 2011) Nebo–Babel intrusion (C – Fig. 9b) and to have oblique sinistral shear sense with a west-side-up normal component (Seat et al., 2007), indicating northeast–southwest extension. The distribution of these north–south oriented shear zones is restricted in the west Musgrave Province to a north–northeasterly trending corridor (Fig. 9a), and they do not appear to have affected the southeastern Tjuni Purlka Zone, the Walpa Pulka Zone, or the Mulga Park Zone. The LGE3 event is interpreted to be the upper-crustal to mid-crustal expression of oblique sinistral shear along on the Lasseter–Mundrabilla Shear Zone at c. 1070 Ma. This lithospheric-scale shear zone has accommodated up to c. 5–10 km of west-side-up offset of the Moho (Fig. 9a; Braun et al., 1991; Aitken, 2010).

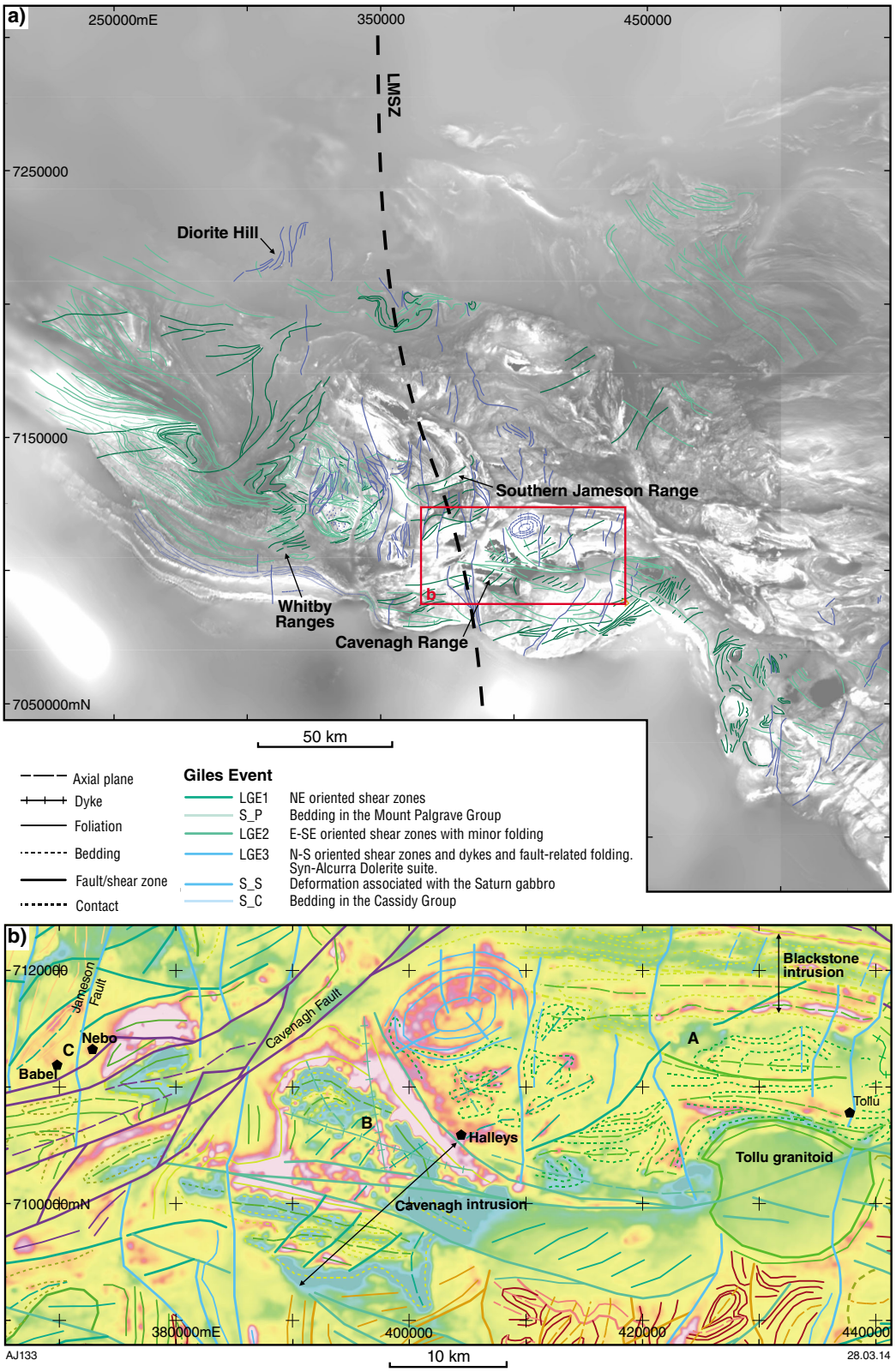

Figure 9. **Structures of the late Giles Event: a) the distribution of structures attributed to the Late Giles Event; and b) its key locality, the Cavenagh–Blackstone region. This region shows in more detail multiple structures of the late Giles Event, including the Cavenagh Fault, and smaller NE-trending LGE1 structures, one cut by a Warakurna granite (A). The ESE-trending LGE2 shear zones cut the LGE1 fabrics, and the conjugate dykes in the Cavenagh intrusion may provide a key constraint on the stress field during this deformation event (B). Several N-trending LGE3 shear zones cross the area (e.g. the Jameson Fault C). Each of these events is likely associated with mineralization: i.e. LGE1 – Nebo–Babel; LGE2 – Halleys; LGE3 – Tollu. The thick dashed line (LMSZ) indicates the approximate trace of the Lasseter–Mundrabilla Shear Zone. See Figs 4–8, 10–12, and Table 1 for legends.**

A cluster of similar north-oriented structures/dykes in South Australia (including one associated with the Harcus intrusion, which is prospective for Ni–Cu mineralization) demarcate a subsidiary splay of this continental-scale shear zone.

Post-Giles Event (c. 1000 Ma)

The post-Giles Event (PGE) involved an episode of localized northeast–southwest shearing and interpreted dyke emplacement (Fig. 10). The dykes cut the Jameson intrusion after the Giles Event but prior to the Petermann Orogeny, and extend into the surrounding Warakurna Supersuite granites (A – Fig. 10b). Their ages remain poorly constrained. One of the shear zones shows prominent dextral drag folding of the igneous layering in the Jameson intrusion, implying ~2 km of dextral offset, but little vertical offset since layers continue across the fault (B – Fig. 10b). Approximately north–south extension (or east–west shortening) is therefore indicated. PGE faults truncate LGE3 faults or dykes at several locations, although the overprinting relationships are generally poorly defined. In some instances, interpreted PGE structures are cut by LGE faults (B – Fig. 10b), which may reflect an error in structural correlation, reactivation of LGE structures during a later event (e.g. Petermann Orogeny), or continuous late- to post-Giles Event deformation in which different fault sets were active at the same time.

Petermann Orogeny (590–530 Ma)

In the WMP, several Petermann structures are recognized based on their timing relative to the main network of crustal-scale shear zones (e.g. Mann Fault, Hinckley Fault). The Petermann-aged structures are prominently imaged as long, linear magnetic lows that crosscut all earlier structures. The extent and effect of the Petermann Orogeny appears to be relatively pervasive in the Walpa Pulka Zone and widespread in the southeast Tjuni Purlka Zone. The intensity of the Petermann Orogeny deformation generally diminishes to the south and west. These Petermann Orogeny shears are most abundant, and earlier features less continuous, in the north and west of the WMP, leaving much of the Tollu, Jameson, Eliza, Bentley, and Warburton Domains undeformed (Fig. 2).

Early Petermann Orogeny (EPO) deformation is characterized by shear zones of various orientations (Fig. 11). They trend dominantly west-southwest to southwest in the Walpa Pulka Zone (A – Fig. 11b), dominantly east-southeast in the Tjuni Purlka Zone (B – Fig. 11a), and north–northeast in the Tollu Domain (C – Fig. 11a). The low-angle, south-dipping shear zones that accommodated this flow are imaged in Figure 11b (D). Significant EPO structures are preserved in the Mulga Park Zone, notably the southeasterly trending Petermann Nappe Complex (E – Fig. 11a). This feature is comprehensively described by Edgoose et al. (2004) and Flöttmann et al. (2004). In Western Australia, its core is characterized by magnetic foliation that is truncated by the Piltardi Detachment Zone. This latter structure is terminated against a sinistral tear fault, which accommodates the differential motion between the Piltardi Detachment Zone and a parallel shear zone to the west (E – Fig. 11a). The Bloods Backthrust is also interpreted as an EPO structure (Edgoose et al., 2004; Flöttmann et al., 2004). K–Ar ages of 586 ± 5 and 568 ± 5 Ma are attributed to the EPO deformation in the Petermann Nappe (Edgoose et al., 2004). Absolute ages for the EPO event are generally lacking elsewhere, although a study covering much of the Walpa Pulka Zone links low-angle, south-dipping shear zones here to southwest-directed lower-crustal flow, with peak metamorphism at c. 570 Ma (Raimondo et al., 2010).

Mid-Petermann deformation (MPO) is represented by an east-southeasterly trending, anastomosing array of mylonite, ultramylonite, and pseudotachylite zones, including several crustal-scale examples (e.g. the Mann Fault). These are very prominent in the east of the Tjuni Purlka Zone (Fig. 11c), where they define the boundaries of high-pressure metamorphic domains exhumed during the Petermann Orogeny.

The northeast and east-southeast orientation of many shear zones (e.g. Cavenagh Fault) suggests reactivation of structures originally formed during the LGE1 and LGE2 events, respectively. Key shear-zone outcrop localities in Western Australia include the Champ de Mars, Mount West, and Latitude Hills areas (Fig. 11a; see Glikson et al., 1996). These particular examples are not isotopically dated, but the coeval Mann Fault has been K–Ar dated at 567 ± 7 Ma in the eastern Mann Ranges, and 549 ± 2 Ma in the Musgrave Ranges, both in South Australia (Maboko et al., 1992; Camacho and Fanning, 1995).

The Woodroffe Thrust (Fig. 11a) is the fundamental geological boundary of the Petermann Orogeny. This shear zone in the WMP is a long, approximately linear east-southeasterly trending lineament with a number of splays, and post-dates the main network of strike-slip shear zones, indicating late Petermann activity (LPO). The Woodroffe Thrust (Fig. 1) is not exposed in WA, but is well exposed further east, and has returned isotopic ages of c. 550–530 Ma (Maboko et al., 1992; Camacho and Fanning, 1995; Camacho et al., 1997).

Alice Springs Orogeny (450–300 Ma)

The WMP hosts two sets of post-Cambrian structures with features that are consistent with deformation during the Alice Springs Orogeny (ASO, Fig. 12). The first of these comprises south-directed thrust faulting at the southern margin of the province, which is shown in a seismic line in South Australia to have caused a monoclinal upturn of the Ordovician and Devonian sedimentary rocks of the Officer Basin (Lindsay and Leven, 1996). The thrusts are not expected in WA, but the Townsend Quartzite at the base of the Centralian Superbasin commonly outcrops along the southern margin of the WMP, where it has moderately steep (c. 60º) south-dipping bedding. This contrasts with the Bentley Supergroup within the WMP in which bedding dips south much more shallowly (20–30º). These basin-margin structures therefore probably continue into Western Australia, and are assigned to the Alice Springs Orogeny.

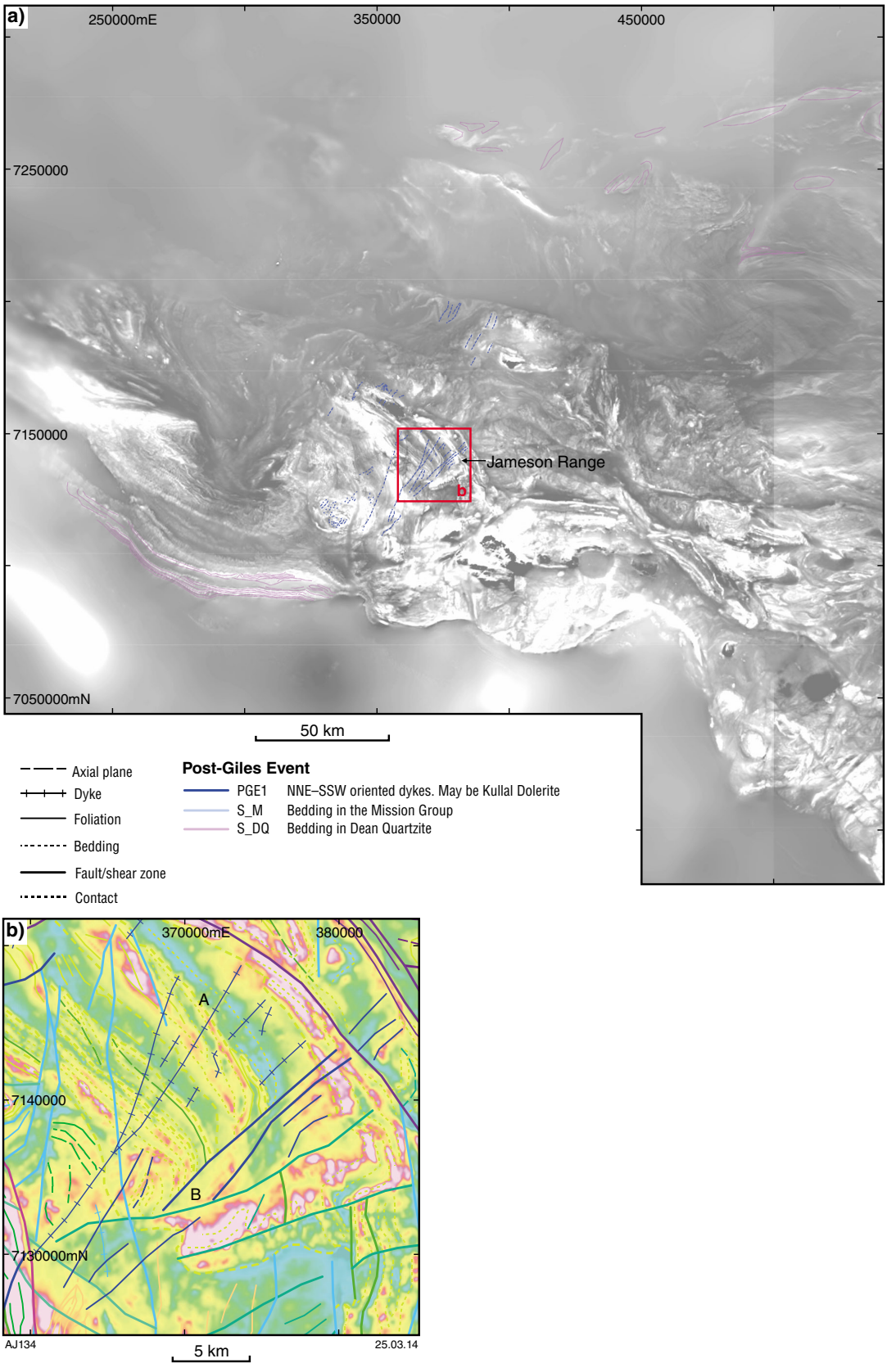

Figure 10. Structures of the post-Giles Event: a) the distribution of structures attributed to the post-Giles Event, and its key locality; b) the Jameson intrusion. In the Jameson intrusion, NE-trending dykes and co-oriented shear zones are observed. Although overprinting relationships are not especially clear (e.g. B), these dykes correlate with the Kullal dyke suite that intrude the Jameson intrusion. Other colours in the insets indicate structures from other events. See Figs 4–9, 11, 12, and Table 1 for legends.

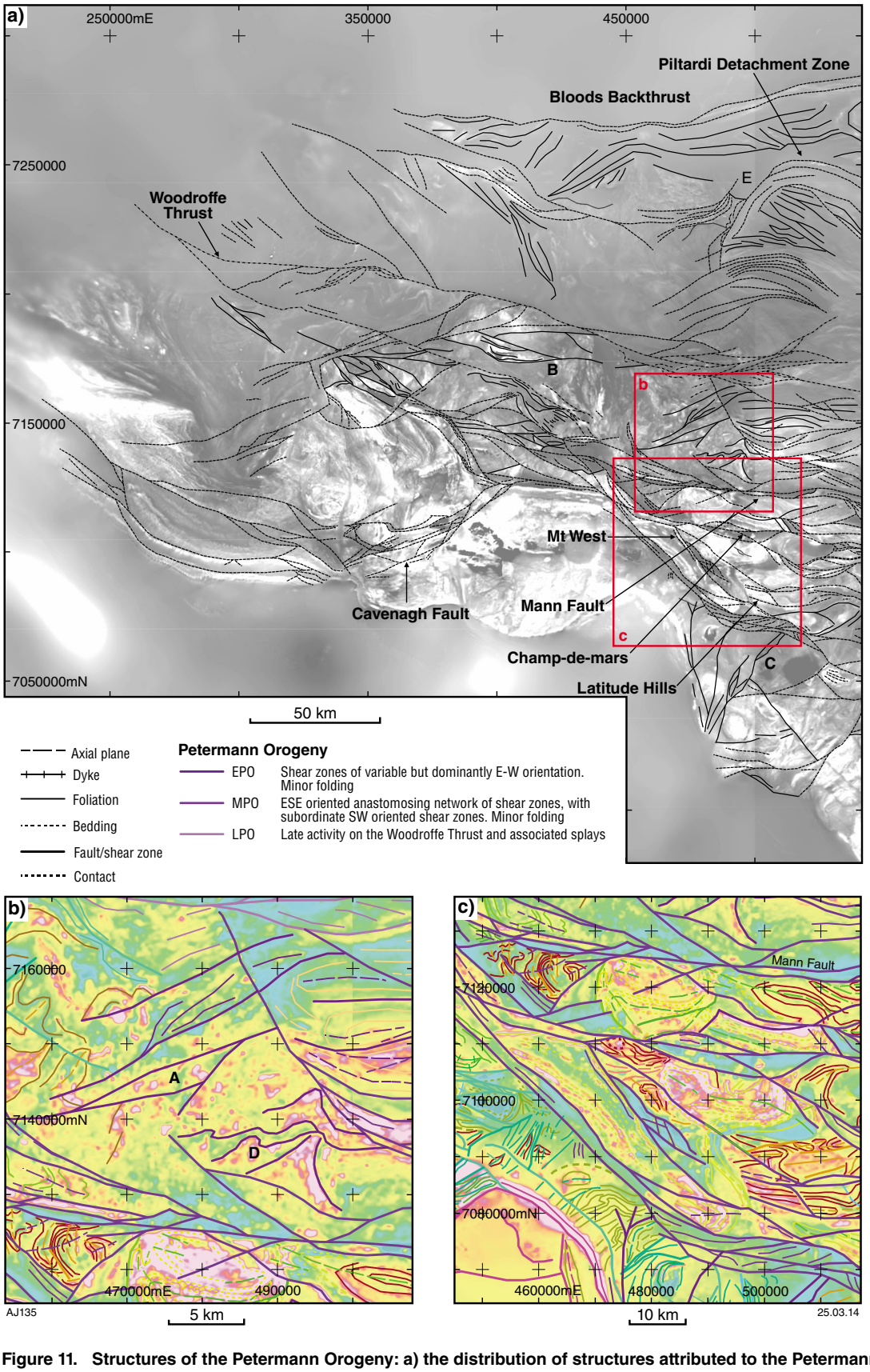

Figure 11. Structures of the Petermann Orogeny: a) the distribution of structures attributed to the Petermann Orogeny, and two key localities; b) the Walpa Pulka Zone; and c) the southeast Tjuni Purlka Zone. The Walpa Pulka Zone shows fabrics and shear zones that correlate with structures interpreted to have accommodated SW-directed lower crustal flow during the early stages of the Petermann Orogeny (A). In the southeast Tjuni Purlka Zone, an anastomosing network of crustal-scale transpressional shear zones (e.g the Mann Fault) dissects and reactivates earlier architecture. Other colours in the insets indicate structures from other events. See Figs 4–10, 12, and Table 1 for legends.

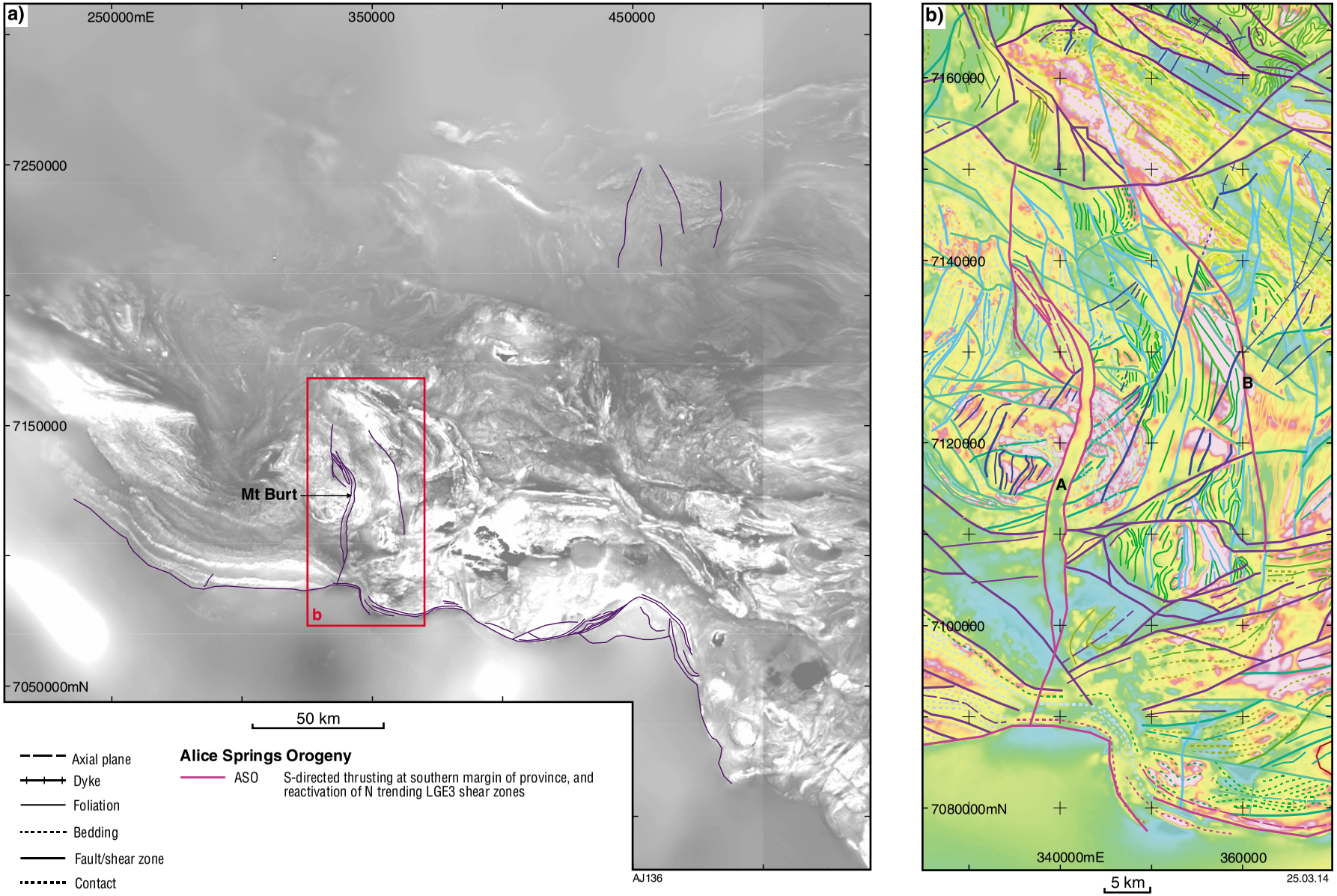

Figure 12. Structures of the Alice Springs Orogeny: a) the distribution of structures attributed to the Alice Springs Orogeny, and its key locality; b) the Lasseter–Mundrabilla Shear Zone region. This region contains a distinctly smooth texture associated with sedimentary rocks (A). A similarly oriented shear zone to the east cuts many Giles Event aged structures (B). Other colours in the insets indicate structures from other events. See Figs 4–11 and Table 1 for legends.

Structures comprising the second set trend roughly north. The most prominent example is marked by a smooth texture within the high-intensity responses of the Mount Palgrave Group (A – Fig. 12b), and is associated with a sandstone unit that outcrops near Mount Burt, and which was tentatively interpreted in early mapping to be of Permian age (Daniels, 1974). Earlier structures are continuous across this structure, which is interpreted as a graben with very limited, if any, strike-slip motion; whereas gravity, magnetic, and magnetotelluric modelling indicate a maximum depth to basement of 1–1.5 km. Other north–south trending shear zones are interpreted as post-Petermann reactivation of LGE3 shear zones, some of which accommodate significant offsets.

Summary

Structures in the WMP record a protracted history of deformation in a variety of tectonic settings (Table 1). Early deformation events relate to the c. 1345–1293 Ma Mount West Orogeny and to the c. 1220–1150 Ma Musgrave Orogeny. Supporting evidence from granite geochemistry suggests that the Mount West Orogeny was associated with a convergent plate margin setting. Structures preserved from the Musgrave Orogeny are dominantly contractional and oriented NE. It is likely that deformation during these orogenic events records the convergence of the South Australian Craton with the West Australian and North Australian Cratons, as part of a broader orogenic belt encompassing much of central and southern Australia (e.g. Aitken and Betts, 2008).

The structural architecture of the WMP is dominated by the c. 1085–1040 Ma Giles Event, which records near-continuous intraplate deformation and magmatism and is also notable for formation of the Nebo–Babel Ni–Cu–PGE deposit. Several stages may be recognized within the Giles Event:

- Early Giles Event deformation was synchronous with emplacement of the Giles G1 mafic plutons, and is characterized by the development of folds and metamorphic foliation in the Kunmarnara Group, and synmagmatic deformation fabrics within and surrounding Giles G1 plutons. These were followed by the development of a fairly localized event characterized by north-northwesterly trending shear zones in the Murray and Hinckley Ranges. Known vanadium–titanium mineral occurrences in the upper parts of the Jameson intrusion are clearly related to EGE structures.
- Mid-Giles Event deformation is characterized by generally east–west oriented close folding and reverse faulting of the Giles G1 plutons and Tollu Group volcanics produced by shortening under north–south compression.
- Late Giles Event deformation is characterized by three major phases. The first involves an array of northeasterly oriented normal shear zones. The second involves another array of east-southeasterly oriented dextral-normal shear zones. The third is characterized by north-trending, possibly transtensional shear zones, typically associated with coeval Alcurra dykes that commonly show limited offsets with apparent sinistral shear sense. The kinematics of these LGE shear zones suggests a switch from northwest–southeast tension during LGE1 to northeast–southwest tension during LGE2 and LGE3. Many mineral occurrences are associated with these LGE structures, including the Nebo–Babel deposit, and the Halleys and Tollu Prospects (Fig. 9b).

Structures younger than those formed during the Giles Event include north-northeasterly striking shears in the Jameson Ranges region, related to an unnamed c. 1000 Ma event with east-trending folds and thrusts (e.g. Woodroffe Thrust, Petermann Nappe), and variably oriented transpressional shear zones related to the c. 590–530 Ma Petermann Orogeny. Thrusts along the southern margin of the province and north-trending structures within the province were reactivated, or perhaps formed, during the Alice Springs Orogeny.

Prospectivity analysis of the west Musgrave Province

Selection of commodity types for prospectivity analysis

Selection of commodities for the prospectivity analysis was partly based on the known endowment (i.e. known mineral deposits) of the WMP, and also on the perception of likely mineral systems for the interpreted geological and tectonic settings that are now reasonably well understood.

Abeysinghe (2003) reviewed mineral occurrences and exploration activity in the WMP up to 2002 and described significant deposits of magmatic nickel, copper, PGE, and nickeliferous laterite. Important mineral discoveries that have influenced our selection of commodities for the prospectivity analysis are detailed below.

The WMP was targeted in 1995 by Western Mining Corporation and BHP Billiton (since 2005) with the objective of discovering a major greenfields Ni–Cu–PGE sulfide deposit similar to that at Voisey's Bay in Canada (e.g. Li and Naldrett, 2000). Nebo–Babel (Fig. 1), a major nickel sulfide deposit in the central part of Cooper*, was subsequently discovered in 2000, associated with a significant, east–west trending, electromagnetic conductor that extends intermittently for more than 5 km (Baker and Waugh, 2005). The deposit comprises massive and disseminated mineralization hosted within a shallowly west-southwesterly plunging pipe (or chonolith) of gabbronorite (Seat et al., 2007; 2011; Godel et al., 2011) emplaced into orthogneiss country rock at c. 1068 Ma (i.e. during the 1085–1040 Ma Giles Event). Drill intersections include 106.5 m @ 2.4% Ni, 2.7% Cu and 0.2 g/t PGE, and a resource estimate of about 1 million tonnes contained Ni and 1 million tonnes contained Cu and Co has been released (Howard et al., 2011).

* Capitalized names refer to GSWA 1:100 000 map sheets, unless otherwise indicated.

Anomalous base metal, nickel, and PGE occurrences have been identified in a number of areas in the Blackstone Range (BLACKSTONE). The Halleys copper–PGE–nickel mineralization (Fig. 1) is situated in a what is thought to be a magmatic flow-through zone on the southeast flank of the Saturn intrusion (interpreted as a late feeder for the Giles intrusions: the 'Alcurra magmatism'). Intercepts from drilling of a mineralized zone up to 74 m thick averaged 0.33% Cu and 0.24 g/t PGE plus Au and included 20 m @ 0.56% Cu, 0.32 g/t PGE plus Au, and 0.14% Ni (Howard et al., 2011). Drilling at Tollu (northeastern BLACKSTONE) intersected maximum values of 5.65% Cu, 50 g/t Ag, 19 ppb Au, 0.03% Pb, and 23 ppb PGE (Howard et al., 2011). High-grade copper mineralization is known over a 2 x 3 km area near Tollu where mineralization styles include fault-related, vein and fracture fill, stringer, and disseminated mineralization in altered gabbro and felsic volcanics.

Although there is as yet no record of significant primary PGE occurrences in the Giles intrusions, recent PGE-bearing magmatic Ni discoveries at Nebo–Babel, Halleys, and Tollu suggest that the Giles Event intrusions should not be discounted as a host for PGEs. In addition, the potential for PGE-rich zones in ultramafic cumulates (e.g. peridotite, pyroxenite) in the basal layers of mafic–ultramafic bodies has not been tested (Howard et al., 2011). Maier et al. (2003) found anomalous PGE abundances in the more evolved magnetitite layers of the Stella layered intrusion, South Africa. This style of mineralization, according to Maier et al. (2003), is found in those layered complexes that lack chromitites, as is the case for the Giles intrusions. Indeed, PGE mineralization has been found within the magnetite-bearing Jameson intrusion at a number of locations (GSWA, 2010c).

The Handpump prospect is a recent discovery of hydrothermal gold mineralization, on the southern margin of the Palgrave area in eastern MOUNT EVELINE, and about 30 km west of Nebo–Babel (Fig. 1; Beadell Resources Ltd, 2009). This is associated with a north-dipping hydrothermally brecciated rhyolite. A five-metre composite analysis gave 65 m @ 0.83 g/t Au, including a central high-grade interval of 5 m @ 5.1 g/t Au and a zone of 15 m @ 2.3 g/t Au.

The bimodal character of magmatism during the 1085–1040 Ma Giles Event constitutes a highly prospective setting for both magmatic and hydrothermal mineral systems. Mineral systems in these settings may include low-sulfidation epithermal precious metal deposits, IOCG deposits, U and reduced Mo–Sn–W porphyry systems, and stratabound Au–Ag deposits, generally associated with potassic, fluorite, and carbonate alteration. Hydrothermal vein systems and stratabound Cu, Pb, Ag, Zn, Au, and fluorite mineral occurrences are widely distributed in the southern part of the WMP, all hosted in felsic volcanic and volcaniclastic rocks of the Bentley Supergroup. The veins in some are structurally controlled (e g. Tollu prospect), inviting speculation that some of these veins may represent the outlying parts of larger mineral systems, such as IOCG, epithermal, or intracontinental-type porphyry Mo deposits.

Based on these mineral discoveries, the conceptual prospectivity of the region, and the known endowment of the WMP, the selection of commodities for the prospectivity analysis includes:

- orthomagmatic nickel–copper
- magmatic platinum group elements (PGE)
- orogenic and intrusion-related gold
- iron oxide–copper–gold (IOCG)
- magmatic tin–tungsten.

In addition, all granites of the WMP are known to be enriched in U and Th (Smithies et al., 2010), and erosion of earlier granite generations is known to provide a detrital source for younger sedimentary rocks of the region (Evins et al., 2010). In view of the widespread occurrence of calcrete as part of the regolith coverage, we have also included surficial uranium prospectivity analysis.

Magmatic nickel–copper (Ni–Cu) mineral systems

Approximately 60% of the world's nickel is produced from Ni–Cu ± PGE sulfides associated with mafic or ultramafic magmas varying in age from Archean to Permian or Triassic, and located in many parts of the world (e.g. Russia, Australia, Canada, and southern Africa; Naldrett, 1997, 2004). These kinds of deposits form when mantle-derived mafic and ultramafic magmas become saturated in sulfide (Arndt et al., 2005). Sulfides usually consist of pyrrhotite, pentlandite, and chalcopyrite and generally constitute a small volume of the host rock(s).

Nickel-sulfide deposits in Archean greenstone belts (e.g. Kambalda and Thompson nickel belts, Australia) are associated with komatiite lavas and basaltic–picritic intrusive magma conduits (Naldrett, 2004). This scenario cannot be applied in the Proterozoic Musgrave Province. Other tholeiitic world-class Ni–Cu sulfide deposits (Fig. 13) occur in mafic sills associated with continental rift flood basalts (e.g. Noril'sk and Duluth, Russia; Hoatson et al., 2006 and references therein), in astrobleme-hosted deposits formed from impact-related mantle melting (e.g. Sudbury Complex, Canada), and in tholeiitic rift-related layered intrusions (e.g. Voisey's Bay, Canada, Barnes and Lightfoot, 2005). A key factor for mafic Ni–Cu systems is the occurrence of highly dynamic systems that experience multiple magma pulses and sulfide entrainment from depth, rather than in situ sulfide segregation.

The presence of Nebo–Babel, a deposit associated with the Warakurna large igneous province, confirms that the WMP contains all the ingredients required to form magmatic nickel–copper deposits. Factors favourable for the formation of such deposits are: 1) primitive, mantle-derived, differentiated, Mg-rich rocks (such as ultramafic and mafic rocks) as a main source; 2) magma flow focused and locally enhanced by alternating compressional/extensional tectonic regimes; 3) fracture-related, high-permeability dilatational zones into which fluids could

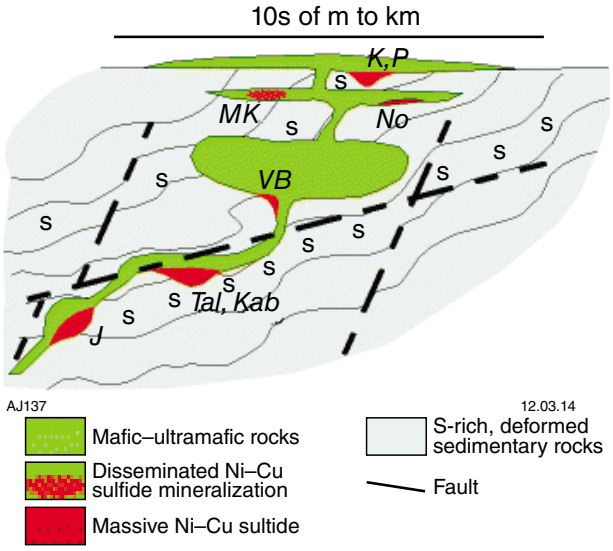

Figure 13. Schematic diagram summarizing important elements of Ni–Cu deposits formed predominantly in tectonically active, deformed terranes containing abundant sulfur-bearing sedimentary rocks. J – Jinchuan; K – Kambalda; MK – Mt Keith; No – Noril'sk, Tal – Talnakh; Kab – Kabanga; P – Pechenga; VB – Voisey's Bay (Maier and Groves, 2011).

migrate; 4) abundant S-rich crustal rocks that could provide the external sulfur required to form ore minerals. In almost all magmatic Ni–Cu sulfide deposits, addition of external sulfur from country rocks plays a key role in causing sulfide saturation (Mavrogenes and O'Neill, 1999; Ripley et al., 1999, 2002, 2003). Although sulfur-bearing country rocks that could contribute external sulfur are absent in the Nebo–Babel area, the presence of sulfur-bearing rock units in the lower crust cannot be ruled out, and the sulfur is not necessarily entirely mantle derived (Seat et al., 2007; Godel et al., 2011).

Predictor maps

In the following sections, details on the fuzzy predictor maps generated for the Ni–Cu prospectivity analysis are given, together with their geological rationale (Table A1). For physical traps, only physical properties such as rheology, permeability, density of faults, were considered, whereas for chemical traps, geochemistry was used. The predictor maps were combined into a three-stage inference network (Fig. 14) to generate the final prospectivity map (Fig. 15).

Source

Potential mantle sources for primitive metal-rich magmas include the convecting mantle and the lithospheric mantle (Maier and Groves, 2011). The involvement of the source rocks is indicated by picrite and tholeiitic basalt magmatic systems emplaced in continental settings as components of large igneous provinces (Naldrett, 2004). Magmatic sulfide deposits with nickel and copper as primary products occur in peridotite (e.g. Jinchuan, China), harzburgite (e.g. Kabanga, Tanzania), pyroxenite (e.g. Santa Rita, Brazil), olivine gabbro (e.g. Noril'sk), gabbronorite (e.g. Sudbury, Canada), and troctolite (e.g. Voisey's Bay, Canada). These lithotypes were used as proxies for source in the prospectivity analysis.

The intrusion hosting the Nebo–Babel deposit was formed during a major magmatic event that produced the Giles intrusions, the Warakurna large igneous province, and the Alcurra Dolerite suite (Seat et al., 2011). The Warakurna Supersuite (and associated mafic intrusions) is therefore assumed to have the greatest potential to host magmatic Ni–Cu sulfides (Wingate et al., 2004, Godel et al., 2011).

We then classified these as 'Warakurna Supersuite' and 'non-Warakurna Supersuite' and established a 10 km-wide buffer zone around each polygon (Figs A1, A2). Relevant occurrences of mafic and ultramafic rocks were extracted, and include peridotite, harzburgite, pyroxenite, dunite, basalt, gabbro, troctolite, gabbronorite, dolerite, and amphibolite. Warakurna Supersuite rocks were assigned a very high map weight of 9, whereas a map weight of 8 was assigned to non-Warakurna Supersuite rocks because they are less prospective.

We also produced a source predictor map based on the MgO/(MgO+FeO) value of mafic and ultramafic suites, as this directly reflects the amount of crystallized olivine (Fig. A3; Le Bas, 2000). Olivine is the main reservoir of nickel and the higher the MgO abundance of a mafic–ultramafic suite, the higher its Ni content can be; hence, the higher its potential to host magmatic sulfides. A map weight of 8 was given to this predictor map MgO/(MgO+FeO), because it does not differentiate the Warakurna Supersuite from the non-Warakurna rocks.

Pathways

Dense, primitive, mantle-derived magmas need translithospheric pathways to develop a sufficient pressure gradient to ascend through the relatively low-density crust (Naldrett, 2010). Crustal-scale faults also promote crustal contamination, sulfur saturation, and segregation of Ni-sulfide to form ore deposits in the upper crust. These pathways are provided by extension of the crust and lithosphere that is mainly driven by mantle convection, and they may be of regional or local scale (Maier and Groves, 2011). The movement history of crustal-scale faults is complicated, with most experiencing several phases of motion. Therefore, we used all crustal-scale faults determined from the structural analysis, placed a 10 km wide buffer zone around each fault, and assigned a high map weight of 9, since such faults are considered to be essential components of the mineral system (Fig. A4; Cox et al., 2001).

Structures associated with the earliest stage of the late Giles Event (LGE1) are coeval with mafic magmatism and Nebo–Babel emplacement; hence, are also likely critical pathways for transporting mineralizing fluids. Therefore, we also produced a predictor map of late Giles Event structures with a 5 km buffer zone and a high map weight score of 9 (Table A1, Fig. A5).

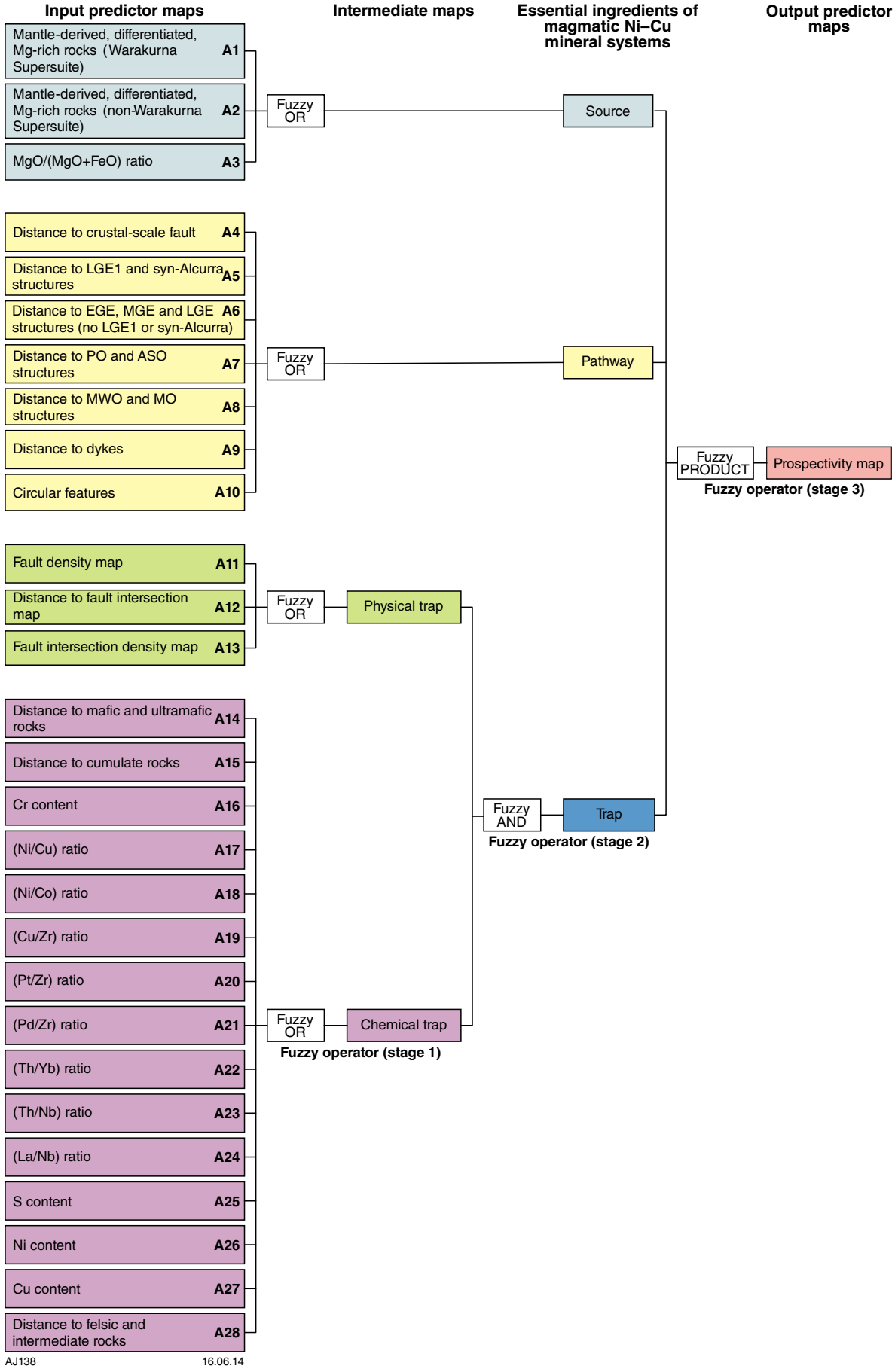

Figure 14. Multi-stage fuzzy inference network used for combining fuzzy Ni–Cu predictor maps

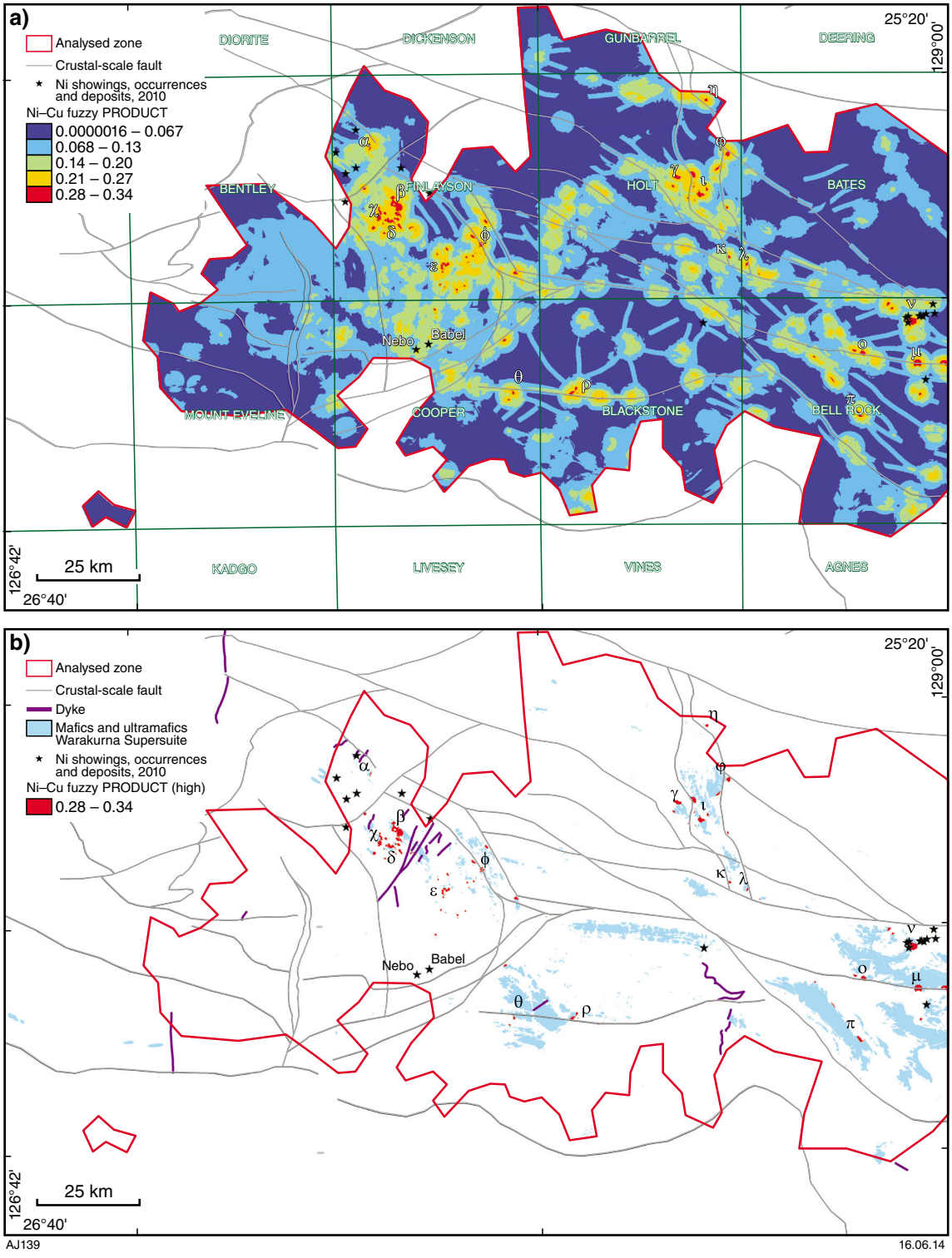

Figure 15. a) Fuzzy prospectivity model for magmatic Ni–Cu mineral system; b) zone of high fuzzy value for the magmatic Ni–Cu prospectivity analysis over the analysed area with even data coverage

Any other Giles Event structures might also control the emplacement of nickel- and copper-bearing Giles intrusions, but would have a lower prospectivity (Fig. A6, map weight = 8.5). Long-lived structures are also good proxies for Ni mineralization. Faults that were active during the Petermann Orogeny and Alice Springs Orogeny were probably also active during the Giles Event, and hence are potential predictors (Fig. A7). The oldest Mount West Orogeny and Musgrave Orogeny structures (Fig. A8) are also used as an indicator of pathways, but are probably less prospective because they were mainly active during the Mount West and Musgrave Orogeny (map weight = 8, Table A1, Fig. A8).

Late-stage Giles Event dolerite dykes delineate magma conduits, and thus may host magmatic sulfides and further support the Ni mineralization potential in the WMP. However, although they are the most prospective permeable pathway, they were given only a 1000 m buffer and the map was given a map weight of only 6.5 (Fig. A9).

Chonoliths are another example of magmatic channels in mafic intrusive systems (Cruden, 2008), and are considered as favourable pathways, and also traps, for nickel-bearing magmas, hence were given a map weight of 7.5. The locations of chonoliths are interpreted from the GSWA magnetic dataset (GSWA, 2010a) using the CET Porphyry Analysis system (Holden et al., 2010). The algorithm only detects features of a given size range with circular to elliptical cross sections in plan. It will therefore only detect potential chonoliths that are steeply tilted and will not differentiate them from other types of circular features. Nor will it detect subhorizontal chonoliths (for example the host to the Nebo–Babel deposit; Seat et al., 2007, 2011) or those that are smaller than the data resolution (c. 400–700 m). We attempted discrimination by limiting radii values between 700 and 1400 m and radial symmetry thresholds to 20 m, to ensure that only features with the strongest responses pass the screening. We also established an exclusion radius of 20 m to constrain the minimum allowable distance between detected features. The resulting predictor map 'presence of circular feature' is illustrated in Figure A10.

Physical traps

Trapping or focusing of mineralizing fluid and magma leading to concentration of metal may occur at sites of localized dilatational deformation, or other sites of increased permeability and can be associated with discontinuities. Fault intersections are prime locations for increased permeability that can be approximated by mapping the density of all types of faults per square kilometre (Fig. A11). Other proxies for focused fluid flow controlling rock permeability are mapped distances to the intersection points of all faults (Fig. A12) and fault intersection density (Fig. A13).

Map weights of 6.5 were attributed to both the 'fault density' and 'fault intersection' maps because these portray good sites for fluid ponding. A slightly higher map weight of 7 is given to the 'fault intersection density' map because these data represent zones of greater structural complexity than the other two fault-related physical traps, and greater chance for fluid to be trapped (Table A1).

Chemical scrubbers

Metal deposition within trap zones is controlled by three critical processes: (1) attainment of sulfur saturation in the mafic to ultramafic magma to cause segregation of liquid sulfide droplets; (2) interaction of liquid sulfide with sufficient volumes of new magma to concentrate chalcophile metals to an economic level at the trap site; (3) concentration of the liquid sulfides within a relatively small volume of rock (e.g. Naldrett, 1989; Hannah and Stein, 2002). Critical elements in the formation of basal segregations of nickel sulfides are therefore: emplacement of S-undersaturated, Ni-bearing tholeiitic magmas into crustal rocks, resulting in rapid S-saturation through crustal contamination; mixing of magma of differing compositions; or a rapid fall in temperature (Li and Naldrett, 1993, 2000; Lambert et al., 1998, 2000; Ripley et al., 1999).

Most Ni–Cu mineralization is hosted by mafic and ultramafic rocks; hence, these are the most critical chemical traps. Therefore, a predictor map showing occurrences of mafic and ultramafic rocks buffered to 1 km, was generated (Fig. A14), with a map weight of 9.

Ni sulfides are commonly concentrated in embayments and depressions at the bases of ultramafic flows or intrusions beneath the thickest cumulate succession (Hoatson and Blake, 2000). Magmatic nickel sulfides are likely associated with cumulates rich in MgO, nickel, or chromite (e.g. Great Dyke, Zimbabwe; Schoenberg et al., 2003). Cumulate rocks could indicate the presence of a trap in which there may also be sulfides. We therefore prepared a predictor map showing chromitite, peridotite, and early Giles ultramafic rocks with a 10 km-wide buffer around the extracted lithology (Fig. A15), and assigned a relatively low map weight of 6 (Table A1) because cumulates are not as important for Ni–Cu precipitation as they are for PGE mineralization (Maier and Groves, 2011).

Enhanced Cr content could also indicate mafic–ultramafic suites that could host Ni–Cu mineralization, and Cr contents above 1000 ppm were arbitrarily chosen as possible indicators for Ni precipitation (Fig. A16). High Cr content is not a guarantee of chemical trapping and chromite layers are lacking in the Giles intrusion (Ballhaus and Glikson, 1995; Glikson et al., 1996). We therefore assigned a relatively low map weight of 6.

Ni/Cu and Ni/Co ratios are very useful parameters for targeting sulfide deposition (Figs A17, A18). High ratios ([Z log Ni/Cu] > 0.63; [Z log Ni/Co] > 0.61) ideally correspond with the upper surface of a deposit, and anomalously low ratios ([Z log Ni/Cu] < –1.22; [Z log Ni/Co] < –1.44) indicate that the magma has been stripped of Ni and lies downstream of any NiS accumulation. A 'normal' ratio (–1.22 < [Z log Ni/Cu] < 0.63; –1.44 < [Z log Ni/Co] < 1.76) indicates the location of the feeder, or that the magma never reached sulfur saturation. These ratios may be used in a variety of ways; we chose to use high ratios as indicators of greater prospectivity (Figs A17, A18), and attributed a map weight of 9 to the Ni/Cu map because it directly shows Ni/Cu concentration and sulfur saturation, and a map weight of 7 to the Ni/Co map because Co only points to sulfur saturation (Table A1).

Copper and zirconium are incompatible elements during fractionation of a magma that is unsaturated with respect to sulfide. Thus, although concentration of both elements increases with progressive fractionation, the Cu/Zr ratio remains relatively constant. Once the magma becomes sulfide saturated, Cu is compatible in the sulfide liquid and is extracted from the parental silicate liquid. This causes a decrease in the Cu/Zr ratio (Seat et al, 2007), so the (Cu/Zr) ratio also indicates degree of sulfur saturation (Fig. A19). If Cu/Zr is less than 1–2, the rock is sulfur undersaturated, and if Cu/Zr is greater than 1–2 the rock is sulfur saturated (Maier et al., 2007a). A high Cu/Zr ratio in mafic–ultramafic rocks is a direct indicator of magmatic sulfides; hence, we accorded this predictor map a map weight of 9.

Pt and Pd contents of magma may indicate close association with Ni sulfide (Maier et al., 2007), hence might also be used to indicate degree of sulfur saturation. High Pt and Pd indicate a magma that is undersaturated with respect to S. Low values of Pt and Pd could indicate early S saturation and metal extraction, and therefore less fertile magmas (Lightfoot, 2007). Accumulation of Pt and Pd can be highlighted using the ratios Pt/Zr and Pd/Zr, as Zr is considered as being relatively immobile, and any increase of these ratios emphasize Pt and Pd content accumulation, respectively (Maier et al., 2007a; Figs A20, A21). We attributed a map weight of 9 to both predictor maps.

Sulfur saturation of magma may also be triggered by addition of external sulfur by devolatization, partial melting, or bulk assimilation of upper continental crustal rocks (Lesher and Campbell, 1993). Rocks that have undergone these processes are enriched in incompatible elements, leading to anomalous concentrations of these elements, or the ratios of incompatible elements such as Th/Yb, Th/Nb, and La/Nb (Yb and Nb are not considered to be very mobile). The accumulation of these elements may indicate contamination of the mafic–ultramafic magma suites with upper-crustal material causing sulfur saturation (e.g. Naldrett, 1997). Hence, these may be proxies for S saturation (Figs A22, A23, A24, respectively). As the maps are only general indicators of prospectivity, they were assigned map weights of 8.

High sulfur content of the magma might also be a general proxy for sulfur saturation (Prendergast, 2004), but it is not necessarily associated with Ni sulfide mineralization, hence the S content predictor map is assigned a map weight of 7 (Fig. A25). The physical presence of a sulfide-rich unit could also indicate S saturation, but no sulfidic units are recorded in the interpreted bedrock geological map (GSWA, 2010b).

Ni and Cu content (Figs A26, A27) above background in the mafic–ultramafic suites might indicate early S saturation and metal extraction, hence potentially fertile magmas (Ni >3000 ppm and Cu >90 ppm). It is important to note that highest Ni values will occur in laterite or ultramafic cumulates; prospective rocks will have lower Ni. Both Ni and Cu contents were extracted from the GSWA state geochemistry database (GSWA, 2010b) and GA Ozchem database (GA, 2007). Ni is potentially a direct proxy for Ni mineralization, and the predictor map was assigned a map weight of 9, whereas anomalous Cu does not necessarily correlate with a nickel deposit, and this map was assigned a map weight of 6.5 (Table A1).

In rare cases, granitic intrusions or felsic rocks can become sulfur saturated and form sulfide segregations (Okiep, South Africa; Caraiba, Brazil; Maier and Groves, 2011). A predictor map showing occurrences of felsic rocks buffered to 5 km was therefore generated (Fig. A28), but with a map weight of only 6 because felsic rocks are unusual hosts for Ni–Cu mineralization.

Fuzzy model

Combining fuzzy membership values

Fuzzy predictor maps were combined using a three-stage inference network designed to combine the 28 fuzzy predictor maps (Table A1, Fig. 14). Those for source, pathway, chemical trap, and physical trap were first combined using the fuzzy OR operator to create a single fuzzy predictor map for each critical component of the magmatic nickel–copper mineral system. The fuzzy OR operator was used because the presence of any one of the predictor maps is sufficient to infer the presence of the respective component. In the second stage, the fuzzy predictor maps for physical throttle and chemical scrubber were combined into a single predictor map for traps using the fuzzy AND operator, because both a physical trap site and a conducive geochemical environment are necessary for precipitation of nickel and copper from the mineralizing fluids. Finally, the three fuzzy predictor maps for source, pathway and trap were combined using the fuzzy PRODUCT operator to create the output fuzzy prospectivity map (Fig.15).

Results of magmatic Ni–Cu prospectivity analysis

The final GIS model map contains 18 prospective clusters ([α], [β], [χ], [δ], [ε], [ϕ], [γ], [η], [ι], [φ], [κ], [λ], [μ], [ν], [ο], [π], [θ] and [ρ], Fig. 15) with a high fuzzy PRODUCT value that varies from 0.28 to 0.34. Interestingly, most of the 18 prospective clusters do not correspond to known nickel occurrences (Fig. 15). Here, nickel occurrences are associated with areas of high to middle fuzzy PRODUCT value (0.14–0.34). The known Ni–Cu Nebo and Babel deposits have high fuzzy PRODUCT values between 0.21 and 0.27. We then analysed the location of the prospective targets with respect to original predictor maps to assess the most critical elements in this mineral system.

The connection between Ni–Cu sources and the new delineated prospective clusters is not very clear. All peak clusters are close to mafic and ultramafic rocks from the Warakurna Supersuite, but only a few are associated with non-Warakurna Supersuite mafic rocks. Therefore, proximity to Warakurna Supersuite mafic rocks is a major influence on the prospectivity calculation. The MgO/(MgO+FeO) source predictor map is also a less important component of the prospectivity model.

On top of the Warakurna Supersuite layer, pathways control the location of prospective clusters, and are a key ingredient of the prospectivity model. Only cluster [ε]

shows no relation to the crustal-scale faults layer, with others either marginal to or directly located on faults. Musgrave and Mount West Orogeny structures have little significance, whereas Giles Event age structures have significance for most prospective clusters except for [π] and [μ]. Many clusters ([α], [γ], [η], [κ], [λ], [μ], [ν], [ο] and [π]) are close to Petermann and Alice Springs Orogeny faults; however, this is probably only a significant layer in the southeast Tjuni Purlka Zone, for clusters [μ], [ν], [ο] and [π], where there is an apparent absence of Giles Event age structures due to later overprinting and reactivation. Only [β] shows any hint of being influenced by dykes, due to their relative scarcity in the mapped data. All prospective areas are close to chonolith-like magnetic features, although only [ν] and [ε] directly overlie one of these features.

Physical traps are represented by fault density, fault intersection distance, and fault intersection density. Apart from clusters [φ], [ο] and [π], all the high-potential targets are associated with at least one of these three physical traps. Strong prospectivity values in each of these three predictor maps characterize the region surrounding the [β], [χ], and [δ] clusters, and may be significant in these cases. However, for other cases, the interaction of this layer with the 'pathways' layers is unclear and it may, or may not, be a significant component of the model.

The association between the different chemical traps and the prospective clusters is unsystematic, even though all chemical scrubber maps have a similar map weight. No apparent positive relationship exists between prospective areas and the high Ni/Cu, Ni/Co, Cu/Zr, Pt/Zr, Pd/Zr, Th/Nb, Th/Yb, and La/Nb ratios. The only positive association with a high geochemistry-based value is with Ni, Cr, and Cu content. These chemical trap layers do not positively contribute to the high clusters, but they may contribute to low overall prospectivity in areas that should otherwise be high, for example in the region adjacent to the north–south Lasseter Graben directly west of Nebo–Babel.

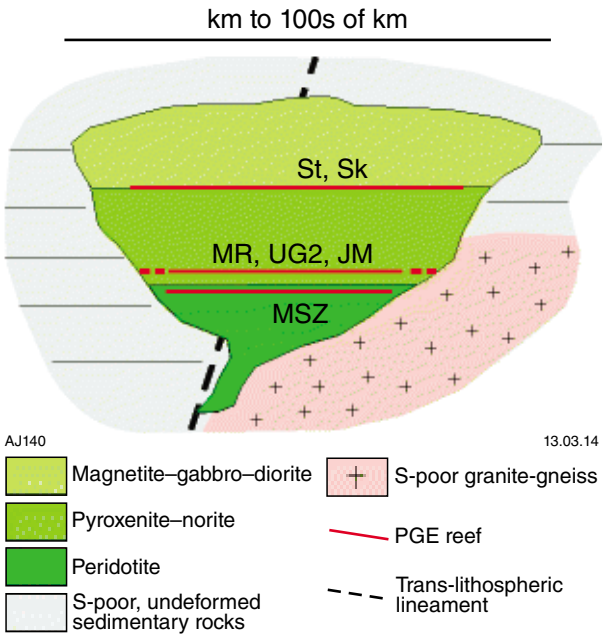

Figure 16. Schematic diagram summarizing important elements of PGE deposits. PGE deposits are emplaced into relatively undeformed, S-poor cratonic lithosphere. JM – JM reef of Stillwater Complex; MR and UG2 – Merensky Reef and UG2 chromitite of Bushveld Complex; MSZ – Main Sulfide Zone of Great Dyke; Sk – Skaergaard PGE reefs; St – PGE reefs of Stella intrusion (Maier and Groves, 2011).

Magmatic PGE mineral systems

The platinum group elements (PGE) include platinum (Pt), palladium (Pd), rhodium (Rh), iridium (Ir), osmium (Os), and ruthenium (Ru). The elements of most commercial significance are platinum and palladium.

Most economic PGE deposits occur as stratiform or stratabound reefs in large, layered, extensively differentiated, mafic–ultramafic intrusions (e.g. the Merensky Reef, UG2 chromitite, and Platreef of the Bushveld Complex in South Africa; the JM Reef of the Stillwater Complex in Montana; the Main Sulfide Zone of the Great Dyke in Zimbabwe; Fig. 16; see Maier (2005) for a summary of global occurrences). PGE ores are generally hosted by sulfides (pyrrhotite–pentlandite–chalcopyrite), except in some chromitite reefs where the PGEs occur largely in platinum-group minerals (Cawthorn et al., 2005 and references therein). The richest and most continuous reefs tend to occur in laterally extensive intrusions (e.g. 65 000 km^2 Bushveld Complex). Less continuous and more irregular reefs are characteristic of smaller intrusions (e.g. 35 km^2 Panton Sill in Australia). In all cases, the PGE are the main products; Ni and Cu are byproducts.

Intrusions were emplaced during the late Archean and early Proterozoic into stabilized, relatively S-poor cratonic lithosphere that provides enhanced preservation potential. Parental magmas were predominantly mantle derived, but involvement of subcontinental lithospheric mantle is also suggested by the relative Pt enrichment in most major deposits. Host magmas are thought to ascend via intracratonic suture zones and trans-lithospheric breaks.

The ingredients required to form magmatic PGE deposits include: 1) mafic–ultramafic rock types (dunite, harzburgite, pyroxenite, norite–gabbronorite–gabbro, troctolite, anorthosite, chromitite, and magnetitite), with chromitite and orthopyroxenite particularly common; 2) alternating compressional–extensional tectonic regimes that encourage magma migration; 3) sites of maximum magma permeability. Most economic PGE deposits are also associated with widespread metasomatism of the host rocks. Pt, Pd, and Cr content are indicative of chemical scrubbers. Potential host rocks are relatively easy to locate and delineate because of their large size and the generally simple geometry of the host intrusions (Maier and Groves, 2011).

Predictor maps

In the following sections, details of the fuzzy predictor maps generated for the PGE prospectivity analysis are given along with their geological rationale (Table A2). The predictor maps were combined into a three-stage inference network (Fig. 17) to generate the final prospectivity map (Fig. 18).

Source

Sources for PGE systems are similar to those for Ni–Cu systems, except that primitive magmas are not required, as long as they were derived from the mantle (Maier and Groves, 2011). The layered mafic–ultramafic Giles 'G1' intrusions may be some of the largest on Earth and may be prospective.

The Halleys prospect hosts PGE sulfide mineralization within the mafic 'Saturn' body (see Fig. 8). Emplacement of this intrusion at 1072 ± 8 Ma was part of a later stage of the Giles Event than the thickly layered G1 intrusions. The Warakurna Supersuite has the greatest potential to host magmatic PGE sulfide mineralization (Wingate et al., 2004). We therefore used the same three source predictor maps for PGE as for Ni–Cu systems, with the same map weight values (Table A2): 'Distance to mantle-derived Mg-rich mafic/ultramafic rocks (Warakurna Supersuite)' (Fig. A1), 'Distance to mantle-derived Mg-rich mafic/ultramafic rocks (non-Warakurna Supersuite)' (Fig. A2) and 'MgO/(MgO+FeO) ratio (Fig. A3).

Pathways

Faults, dykes and chonoliths are all potential pathways for magma to reach a trap. Crustal-scale faults are considered to be one of the most important pathways (Fig. A4, map weight = 9). Trans-lithospheric pathways can channel dense primitive mantle-derived magmas into the upper crust (Naldrett, 2010).

Emplacement of the earliest and largest layered igneous intrusions was controlled by structures related to the early to mid-Giles Event. Mineralized magma migration may have been facilitated by a switch in stress regime between early Giles and the mid-Giles events from approximately north–south extension to approximately north–south compression, and later, by a switch in regime from east-southeasterly oriented dextral transpression to north–south oriented sinistral transpression during the late Giles Event. The Saturn intrusion, and by implication the Halleys prospect, was intruded between the mid and late Giles Events. Hence, many structures related to the Saturn intrusion and Halleys prospect were combined into a predictor map with a 5 km wide zone around these structures (Fig. A29, map weight = 9).

Other Giles Event age structures (EG2, MGE, LGE1, LGE2; Table 1) were active during mafic magmatism and could have controlled the emplacement of PGE-hosting intrusions. However, they were not necessarily active during the emplacement of the Halleys prospect, and therefore are considered less prospective (Fig. A30; map weight = 8.5). We also used the pathway predictor maps for 'Petermann and Alice Springs Orogeny faults' (Fig. A7) and Mount West Orogeny and Musgrave Orogeny structures (Fig. A8), because they were long-lived structures and were also potential conduits for magma.

Vertically stacked magma chambers and associated feeder dykes (Glikson et al., 1996) may also have acted as pathways for mineralizing magmas. We therefore used the 'presence of circular feature' (Fig. A10) and 'dykes' (Fig. A9) pathway predictor maps developed for Ni–Cu systems. Large dykes and chonoliths are prospective for PGE elsewhere in the world that (e.g. Great Dyke in Zimbabwe); hence, we assigned a map weight of 9 to these predictor maps (Table A2).

Physical traps

Magmas can travel for considerable distances before encountering a major discontinuity that allows them to ascend into suitable physical traps, where they can precipitate most minerals. Essential ingredients are an extensive network of faults and favourably oriented contacts, which act as barriers to flow and reduce magma velocity to the point where metals can efficiently accumulate (e.g. Maier and Groves, 2011).

A common feature of sulfide reef-type deposits in layered intrusions is the tendency to occur at, or some distance above, the contact between the lower ultramafic and upper mafic zones. For instance, reefs in the Stillwater (USA) and Bushveld (South Africa, Maier et al., 2008) complexes occur some distance above the contact, although the Hartley and Munni Munni reefs (Australia) lie immediately below this contact (Barnes et al., 1992). Contact-style mineralization at Shakespeare in Ontario (Canada) occurs at the base of the intrusion (Sproule et al., 2007). We believe contact-style mineralization to be the most important physical trap. We therefore produced a predictor map using 'distance to contacts of mafic and ultramafic rocks' with the host rocks from the bedrock map by GSWA (2010a), buffered to 10 km, and assigned a map weight of 9 (Table A2, Fig. A31).

We also used the 'fault density' (Fig. A11), 'distance to fault intersection' (all faults) (Fig. A12), and 'fault intersection density' (Fig. A13) predictor maps from the Ni–Cu analysis as indicators of potential fluid focusing.

Chemical scrubbers

Most Ni–Cu mineralization is hosted by the mafic and ultramafic rocks; hence, those are the most critical chemical traps (Fig. A14, map weight = 9).

Sulfide mineral cumulates in layered intrusions are an important source of PGE, hence we used the same cumulate predictor map that we applied to magmatic Ni–Cu systems (Fig. A15), but applied a map weight of 9 to reflect the absolute necessity of cumulates to precipitate PGE (which is not the case for Ni mineralization; Maier and Groves, 2011).

PGE mineralized rocks commonly contain abundant xenoliths of dolomite and shale suggesting interaction of the magma with relatively reactive floor rocks. Assimilation of dolomite probably did not introduce significant amounts

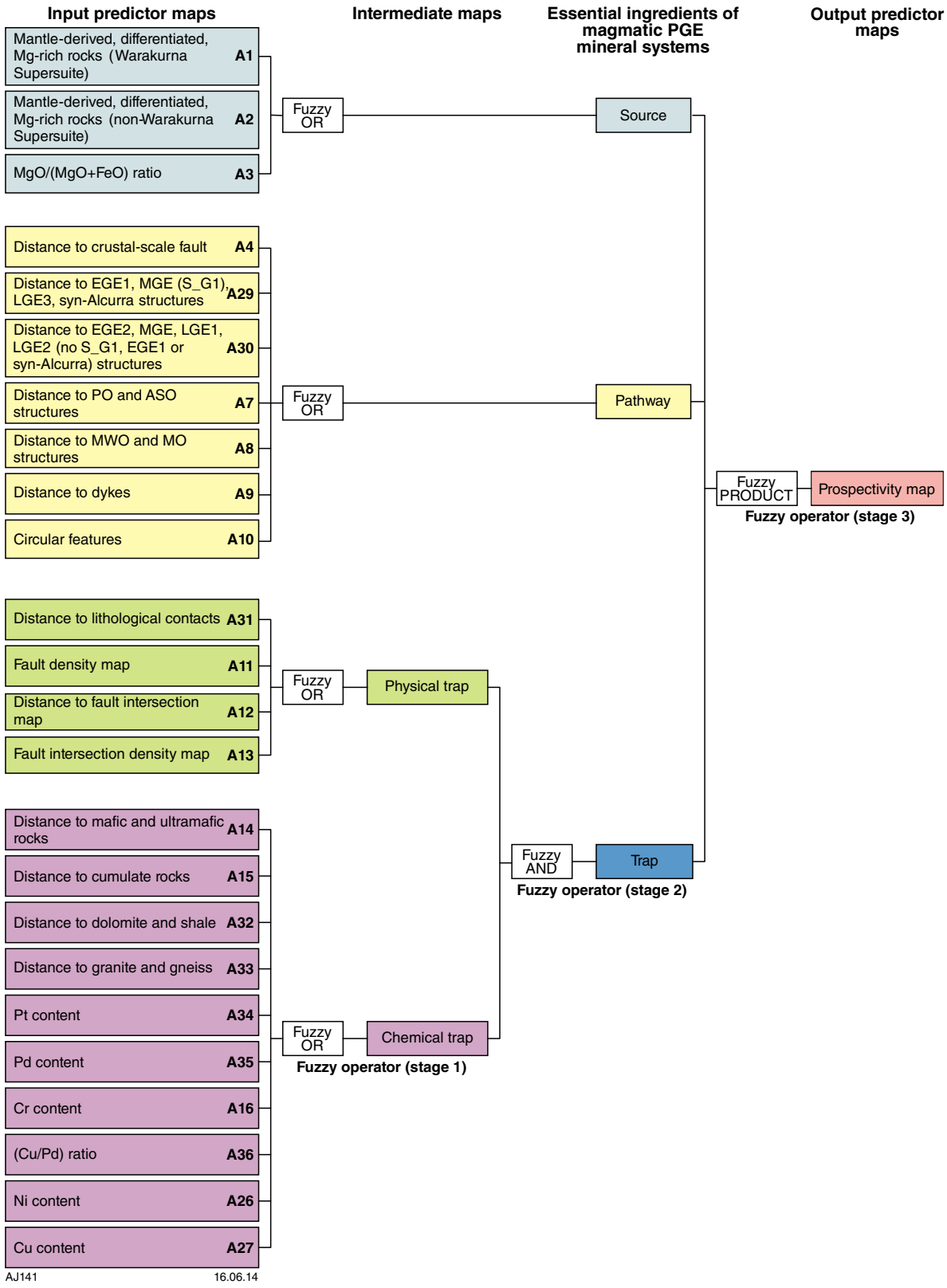

Figure 17. Multi-stage fuzzy inference network used for combining fuzzy PGE predictor maps

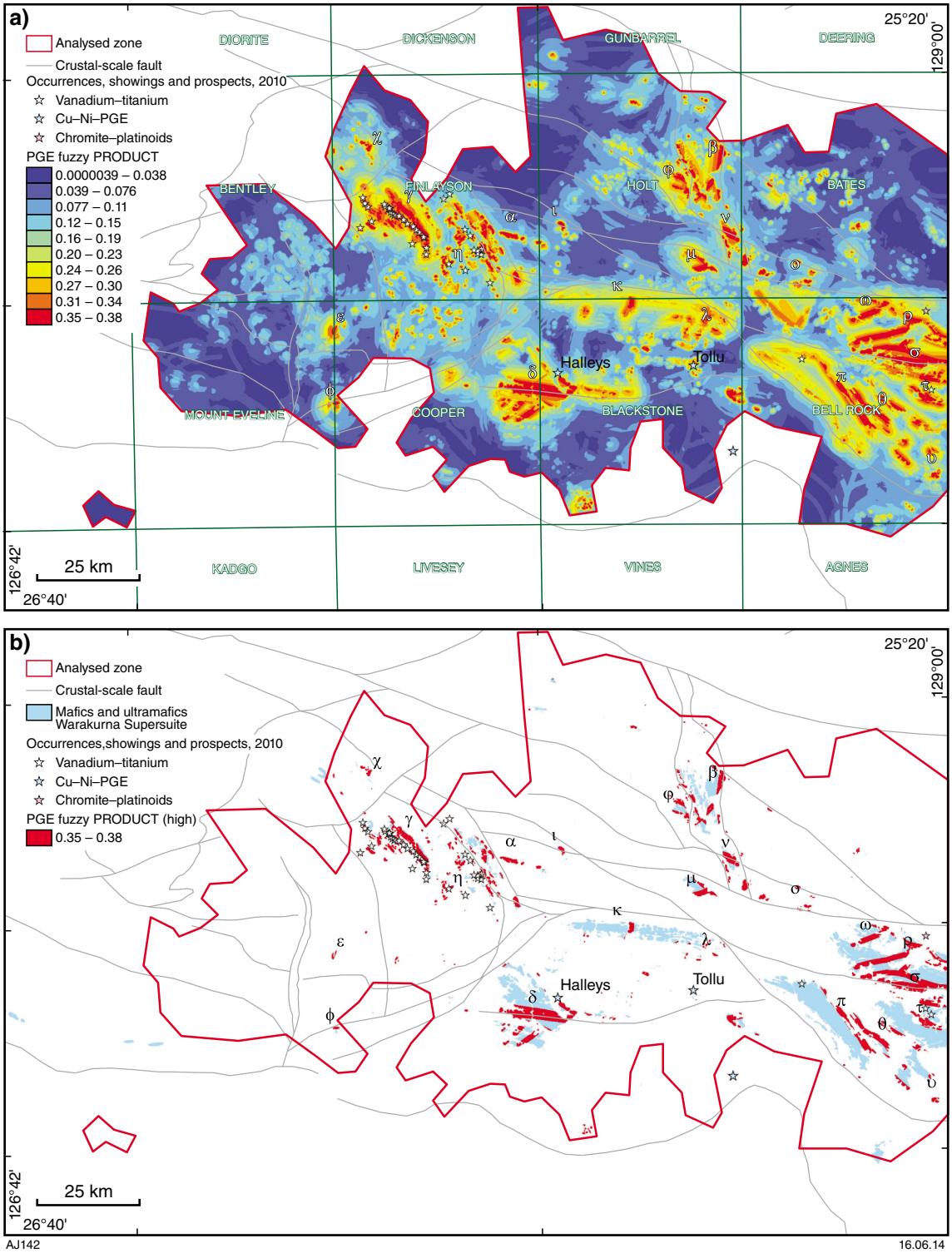

Figure 18. a) Fuzzy prospectivity model for magmatic PGE mineral system; b) zone of high fuzzy value for the magmatic PGE prospectivity analysis over the analysed area with even data coverage

of external sulfur to the magma. Instead, assimilation of dolomite may have lowered the sulfur solubility of the magma in response to devolatization and oxidation (De Waal, 1975; Buchanan et al., 1981; Gain and Mostert, 1982; White, 1994). The control on contact-style PGE mineralization by contamination of magmas by country rocks (Buchanan et al., 1981; Gain and Mostert, 1982; White, 1994) was analysed using 'dolomite and shale' (Fig. A32, possibly partly metasomatic) and 'granite–gneiss rocks' (Fig. A33) predictor maps, extracted from the interpreted bedrock geology map of GSWA (2010a), and buffered to 1000 m. We consider these less significant than the cumulate predictor map, hence assigned a map weight of 8.

The presence of magmatic sulfides enriched in PGE may be indicated by high Pt and Pd contents (Z log Pt > 4; Z log Pd > 2.75). These are potentially direct indicators of melt fertility and were assigned a map weight of 9 (Figs A34, A35).

Chromite is commonly concentrated within pods in layered intrusions, and may be locally enriched in PGE. Positive values (Z log Cr >2) could indicate mafic–ultramafic suites and the presence of chromitites. Hence we regarded Cr content to be an excellent indicator for PGE, and assigned the predictor map a weight of 9 (Fig. A16).

Cu/Pd ratios (Fig. A36) are particularly useful for evaluating the PGE potential of intrusions, and for delineating the position of the reefs within the intrusions (Halter et al., 2002). The strongly chalcophile Pd is preferentially depleted during sulfide segregation, increasing the Cu/Pd ratio of the subsequently crystallizing overlying cumulates. We assigned this predictor map a weight of 9.

Ni and Cu are byproducts in the PGE system, but could indicate mafic–ultramafic suites. We therefore used 'Ni content' and 'Cu content' predictor maps (Figs A26, A27) from the Ni–Cu analysis but assigned a less significant map weight of 6.5 because high Ni/Cu is not necessarily associated with high PGE content.

Fuzzy model

Combining fuzzy membership values

A three-stage inference network was used to combine the 24 predictor maps (Table A2, Fig. 17). Respective predictor maps of each of the four key components of PGE mineral systems (namely source, pathways, and physical and chemical traps) were combined using the fuzzy OR because the presence of any one of the predictor maps is sufficient to infer the presence of the respective component. The physical and chemical trap maps were then combined using fuzzy AND. Finally, the three residual components were combined using the fuzzy PRODUCT operator to derive the fuzzy prospectivity map for PGEs deposits in the WMP (Fig. 18).

Results of magmatic PGE prospectivity analysis

The resulting prospectivity map (Fig. 18) includes 22 highly prospective areas: [α], [β], [χ], [δ], [ε], [ϕ], [γ], [η], [ι], [φ], [κ], [λ], [μ], [ν], [ο], [π], [θ], [ρ], [σ], [τ], [υ] and [ω]. Their fuzzy PRODUCT values vary between 0.35 and 0.38 (Fig. 18b). Areas [γ], [ρ] and [τ] correspond to known PGE prospects. All the other known sites of PGE mineralization in the WMP are occurrences and showings (Fig. 18), meaning that they are not necessarily linked to any economic deposit. All occurrences in the FINLAYSON map fall into the high fuzzy PRODUCT value. The two prospects with potentially economic PGE levels, Halleys and Tollu, have high fuzzy PRODUCT values between 0.27 and 0.34. The most critical elements for the magmatic PGE mineral system model are identified through the predictor maps and, in the following, their relevance to the overall model is assessed with respect to the locations of the high prospectivity areas.

The correlation between the different PGE sources and the prospective regions is inconsistent. All prospective sites fall into mafic and ultramafic rocks from the Warakurna Supersuite, but not necessarily from the non-Warakurna Supersuite or high MgO/(MgO+FeO) ratio.

All high prospectivity clusters are associated with pathways, implying a key role for this component of the PGE mineral system model. Most of the prospective areas are located right on crustal-scale faults (e.g. [ϕ], [ι], [δ], [β], [σ] and [ρ]) or near Late Giles structures. Mount West and Musgrave Orogeny faults as well as other Giles Event structures are the least prospective pathways (e.g. [χ], [π] and [υ]). There is no obvious relationship between chonolith-like magnetic features or dykes and high prospectivity.

Physical traps and potential clusters display a strong correlation with prospective zones, enhancing the importance of the trap MSA ingredient. It appears that every site is located close to features considered indicative of potential for contact-style mineralization (Fig. A31), of intersecting faults (Fig. A12), and of high fault density (Fig. A11). However, no positive correlation is evident between high fault intersection density (Fig. A13) and highly prospective clusters.

Occurrence of potential chemical scrubbers does not necessarily coincide with potential targets. Clusters located in the centre of the WMP are not associated with metasomatic rocks such as dolomite and shale (e.g. [γ] and [η]). All highly prospective sites are associated with granites and gneisses as well as cumulates. However, no clear relationship exists with the high Cr content values. A few prospective clusters are associated with low Pt values (e.g. [ε], [γ]) and Pd values (e.g. [ι], [λ]), suggesting that these are not an essential component of the mineral system. Highly prospective areas [φ] and [τ] are associated with high Cu/Pd ratios but not systematically with high nickel and copper contents (e.g. [ϕ]).

Orogenic and intrusion-related gold mineral systems

Groves et al. (1998) proposed the term orogenic gold deposit to include all deposits variously described as mesothermal gold, metamorphic gold, gold-only, lode gold, shear zone hosted, and structurally controlled gold deposits. Orogenic gold deposits are interpreted to be genetically distinct from intrusion-related gold systems by a number of authors (e.g. Lang and Baker, 2001; Hart, 2007), but recent work interprets intrusion-related to be a subclass of orogenic gold deposits on the basis of temporal, spatial, and genetic similarities (SG Hagemann, written comm.). For this analysis, we attempted to develop a single prospectivity model that incorporates the two types of gold systems.

Predictor maps

In the following subsections, details on the fuzzy predictor maps generated for the gold prospectivity analysis are given along with their geological rationale (Table A3). The predictor maps were combined using a three-stage inference network (Fig. 19) to generate the final prospectivity maps (Figs 20 and 21).

Source

In intrusion-related gold systems, gold-bearing hydrothermal fluids are typically derived from granitic intrusions. Hence, gold mineralization is most likely to occur in the vicinity of granitic bodies, with the probability of mineralization decreasing with the increasing distance from the granites (Fig. A37). We assigned this predictor map a map weight of 7 (Table A3). For orogenic gold systems, the metal and fluids are generally considered to be related to regional metamorphism and to have no direct genetic relationship to granitic intrusions. For this system we disregarded source for orogenic gold as there is no obvious basis on which to discrimate regional variations in gold-bearing fluid production within the west Musgrave Province.

Pathways

Gold is leached from crustal rocks and deposited by large-scale hydrothermal systems involving extensive plumbing systems at, or above, the brittle–ductile transition (Groves and Phillips, 1987; Groves, 1993; Phillips and Powell, 1993; Groves et al., 1998). Faults are therefore the most likely critical pathways for mineralizing fluids, and crustal-scale examples are probably the most important (McCuaig et al., 2010; Joly et al., 2011). We therefore used the predictor map 'distance to crustal-scale fault' developed for Ni–Cu systems and assigned a map weight of 9 (Fig. A4).

The Handpump gold deposit, the only known gold deposit in the WMP, coincides spatially with late Giles Event 2 structures, implying that the most likely critical pathways for mineralizing fluids were faults active during this event. A predictor map showing the distance to structures of this age was created and assigned a map weight of 9 (Fig. A38).

Any structures active during regional metamorphism and granite emplacement may potentially have been fluid conduits. Hence, we combined early, middle and late Giles (other than late Giles 2) structures into a separate map (Fig. A39). This map had a lower map weight of 8.5 to reflect slightly lower perceived prospectivity compared to late Giles 2 event structures. Faults active during the Petermann Orogeny and Alice Springs Orogeny probably also existed during the Giles Event, hence are also prospective pathways. We used the 'distance to Petermann Orogeny and Alice Springs Orogeny structures' Ni–Cu predictor map for these structures and assigned a map weight of 8.5 (Fig. A7). We also used structures associated with the Mount West Orogeny and Musgrave Orogeny (Fig. A8) and assigned a map weight of 8 because they may still have provided fluid pathways during the late Giles Event, or perhaps earlier gold-mineralizing events (Table A3).

We created a predictor map to represent proximity any fault and gold concentrations. Gold concentrations from the GSWA geochemical data vary between 0.01 – 0.17 ppm. Each fault was buffered to 5 km and the median gold value in each buffer was extracted and attributed to the buffer (Fig. A40). This result is a derivative predictor map that combines these indicators, and to which we assigned a map weight of 9.

Physical traps

Favourable gold traps are physical throttles (e.g. brittle–ductile shear zones, stockwork, and breccias) where mineralizing fluid flow is focused, also requiring a favourable geochemical environment (Groves et al., 1998; Hagemann and Cassidy, 2000). Such throttles may include impermeable stratigraphy or localized damage zones on regional faults. We believe that contacts between geological units that have a high competency contrast are particularly favourable physical traps. We have created a predictor map (Fig. A41) by assigning to each generalized lithological unit a (relative) rheology value (Fig. 22) then attributing each geological contact with the difference in rheology between units on each side. The 'competency contrast' map was then derived by allocating to each unit cell the value of the rheology difference of the nearest contact, up to a maximum distance of 1 km. We assigned this a map weight of 8.

Higher geological contact densities imply increased probabilities of competency differences, and hence increased fault/fracture densities and space for trapping metal. We therefore derived a 'geological contact density' map by mapping the density of geological contacts in areas of one square kilometre (Fig. A42) and attributed this a map weight of 7.

We also created a 'geological contact density weighted by competency contrast' map to capture the competency contrast at some contact (Fig. A43). This was derived by mapping the geological contact densities per square kilometre weighted by competency contrast. This map was assigned a map weight of 9.

Maps of 'fault density' (Fig. A11), 'distance to fault intersection' (all faults) (Fig. A12) and 'all fault

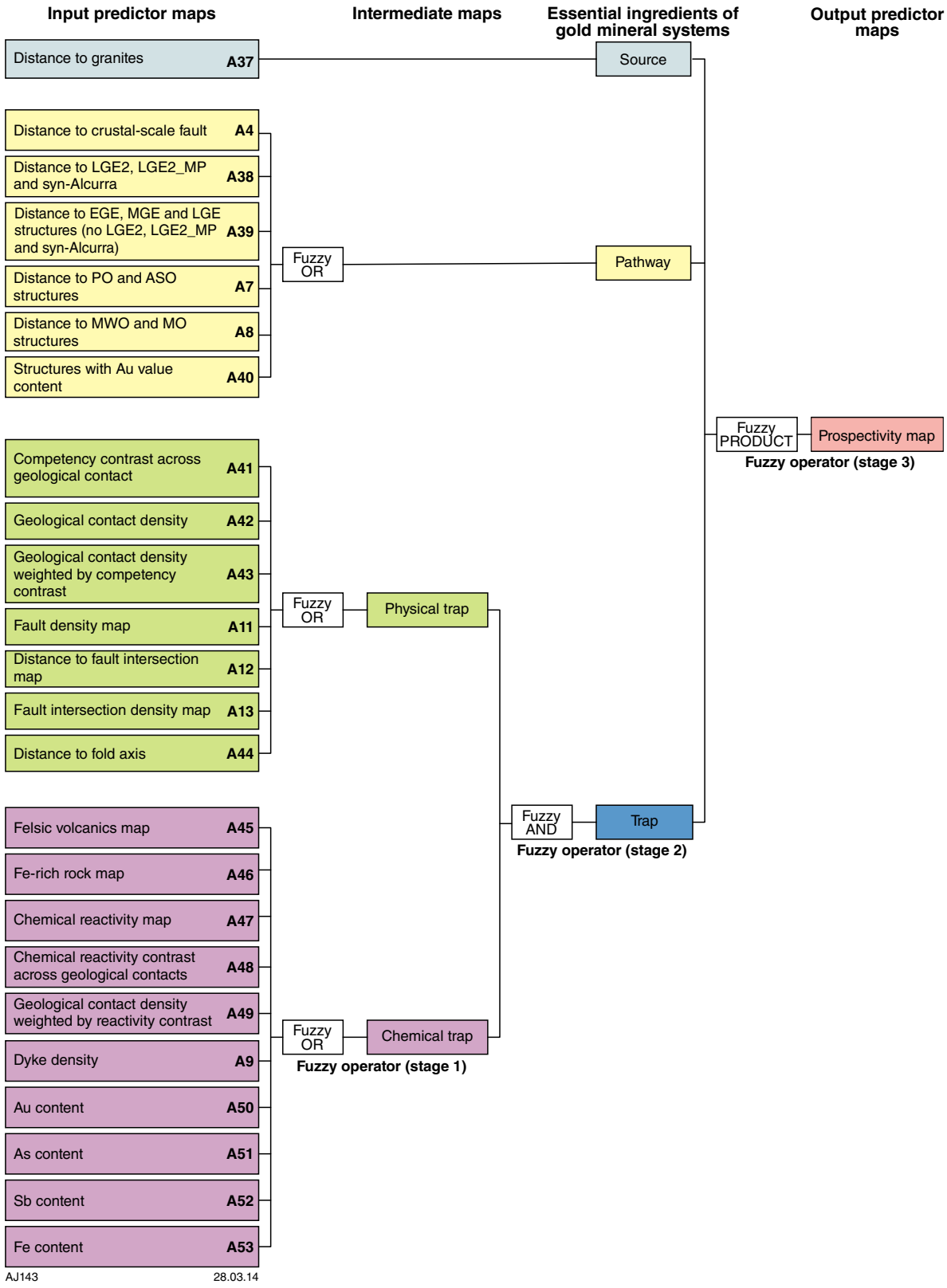

Figure 19. Multi-stage fuzzy inference network used for combining fuzzy gold predictor maps

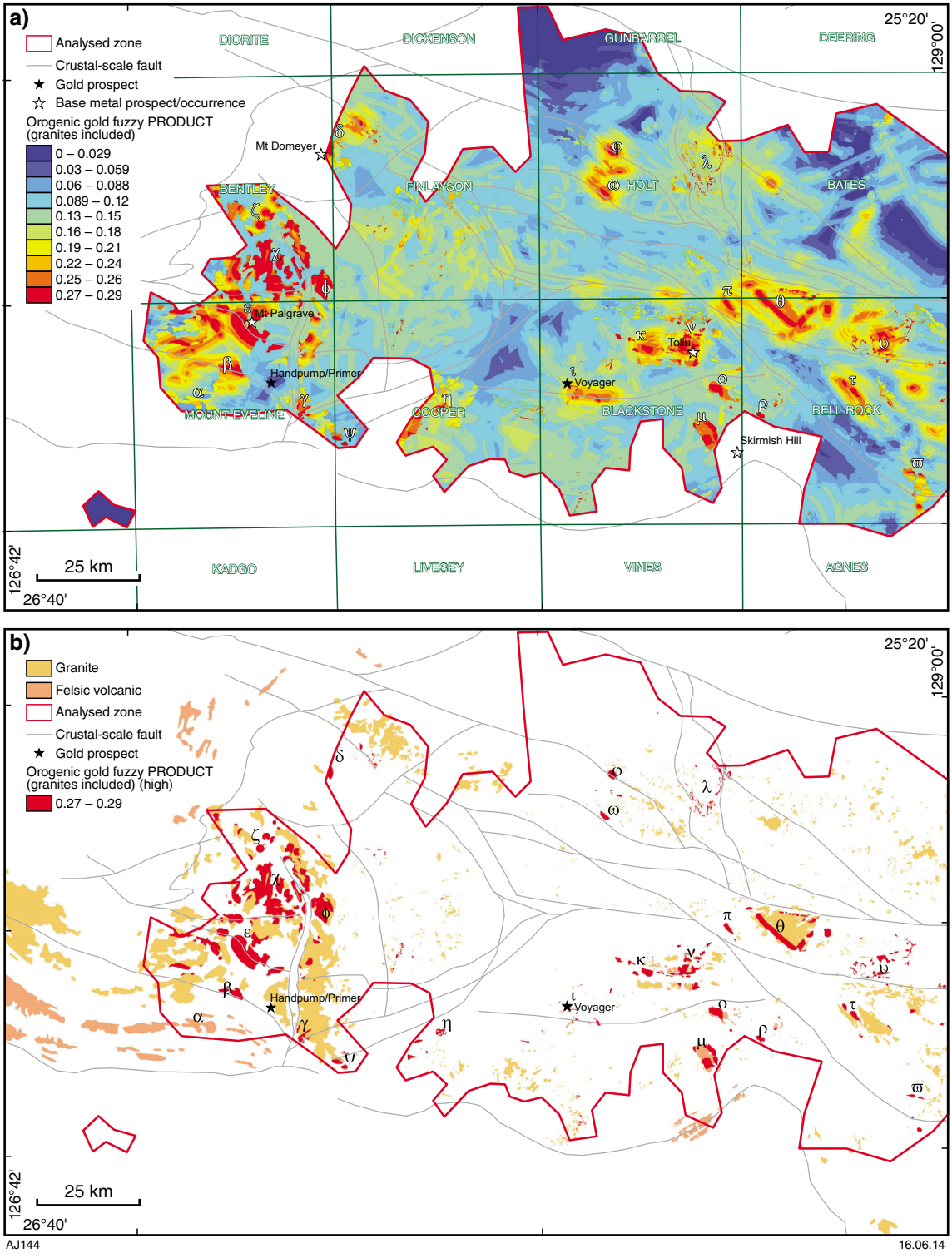

Figure 20. a) Fuzzy prospectivity model for the intrusion-related gold mineral system; b) zone of high fuzzy value for the intrusion-related gold prospectivity analysis over the analysed area with even data coverage

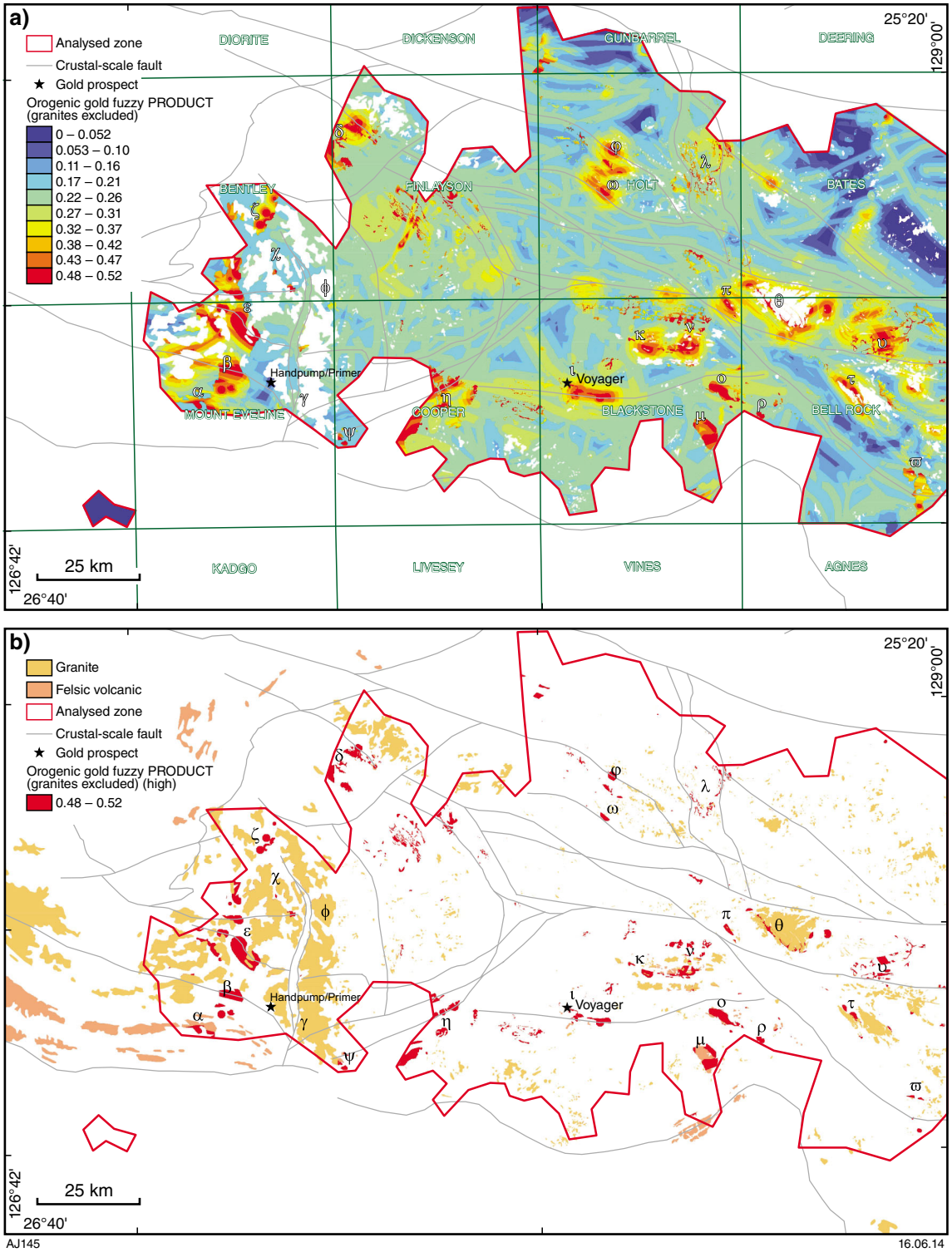

Figure 21. **a) Fuzzy prospectivity model for the orogenic gold mineral system with 'granite as a source predictor' disregarded; b) zone of high fuzzy value for the orogenic gold prospectivity analysis over the analysed area with even data coverage. Cluster locations are the same as Figure 20 for comparison purposes.**

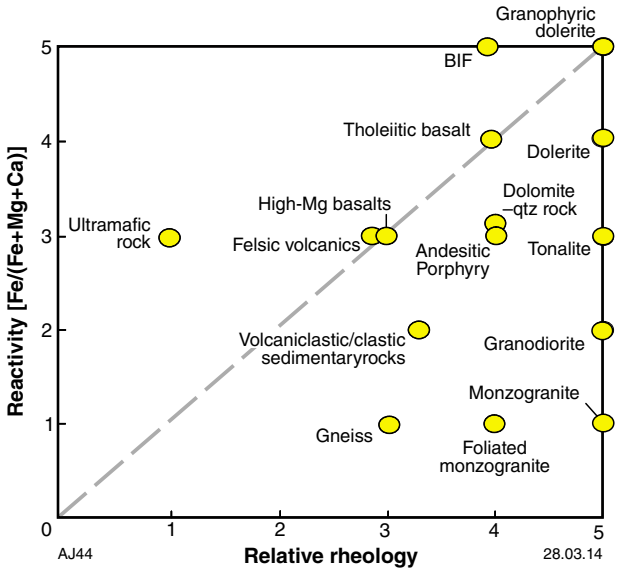

Figure 22. Relative chemical reactivity and rheological strengths for selected rocks (from Brown, 2002)

intersection density' (Fig. A13) resulting from the previously described Ni–Cu model were reused to also identify greater structural complexity, taken as a proxy for an increased probability of sites for fluid focusing and deceleration. Conceptually, anticline fold axes, which are under tension due to bending stresses, are good traps for hydrothermal fluids. We created a predictor map 'distance to fold axis' (Fig. A44) to represent this. These four factors are probably less important than 'geological contact density weighted by competency contrast' map; hence, were assigned map weights of 7.5 or 8 (Table A3).

Chemical scrubbers

Gold deposition can occur during changes in physical conditions, abrupt changes in chemical gradient, phase separation, and fluid mixing. Dramatic reductions in fluid pressure can induce chemical changes that can trigger gold precipitation (McCuaig and Kerrich, 1998). Reactive rocks are more susceptible to these processes and hence we used this concept as a proxy for the likelihood of chemical change during mineralization.

The Handpump prospect occurs in felsic volcanic rocks of the Bentley Supergroup. Depending on location, these units were erupted onto basal Kunmarnara Group basalts and conglomerates, mafic–ultramafic intrusions, or basement gneiss/granite (Fig. 1), providing a contrast in lithology. The Mount Palgrave Group has relatively high reactivity. We therefore mapped the occurrence of all felsic volcanic rocks and assigned a map weight of 9 (Fig. A45).

Gold deposition can occur through fluid — wall rock reactions where iron-rich minerals in the wall rocks react with gold-sulfide complexes in the fluids, resulting in desulfidation of the fluids and breakdown of gold-sulfide complexes (Phillips and Groves, 1983; Mikucki, 1998; Groves et al., 1998; Hagemann and Cassidy, 2000). We therefore created a map showing the occurrence of iron-rich rocks (defined, for example, by the presence of magnetite, hematite, banded iron-formation; Fig. A46) using the interpreted bedrock geological map from GSWA (2010a), and assigned a map weight of 9.

Rocks with a high Fe/(Mg+Fe+Ca) ratio are more prone to sulfidation reactions. We allocated each generalized lithology with a (relative) chemical reactivity value that was estimated based on the sulfidation index given by the $Fe^{2+}/(Fe_{total} + Ca^{2+} + Mg^{2+})$ ratio (Fig. 22; Groves, 1993). Units with a sulfidation index of 4 and 5 were selected to generate a predictor map 'distance to high reactivity rocks with 10 km-wide buffer (Fig. A47). Sulfidation is an important process in gold mineralization, hence we assigned the highest map weight of 9 to this reactivity map (Table A3).

We also created a map of 'chemical reactivity contrast across geological contact' (Fig. A48) by using the generalized lithology allocated with the chemical reactivity value (Fig. 22). Each contact was attributed with the difference in chemical reactivity between the lithological units on each side of the contact. The reactivity contrast map (Fig. A48) was derived by allocating to each unit cell the value of the chemical reactivity difference from the nearest contact, up to a maximum distance of 1 km.

A map of 'geological contact density weighted by reactivity contrast' was derived using the values in the chart shown in Figure 22, then mapping the geological contact densities per square kilometre weighted by reactivity contrast (Fig. A49). We assigned this map a map weight of 7 (Table A3).

Mafic dykes are conceptually prospective hosts for gold because of their (relatively) high iron content, hence reactivity (map weight = 9, Fig. A9).

Au, As, and Sb concentrations are potential indicators of the presence of gold (Phillips and Groves, 1983) and may be used as predictor maps (Figs A50, A51, A52). The gold prospectivity map is a direct indicator of gold content, and hence was assigned a map weight of 9. Antimony and arsenic sulfide mineral precipitation are often associated with gold mineralization (Cline, 2001), and Sb and As are common byproducts of gold mineralization, but are not necessarily directly indicative of gold mineralization. Hence we attributed to these maps a weight of 7. Fe content (map weight = 8) is a good proxy for areas prone to desulfidation and the breakdown of gold complexes due to fluid–wallrock reactions (Fig. A53).

Fuzzy model

Combining fuzzy membership values

Insights gained from the combined geological and geophysical studies and knowledge of the gold MSA in the context of the WMP (Table A3) were used to assign the map weights and class weights. Twenty-four fuzzy predictor maps were combined using a three-stage inference network (Table A3, Fig. 19). Fuzzy predictor maps for source, pathway, and chemical and physical traps were firstly combined using the fuzzy OR operator to create a single fuzzy predictor map for each critical component of the gold mineral system. This operator was selected because the presence of any predictor maps is sufficient to infer the presence of the respective component. The fuzzy predictor maps for physical throttle and chemical trap were then combined using the fuzzy AND operator to derive a single predictor map for traps. The fuzzy AND operator was selected because both the physical trap sites and the conducive geochemical environment are necessary for precipitation of gold from the mineralization fluids. Finally, the three fuzzy predictor maps for source, pathway, and trap were combined using the fuzzy PRODUCT operator to create the output fuzzy prospectivity map for intrusion-related gold (Fig. 20). A second inference network was then applied to assess orogenic gold prospectivity by disregarding the source component (proximity to granite) and deriving the prospectivity map based only on pathway and trap (Fig. 21). The orogenic gold model assumes that proximity to granite (source) is not a critical input for a camp-scale prospectivity analysis in the WMP. Source plays a more important role at craton scales (McCuaig et al., 2010).

Results of gold prospectivity analysis

The majority of the prospective targets delineated using the fuzzy analysis for intrusion-related gold (with granite source included) fall in the west of the WMP, within the Bentley Supergroup (Fig. 20a). Twenty-four target zones (Fig. 20b) are highlighted [α], [β], [χ], [δ], [ε], [γ], [η], [ι], [φ], [κ], [λ], [μ], [ν], [ο], [π], [θ], [ρ], [ψ], [τ], [υ], [ϖ], [ϕ], [ζ]and [ω]. Their fuzzy PRODUCT value varies between 0.27 and 0.29. The location of Handpump is not directly associated with high prospectivity, suggesting that this part of the model lacks several key components, either in the definition of the mineral system, or through lack of knowledge of the local area.

The results for orogenic gold prospectivity analysis (granite source excluded, Fig. 21) are very similar to the results from intrusion-related gold prospectivity analysis (Fig. 20). The prospective clusters from the orogenic gold prospectivity analysis have fuzzy PRODUCT values varying between 0.48 and 0.52, with many of the same zones (as those for intrusion-related prospectivity) highlighted — except that zones [χ], [θ], [γ], and [ϕ] are not observed in this orogenic gold prospectivity model as they coincide with the presence of granites.

The fuzzy analysis shows that the most prospective sites in the model are defined by the following features. All high-prospectivity regions are associated with proximity to granite (Fig. A37) and by the cumulative influence of pathway elements. These are requirements in the model to generate high prospectivity, but they do not discriminate the clusters as they are high across much of the area, including unprospective zones. More local discriminators from the trap element include the presence of iron-rich rocks (Fig. A46), reactivity contrast (Fig. A48), and geological contact density (Fig. A42). Other trap proxies are not obviously important.

For the west Musgrave Province, the trap elements are predominantly defined by geological information that is spatially biased towards areas with outcrop, i.e. areas lacking outcrop tend to have very low values for these proxies. This may partially explain the low values in the vicinity of the Handpump prospect where exposure is quite limited.

Iron oxide–copper–gold (IOCG) mineral system

IOCG deposits are a group of epigenetic Cu–Au deposits that are associated with iron oxides. Many of these have only subeconomic to trace copper and gold contents, or have controversial associations (Williams et al., 2005), but the IOCG group includes several economically important deposits. The discovery in 1975 by Western Mining Corporation of the giant Olympic Dam breccia-hosted deposit in South Australia focused attention on a hitherto poorly known type of ore system (Roberts and Hudson, 1983). Following studies by Oreskes and Einaudi (1990, 1992), the term IOCG deposit was introduced by Hitzman et al. (1992) and has become generally accepted (e.g. Porter, 2000, 2002).

IOCG deposits encompass a wide spectrum of sulfide-deficient, low-Ti magnetite and/or hematite ore bodies of hydrothermal origin. Breccias, veins, disseminations, and massive lenses with polymetallic enrichments (Cu, Au, Ag, U, REE, Bi, Co) are genetically associated with A-type to I-type magmatism, alkaline-carbonatite stocks, and crustal-scale fault zones (Fig. 23; Groves et al., 2010). IOCG host lithologies and ages are non-diagnostic but their alteration zones are, with calci-sodic regional alteration juxtaposed against potassic and iron-oxide alteration. The deposits form at shallow to mid-crustal levels in extensional, anorogenic or orogenic, continental settings such as intraplate and intra-arc rifts, continental magmatic arcs, and back-arc basins. Groves and Vielreicher (2001) suggested that most IOCG deposits (especially the largest deposits in the class, e.g. Carajás, Brazil; Olympic Dam, Australia) are located close to a craton margin or other major lithospheric boundary, where decompression melting of metasomatized mantle produces volatile-rich alkaline magmas rich in REE, P, F, and other incompatible elements such as S, Cu, and Au.

The WMP contains all the ingredients required to form polymetallic IOCG-type deposits: 1) mafic rocks and A-type and I-type granites as the main metal source; 2) crustal-scale structures that would permit fluid migration; 3) sites where basinal brines could be trapped

beneath regional seals; 4) the presence of skarn potentially indicative of hydrothermal alteration.

A spatial and temporal relationship between IOCG deposits and A-type granite intrusions, similar in composition to the 1600–1580 Ma A-type Hiltaba Suite widespread in South Australia (Pollard, 2000), suggests the potential for similar deposits in the WMP.

Predictor maps

In the following subsections, details of the fuzzy predictor maps generated for the IOCG prospectivity analysis are given along with their geological rationale (Table A4). The predictor maps were combined in a three-stage inference network (Fig. 24) to generate the final prospectivity map (Fig. 25).

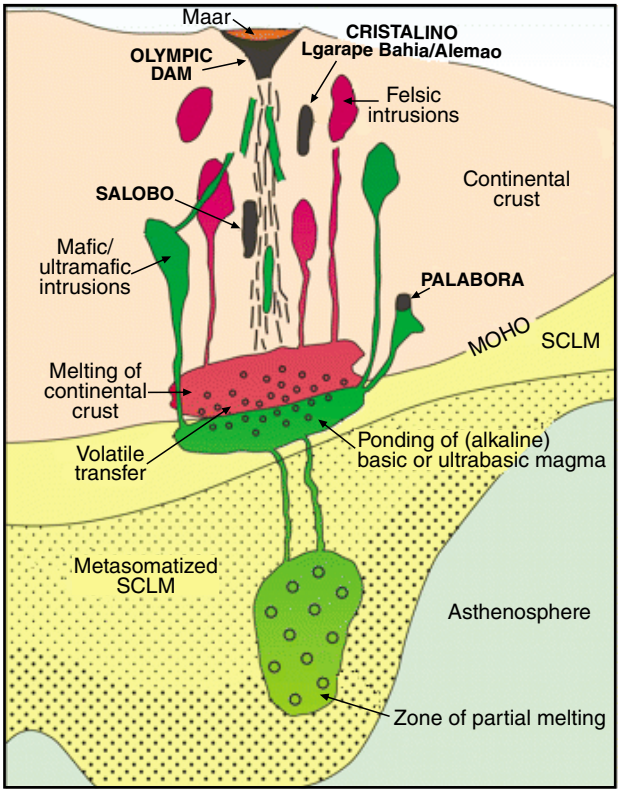

Figure 23. Schematic diagram showing model for genesis of IOCG deposits. Small degrees of partial melting of metasomatized subcontinental lithospheric mantle (SCLM) produces basic and ultrabasic melts, probably of alkaline affinity and enriched in volatiles, Cu, and Au. This melt ponds at the crust–lithosphere boundary and causes partial melting of the continental crust to produce felsic melts. Volatiles and metals transfer across the melt boundary. Felsic magmas ascend to produce felsic plutons, allowing higher density basic or ultrabasic magmas to follow and produce mafic–ultramafic intrusions in same district. Deep volatile exsolution produces giant breccia pipes with silicate rocks replaced by iron oxides, followed by Cu, Au, U, and other enriched elements (Groves et al., 2010).

Source

IOCG deposits require volatile-charged magmas generated from metasomatized mantle lithosphere. Hydrothermal activity associated with such magmas produces deposits with an element association compatible with their source, including variable combinations of Au, Co, Cu, F, Fe, LREE, Ni, P, Pd, P, Th, and U (e.g. Mathur et al., 2002). Mafic intrusions are the most likely donors of Cu (Johnson and Cross, 1995), hence we generated a 'distance to mafics' predictor map using a 1000 m wide zone around these units, the distribution of which was extracted from the interpreted bedrock geological map (GSWA, 2010a), and assigned a map weight of 9 (Fig. A54).

A-type and I-type granites are considered critical for IOCG deposit formation (map weight = 9, Table A4), although in some cases the deposits can be spatially distinct from these intrusive rocks (e.g. Olympic Dam deposit). Consequently, a lack of surface expression of magmatism does not necessarily translate into unfavourable conditions for IOCG mineralization. In the WMP, the Pitjantjatjara and Warakurna granites are A-type granites, whereas Wankanki granites are I-type (Smithies et al., 2010). We created two predictor maps showing 'distance to A-type granite' (Fig. A55) and 'distance to I-type granite' (Fig. A56), each with a 500 m wide zone around intrusions, and assigned map weights of 9 to both.

Pathways

Extensional and transtensional faults can channel hot, deep-seated fluids upward and cold, surface waters downward, facilitating fluid mixing, large-scale alteration, and mineralization. The depth at which fluid and metal recharge and discharge take place will influence the resulting alteration and mineralization patterns. In a general sense, all faults can be prospective within this scenario, but structures active during the Giles Event (early, mid, late and post) and crustal-scale faults are considered the most prospective. In the first case, this is because the Giles Event was a highly magmatic intraplate rifting event that tapped mantle magmas and resulted in voluminous mafic and granitic intrusions, while in the second case crustal-scale fault networks are required as fluid conduits in an IOCG system. We created several predictor maps: 'distance to crustal-scale faults' (Fig. A4, map weight = 9), 'distance to early, mid, late and post-Giles structures' (Fig. A57, map weight = 9), 'distance to Petermann and Alice Springs Orogeny faults' (Fig. A7, map weight = 8.5), and 'distance to Mount West and Musgrave Orogeny structures' (Fig. A8, map weight = 8).

The presence of hydrothermal breccias is also an indicator of favourable pathways, and potentially of traps, but there are too few occurrences in the WMP to allow a useful predictor map to be created.

Physical traps

IOCG deposits commonly form within intense zones of deformation in the vicinity of crustal-scale lineaments (Groves and Vielreicher, 2001). We therefore use the six predictor maps from the orogenic gold systems: 'competency contrast across geological contact' (Fig. A41),

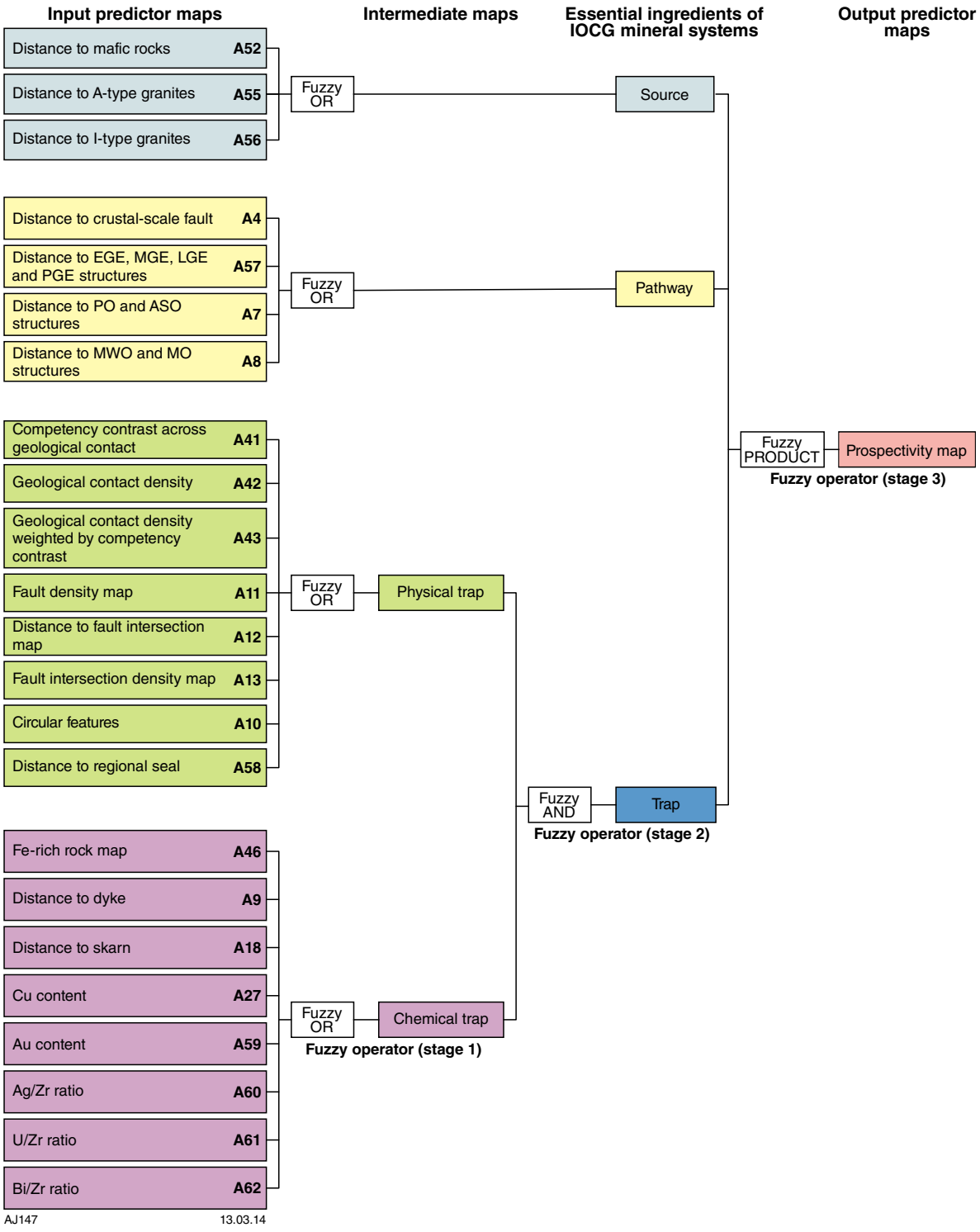

Figure 24. Multi-stage fuzzy inference network used for combining fuzzy IOCG predictor maps

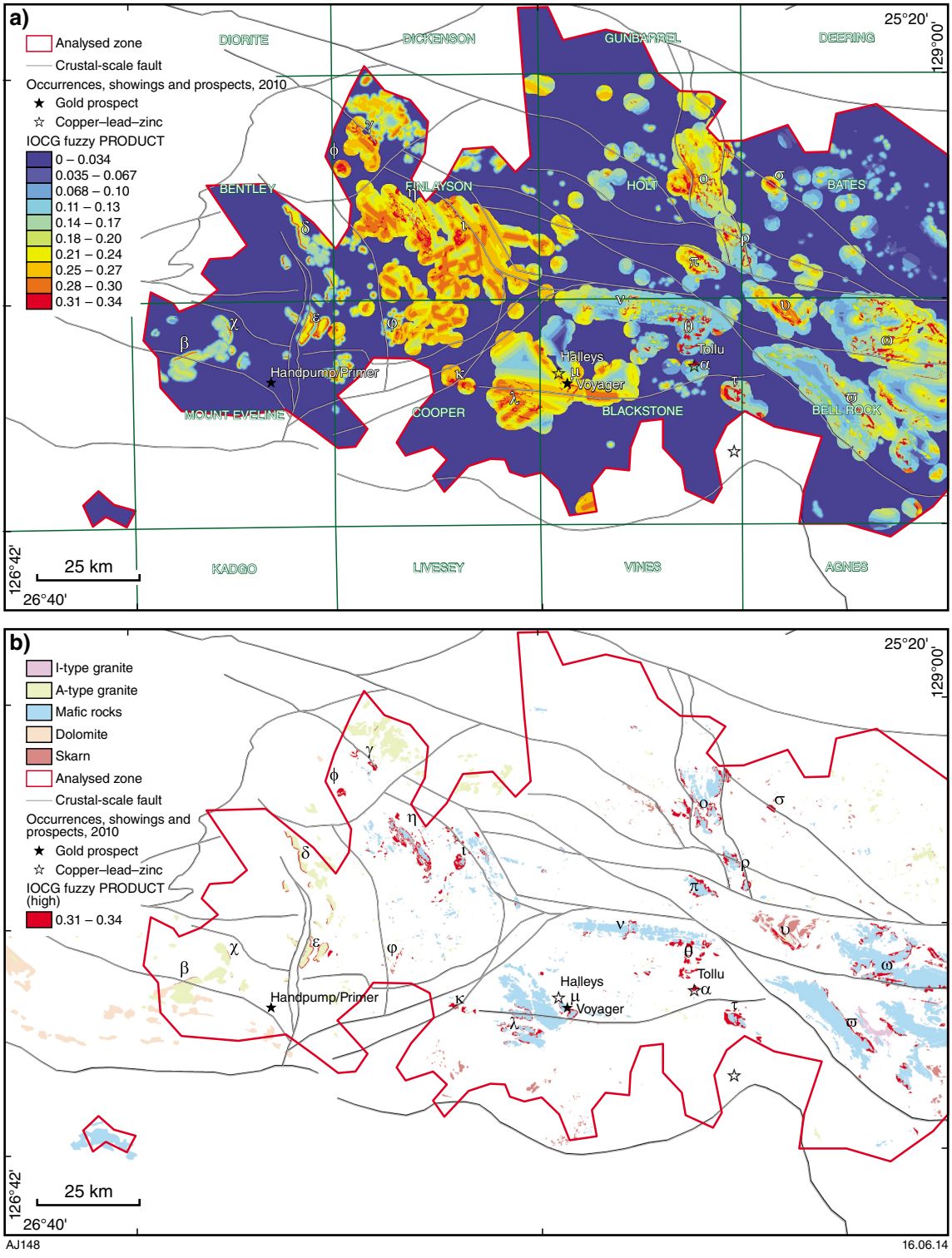

Figure 25. a) Fuzzy prospectivity model for the IOCG mineral system; b) zone of high fuzzy value for the IOCG prospectivity analysis over the analysed area with even data coverage

'geological contact density' (Fig. A42), 'geological contract density weighted by competency contrast' (Fig. A43), 'fault density' (Fig. A11), 'distance to fault intersection' (Fig. A12), and 'fault intersection density' (Fig. A13), applying the same map weights for the same reasons.

IOCG deposits are commonly, but not exclusively, contained within large, pipe-like breccia bodies that contain S-poor assemblages enriched in incompatible elements. These breccia bodies are a physical trap and hydrothermal alteration associated with IOCG-style mineralization will typically comprise concentric zones surrounding a roughly circular body. The breccia and proximal alteration zone are usually associated with positive magnetic anomalies, whereas the outer alteration zones are much less magnetic. The 'presence of circular feature' predictor map (Fig. A10), generated using the CET Porphyry Analysis system (Holden et al., 2010), was used for inferring the possible presence of pipe-like breccia bodies (map weight = 9 and confidence factor = 6).

Regional seals, such as impermeable lithologies, inhibit the ascent of volatile-charged magmas or fluids and are indispensable for forming IOCG deposits. Potential regional seals in the WMP are: 1) the extensive basaltic units of the Kurnamarnara Group which preceded the Giles 'G1' intrusions; 2) the extensive bimodal volcanics in the Bentley Supergroup, which is synchronous with the Alcurra Suite; 3) the strongly banded gneisses of the Wirku Metamorphics rocks. We extracted these units from the GSWA interpreted bedrock geological map (GSWA, 2010a) to generate the predictor map 'distance to regional seal' and assigned a map weight of 9 (Fig. A58).

Chemical scrubbers

The host rocks for IOCG deposits include coeval or pre-existing sedimentary, mafic to felsic volcanic or plutonic rocks, schists, and gneisses and are not a diagnostic feature. However, host rocks overprinted by extensive hydrothermal alteration characterized by iron oxides, sericite, and silica are significant. Consequently, we used the predictor map 'iron-rich rocks' (including presence of magnetite and hematite), with a map weight of 8 (Fig. A46).

Metal associations in IOCG deposits are influenced by circulation of magmatic hydrothermal fluids with resultant fluid – host rock exchange reactions (Groves et al., 2010). In this context, a dyke is conceptually a prospective host for IOCG mineralization because of its high chemical reactivity and its interaction with the country rocks. This is represented by the predictor map 'distance to dyke' (Fig. A9, map weight = 8).

The morphology of IOCG mineralization varies significantly from breccia zones to stratiform-like deposits but skarns are a high-likelihood trap. Skarns are described from the base of the Wirku Metamorphics, and these were extracted from the interpreted bedrock geology map (GSWA, 2010a) to build the predictor map 'distance to skarn' using a 1 km wide buffer zone and assigned a map weight of 8 (Fig. A59).

Copper and gold contents are the most direct geochemical evidence of IOCG chemical (or physical) traps. The Cu and Au contents were used to create the Cu and Au predictor maps, both with a map weight of 9 (Figs A27, A50).

IOCG polymetallic enrichments contain other very mobile, but less significant, elements such as Ag, U, and Bi. We normalized these data against Zr content (which is inferred to be immobile) to evaluate mass transfer processes (following Stanley and Madeisky, 1994). High Ag/Zr, U/Zr, and Bi/Zr ratios are likely to be indicative of IOCG-type chemical (or physical) traps and we used these to create the predictor maps in Figures A60, A61, A62, assigning a map weight of 8 to each.

Fuzzy model

Combining fuzzy membership values

We used a three-stage inference network to combine the 23 predictor maps (Fig. 24, Table A4). After combining the fuzzy OR chemical scrubber predictor map to the fuzzy OR physical throttle predictor map, the respective predictor maps of the three key components of the IOCG mineral system, namely source, pathways and traps, were combined using the fuzzy OR because the presence of any one of the predictor maps is sufficient to infer the presence of the respective component. In the second stage, these three maps were combined using the fuzzy PRODUCT operator to derive the fuzzy prospectivity map for IOCG deposits in the WMP (Fig. 25).

Results of IOCG prospectivity analysis

The final prospectivity map identifies 23 target zones (Fig. 25b) marked as [α], [β], [χ], [δ], [ε], [ϕ], [γ], [η], [ι], [φ], [κ], [λ], [μ], [ν], [ο], [π], [θ], [ρ], [σ], [τ], [υ], [ϖ] and [ω]. Their fuzzy PRODUCT value varies between 0.31 and 0.34. The cluster [μ] coincides with the Voyager copper–gold deposit and corresponds to high fuzzy PRODUCT value between 0.28 and 0.34. The Tollu prospect has a locally high fuzzy PRODUCT at the cluster [α]. IOCG targets (Fig. 25b) display a clear relationship with the predictor maps for IOCG sources, and more especially with mafic rocks and A-type granites. However, no clear association exists between high prospectivity targets and I-type granites.

The correlation between IOCG pathways and the prospective areas is consistent. For example, there is clear association between clusters and the early, mid and late Giles structures, and areas lacking inferred structures of this age show low prospectivity model values. Crustal-scale faults show a correlation with several sites, but others are not so intimately related, suggesting that this factor is not essential to the model at this scale. Cluster [υ] is linked to Mount West and Musgrave Orogeny structures, whereas sites [γ] and [ϖ] are linked to Petermann and Alice Springs Orogeny faults.

High-potential clusters are commonly associated with physical throttles such as a high fault occurrence density zone, a regional seal, geology contact density weighted by a high competency contrast (e.g. [ε] and [μ]), or high competency contrast across geology contact (e.g. [υ] and [ϖ]). However, there is an inconsistent relationship between

fault intersection, high fault intersection density, and the location of the prospective targets, suggesting that these are not important components of the model.

Prospective chemical traps and potential deposits display few connections. For example, sites [ο], [ϖ], and [ι] are found in iron-rich sediments, sites [η] and [τ] are located close to dykes, and sites [φ] and [υ] occur in skarns. Most of the sites are located within high copper content areas; however, this is not inevitably the case with high gold content (e.g. [θ] and [μ]), and no clear association exists between the ratios: Ag/Zr, U/Zr and Bi/Zr, and potential clusters.

Tin–tungsten (Sn–W) mineral system

Tin deposits that contain subordinate tungsten have been reviewed by Heinrich (1990), and deposits in which tungsten is the dominant metal with tin as next most abundant metal have been reviewed by Wood and Samson (2000). Most tin–tungsten (± molybdenum) deposits are spatially associated with granitic magmatism (e.g. Ferguson and Bateman, 1912; Taylor, 1979; Eugster, 1985). Mineralization is typically situated towards the apical regions of granitic cupolas within pegmatites, quartz veins, stockwork, or as disseminations (Lehmann, 1990).

Most of Australia's historical tin and tungsten production has been from pipes and skarns associated with tungsten–molybdenum-bearing, post-orogenic, subduction-related granites (Solomon and Groves, 1994). The nature and timing of Sn–W mineralization suggests a complex magmatic–hydrothermal continuum during the mineralizing process (Landis and Rye, 1974; Pollard and Taylor, 1986; Heinrich, 1990; Roberts et al., 1998). In general, these deposits have multiple stages of mineralization (Solomon and Groves, 1994).

There are currently no known Sn–W deposits in the WMP, but the province contains all the ingredients required to form them: 1) felsic, highly fractionated, reduced S-type or I-type tin granite as a source (Karimzadeh-Somarin and Ashley, 2004); 2) deep-penetrating structures that permit fluid migration; 3) rocks with very high chemical reactivity, such as skarns and dolomites.

Predictor maps

A two-stage inference network (Fig. 26) was used to estimate Sn–W (± Mo) prospectivity. The geological basis for the source, pathway, and trap components of MSA is described below (Table A5).

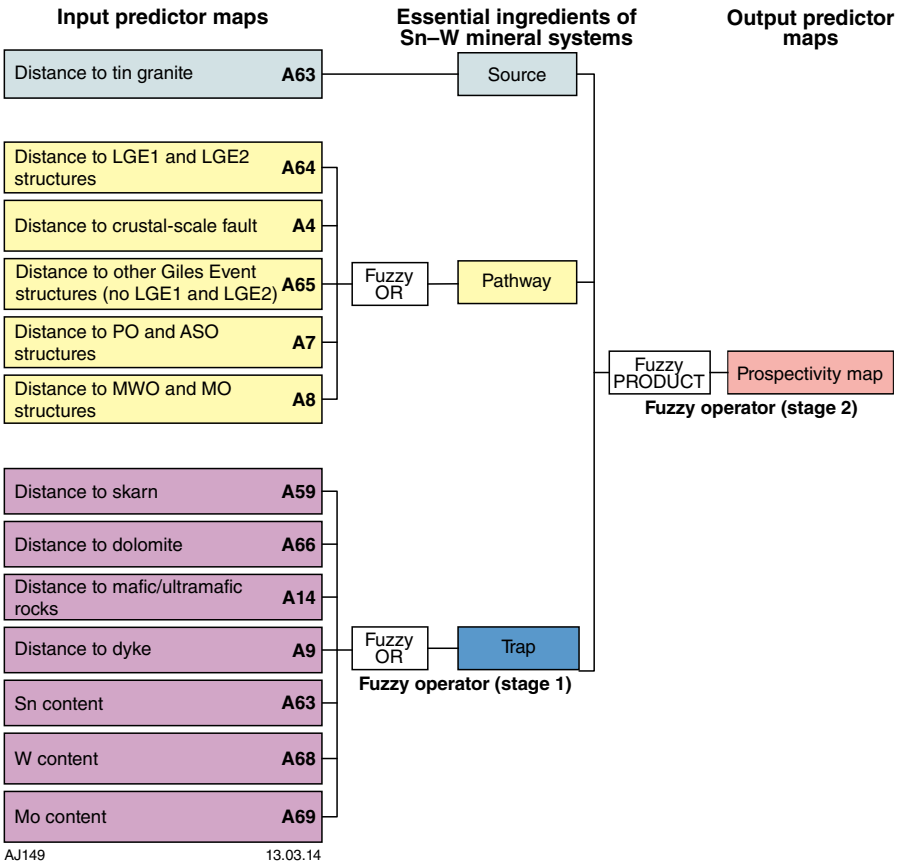

Figure 26. Multi-stage fuzzy inference network used for combining fuzzy Sn–W predictor maps

Source

We created a 'distance to tin granite' map by extracting all A-type and I-type granites (i.e. Pitjantjatjara, Warakurna, and Wankanki granitic rocks; Smithies et al., 2010), with a buffering distance of 10 km, and assigned a map weight of 9 to reflect the fundamental role of tin granites in deposit formation (Fig. A63).

Pathways

Major fluid pathways that are likely to focus fluid enriched in Sn and W will be those that undergo repeated hydraulic opening (Lehmann, 1990). The most prospective structures in the WMP are coeval with the late Giles Event because the stress regime changed from northwest–southeast extension to northeast–southwest extension, potentially inducing flow of mineralizing fluids. The predictor map 'distance to late Giles Event 1 and late Giles Event 2 structures' is therefore an important indicator of prospectivity (Fig. A64, map weight = 9, Table A5). Crustal-scale features (Fig. A4) are also potentially important fluid conduits (McCuaig et al., 2010; Joly et al., 2012) and this map was also assigned a map weight of 9.

We also used 'distance to other Giles Event structures' (Fig. A65) and 'distance to Petermann and Alice Springs Orogeny structures' (Fig. A7) with a 5 km buffer, because they are permeable structures that are likely to have been reactivated through time. We considered these structures somewhat less prospective, hence they were assigned a map weight of 8.5. We assigned the 'distance to Mount West Orogeny and Musgrave Orogeny structures' a map weight of 8 (Fig. A8), because these structures are less likely to have been active during the Giles Event. Hydrothermal breccias would also have provided a useful predictor map because they are an important pathway ingredient, but there are too few known occurrences to produce this map.

Physical traps

Most tin and tungsten deposits occur in the apical regions of granitic cupolas, because this is where exsolved magmatic fluids have evolved, been focused, and/or ponded (Lehmann, 1990). The most prospective tin granites should be either shallowly buried or, if exposed, have preserved roof zones. The lack of petrophysical contrast between granite suites prevents mapping of their distribution and geometries, and hence their use in the prospectivity analysis. No physical trap is considered in the analysis.

Chemical scrubbers

Tin–tungsten mineralization is related to post-magmatic alteration at contacts between intrusive felsic bodies and the country bedrock. Skarns are significant potential host rocks for Sn–W mineralization (e.g. Red Dome, Queensland, Australia, Thompson et al., 1999; Mount Bischoff, Tasmania, Solomon and Groves, 1994). We therefore created 'distance to skarn' (Fig. A59) as a predictor map.

Albitization, greisenization and tourmalinization are other frequently encountered manifestations of alteration associated with Sn, W, and Mo mineralization (Thompson et al., 1999). Hence these are proxies for chemical scrubbers. These alteration processes are not sufficiently well known in the west Musgrave Province to create predictor maps. However, dolomites and mafic and ultramafic igneous rocks are particularly amenable to these alteration processes (e.g. Lucky Draw in New South Wales, Australia). Hence, we created 'distance to dolomite' (Fig. A66) and 'distance to mafic and ultramafic rocks' predictor maps (Fig. A14) with a 1000 m wide buffer zone around occurrences of these litho-types using the GSWA interpreted bedrock geological map (GSWA, 2010a). Skarns and dolomites are more likely to host Sn–W mineralization, hence were assigned map weights of 9, whereas a map weight of 8 was assigned to mafic and ultramafic rocks.

Sn–W deposits can have a close relationship with sills and dykes due to the chemical reactivity of these intrusive rocks (e.g. Red Dome, Kidston in Queensland). We therefore also used 'distance to dyke' as an indication of possible chemical trapping with a 1000 m-wide buffer around dykes (Fig. A9), and assigned a map weight of 8 to reflect their lower importance than skarns and dolomites.

Sn, W, and Mo contents can be proxies for granite-related Sn–W deposits (Figs A67, A68, A69) and were considered together because they are found together in tin granite. We assigned a map weight of 9 to both Sn and W maps, whereas we used a map weight of 8 for the Mo map because this is not a direct proxy for Sn–W mineralization.

Fuzzy model

Combining fuzzy membership values

A two-stage inference network was used to combine the 13 predictor maps (Table A5, Fig. 26). We first combined respective predictor maps for the source, pathway, and trap components of the Sn–W mineral system, using the fuzzy OR operator because the presence of any one of the predictor maps is sufficient to infer the presence of the respective component. We then combined these three maps using the fuzzy PRODUCT operator to derive the fuzzy prospectivity map for Sn–W deposits in the WMP (Fig. 27).

Results of Sn–W prospectivity analysis

The final prospectivity map (Fig. 27b) identifies 23 high-prospectivity zones (marked by [α], [β], [χ], [δ], [ε], [ϕ], [γ], [η], [ι], [φ], [κ], [λ], [μ], [ν], [ο], [π], [θ], [ρ], [σ], [τ], [υ], [ϖ] and [ω]). The fuzzy PRODUCT of these high prospectivity zones varies from 0.30 – 0.33.

All sites are located within 10 km of a tin-type granite 'source' and all are associated with potential fluid pathways, suggesting these are the most important components of the model. For instance, sites [α] and [β] are located on crustal-scale faults, the most important fluid pathways. Cluster [ι] is associated with Mount West and Musgrave Orogeny structures, [ν] with late Giles 1 and 2 structures, [υ] and [ϖ] with early, mid and late Giles (other

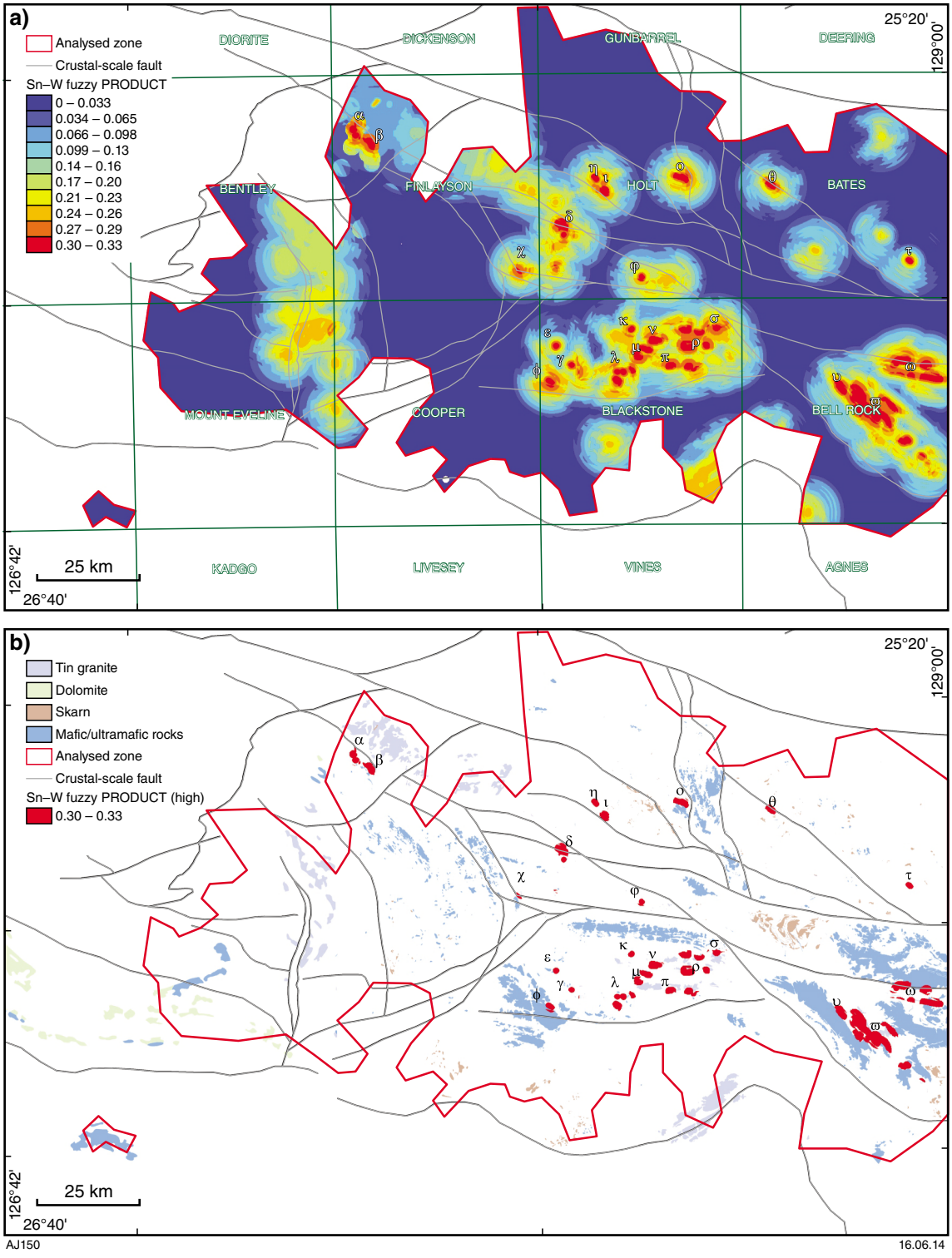

Figure 27. a) Fuzzy prospectivity model for the Sn–W mineral system; b) zone of high fuzzy value for the Sn–W prospectivity analysis over the analysed area with even data coverage

than late Giles 1 and 2) faults, and [χ] with Petermann and Alice Springs faults. The inferred age of the structure is not a critical factor in our model.

The relationship between potential targets and the different chemical scrubbers is not clear, and the location of the skarns and dolomites does not, in general, coincide with high-prospectivity clusters. The map weights associated with the predictor maps dolomites and skarns are 9 (i.e. very high, Table A5) and should have led to a closer relationship with the position of the clusters. The very limited extent of the dolomite and skarns in outcrop is the fundamental cause giving little opportunity for these traps to interact with source and pathway regions in the model, and little relevance to the overall result. On the other hand, the more extensive mafic and ultramafic rocks layer contains all mapped clusters.

Surficial uranium mineral system

Uranium deposits have been classified historically into 14 categories on the basis of host rocks, structural setting, and mineralogy of the deposit (Dahlkamp, 1978, 2009; Mashkovtsev et al., 1995; International Atomic Energy Agency, 2000; McKay and Miezitis, 2001; Organisation for Economic Co-operation and Development Nuclear Energy Agency and International Atomic Energy Agency, 2006). However, this scheme is not optimal for prospectivity analyses. Kreuzer et al. (2010) instead grouped different uranium deposit types into six system models: surficial, sedimentary, igneous-related, metamorphic/metasomatic, unconformity-related, and vein-related uranium systems. The grouping is based on similarities in genetic processes, environments of ore formation, and also similar mineral system proxies that are mappable at the regional to continent scale.

Western Australia has total known resources of 188 000 t of contained U_3O_8, of which surficial uranium is the dominant deposit type. These deposits typically occur in young (Cenozoic), unconsolidated sediments and soils, although they also occur in peat bogs and karst caverns (Fig. 28; McKay and Miezitis, 2001). Uranium mineralization typically occurs as carnotite ($K_2(UO_2)_2(VO_4)_2{\cdot}3H_2O$), commonly cemented by secondary minerals including calcite, gypsum, dolomite, ferric oxide, and halite. There are three types of surficial uranium deposits: fluviatile, lacustrine (or playa), and pedogenic. All of these usually form in regions where uranium-rich granites are weathered and leached in a semi-arid to arid climate by both surficial and underground water (Fig. 28; Carlisle, 1983). Western Australian examples occur in valley-fill sediments along Cenozoic drainage channels (e.g. Yeelirrie) and in playa lake sediments (e.g. Lake Maitland). Associated vanadium is derived from mafic–ultramafic rocks.

There are no known surficial-hosted uranium deposits in the WMP, nor is there presently exploration for this style of mineralization. Nevertheless, the WMP contains all the ingredients required to form surficial uranium deposits, including an extensive paleodrainage system, calcrete accumulations within and adjacent to drainage lines, appropriate sources of uranium (felsic volcanics) and vanadium (mafic volcanics), and arid climatic conditions (Kreuzer et al., 2010).

Predictor maps

A four-stage inference network (Fig. 29) was used to estimate prospectivity. The geological basis for the source, pathway, and trap components of the mineral systems approach is given in the following paragraphs and in Table A6.

Source

A nearby basement source enriched in uranium may or may not be necessary to form surficial-hosted deposits. Uranium is highly soluble under oxidizing conditions and insoluble under reducing conditions, meaning that it is highly mobile in the near-surface environment and may be concentrated extremely efficiently even though the source may be low in U. Despite this, the presence of uranium-rich granites is considered to be an advantageous component of the mineral system and we therefore used ‘distance to granitic rock of any age’ as a spatial proxy for source (Fig. A70, map weight = 8).

Pathways

Oxidized groundwater is the primary medium for uranium transportation in solution. Groundwater is drawn to the surface by evaporation in fluviatile (paleochannel valleys) and playa systems. Paleochannels are the main pathways for groundwater flow.

The WMP has experienced no major known tectonic events during the Cenozoic. The present-day drainage system is likely to follow the ancient one and may be used as a proxy for the presence of paleochannels. We therefore mapped the ‘distance to third-order and higher present-day drainage systems’ (i.e. ‘distance to paleochannel’, Fig. A71) using SRTM topographic data and a drainage-tracing algorithm. Possible minor shifts in the drainage network were accommodated by establishing a 500 m-wide buffer around the drainage system and assigning the predictor map a weight of 9.

Physical traps

Valley calcrete and playa sediments provide a favourable environment for carnotite deposition. The predictor map of ‘distance to valley calcrete’ (Fig. A72) was derived from the surface geological data for calcrete provided by the GSWA (2010a) with a 100 m buffer. The ‘distance to playa sediment’ map (Fig. A73) was derived from surface geological data in GSWA (2010a), with a 100 m buffer. The permeability of coarse-grained calcrete is more important than the permeability in playa sediment. Highly permeable rock provides the most favourable host rocks for large, relatively high-grade surficial uranium deposits. A map weight of 8 was given to the map of valley calcrete, and a map weight of 7 was attributed to the playa sediment map.

Chemical scrubbers

Uranium precipitation is a reduction–oxidation process that involves U fixation by vanadium. We therefore created a ‘vanadium content’ predictor map (Fig. A74). Vanadium

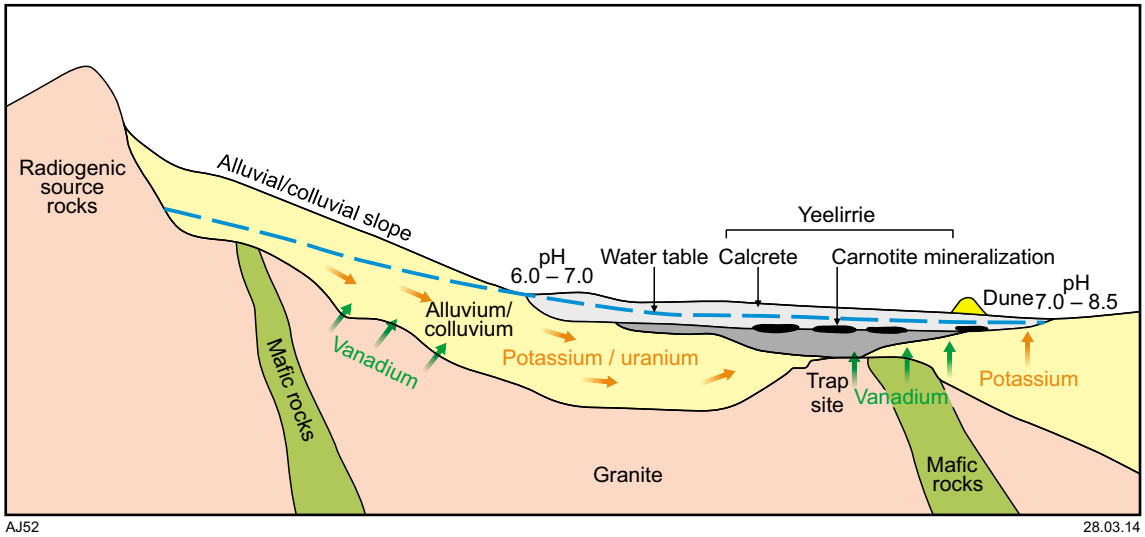

Figure 28. Model depicting the setting and processes involved in the formation of carnotite deposits in calcretized channels (after Carlisle, 1983 and Hou et al., 2007).

can equally well be provided by mafic and ultramafic rocks, dykes, and felsic volcanic units; hence, those units can also be used to produce chemical scrubber maps (Figs A14, A9, A75, respectively).

Radiometric data are the best available predictor for uranium content, provided that occurrences are very close to the surface. We generated the radiometric-U content map for surface deposits using all such data above the threshold ζ (with $\zeta = x(\log [U]) + 2\sigma(\log [U])$; Singer and Kouda, 1999; Fig. A76). We also used uranium content, extracted from the GSWA geochemistry database (GSWA, 2010b) and GA Ozchem (Geoscience Australia, 2007) to generate a predictor map for this parameter (Fig. A77).

We assigned all the chemical trap predictor maps a map weight of 8, except for the volcanic units to which we assigned a map weight of 7.5 because these may contain felsic rocks that are less chemically reactive.

Fuzzy model

Combining fuzzy membership values

A four-stage inference network was designed to combine the 10 fuzzy predictor maps (Table A6, Fig. 29). U-content maps from the geochemistry data and radiometric data are combined using the fuzzy AND operator, since both represent the same attribute. All elements from the chemical trap were then combined using the fuzzy OR operator, because the presence of any one of the elements is sufficient. The 'distance to calcrete' and 'distance to playa sediment' predictor maps were combined into a physical trap map using the fuzzy OR operator. Derivative physical and chemical trap maps were then combined using the fuzzy AND operator because both types of trap sites are necessary for precipitation of uranium from oxidized waters. The 'distance to granites' map was used directly as the predictor map for source, as was the paleochannels map for pathways. Finally, the three fuzzy predictor maps for source, pathway, and traps were combined using the fuzzy GAMMA operator to derive the output fuzzy prospectivity map (Fig. 30).

The fuzzy GAMMA operator combines the fuzzy algebraic PRODUCT and the fuzzy algebraic SUM (Zimmermann and Zysno, 1980). The GAMMA operator is a useful tool for calculating a range of values going from a minimum, corresponding to the algebraic PRODUCT (= 0), to a maximum, corresponding to the algebraic SUM (= 1). It is used here instead of the PRODUCT operator because it moderates the tendency of the algebraic SUM operator to increase and the tendency of the algebraic PRODUCT operator to decrease, thereby enhancing subtle differences in the prospectivity of different areas.

Results of surficial uranium prospectivity analysis

Figure 30 illustrates potentially prospective targets for exploration. All targets [α], [β], [χ], [δ], [ε], [ϕ] and [γ] (Fig. 30b) are close to granites, paleochannels, and calcrete. The fuzzy GAMMA values vary between 0.74 and 0.82 (range = 0.1, Fig. 30b), and fuzzy PRODUCT values vary between 0.22 and 0.23 (range = 0.01, Fig. 30c). The fuzzy GAMMA operator enhances significantly the prospectivity differences. Only areas [β] and [δ] are associated with playa sediments (Fig. A73).The target [ϕ] is located on a dyke but this is the only example of its kind. [χ], [δ] and [ε] are situated in mafic and ultramafic chemical traps. Only the high-prospectivity target [α] is located on felsic volcanic rocks. Similarly, [α] is the only area associated with low V content and high radiometric-U channel content. The prospective areas [α] and [β] are related to high uranium content samples from the geochemical datasets.

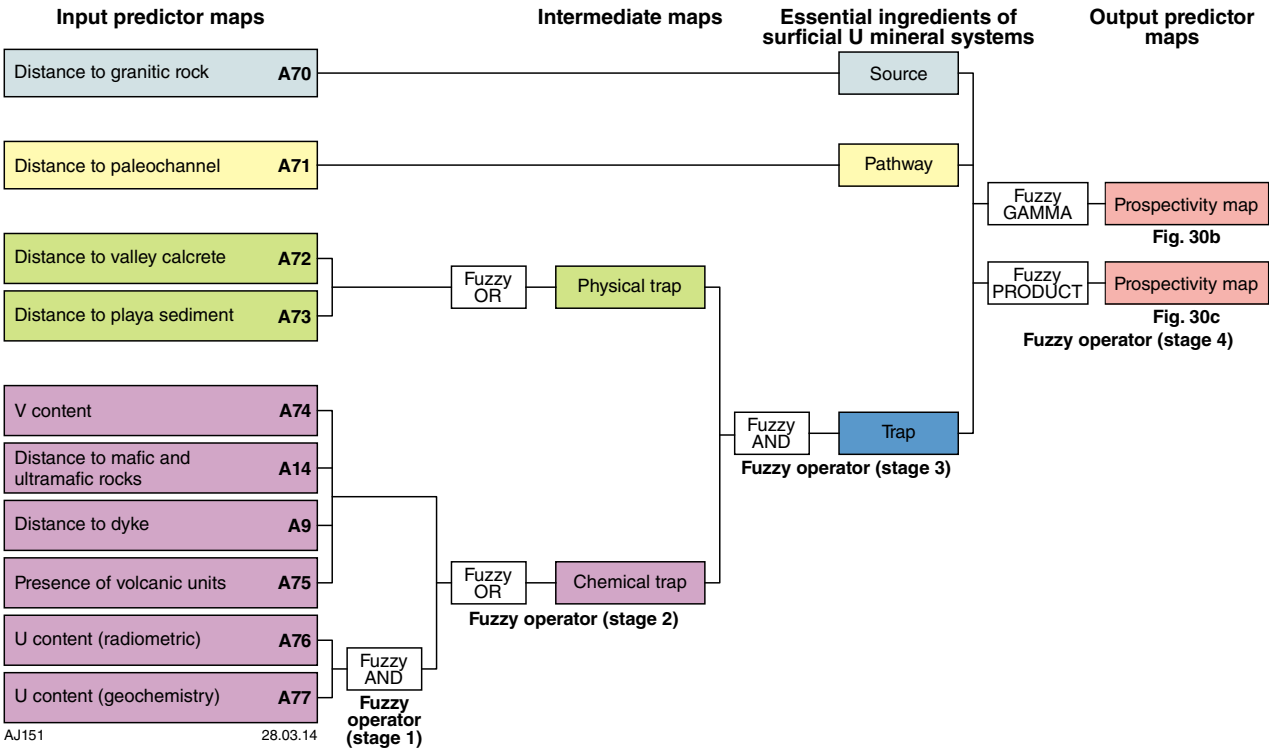

Figure 29. Multi-stage fuzzy inference network used for combining fuzzy surficial uranium predictor maps

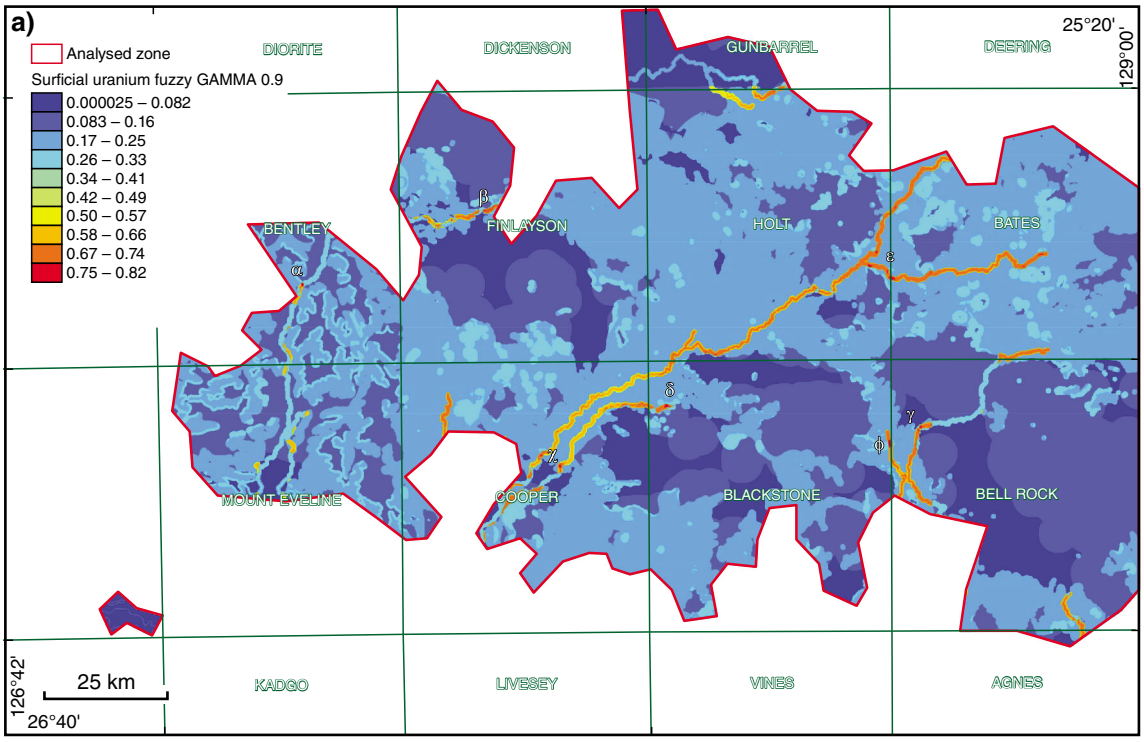

Figure 30. a) Fuzzy prospectivity model for the surficial uranium mineral system

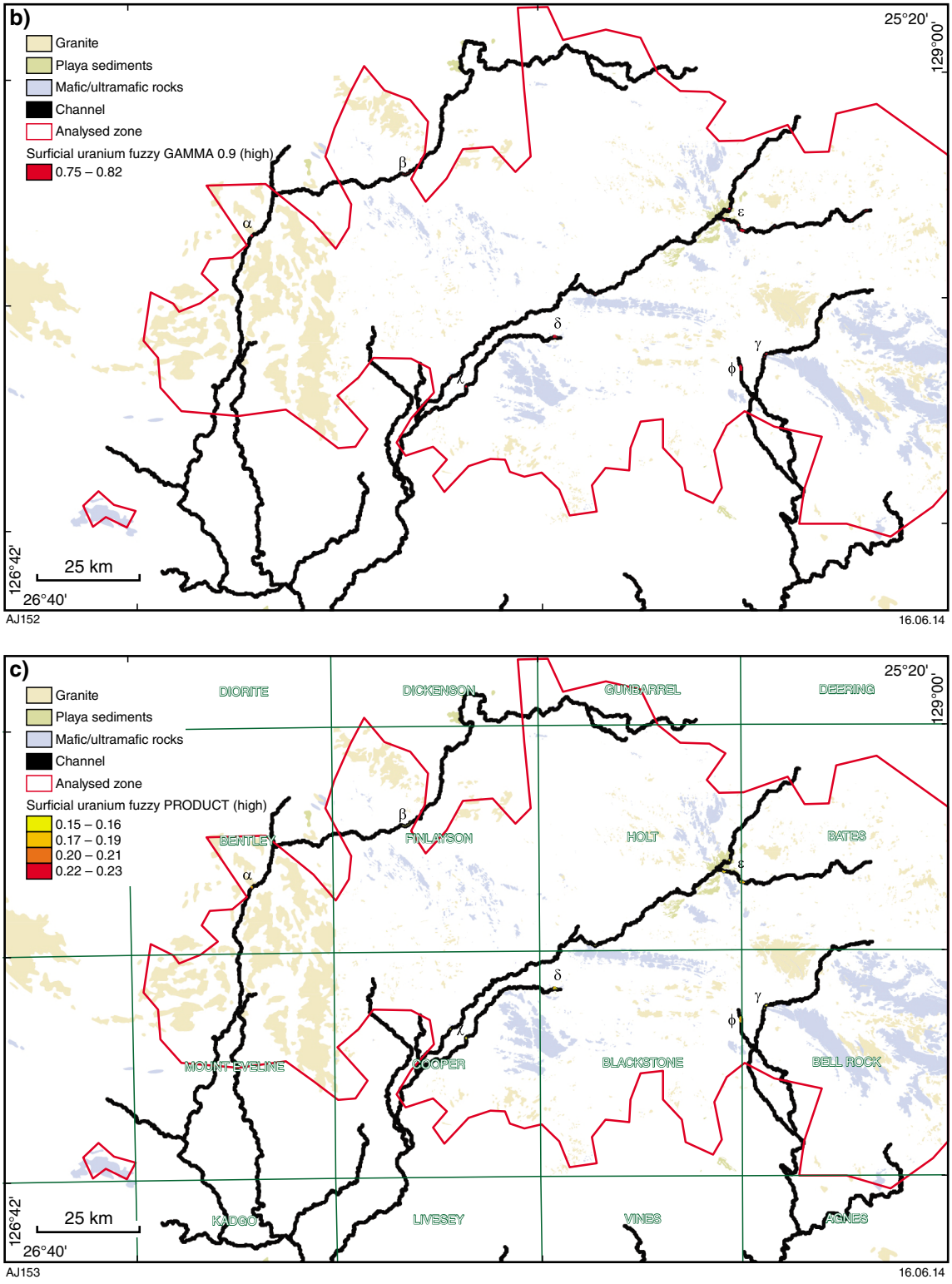

Figure 30. (continued) b) zone of high fuzzy GAMMA values for the surficial uranium prospectivity analysis over the analysed area with even data coverage; c) zone of high fuzzy PRODUCT values for the surficial uranium prospectivity analysis over the analysed area with even data coverage

Discussion and conclusions

The new interpreted geology of the west Musgrave Province is derived from detailed mapping, sampling, and geophysical surveys by GSWA. Knowledge of the 3D architecture of the WMP (particularly which of the known major structures penetrate the deep crust; Aitken et al., 2013), and the relative timings of the many structures with respect to the various tectonic events that have affected the WMP, suggest that the major structures probably originated early in the tectonic evolution of the province, were active during the c. 1085–1040 Ma Giles Event, and were subsequently reactivated during the Petermann Orogeny and Alice Springs Orogeny. The geological history of the WMP is complex, comprising repeated magmatic, metamorphic and tectonic events. This has hindered our geological understanding of the area but created repeated opportunities for mineralizing events.

The purpose of this study was to apply a mineral prospectivity analysis to a little-explored greenfields area with few or no known deposits. We selected the WMP as a candidate terrane for this analysis. The study aimed to generate representative models of the prospectivity of the WMP, but was also an investigation into the method and its limitations. Based on the review of the geology of the WMP and on our mineral system expertise, the WMP is likely to be prospective for orthomagmatic nickel–copper and platinum group element (PGE) deposits (as demonstrated by the presence of the Nebo–Babel Ni–Copper–PGE deposit), and also for orogenic and intrusion-related gold, iron oxide–copper–gold (IOCG), granite-hosted tin–tungsten and surficial uranium. We undertook a GIS-based fuzzy prospectivity analysis at terrane scale for the selected mineral systems. The fuzzy method is well adapted for greenfields areas, where other approaches often fail.

We used a mineral systems approach that considered sources of metals, magma/hydrothermal fluid pathways for transport of those metals, and physical and/or chemical traps that would concentrate the metals. In each case, geological proxies for metal source, metal transport pathways, and metal depositional sites were sought based on the known characteristics of such deposits and their mechanisms of formation, and the interpreted geology of the WMP.

A series of prospectivity maps were generated showing the spatial distribution of prospectivity in the mineral system models, for cells with an area of 1 km^2. In using the results of this analysis it is important to understand the limitations of the study. In many cases, the prospectivity model is driven primarily by one or two of the individual predictor maps. Furthermore, the predictor maps are not free from error. Those that depend on geological data have spatial biases as a result of data sampling, biases towards erosionally resistant units, interpretational uncertainty, and other such factors. The geophysical data are more consistently sampled; however, their interpretation also carries uncertainty, and there is scope for error, especially in the assignment of structures to specific events. Finally, the mineral system models themselves are driven by interpretations of the ore genesis process, and are also very generalized.

These factors mean we cannot consider this model to be a complete representation of the mineral system, and the end products are not necessarily expected to show the locations of the deposits themselves. Rather, they illustrate the spatial variation in geological favourability for each type of deposit, within the constraints of the model. They are intended to be tools to reduce risk in exploration and to assist decision making. Most predictor maps used in the modelling are assigned high weights because those are deemed the most relevant proxies for exploration. Using a large number of irrelevant maps with very low map weights would have increased the model complexity without any significant change in the model outputs. Map weights and class weights of all predictor maps were assigned subjectively by an expert. In the absence of mineral deposits with which to 'train' the combinatorial framework, this is a necessarily subjective exercise. Nonetheless, the selected proxies and their weights represent the present state of knowledge, and its applicability in the general sense to a region with limited data. Readers are encouraged to critically assess the individual predictor maps, their role in the fuzzy logic analysis, and the reasonableness of the final results. The models can be modified or updated accordingly using simple GIS procedure available in ArcGIS.

Four main drawbacks were highlighted in the description of the fuzzy method:

1. *Loss of information when converting raw data values to fuzzy membership values*. Discretization of continuous data invariably results in loss of information; however, this is necessary for mathematical modelling. In the present study, distance ranges were mapped to a single class weight (and, therefore, a single fuzzy membership value). For example, distance ranges from 0–1 km were mapped to a class weight of 10, in which case, the output prospectivity map would show the same prospectivity for distances between 0 and 1 km. In reality, there is change in prospectivity within that range.

2. *Every model-based prospectivity analysis draws input model variables from the conceptual genetic model of the targeted mineralization*. The mineral system model is based on the present ideas on the genesis of the targeted deposit type; therefore, any changes in the conceptual model would entail a change in model variables, and hence in the output prospectivity map. It is not possible to quantify, or qualify, the effect this would have on the output prospectivity map.

3. *Assignment of weights reflects the present state of knowledge*. Any change would necessitate an update of weights, and consequently an update of models. The prospectivity models can be easily updated using standard GIS procedures as new data/knowledge becomes available. Weights could not be empirically tested without more training points (in the forms of known deposits) in the region.

4. *There may be some proxy dependence*. As an example, the couples Pt–Pd or Yb–Nb have similar chemical behaviours in the magmatic mineralizing systems

considered. However, the fuzzy model we used is non-linear and, unlike linear probabilistic models (e.g. weights-of-evidence), it is not strongly affected by dependence between input variables. Any such dependence is filtered out to a large degree by the use of non-linear operators such as AND, OR, MIN, PRODUCT, and GAMMA.

The prospectivity analysis shows that the most favourable areas for magmatic nickel–copper deposits are in the FINLAYSON and HOLT map sheet areas (Fig. 15), whereas those for magmatic PGE deposits is in the BELL ROCK map sheet area (Fig. 18). Favourable areas for intrusion-related gold mineralization are mainly in the southern part of the BENTLEY and northern part of the MOUNT EVELINE map sheets (Fig. 20). For orogenic gold deposits, the COOPER map sheet area is most prospective (Fig. 21). The analysis for IOCG deposits (Fig. 25) indicates high potential in the FINLAYSON, HOLT, and BELL ROCK map sheet areas. The BLACKSTONE and BELL ROCK map sheet areas have greatest potential for tin and tungsten deposits (Fig. 27). Surficial uranium targets are identified in the BLACKSTONE map sheet area (Fig. 30).

Acknowledgements

Our work on the west Musgrave Province has benefitted from the open discussions with GSWA and the CET team. We acknowledge all involved at every level. We are grateful to Dr Jason Wong for guidance on the use of the CET porphyry system Geosoft plug-in and Dr Daniel Wedge for help with some Python commands in ArcGIS. Professor Wolfgang Maier, Dr Marco Fiorentini, Dr Steve Barnes and Dr Steve Beresford are acknowledged for their discussions on Ni–Cu and PGE mineralization systems.

References

Abeysinghe, PB 2003, Mineral occurrences and exploration potential of the Arunta-Musgrave area: Geological Survey of Western Australia, Record 2002/9, 33p.

Agterberg, FP 1989, Systematic approach to dealing with uncertainty of geoscience information, *in* Application of Computers and Operations in the Mineral Industry *edited by* A Weiss: Colorado Society of Mining Engineers; 21st APCOM Symposium, Las Vegas, USA, February 1989, p. 165–178.

Agterberg, FP and Bonham-Carter, GF 1990, Deriving weights of evidence from geoscience contour maps for the prediction of discrete events, *in* Applications of Computers and Mathematics in the Mineral Industries: Technical University of Berlin; 22nd APCOM Symposium, Berlin, Germany, 17 September 1990, p. 381–395.

Aitken, ARA 2010, Moho geometry gravity inversion experiment (MoGGIE): a refined model of the Australian Moho, and its tectonic and isostatic implications: Earth and Planetary Science Letters, v. 297, p. 71–83.

Aitken, ARA, Dentith, MC, Evans, SF, Gallardo, LA, Joly, A, Thiel, S, Smithies, RH and Tyler, IM 2013, Imaging crustal structure in the west Musgrave Province from magnetotelluric and potential field data: Geological Survey of Western Australia, Report 114, 81p.

Aitken, ARA and Betts, PG 2008, High-resolution aeromagnetic data over central Australia assist Grenville-era (1300–1100 Ma) Rodinia reconstructions: Geophysical Research Letters, v. 35 (L01306).

Aitken, ARA and Betts, PG 2009a, Constraints on the Proterozoic supercontinent cycle from the structural evolution of the south-central Musgrave Province, central Australia: Precambrian Research, v. 168, no. 3–4, p. 284–300.

Aitken, ARA and Betts, PG 2009b, Multi-scale integrated structural and aeromagnetic analysis to guide tectonic models: an example from the eastern Musgrave Province, central Australia: Tectonophysics, v. 476, no. 3–4, p. 418–435.

Aitken, ARA, Betts, PG and Ailleres, L 2009a, The architecture, kinematics, and lithospheric processes of a compressional intraplate orogen occurring under Gondwana assembly: the Petermann Orogeny, central Australia: Lithosphere, v. 1, no. 6, p. 343–357.

Aitken, ARA, Betts, PG, Schaefer, BF and Rye, SE 2008, Assessing uncertainty in the integration of aeromagnetic data and structural observations in the Deering Hills region of the Musgrave Province: Australian Journal of Earth Sciences, v. 55, no. 8, p. 1127–1138.

Aitken, ARA, Betts, PG, Weinberg, RF and Gray, DJ 2009b, Constrained potential field modeling of the crustal architecture of the Musgrave Province in central Australia: Evidence for lithospheric strengthening due to crust-mantle boundary uplift: Journal of Geophysical Research, v. 114, no. B12.

An, P, Moon, WM and Rencz, AN 1991, Application of fuzzy set theory to integrated mineral exploration: Canadian Journal of Exploration Geophysics, v. 27, p. 1–11.

Arndt, NT, Lesher, CM and Czamanske, GK 2005, Mantle-derived magmas and magmatic Ni–Cu–(PGE) deposits: Economic Geology, v. 100, no. 1 (100th Anniversary Volume), p. 5–23.

Baker, PM and Waugh, RS 2005, The role of surface geochemistry in the discovery of Babel and Nebo magmatic nickel–copper–PGE deposits: Geochemistry: Exploration, Environment, Analysis, v. 5, p. 195–200.

Ballhaus, C and Berry, RF 1991, Crystallization pressure and cooling history of the Giles layered igneous complex, central Australia: Journal of Petrology, v. 32, no. 1, p. 1–28.

Ballhaus, CG and Glikson, AY 1989, Magma mixing and intraplutonic quenching in the Wingellina Hills Intrusion, Giles Complex, Central Australia: Journal of Petrology, v. 30, no. 6, p. 1443–1469.

Ballhaus, CG and Glikson, AY 1995, The petrology of layered mafic–ultramafic intrusions of the Giles Complex, western Musgrave block, central Australia: AGSO Journal of Australian Geology and Geophysics, v. 16, p. 69–89.

Barnes, S-J and Lightfoot, PC 2005, Formation of magmatic nickel sulfide ore deposits and processes affecting their copper and platinum group element contents, *in* Economic Geology 100th Anniversary Volume *edited by* JW Hedenquist, JFH Thompson, RJ Goldfarb and JP Richards: Economic Geology 100, p. 179–214.

Barnes, SJ, Keays, RR and Hoatson, DM 1992, Distribution of sulfides and PGE within the porphyritic websterite zone of the Munni Munni Complex, Western Australia: Australian Journal of Earth Sciences, v. 39, p. 289–302.

Barton, MD and Johnson, DA 1996, Evaporitic-source model for igneous-related Fe oxide–(REE–Cu–Au–U) mineralization: Geology, v. 24, no. 3, p. 259–262.

Beadell Resources Ltd 2009, Beadell discovery may herald new Australian gold province: Report to Australian Securities Exchange, 7 December 2009, 5p.

Begg, GC, Hronsky, JMA, Arndt, NT, Griffin, WL, O'Reilly, S and Hayward, N 2010, Lithospheric, cratonic, and geodynamic setting of Ni–Cu–PGE sulfide deposits: Economic Geology, v. 105, p. 1057–1070.

Blewett, R, Champion, D, Czarnota, K, Henson, P, Goscombe, B, Hailey, S, Miller, J, Neumayr, P, Nugus, M, Roache, T, Sheldon, H, Walshe, J, Tunjic, J and Young, C 2009, Five answers to five questions: a scale-integrated mineral systems study of the East Yilgarn Craton, *in* Smart Science for Exploration and Mining *edited by* PJ Williams: 10th Biennial SGA Meeting of the Society for Geology Applied to Mineral Deposits, Townsville, QLD, 17 October 2009, p. 84–86.

Bodorkos, S, Wingate, MTD and Kirkland, CL 2008, 174737: foliated metamonzogranite, Mount Fanny; Geochronology Record 718: Geological Survey of Western Australia, 5p.

Bonham-Carter, GF 1994, Geographic Information Systems for geoscientists: modelling with GIS: Pergamon Press, Elsevier B.V., Amsterdam, The Netherlands, 416p.

Bonham-Carter, GF and Agterberg, FP 1990, Application of a microcomputer-based geographic information system to mineral-potential mapping, *in* Microcomputer-based Applications in Geology *edited by* JT Hanley and DF Merriam: Pergamon Press, New York, US, p. 49–74.

Braun, J, McQueen, H and Etheridge, M 1991, A fresh look at the Late Palaeozoic tectonic history of western-central Australia: Exploration Geophysics, v. 22, p. 49–54.

Brown, WM 2002, Artificial neural networks: a new method for mineral-prospectivity mapping: The University of Western Australia, Perth, Western Australia, PhD thesis (unpublished).

Buchanan, DL, Nolan, J, Suddaby, P, Rouse, JE, Viljoen, MJ and Davenport, JWJ 1981, The genesis of sulfide mineralization in a portion of the Potgietersrus limb of the Bushveld Complex: Economic Geology, v. 76, p. 568–579.

Camacho, A, Compston, W, McCulloch, MT and McDougall, I 1997, Timing and exhumation of eclogite facies shear zones, Musgrave Block, central Australia: Journal of Metamorphic Geology, v. 15, p. 735–751.

Camacho, A and Fanning, CM 1995, Some isotopic constraints on the evolution of the granulite and upper amphibolite facies terranes in the eastern Musgrave Block, central Australia: Precambrian Research, v. 71, p. 155–172.

Carlisle, D 1983, Concentration of uranium and vanadium in calcrete and gypcrete, *in* Residual Deposits *edited by* RCL Wilson: Geological Society, London, UK, Special Publication 11, p. 185–195.

Carranza, EJM and Hale, M 2000, Geologically constrained probabilistic mapping of gold potential, Baguio District, Philippines: Natural Resources Research, v. 9, no. 3, p. 237–253.

Cawthorn, RG, Barnes, S-J, Ballhaus, C and Malitch, KN 2005, Platinum-group element, chromium and vanadium deposits in mafic and ultramafic rocks: Economic Geology, v. 100, no. 2 (100th Anniversary Volume), p. 215–250.

Cheng, Q 2007, Mapping singularities with stream sediment geochemical data for prediction of undiscovered mineral deposits in Gejiu, Yunnan Province, China: Ore Geology Reviews, v. 32, p. 314–324.

Cline, JS 2001, Timing of gold and arsenic sulfide mineral deposition at the Getchell carlin-type gold deposit, North-Central Nevada: Economic Geology, v. 96, p. 75–89.

Coleman, PM, Kirkland, CL, Wingate, MTD and Smithies, RH 2010, 191728: rhyolite, Mount Jane; Geochronology Record 917: Geological Survey of Western Australia, 4p.

Cox, SF, Knackstedt, MA and Braun, J 2001, Principles of structural control on permeability and fluid flow in hydrothermal systems: Reviews in Economic Geology, v. 14, p. 1–24.

Cruden, AR 2008, Emplacement mechanisms and structural influences of a younger granite intrusion into older wallrocks: a principal study with application to the Gotemar and Uthammar granites: SKB Rapport 138, 48p.

D'Ercole, C, Groves, DI and Knox-Robinson, CM 2000, Using fuzzy logic in a geographic information system environment to enhance conceptually based prospectivity analysis of Mississippi Valley-type mineralisation: Australian Journal of Earth Sciences, v. 47, no. 5, p. 913–927.

Dahlkamp, FJ 1978, Classification of uranium deposits: Mineralium Deposita, v. 13, p. 83–104.

Dahlkamp, FJ 2009, Uranium deposits of the world: Springer, Berlin, Heidelberg, p. 31–156.

Daniels, JL 1974, The geology of the Blackstone region, Western Australia: Geological Survey of Western Australia, Bulletin 123, 257p.

De Waal, SA 1975, Carbon dioxide and water from metamorphic reactions as agents for sulfide and spinel precipitation in mafic magmas: Transactions of the Geological Society of South Africa, v. 80, p. 193–196.

Edgoose, CJ, Scrimgeour, IR and Close, DF 2004, Geology of the Musgrave Block, Northern Territory: Northern Territory Geological Survey, Report 15, 46p.

Eugster, HP 1985, Granites and hydrothermal ore-deposits: a geochemical framework: Mineralogical Magazine, v. 49, p. 7–23.

Evins, PM, Smithies, RH, Howard, HM, Kirkland, CL, Wingate, MTD and Bodorkos, S 2010, Devil in the detail; The 1150–1000 Ma magmatic and structural evolution of the Ngaanyatjarra Rift, west Musgrave Province, Central Australia: Precambrian Research, v. 183, p. 572–588.

Ferguson, HG and Bateman, AM 1912, Geologic features of tin deposits: Economic Geology, v. 7, p. 209–262.

Flöttmann, T, Hand, M, Close, DF, Edgoose, C and Scrimgeour, IR 2004, Thrust tectonic styles of the intracratonic Alice Springs and Petermann Orogens, Central Australia, *in* Thrust Tectonics and Hydrocarbon Systems *edited by* KR McClay: American Association of Petroleum Geologists, Memoir 82, p. 538–557.

Gain, SB and Mostert, AB 1982, The geological setting of the platinoid and base metal sulfide mineralization in the Platreef of the Bushveld Complex on Drenthe, north of Potgietersrus: Economic Geology, v. 77, p. 1395–1404.

Geological Survey of Western Australia (GSWA) 2010a, West Musgrave, 2010 update: Geological Survey of Western Australia, 1:100 000 Geological Information Series.

Geological Survey of Western Australia (GSWA) 2010b, GeoChem Extract: Department of Mines and Petroleum, Western Australia, <geochem.dmp.wa.gov.au/geochem>, viewed June 2011.

Geological Survey of Western Australia (GSWA) 2010c, MINEDEX: mines and minerals deposits database: Department of Mines and Petroleum, Perth, Western Australia, <www.dmp.wa.gov.au/minedex>, viewed June 2011.

Geological Survey of Western Australia (GSWA) 2012, West Musgrave, 2012 update: Geological Survey of Western Australia, 1:100 000 Geological Information Series.

Geoscience Australia 2007, OZCHEM National Whole Rock Geochemistry Database (digital data repository): Geoscience Australia, Canberra, ACT, <www.ga.gov.au/metadata-gateway/metadata/record/gcat_65464>.

Glikson, AY, Stewart, AT, Ballhaus, GL, Clarke, GL, Feeken, EHT, Level, JH, Sheraton, JW and Sun, S-S 1996, Geology of the western Musgrave Block, central Australia, with reference to the mafic–ultramafic Giles Complex: Australian Geological Survey Organisation, Bulletin 239, 206p.

Godel, B, Seat, Z, Maier, WD and Barnes, S-J 2011, The Nebo–Babel Ni–Cu–PGE sulfide deposit (west Musgrave Block, Australia), Pt 2. Constraints on parental magma and processes, with implications for mineral exploration: Economic Geology, v. 106, p. 557–584.

Groves, DI 1993, The crustal continuum model for late-Archaean lode-gold deposits of the Yilgarn Block, Western Australia: Mineralium Deposita, v. 28, no. 6, p. 366–374.

Groves, DI, Bierlein, FP, Meinert, LD and Hitzman, MW 2010, Iron oxide copper–gold (IOCG) deposits through Earth history: implications for origin, lithospheric setting, and distinction from other epigenetic iron oxide deposits: Economic Geology, v. 105, no. 3, p. 641–654.

Groves, DI, Goldfarb, RJ, Gebre-Mariam, M, Hagemann, SG and Robert, F 1998, Orogenic gold deposits: a proposed classification in the context of their crustal distribution and relationship to other gold deposit types: Ore Geology Reviews, v. 13, no. 1–5, p. 7–27.

Groves DI, Goldfarb RJ, Knox-Robinson CM, Ojala J, Gardoll S, Yun GY and Holyland P 2000, Late-kinematic timing of orogenic gold deposits and significance for computer-based exploration techniques with emphasis on the Yilgarn Block, Western Australia: Ore Geology Reviews, v. 17, p. 1–38.

Groves, DI and Phillips, GN 1987, The genesis and tectonic controls on Archean lode gold deposits of the Western Australian shield: a metamorphic-replacement model: Ore Geology Reviews, v. 2, p. 287–322.

Groves, DI and Vielreicher, NM 2001, The Phalabowra (Palabora) carbonatite-hosted magnetite–copper sulfide deposit, South Africa: an end-member of the iron oxide–copper–gold–rare earth element deposit group?: Mineralium Deposita, v. 36, p. 189–194.

Hagemann, SG and Cassidy, KF 2000, Archaean lode gold deposits, *in* Gold in 2000 *edited by* SG Hagemann and PE Brown: Reviews in Economic Geology 13, p. 9–68.

Halter, WE 1996, The role of greisenization in cassiterite precipitation at the East Kemptville tin deposit, Nova Scotia: Economic Geology, v. 91, p. 368–385.

Halter, WE, Pettke, T and Heinrich, CA 2002, The origin of Cu/Au ratios in porphyry-type ore deposits: Science, v. 296, no. 5574, p. 1844–1846.

Halter, WE, Williams-Jones, AE and Kontak, DJ 1995, Origin and evolution of the greisenizing fluid at the East Kemptville tin deposit, Nova Scotia, Canada: Economic Geology, v. 93, p. 1026–1051.

Hannah, JL and Stein, HJ 2002, Re–Os model for the origin of sulfide deposits in anorthosite-associated intrusive complexes: Economic Geology, v. 97, p. 371–383.

Hart, CJR 2007, Reduced intrustion-related gold systems, *in* Mineral deposits of Canada: a synthesis of major deposit types, district metallogeny, the evolution of geological provinces, and exploration methods *edited by* WD Goodfellow: Geological Association of Canada, Mineral Deposits Division, Special Publication 5, p. 95–112.

Haynes, DW 2000, Iron oxide copper(-gold) deposits: their position in the ore deposit spectrum and modes of origin, *in* Hydrothermal iron oxide–copper–gold and related deposits: A global perspective (Volume 1) *edited by* TM Porter: PGC Publishing, Linden Park, South Australia, p. 71–90.

Heinrich, CA 1990, The chemistry of hydrothermal tin(–tungsten) ore deposition: Economic Geology, v. 85, no. 3, p. 457–481.

Heinrich, CA 1995, Geochemical evolution and hydrothermal mineral deposition in Sn (–W–base metal) and other granite-related ore systems: some conclusions from Australian examples, *in* Magmas, fluids and ore deposits *edited by* JFH Thompson: Mineral Association of Canada Short Course Series 23, p. 203–220.

Hitzman, MW, Oreskes, N and Einaudi, MT 1992, Geological characteristics and tectonic setting of Proterozoic iron oxide (Cu–U–Au–REE): Precambrian Research, v. 58, p. 241–287.

Hoatson, DM and Blake, DH (editors) 2000, Geology and economic potential of the Palaeoproterozoic layered mafic–ultramafic intrusions in the East Kimberley, Western Australia: Australian Geological Survey Organisation, Canberra, ACT, Bulletin 246, 476p.

Hoatson, DM, Subhash, J and Jaques, AL 2006, Nickel sulfide deposits in Australia: characteristics, resources and potential: Ore Geology Reviews, v. 29, p. 177–241.

Holden, E-J, Fu, SC, Kovesi, P, Dentith, MC, Bourne, B and Hope, M 2010, Automated identification of magnetic responses from porphyry systems, *in* Extended abstracts: AESG 21st International Geophysical Conference and Exhibition, Sydney, Australia, 4p.

Hou, B, Fabris, AJ, Keeling, JL and Fairclough, MC 2007, Cainozoic palaeochannel-hosted uranium and current exploration methods, South Australia: MESA Journal 46, p. 34–39.

Howard, HM, Smithies, RH, Pirajno, F and Skwarnecki, MS 2007, Bell Rock, WA Sheet 4645: Geological Survey of Western Australia, 1:100 000 Geological Series.

Howard, HM, Werner, M, Smithies, RH, Evins, PM, Kirkland, CL, Kelsey, DE, Hand, M, Collins, AS, Pirajno, F, Wingate, MTD, Maier, WD and Raimondo, T 2011, The geology of the west Musgrave Province and the Bentley Supergroup — a field guide: Geological Survey of Western Australia, Record 2011/4, 116p.

Hronsky, JMA 2004, The science of exploration targeting, in SEG 2004: Predictive mineral discovery under cover edited by J Muhling: The University of Western Australia, Centre for Global Metallogeny, Publication 33, p. 129–133.

International Atomic Energy Agency 2000, Methods of exploitation of different types of uranium deposits: International Atomic Energy Agency, Vienna, Austria, 75p.

Johnson, JP and Cross, KC 1995, U–Pb geochronological constraints on the genesis of the Olympic Dam Cu–U–Au–Ag deposit, South Australia: Economic Geology, v. 90, p. 1046–1063.

Joly, A, Dentith, MC, Porwal, A, Spaggiari, CV, Tyler, IM and McCuaig, TC 2013, An integrated geological and geophysical study of the West Arunta Orogen and its mineral prospectivity: Geological Survey of Western Australia, Report 113, 89p.

Joly, A, Porwal, A and McCuaig, TC 2012, Exploration targeting for orogenic gold deposits in the Granites–Tanami Orogen: Mineral system analysis, targeting model and prospectivity analysis: Ore Geology Reviews, v. 48, p. 349–383.

Karimzadeh-Somarin, A and Ashley, P 2004, Hydrothermal alteration and mineralization of the Glen Eden Mo–W–Sn deposit, a leucogranite-related hydrothermal system, southern New England Orogen, NSW, Australia: Mineralium Deposita, v. 39, no. 3, p. 282–300.

Kerrich, R, Goldfarb, RJ, Groves, D and Garwin, S 2000, The geodynamics of world-class gold deposits: characteristics, space-time distribution and origins: Reviews of Society of Economic Geologists, v. 13 (Gold in 2000), p. 501–551

Kerrich, R, Goldfarb, RJ and Richards, JP 2005, Metallogenic provinces in an evolving geodynamic framework, *in* Economic Geology 100th Anniversary Volume *edited by* JW Hedenquist, JFH Thompson, RJ Goldfarb and JP Richards: Society of Economic Geologists, Inc., US, p. 1097–1136.

Kirkland, CL, Bodorkos, S and Wingate, MTD 2009a, 183596: laminated paragneiss, Mount Fanny; Geochronology Record 758: Geological Survey of Western Australia, 5p.

Kirkland, CL, Smithies, RH, Woodhouse, AJ, Howard, HM, Wingate, MTD, Belousova, EA, Cliff, JB, Murphy, RC and Spaggiari, CV 2013, Constraints and deception in the isotopic record; the crustal evolution of the west Musgrave Province, central Australia: Gondwana Research, v. 23, no. 2, p. 759–781.

Kirkland, CL, Wingate, MTD and Bodorkos, S 2008, 174761: porphyritic granite dyke, Charnockite Flats; Geochronology Record 721: Geological Survey of Western Australia, 4p.

Kirkland, CL, Wingate, MTD, Bodorkos, S and Smithies, RH 2009b, 185583: K-feldspar porphyritic granite, Mummawarrawarra Hill; Geochronology Record 765: Geological Survey of Western Australia, 5p.

Kirkland, CL, Wingate, MTD and Werner, M 2011, 195723: rhyolitic ignimbrite, Mount Glyde; Geochronology Record 939: Geological Survey of Western Australia, 4p.

Kirkland, CL, Wingate, MTD, Howard, HM, Quentin De Gromard, R and Smithies, RH 2014, 189563: hornblende–biotite syenogranite, Barnard Rocks; Geochronology Record 1196: Geological Survey of Western Australia, 4p.

Knox-Robinson, CM 2000, Vectorial fuzzy logic: a novel technique for enhanced mineral prospectivity mapping, with reference to the orogenic gold mineralisation potential of the Kalgoorlie Terrane, Western Australia: Australian Journal of Earth Sciences, v. 47, p. 929–941.

Knox-Robinson, CM and Wyborn, LAI 1997, Towards a holistic exploration strategy: using Geographic Information Systems as a tool to enhance exploration: Australian Journal of Earth Sciences, v. 44, no. 4, p. 453–463.

Kreuzer, OP, Etheridge, MA, Guj, P, McMahon, ME and Holden, DJ 2008, Linking mineral deposit models to quantitative risk analysis and decision-making in exploration: Economic Geology, v. 103, no. 4, p. 829–850.

Kreuzer, OP, Markwitz, V, Porwal, AK and McCuaig, TC 2010, A continent-wide study of Australia's uranium potential: Part I: GIS-assisted manual prospectivity analysis: Ore Geology Reviews, v. 38, no. 4, p. 334–366.

Lambeck, K and Burgess, G 1992, Deep crustal structure of the Musgrave Block, central Australia: results from teleseismic travel-time anomalies: Australian Journal of Earth Sciences, v. 39, p. 1–20.

Lambert, DD, Foster, JG, Frick, LR, Hoatson, DM and Purvis, AC 1998, Application of the Re–Os isotopic system to the study of Precambrian magmatic sulfide deposits of Western Australia: Australian Journal of Earth Sciences, v. 45, p. 265–284.

Lambert, DD, Frick, LR, Foster, JG, Li, C and Naldrett, AJ 2000, Re–Os isotope systematics of the Voisey's Bay Ni–Cu–Co magmatic sulfide system, Labrador, Canada. II. Implications for parental magma chemistry, ore genesis, and metal redistribution: Economic Geology, v. 95, p. 867–888.

Landis, GP and Rye, RO 1974, Geologic, fluid inclusion, and stable isotope studies of the Pasto Buena tungsten-base metal ore deposit, Northern Peru: Economic Geology, v. 69, no. 7, p. 1025–1059.

Lang, JR and Baker, T 2001, Intrusion-related gold systems: the present level of understanding: Mineralium Deposita, v. 36, no. 6, p. 477–489.

Le Bas, MJ 2000, IUGS reclassification of the high-Mg and picritic volcanic rocks: Journal of Petrology, v. 41, p. 1467–1470.

Lehmann, B 1990, Metallogeny of tin: Lecture Notes in Earth Sciences 32: Springer-Verlag, Heidelberg, Germany, 211p.

Lesher, CM and Campbell, IH 1993, Geochemical and fluid-dynamic modeling of compositional variations in Archean komatiite-hosted nickel sulfide ores in Western Australia: Economic Geology, v. 88, p. 804–816.

Li, C and Naldrett, AJ 1993, Sulfide capacity of magma: a quantative model and its application to the formation of sulfide ores at Sudbury: Economic Geology, v. 88, p. 1253–1260.

Li, C and Naldrett, AJ 2000, Melting reactions of gneissic inclusions with enclosing magma at Voisey's Bay, Labrador, Canada: implications with respect to ore genesis: Economic Geology, v. 95, p. 801–814.

Li, C, Ripley, EM, Naldrett, AJ, Schmitt, AK and Moore, CH 2009, Magmatic anhydrite-sulfide assemblages in the plumbing system of the Siberian Traps: Geology, v. 37, no. 3, p. 259–262.

Lightfoot, PC 2007, Advances in Ni–Cu–PGE sulphide deposit models and implications for exploration technologies, *in* Proceedings of the 5th Decennial International Conference on Mineral Exploration *edited by* B Milkereit: Decennial Mineral Exploration Conferences; Exploration '07, Toronto, Canada, 9 September 2007, p. 629–646.

Lindsay, JF and Leven, JH 1996, Evolution of a Neoproterozoic to Palaeozoic intracratonic setting, Officer Basin, South Australia: Basin Research, v. 8, p. 403–424.

Lord, D, Etheride, MA, Willson, M, Hall, G and Uttley, PJ 2001, Measuring exploration success: an alternative to the discovery-cost-per-ounce method of quantifying exploration success: Society of Economic Geologists Newsletter, v. 45, no. 1, p. 10–16.

Maboko, MAH, McDougall, I, Zeitler, PK and Williams, IS 1992, Geochronological evidence for ~530–550 Ma juxtaposition of two Proterozoic metamorphic terranes in the Musgrave Ranges, central Australia: Australian Journal of Earth Sciences, v. 39, no. 4, p. 457–471.

Maier, WD 2005, Platinum-group element (PGE) deposits and occurrences: mineralization styles, genetic concepts, and exploration criteria: Journal of African Earth Sciences, v. 41, no. 3, p. 165–191.

Maier, WD, Barnes, SJ, Gartz, V and Andrews, G 2003, Pt–Pd reefs in magnetitites of the Stella layered intrusion, South Africa: A world of new exploration opportunities for platinum group elements: Geology, v. 31, no. 10, p. 885–888 .

Maier, WD, Barnes, S-J, Chinyepi, G, Barton, JM, Eglington, B and Setshedi, I 2007, The composition of magmatic Ni–Cu–(PGE) sulfide deposits in the Tati and Selebi-Phikwe belts of eastern Botswana: Mineralium Deposita, v. 43, p. 37–60.

Maier, WD, de Klerk, L, Blaine, J, Manyeruke, T, Barnes, S-J, Stevens, MVA and Mavrogenes, JA 2008, Petrogenesis of contact-style PGE mineralization in the northern lobe of the Bushveld Complex: comparison of data from the farms Rooipoort, Townlands, Drenthe and Nonnenwerth: Mineralium Deposita, v. 43, no. 3, p. 255–280.

Maier, WD and Groves, DI 2011, Temporal and spatial controls on the formation of magmatic PGE and Ni–Cu deposits: Mineralium Deposita, v. 46, no. 8, p. 841–857.

Mark, G, Oliver, NHS, Williams, PJ, Valenta, RK and Crookes, RA 2000, The evolution of the Ernest Henry Fe-Oxide–(Cu–Au) hydrothermal system, *in* Hydrothermal iron oxide copper-gold and related deposits: A global perspective *edited by* TM Porter: PGC Publishing, Linden Park, South Australia, p. 123–136.

Marshall, LJ 2003, Brecciation within the Mary Kathleen Group of the Eastern Succession, Mt Isa Block, Australia. Implications of district-scale structural and metasomatic processes for Fe-oxide–Cu–Au mineralisation: James Cook University, Townsville, Queensland, PhD thesis (unpublished).

Mashkovtsev, GA, Kislyakov, YM, Miguta, AK, Modnikov, IS and Shchetochkin, VN 1995, Uranium deposits: main types and concepts for detection, *in* Changes and events in uranium deposit development, exploration, resources, production, and the world supply–demand relationship: International Atomic Eenergy Agency and OECD Nuclear Energy Agency; Technical Committee meeting, Kiev, Ukraine, 22 May 1995; Proceedings, p. 297–306.

Mathur, R, Marschik, R, Ruiz, J, Munizaga, F, Leveille, RA and Martin, W 2002, Age of mineralization of the Candelaria Fe oxide Cu–Au deposit and the origin of the Chilean iron belt, based on Re–Os isotopes: Economic Geology, v. 97, p. 59–71.

Mavrogenes, JA and O'Neill, HSC 1999, The relative effects of temperature, pressure and oxygen fugacity on the solubility of sulfide in mafic magmas: Geochimica et Cosmochimica Acta, v. 63, no. 7–8, p. 1173–1180.

McCuaig, TC, Beresford, S and Hronsky, J 2010, Translating the mineral systems approach into an effective exploration targeting system: Ore Geology Reviews, v. 38, p. 128–138.

McCuaig, TC and Kerrich, R 1998, P–T–t–deformation–fluid characteristics of lode gold deposits: evidence from alteration systematics: Ore Geology Reviews, v. 12, no. 6, p. 381–453.

McKay, AD and Miezitis, Y 2001, Australia's uranium resources, geology and development of deposits: Australian Geological Survey Organisation – Geoscience Australia, Mineral Resource Report 1, 184p.

Mikucki, EJ 1998, Hydrothermal transport and depositional processes in Archean lode-gold systems: a review: Ore Geology Reviews, v. 13, no. 1–5, p. 307–321.

Milligan, PR and Franklin, R 2004, Magnetic anomaly grids of Australia, 4th edition (metadata): Geoscience Australia, Canberra, ACT, <www.ga.gov.au/meta/ANZCW0703007121.html>, viewed December 2010.

Mishra, B and Panigrahi, MK 1999, Fluid evolution in the Kolar Gold Field: evidence from fluid inclusion studies: Mineralium Deposita, v. 34, p. 173–181.

Morris, PA and Pirajno, F 2005, Mesoproterozoic sill complexes in the Bangemall Supergroup, Western Australia: geology, geochemistry, and mineralization potential: Geological Survey of Western Australia, Report 99, 75p.

Mutschler, FE and Mooney, TC 1993, Precious metal deposits related to alkaline igneous rocks — provisional classification, grade-tonnage data, and exploration frontiers, *in* Mineral desposit modeling *edited by* RV Kirkham, WD Sinclair, RI Thorpe and JM Duke: Geological Association of Canada, Special Paper 40, p. 479–520.

Myers, JS, Shaw, RD and Tyler, IM 1996, Tectonic evolution of Proterozoic Australia: Tectonics, v. 15, p. 1431–1146.

Naldrett, AJ 1989, Stratiform PGE deposits in layered intrusions: Reviews in Economic Geology, v. 4, p. 135–165.

Naldrett, AJ 1997, Key factors in the genesis of Noril'sk, Sudbury, Jinchuan, Voisey's Bay and other world-class Ni–Cu–PGE deposits: implications for exploration: Australian Journal of Earth Sciences, v. 44, p. 283–315.

Naldrett, AJ 2004, Magmatic sulfide deposits — geology, geochemistry and exploration: Springer-Verlag, Berlin, Germany, 728p.

Naldrett, AJ 2010, Secular variation of magmatic sulfide deposits nad their source magmas: Economic Geology, v. 105, p. 669–688.

Nisbet, B, Cooke, J, Richards, M and Williams, C 2000, Exploration for iron oxide copper gold deposits in Zambia and Sweden: Comparison with the Australian experience, *in* Hydrothermal iron oxide copper-gold and related deposits: A global perspective (Volume 1) *edited by* TM Porter: PGC Publishing, Linden Park, South Australia, p. 297–308.

Oreskes, N and Einaudi, MT 1990, Origin of rare earth element-enriched hematite breccias at the Olympic Dam Cu–U–Au–Ag deposit, Roxby Downs, South Australia: Economic Geology, v. 85, no. 1, p. 1–28.

Oreskes, N and Einaudi, MT 1992, Origin of hydrothermal fluids at Olympic Dam: preliminary results from fluid inclusions and stable isotopes: Economic Geology, v. 87, no. 1, p. 64–90.

Organisation for Economic Co-operation and Development Nuclear Energy Agency and International Atomic Energy Agency (compilers) 2006, Uranium 2005: resources, production and demand ('Red Book'): OECD Publications, Paris, France, 391p.

Phillips, GN and Groves, DI 1983, The nature of Archaean gold-bearing fluids as deduced from gold deposits of Western Australia: Journal of the Geological Society of Australia, v. 30, no. 1, p. 25–39.

Phillips, GN and Powell, R 1993, Link between gold provinces: Economic Geology, v. 88, no. 5, p. 1084–1098.

Pollard, PJ 2000, Evidence of a magmatic fluid and metal source for Fe Oxide–Cu–Au mineralisation, *in* Hydrothermal iron oxide copper-gold and related deposits: A global perspective (Volume 1) *edited by* TM Porter: PGC Publishing, Linden Park, South Australia, p. 27–46.

Pollard, PJ and Taylor, RG 1986, Progressive evolution of alteration and tin mineralization; controls by interstitial permeability and fracture-related tapping of magmatic fluid reservoirs in tin granites: Economic Geology, v. 81, no. 7, p. 1975–1800.

Porter, TM (editor) 2000, Hydrothermal iron-oxide copper-gold and related deposits: a global perspective (Conference proceedings edition): Australian Mineral Foundation, Glenside, South Australia, 349p.

Porter, TM (editor) 2002, Hydrothermal iron oxide copper-gold and related deposits: a global perspective (2nd edition): PGC Publishing, Linden Park, South Australia, 377p.

Porwal, A 2006, Mineral potential mapping with mathematical geological models: University of Utrecht, Eschende, The Netherlands, PhD thesis (unpublished), 289p.

Porwal, A, Carranza, EJM and Hale, M 2003, Artificial neural networks for mineral-potential mapping: a case study from Aravalli Province, western India: Natural Resources Research, v. 12, no. 3, p. 155–171.

Porwal, A, González-Álvarez, I, Markwitz, V, McCuaig, TC and Mamuse, A 2010, Weights-of-evidence and logistic regression modeling of magmatic nickel sulfide prospectivity in the Yilgarn Craton, Western Australia: Ore Geology Reviews, v. 38, no. 3, p. 184–196.

Prendergast, MD 2004, Contact relations between the Koodoovale- and Manjeri-type lithostratigraphic units of the late Archaean Bulawayan Supergroup at Hunters Road, central Zimbabwe: South African Journal of Geology, v. 107, no. 3, p. 325–332.

Raimondo, T, Collins, AS, Hand, M, Walker-Hallam, A, Smithies, RH, Evins, PM and Howard, HM 2010, The anatomy of a deep intracontinental orogen: Tectonics, v. 29 (TC4024).

Reeve, JS, Cross, KC, Smith, RN and Oreskes, N 1990, The Olympic Dam copper–uranium–gold–silver deposit, South Australia, *in* Geology and mineral deposits of Australia and Papua New Guinea *edited by* F Hughes: Australasian Institute of Mining and Metallurgy, Monograph 14, p. 1009–1035.

Ripley, EM, Li, C and Shin, D 2002, Paragneiss assimilation in the genesis of magmatic Ni–Cu–Co sulfide mineralization at Voisey's Bay, Labrador: $\delta^{34}S$, $\delta^{13}C$, and Se/S evidence: Economic Geology, v. 97, p. 1307–1318.

Ripley, EM, Lightfoot, PC, Li, C and Elswick, ER 2003, Sulfur isotopic studies of continental flood basalts in the Noril'sk region: implications for the association between lavas and ore-bearing intrusions: Geochimica et Cosmochimica Acta, v. 67, no. 15, p. 2805–2817.

Ripley, EM, Park, Y-R, Li, C and Naldrett, AJ 1999, Sulfur and oxygen isotopic evidence of country rock contamination in the Voisey's Bay Ni–Cu–Co deposit, Labrador, Canada: Lithos, v. 47, no. 1–2, p. 53–68.

Roberts, DE and Hudson, GRT 1983, The Olympic Dam copper–uranium–gold deposit, Roxby Downs, South Australia: Economic Geology, v. 78, no. 5, p. 799–822.

Roberts, S, Sanderson, DJ and Gumiel, P 1998, Fractal analysis of Sn–W mineralization from central Iberia; insights into the role of fracture connectivity in the formation of an ore deposit: Economic Geology, v. 98, no. 3, p. 360–365.

Schoenberg, R, Nagler, TF, Gnos, E, Kramers, JD and Kamber, BS 2003, The source of the Great Dyke, Zimbabwe, and its tectonic significance: evidence from Re–Os isotopes: The Journal of Geology, v. 111, no. 5, p. 565–578.

Scrimgeour, IR and Close, DF 1999, Regional high pressure metamorphism during intracratonic deformation: the Petermann Orogeny, central Australia: Journal of Metamorphic Geology, v. 17, p. 557–572.

Seat, Z, Beresford, SW, Grguric, BA, Gee, MAM and Grassineau, NV 2009, Reevaluation of the role of external sulfur addition in the genesis of Ni–Cu–PGE deposits: evidence from the Nebo–Babel Ni–Cu–PGE deposit: west Musgrave, Western Australia: Economic Geology, v. 104, p. 521–538.

Seat, Z, Beresford, SW, Grguric, BA, Waugh, RS, Hronsky, JMA, Gee, MAM, Groves, DI and Mathison, CI 2007, Architecture and emplacement of the Nebo–Babel gabbro–norite-hosted magmatic Ni–Cu–PGE sulfide deposits, west Musgrave, Western Australia: Mineralium Deposita, v. 42, p. 551–582.

Seat, Z, Gee, MAM, Grguric, BA, Beresford, SW and Grassineau, NV 2011, The Nebo-Babel Ni–Cu–PGE Sulfide Deposit (West Musgrave, Australia): Pt. 1. U/Pb Zircon Ages, Whole-Rock and Mineral Chemistry, and O–Sr–Nd Isotope Compositions of the Intrusion, with Constraints on Petrogenesis: Economic Geology, v. 106, no. 4, p. 527–556.

Sen, A, Kirkland, CL, Wingate, MTD and Smithies, RH 2010a, 191751: migmatitic granite, Red Rock; Geochronology Record 918: Geological Survey of Western Australia, 4p.

Sen, A, Kirkland, CL, Wingate, MTD and Smithies, RH 2010b, 191763: granitic pegmatite dyke, Minnie Hill; Geochronology Record 919: Geological Survey of Western Australia, 4p.

Singer, DA and Kouda, R 1999, A comparison of the weights-of-evidence method and probabilistic neural networks: Natural Resources Research, v. 8, no. 4, p. 287–298.

Skirrow, RG and Walshe, JL 2002, Reduced and oxidized Au–Cu–Bi–iron oxide deposits of the Tennant Creek Inlier, Australia: Economic Geology, v. 97, p. 1167–1202.

Smithies, RH, Evins, PM and Howard, HM 2008, Myths and mylonites — some new perspectives on the Proterozoic evolution of the west Musgrave Complex, *in* GSWA 2008 extended abstracts: promoting the prospectivity of Western Australia: Geological Survey of Western Australia, Record 2008/2, p. 10–12.

Smithies, RH, Howard, HM, Evins, PM, Kirkland, CL, Kelsey, DE, Hand, M, Wingate, MTD, Collins, AS and Belousova, E 2011, High-temperature granite magmatism, crust–mantle interaction and the Mesoproterozoic intracontinental evolution of the Musgrave Province, Central Australia: Journal of Petrology, v. 52, no. 5, p. 931–958.

Smithies, RH, Howard, HM, Evins, PM, Kirkland, CL, Kelsey, DE, Hand, M, Wingate, MTD, Collins, AS, Belousova, E and Allchurch, S 2010, Geochemistry, geochronology, and petrogenesis of Mesoproterozoic felsic rocks in the west Musgrave Province, Central Australia, and implications for the Mesoproterozoic tectonic evolution of the region: Geological Survey of Western Australia, Report 106, 73p.

Smithies, RH, Howard, HM, Evins, PM, Kirkland, CL and Wingate, MTD 2009, New insights into the geological evolution of the west Musgrave Complex, *in* GSWA 2009 extended abstracts: promoting the prospectivity of Western Australia: Geological Survey of Western Australia, Record 2009/2, p. 19–22.

Soloman, M, Groves, DI and Jaques, AL 1994, The geology and origin of Australia's mineral deposits: Oxford mongraphs on geology and geophysics, v. 24: Oxford University Press, Oxford, UK, 951p.

Sproule, RA, Sutcliffe, H, Tracanelli, C and Lesher, CM 2007, Palaeoproterozoic Ni–Cu–PGE mineralisation in the Shakespeare intrusion, Ontario, Canada: a new style of Nipissing gabbro-hosted mineralisation: Applied Earth Science, v. 116, no. 4, p. 188–200.

Stanley, CR and Madeisky, HE 1994, Lithogeochemical exploration for hydrothermal ore deposits using Pearce element ratio analysis: Geological Association of Canada, Short Course Notes 11, p. 193–212.

Stewart, AJ 1995, Resolution of conflicting structures and deformation history of the Mount Aloysius granulite massif, western Musgrave Block, central Australia: AGSO Journal of Australian Geology and Geophysics, v. 16, p. 91–105.

Sun, S-S and McDonough, WF 1989, Chemical and isotopic systematics of oceanic basalts: implications for mantle composition and processes, *in* Magmatism in the Ocean Basins *edited by* AD Saunders and MJ Norry: Geological Society, London, Special Publication 42, p. 313–345.

Sun, S-S, Sheraton, JW, Glikson, AY and Stewart, AJ 1996, A major magmatic event during 1050–1080 Ma in central Australia, and an emplacement age for the Giles Complex: AGSO Journal of Australian Geology and Geophysics, v. 24, p. 13–15.

Taylor, RG 1979, Geology of tin deposits: Developments in Economic Geology 11: Elsevier, Amsterdam, The Netherlands, 534p.

Thompson, JFH, Stilltoe, RH, Baker, T, Lang, JR and Mortensen, JK 1999, Intrusion-related gold deposits associated with tungsten–tin provinces: Mineralium Deposita, v. 34, no. 4, p. 323–334.

Wade, BP, Barovich, KM and Hand, MP 2005, Geochemistry and provenance of a Mesoproterozoic (1.4 Ga) eastern Musgrave Block basin: buddying up to the Belt-Purcell Basin, *in* Program and abstracts *edited by* MTD Wingate and SA Pisarevsky: Supercontinents and Earth Evolution Symposium, Fremantle, Western Australia, 26 September 2005, p. 43.

Walter, MR, Veevers, JJ, Calver, CR and Grey, K 1995, Neoproterozoic stratigraphy of the Centralian Superbasin, Australia: Precambrian Research, v. 73, no. 1–4, p. 173–195.

Williams, PJ, Barton, MD, Johnson, DA, Fontbot, L, de Haller, A, Mark, G, Oliver, NHS and Marschik, R 2005, Iron oxide copper–gold deposits: Geology, space-time distribution, and possible modes of origin: Economic Geology, v. 100, no. 2 (100th Anniversary Volume), p. 371–405.

Wingate, MTD, Pirajno, F and Morris, PA 2004, Warakurna large igneous province: a new Mesoproterozoic large igneous province in west-central Australia: Geology, v. 32, no. 2, p. 105–108.

Wood, SA and Samson, IM 2000, The hydrothermal geochemistry of tungsten in granitoid environments: I. Relative solubilities of ferberite and scheelite as a function of T, P, pH and mNaCl: Economic Geology, v. 95, p. 143–182.

Wyborn, LAI, Heinrich, CA and Jaques, AL 1994, Australian Proterozoic mineral systems: essential ingredients and mappable criteria, *in* Australian mining looks north — the challenges and choices *edited by* PC Hallenstein: Australian Institute of Mining and Metallurgy; 1994 AusIMM Annual Conference, Darwin, Northern Territory, 5 August 1994, p. 109–115.

Zimmermann, HJ and Zysno, P 1980, Latent connectives in human decision making: Fuzzy Sets and Systems, v. 4, no. 1, p. 37–51.

Appendix

Predictor maps for source and physical and chemical traps, used to generate maps of mineral prospectivity in the west Musgrave Province

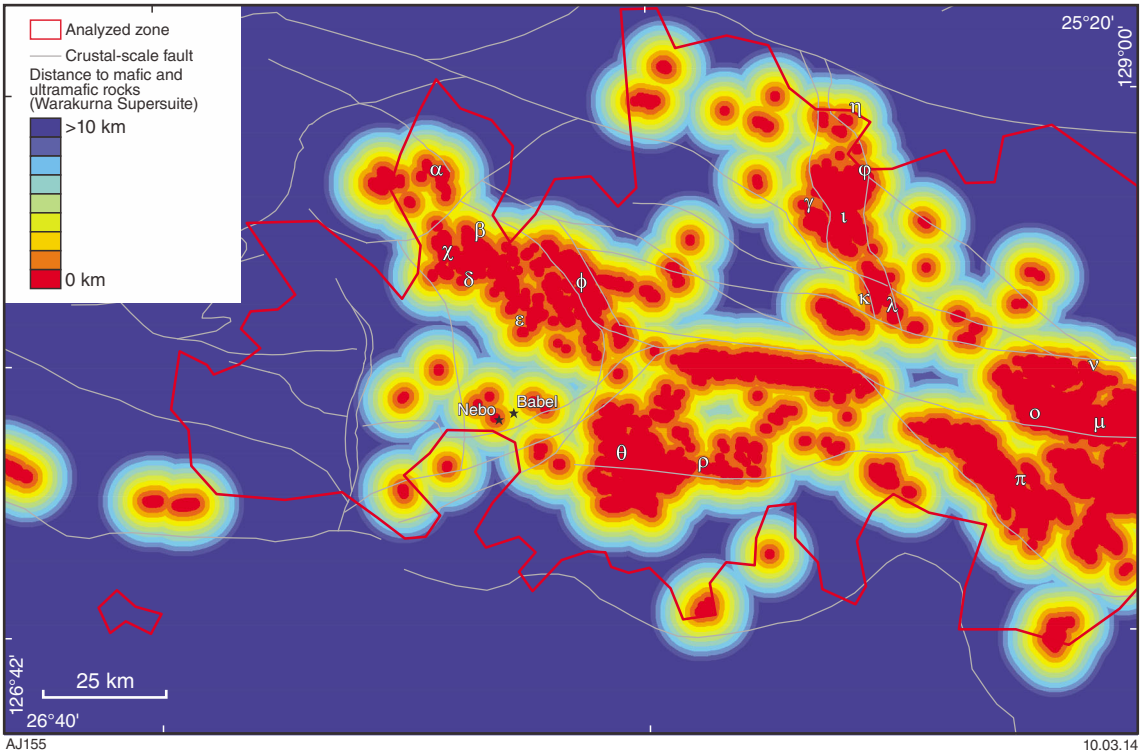

Figure A1. **Predictor map for Ni–Cu and PGE source: proximity to mafic and ultramafic rocks – Warakurna Supersuite (up to 10 km). Greek letters correspond to the Ni–Cu prospective zones (Fig.15).**

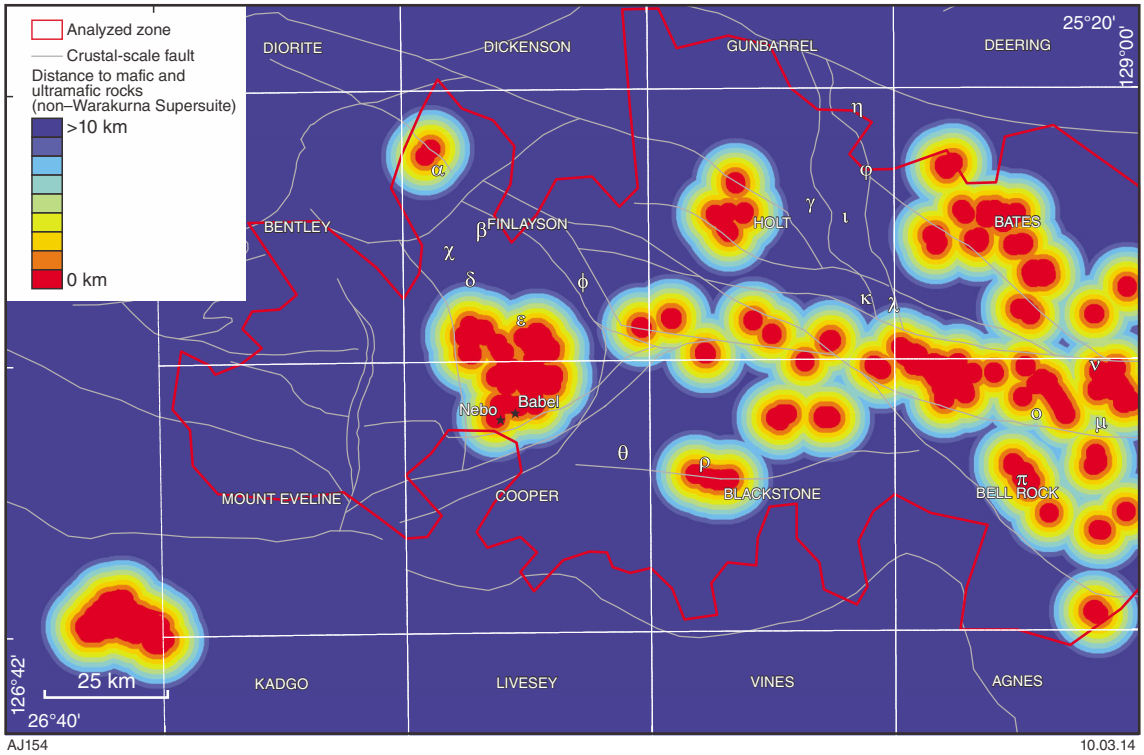

Figure A2. **Predictor map for Ni–Cu and PGE source: proximity to mafic and ultramafic rocks – non-Warakurna Supersuite (up to 10 km). Greek letters correspond to the Ni–Cu prospective zones (Fig.15).**

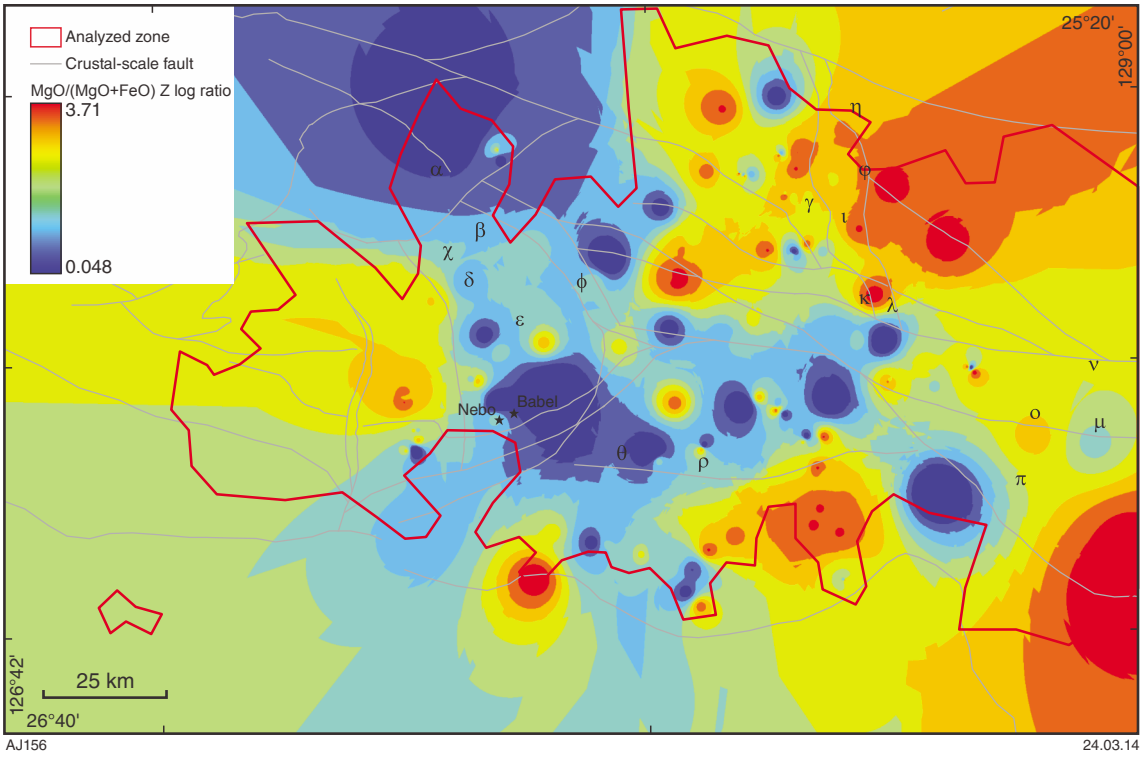

Figure A3. **Predictor map for Ni–Cu and PGE source: MgO/(MgO+FeO) ratio. Greek letters correspond to the Ni–Cu prospective zones (Fig.15).**

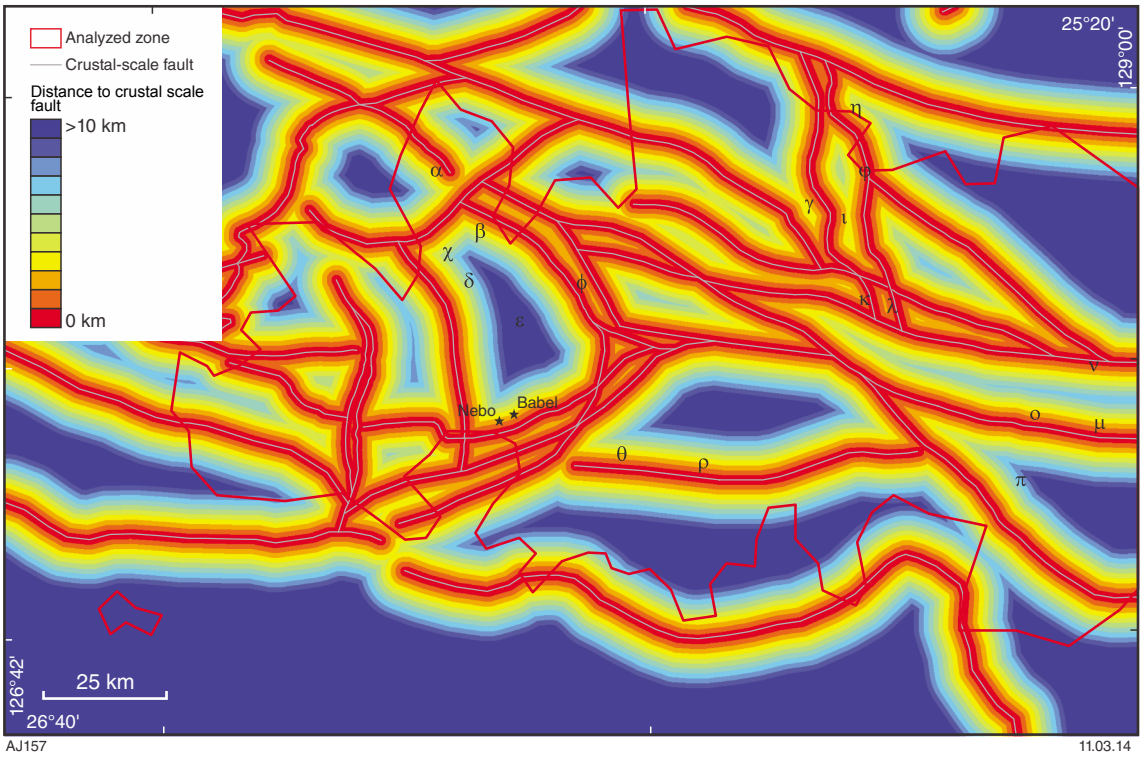

Figure A4. **Predictor map for Ni–Cu, PGE, orogenic and intrusion-related gold, IOCG and Sn–W pathway: proximity to crustal-scale faults with 10 km buffer zone. Greek letters correspond to the Ni–Cu prospective zones (Fig.15).**

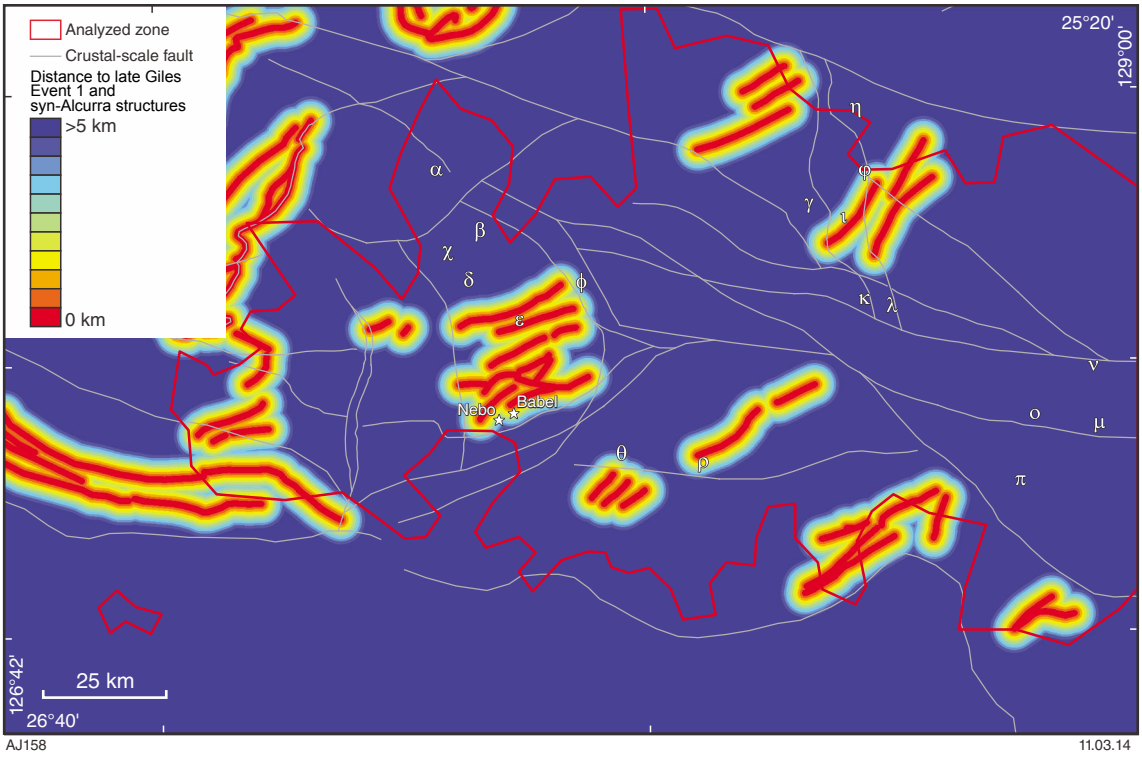

Figure A5. **Predictor map for Ni–Cu pathway: proximity to LGE1 faults with 5 km buffer zone. Greek letters correspond to the Ni–Cu prospective zones (Fig.15).**

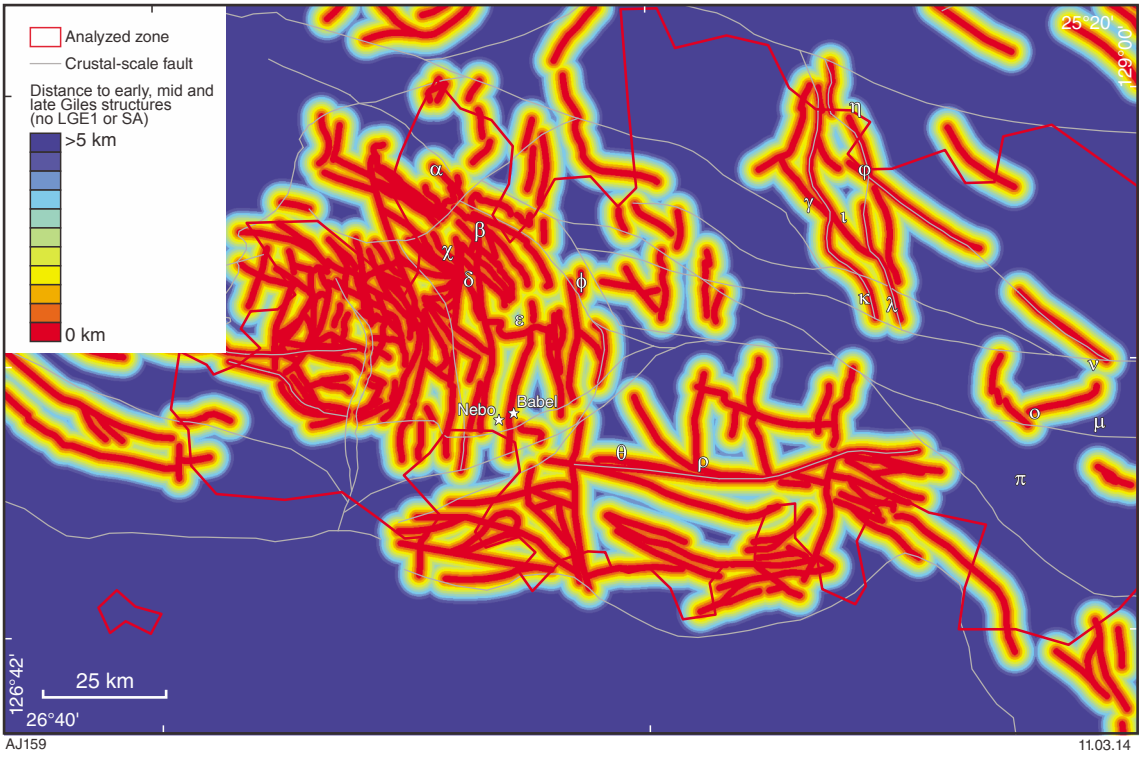

Figure A6. **Predictor map for Ni–Cu pathway: proximity to early (EGE), middle (MGE) and late Giles (LGE) faults (except for LGE1) with 5 km buffer zone. Greek letters correspond to the Ni–Cu prospective zones (Fig.15).**

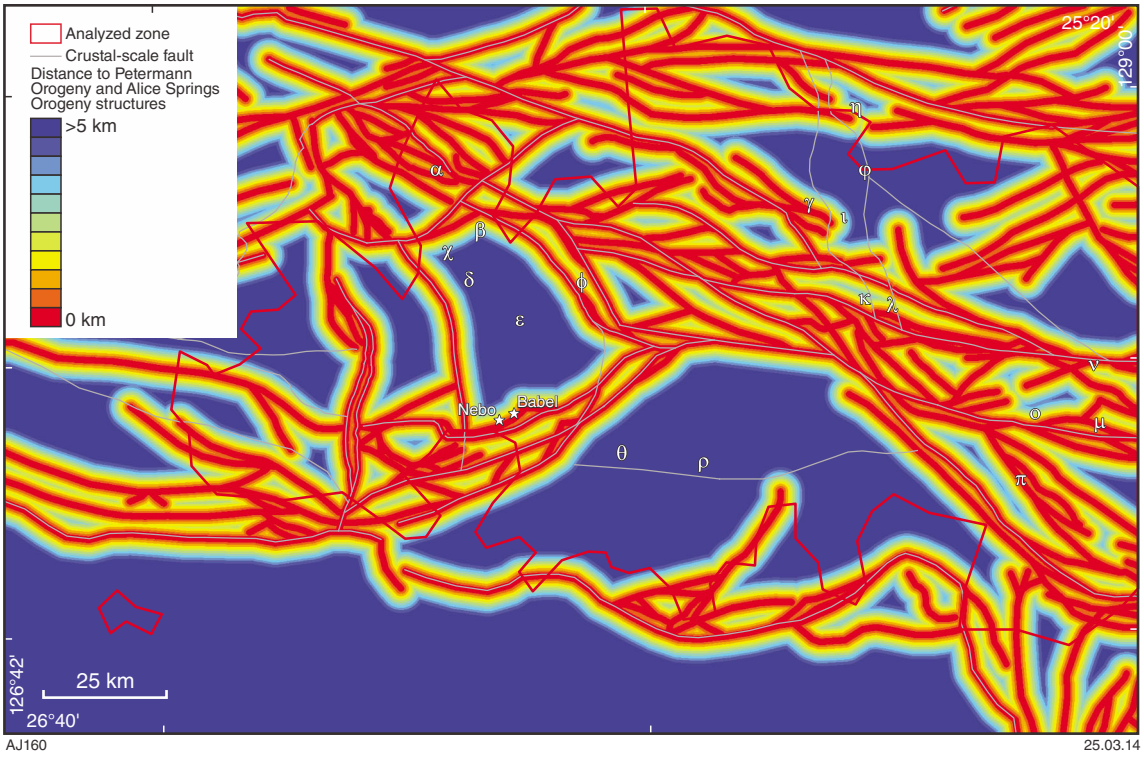

Figure A7. **Predictor map for Ni–Cu, PGE, orogenic and intrusion-related gold, IOCG and Sn–W pathway: proximity to Petermann Orogeny (PO) and Alice Springs Orogeny (ASO) structures with 5 km buffer zone. Greek letters correspond to the Ni–Cu prospective zones (Fig.15).**

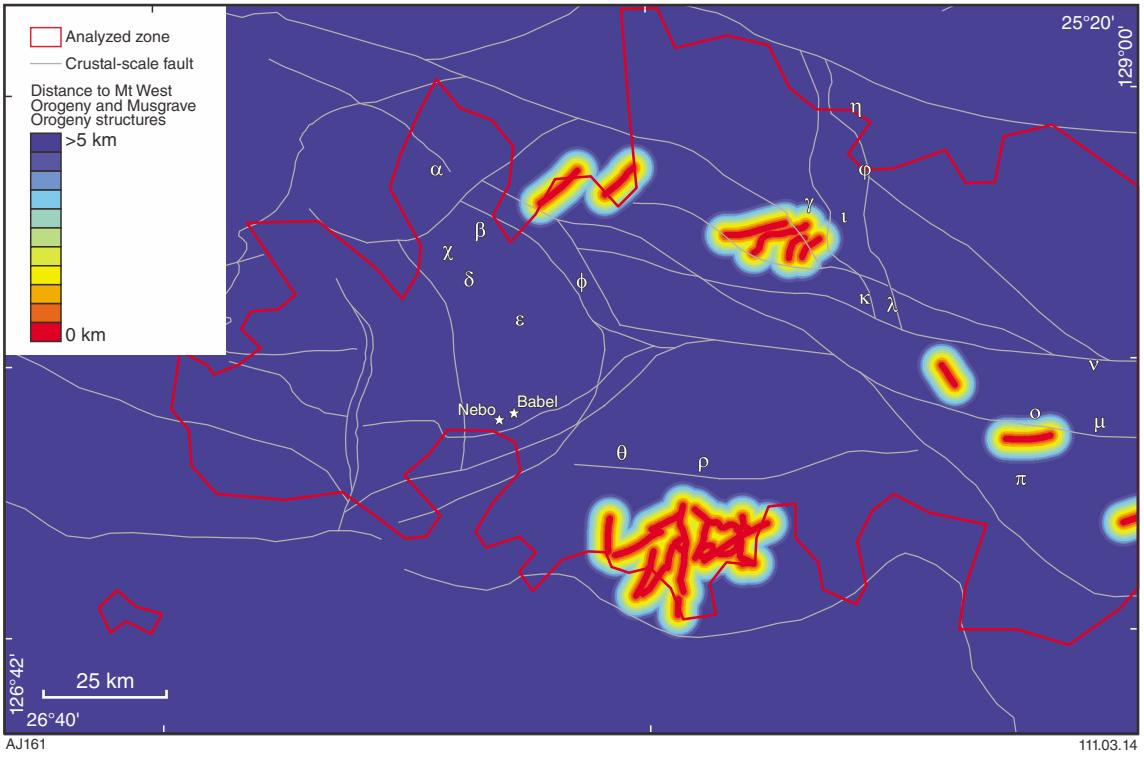

Figure A8. **Predictor map for Ni–Cu, PGE, orogenic and intrusion-related gold, IOCG and Sn–W pathway: proximity to Mount West Orogeny (MWO) and Musgrave Orogeny (MO) structures with 5 km buffer zone. Greek letters correspond to the Ni–Cu prospective zones (Fig.15).**

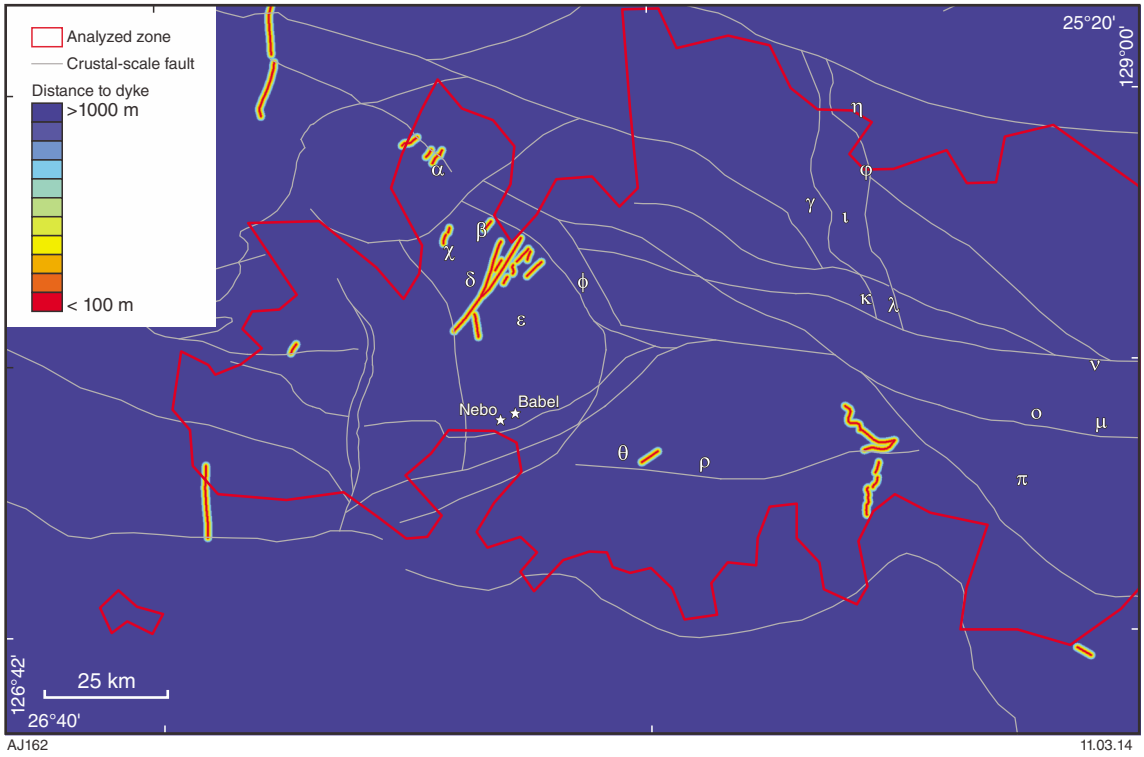

Figure A9. **Predictor map for Ni–Cu and PGE pathway and for orogenic and intrusion-related gold, IOCG, Sn–W and surficial uranium chemical scrubbers: distance to dyke with a 1000 m buffer zone. Greek letters correspond to the Ni–Cu prospective zones (Fig.15).**

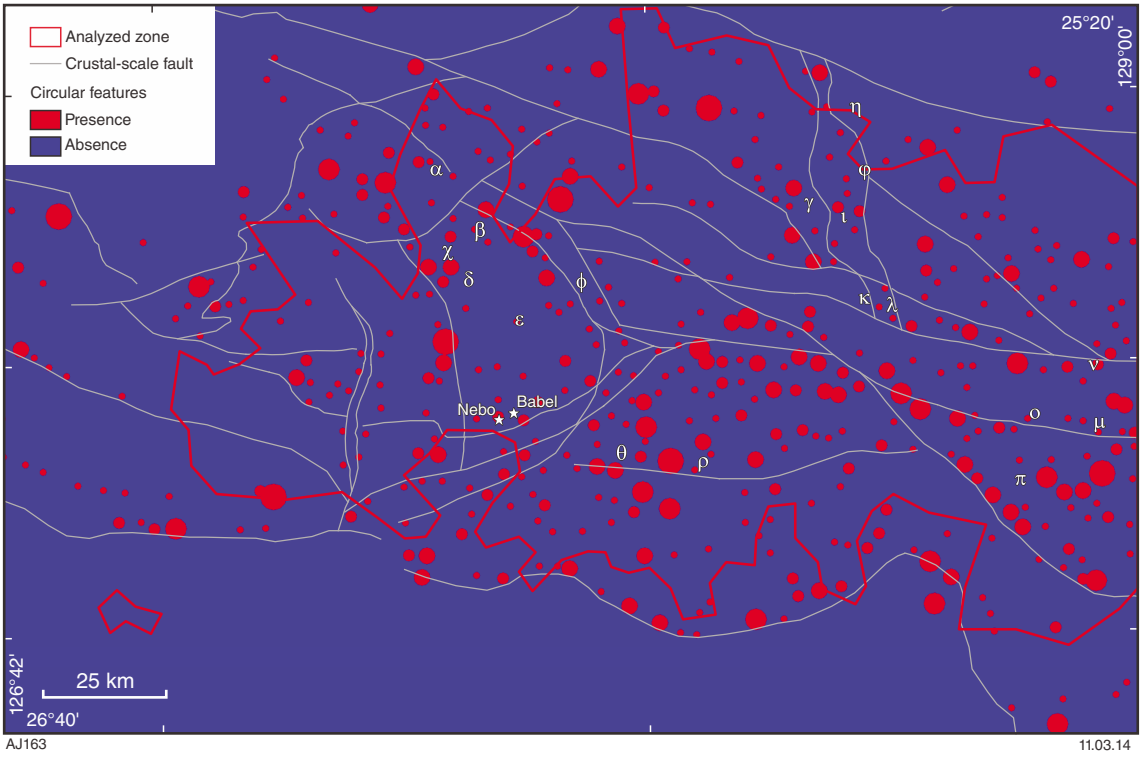

Figure A10. **Predictor map for Ni–Cu and PGE pathway (as chonoliths) and for IOCG physical throttle (as porphyry): circular features. Greek letters correspond to the Ni–Cu prospective zones (Fig.15).**

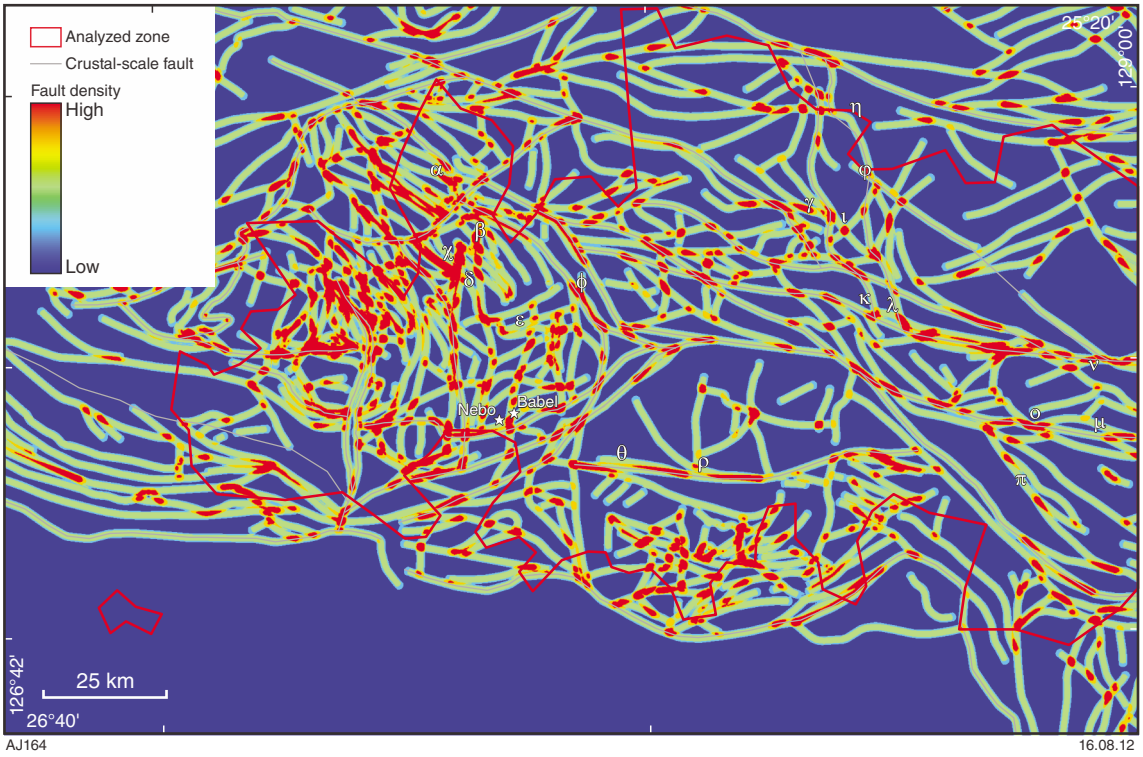

Figure A11. **Predictor map for Ni–Cu, PGE, orogenic and intrusion-related gold and IOCG physical trap: fault density. Red indicates areas with the most numerous faults; blue corresponds to the contrary. Greek letters correspond to the Ni–Cu prospective zones (Fig.15).**

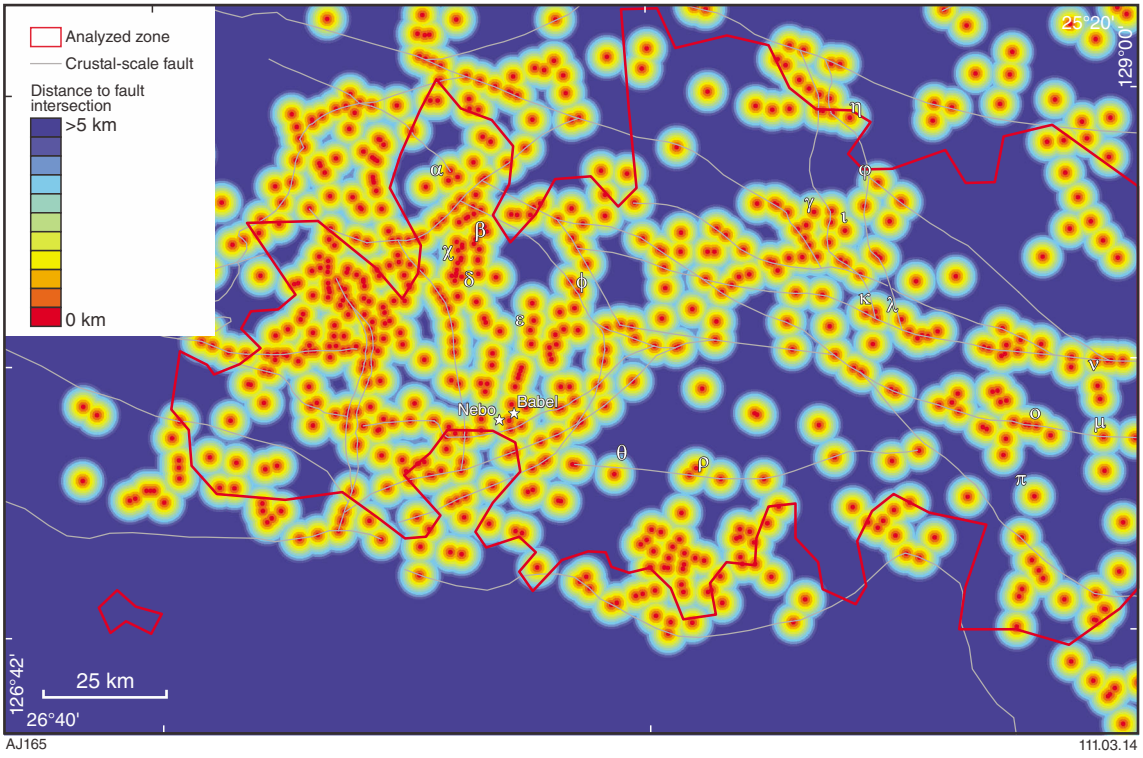

Figure A12. **Predictor map for Ni–Cu, PGE, orogenic and intrusion-related gold and IOCG physical trap: proximity to fault intersections with a 5 km buffer zone. Greek letters correspond to the Ni–Cu prospective zones (Fig.15).**

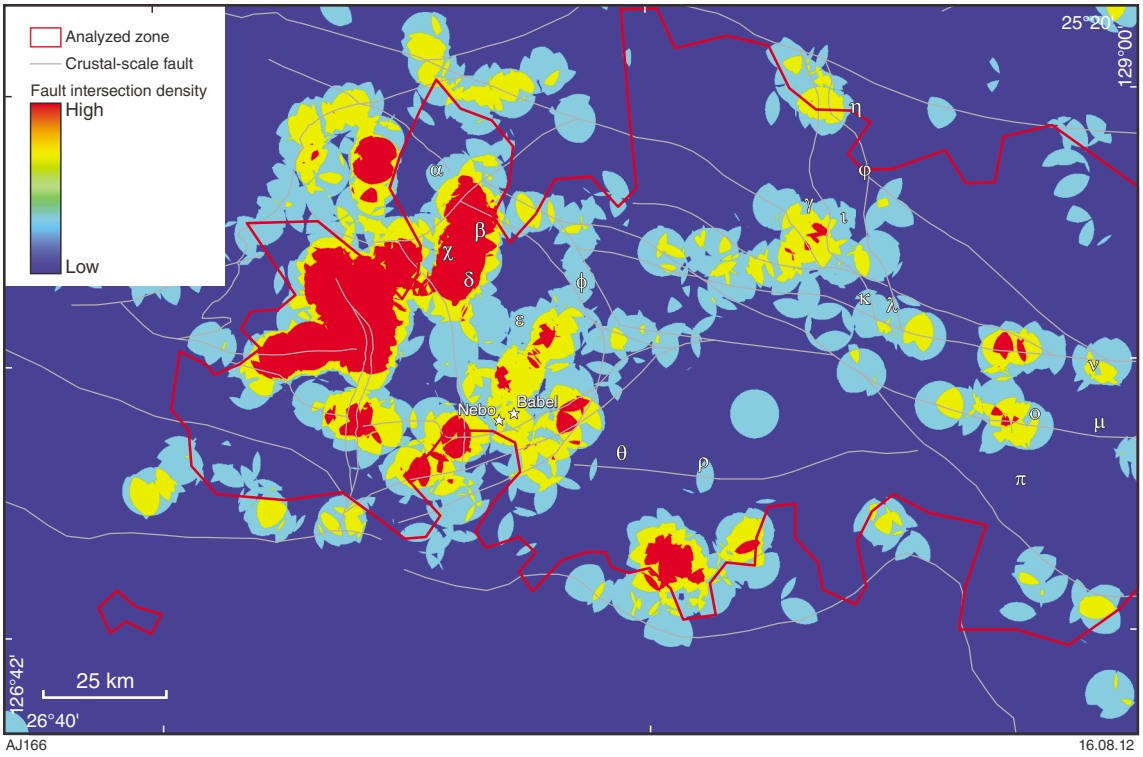

Figure A13. Predictor map for Ni–Cu, PGE, orogenic and intrusion-related gold and IOCG physical trap: fault intersection density. Red indicates areas of high fault intersection density; blue corresponds to areas of lower fault intersection density. Greek letters correspond to the Ni–Cu prospective zones (Fig.15).

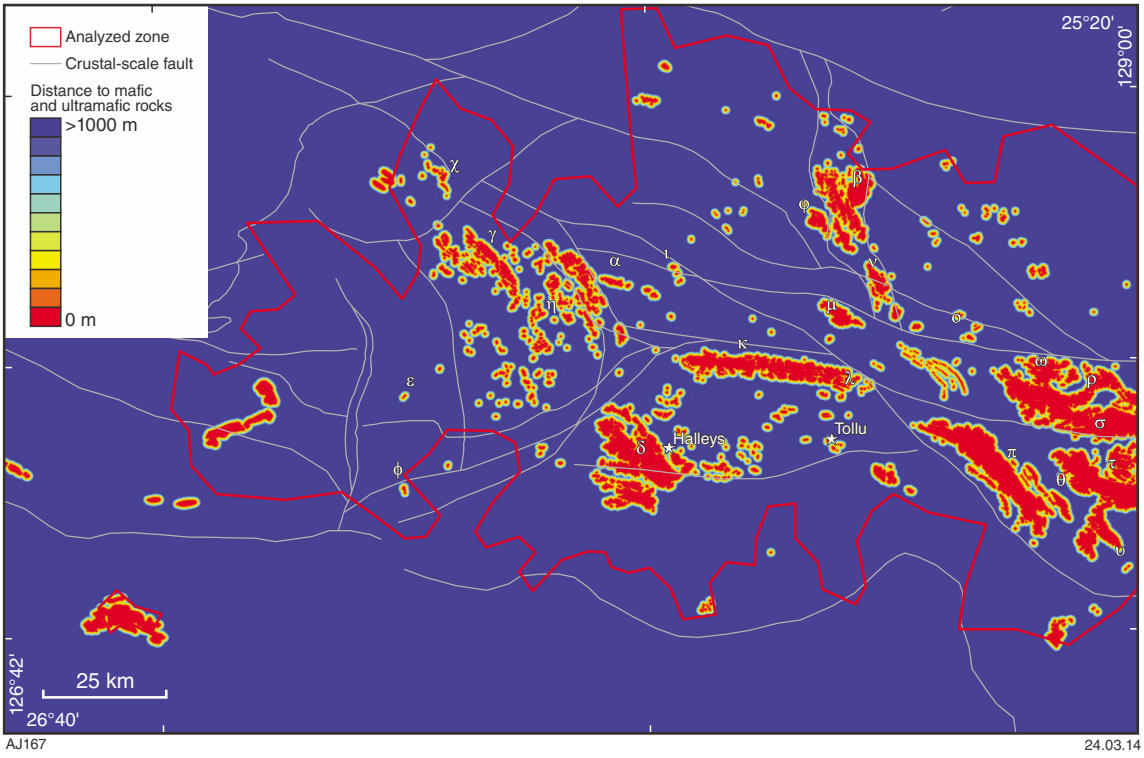

Figure A14. Predictor map for Ni–Cu, PGE, Sn–W chemical trap: distance to mafic and ultramafic rocks. Greek letters correspond to the PGE prospective zones (Fig.18).

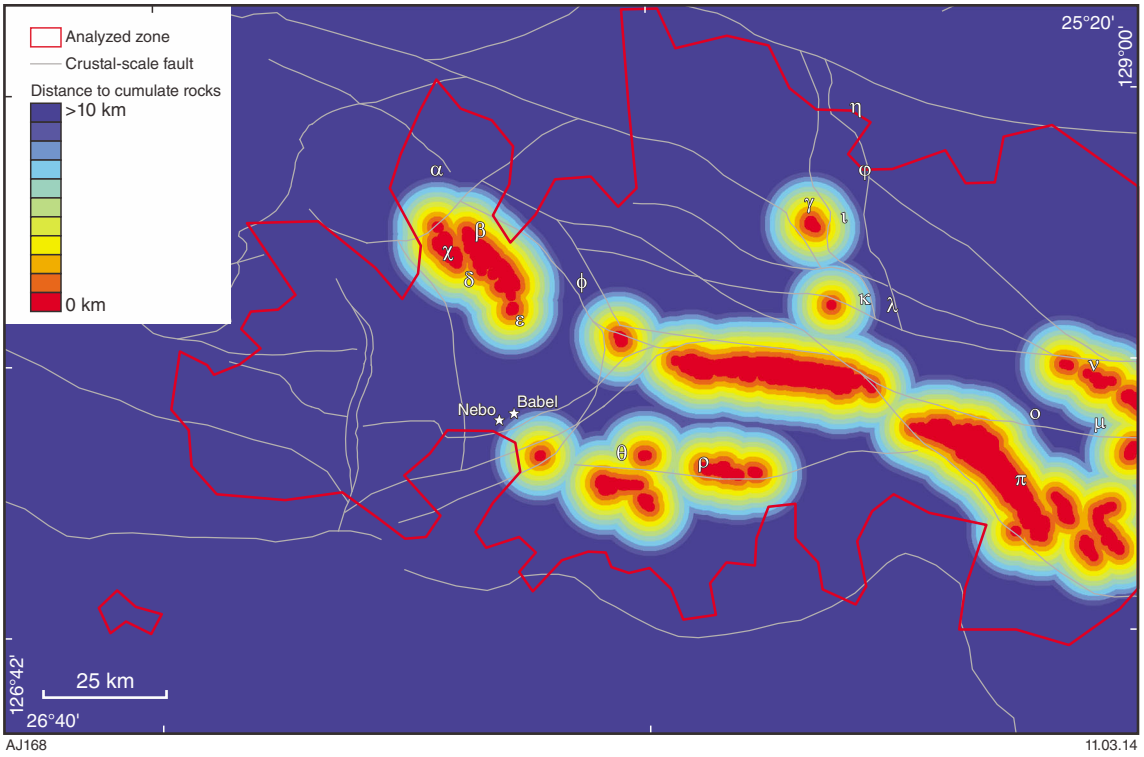

Figure A15. **Predictor map for Ni–Cu and PGE chemical trap: distance to cumulate rocks (chromitite, peridotite and early Giles ultramafics) with a 10 km buffer zone. Greek letters correspond to the Ni–Cu prospective zones (Fig.15).**

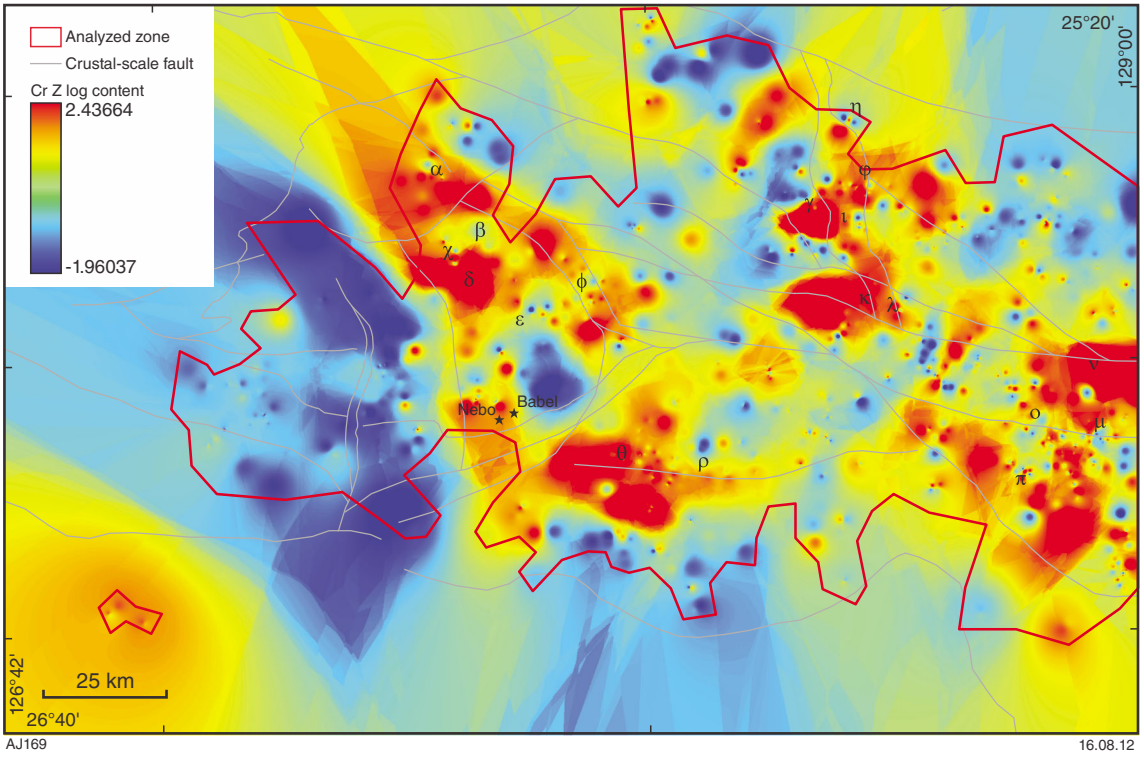

Figure A16. **Predictor map for Ni–Cu and PGE chemical trap: Cr content (Z value, cf. text for explanation). Greek letters correspond to the Ni–Cu prospective zones (Fig.15).**

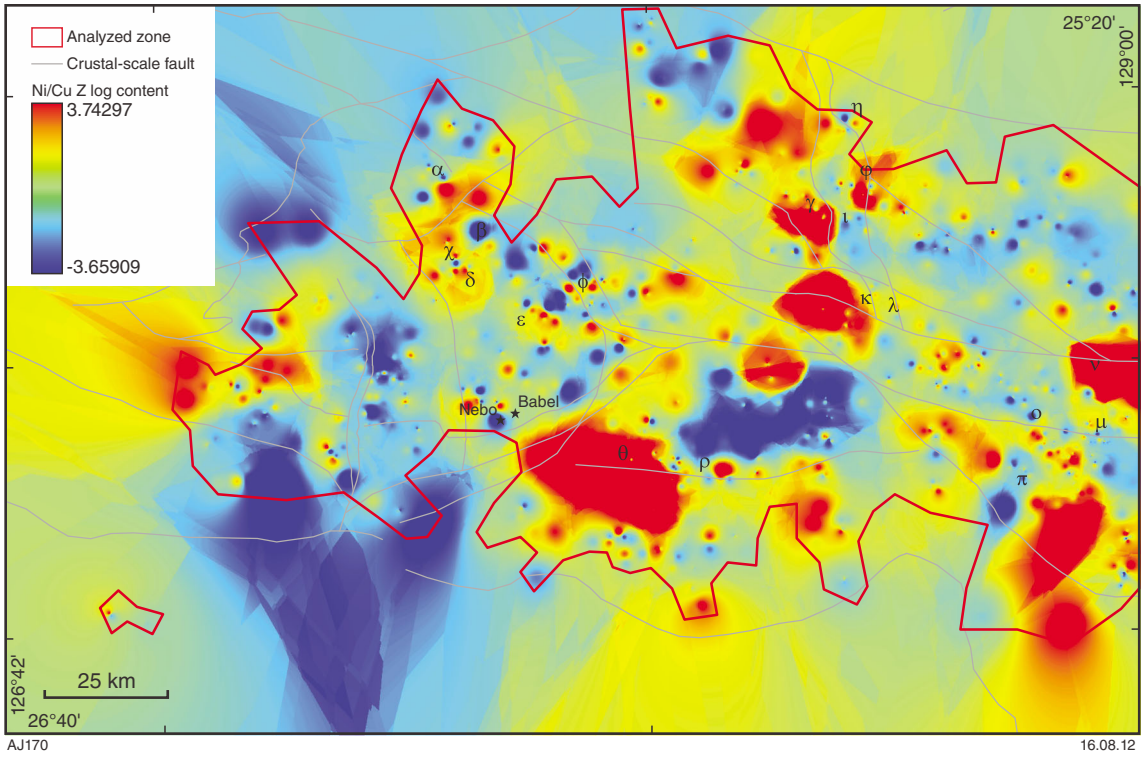

Figure A17. Predictor map for Ni–Cu chemical trap: Ni/Cu ratio (Z value, cf. text for explanation). Greek letters correspond to the Ni–Cu prospective zones (Fig.15).

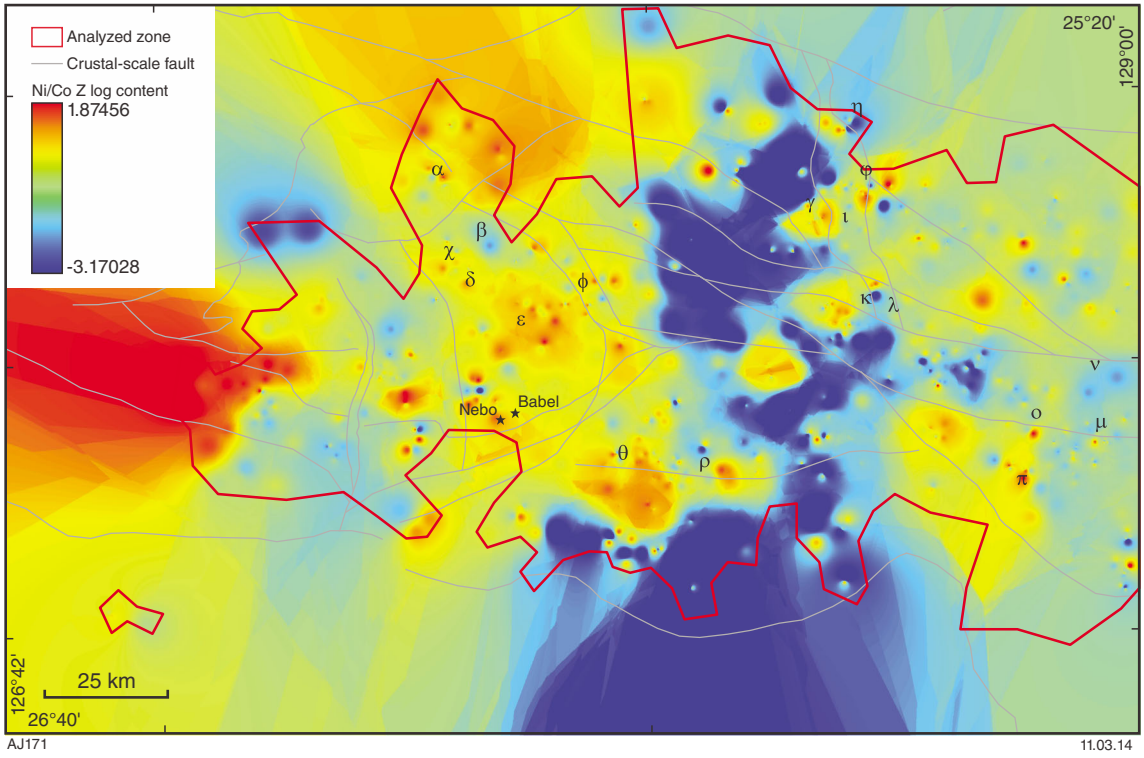

Figure A18. Predictor map for Ni–Co chemical trap: Ni/Co ratio (Z value, cf. text for explanation). Greek letters correspond to the Ni–Cu prospective zones (Fig. 15).

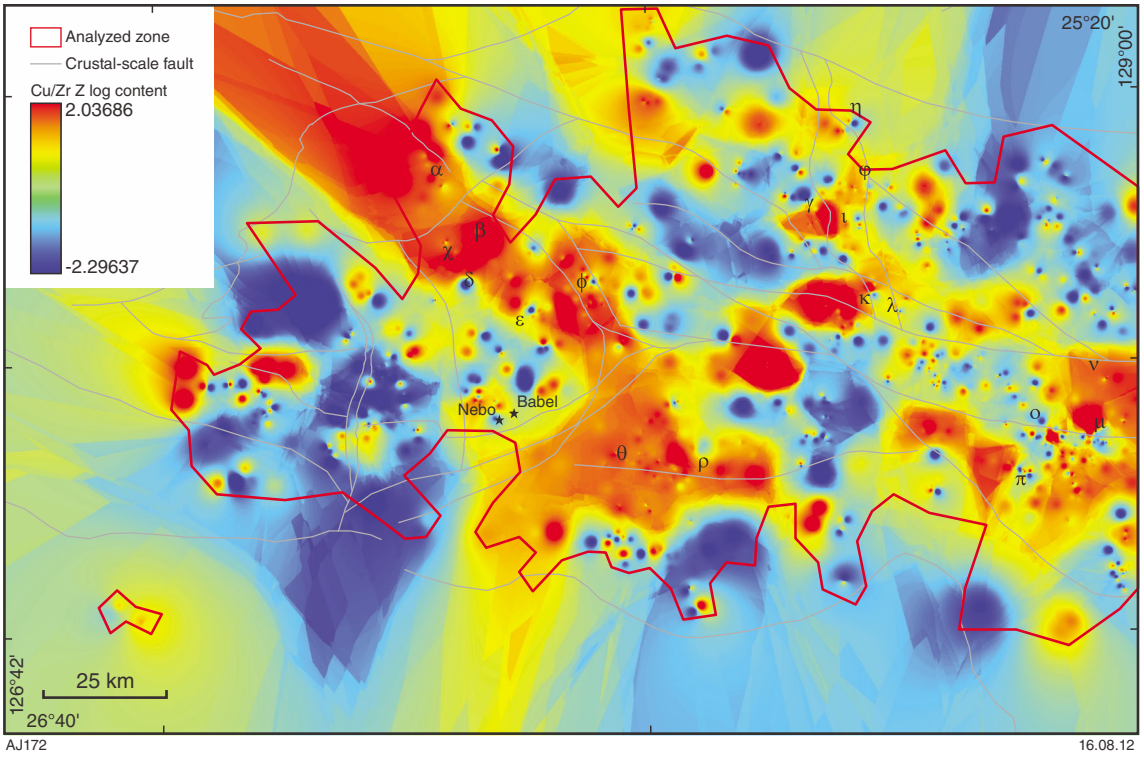

Figure A19. **Predictor map for Ni–Cu chemical trap: Cu/Zr ratio (Z value, cf. text for explanation). Greek letters correspond to the Ni–Cu prospective zones (Fig. 15).**

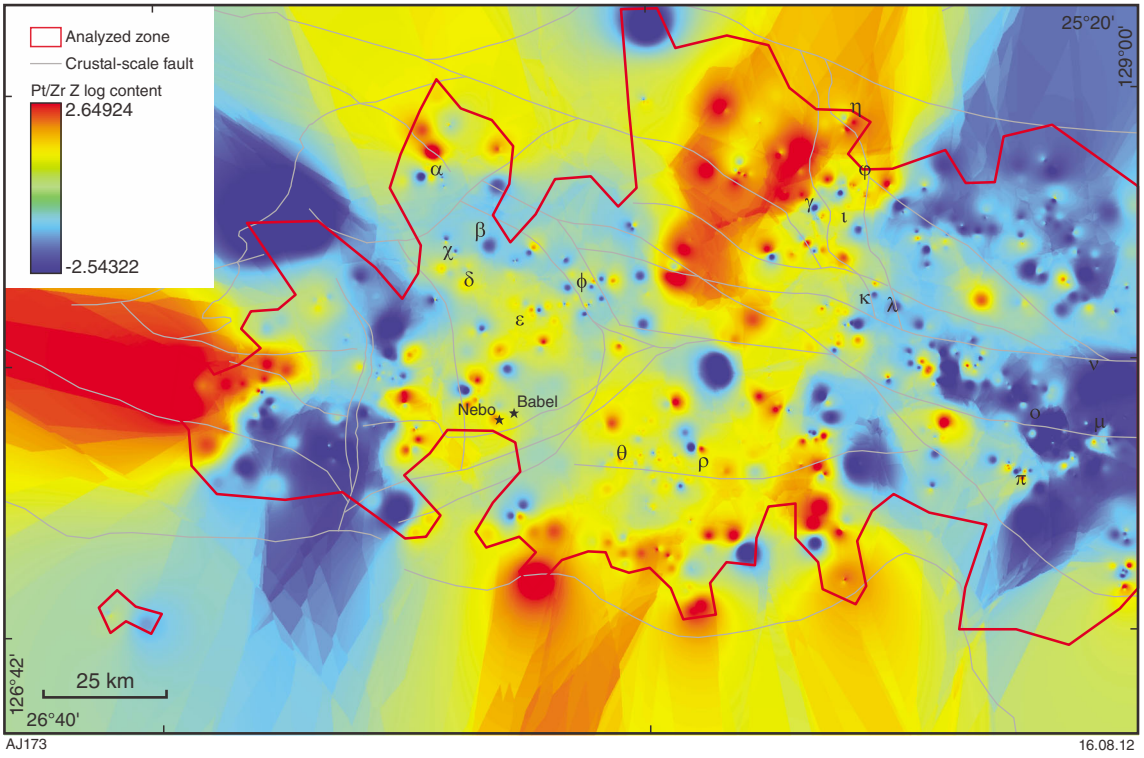

Figure A20. **Predictor map for Ni–Cu chemical trap: Pt/Zr ratio (Z value, cf. text for explanation). Greek letters correspond to the Ni–Cu prospective zones (Fig. 15).**

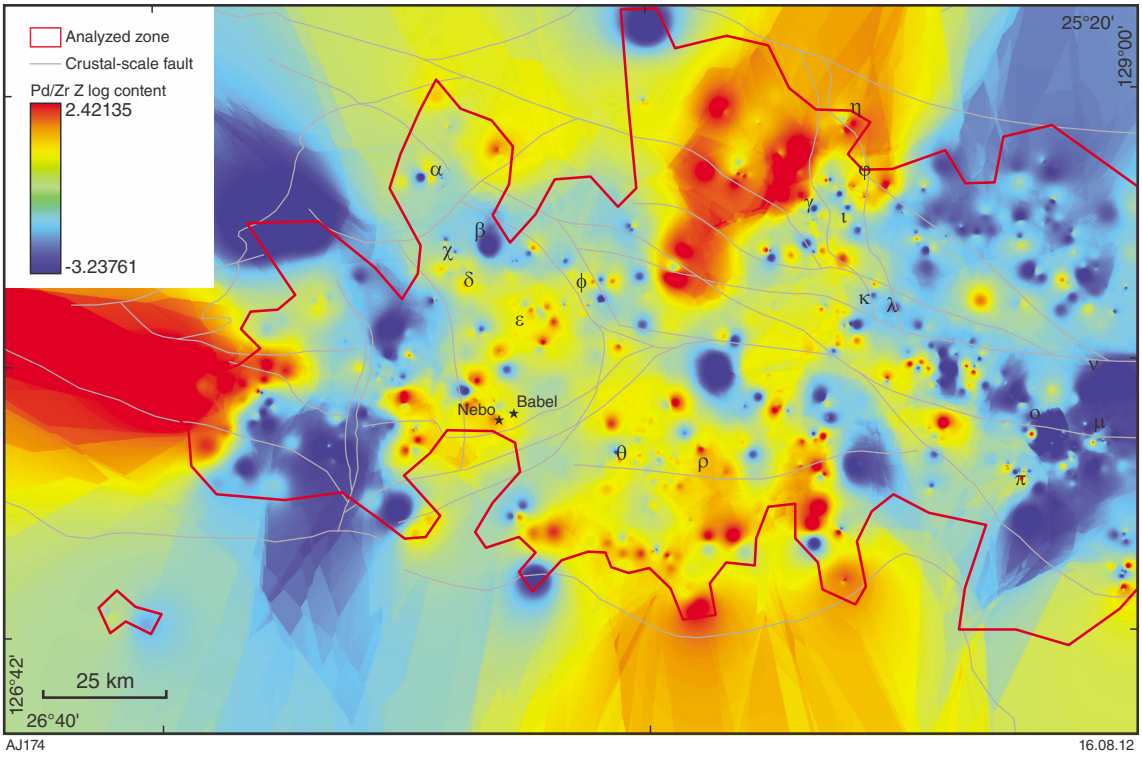

Figure A21. Predictor map for Ni–Cu chemical trap: Pd/Zr ratio (Z value, cf. text for explanation Greek letters correspond to the Ni–Cu prospective zones (Fig. 15).

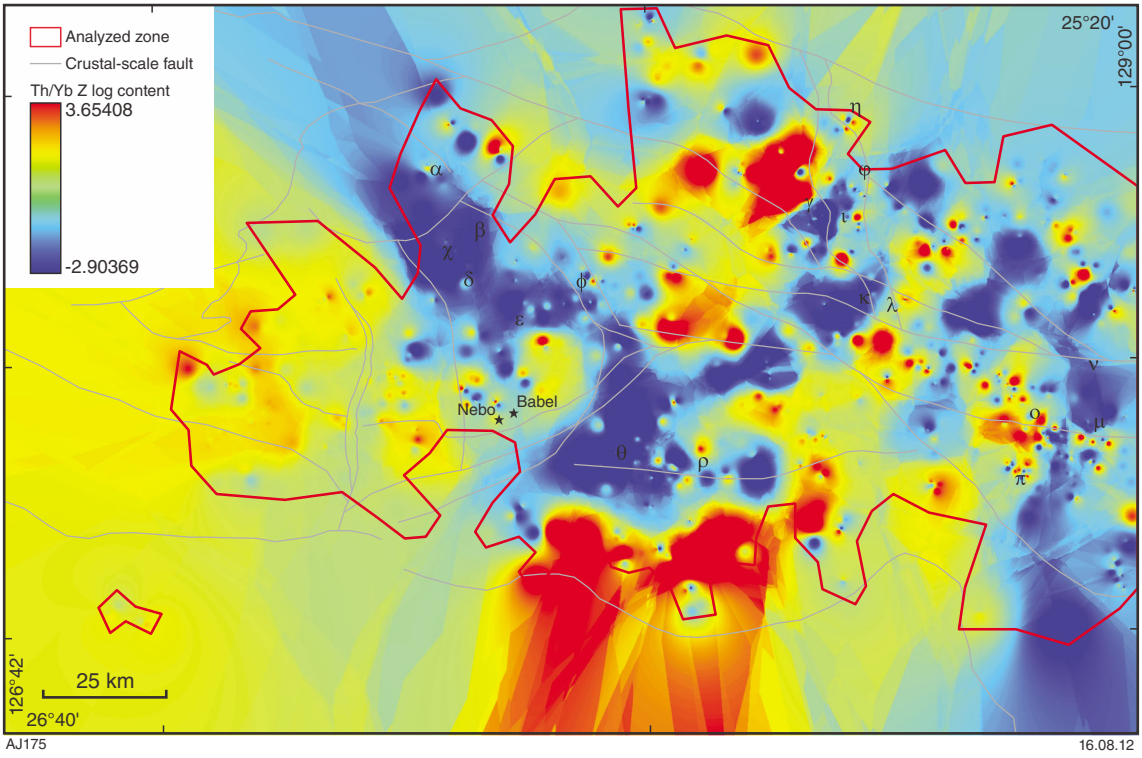

Figure A22. Predictor map for Ni–Cu chemical trap:Th/Yb ratio (Z value, cf. text for explanation). Greek letters correspond to the Ni–Cu prospective zones (Fig. 15).

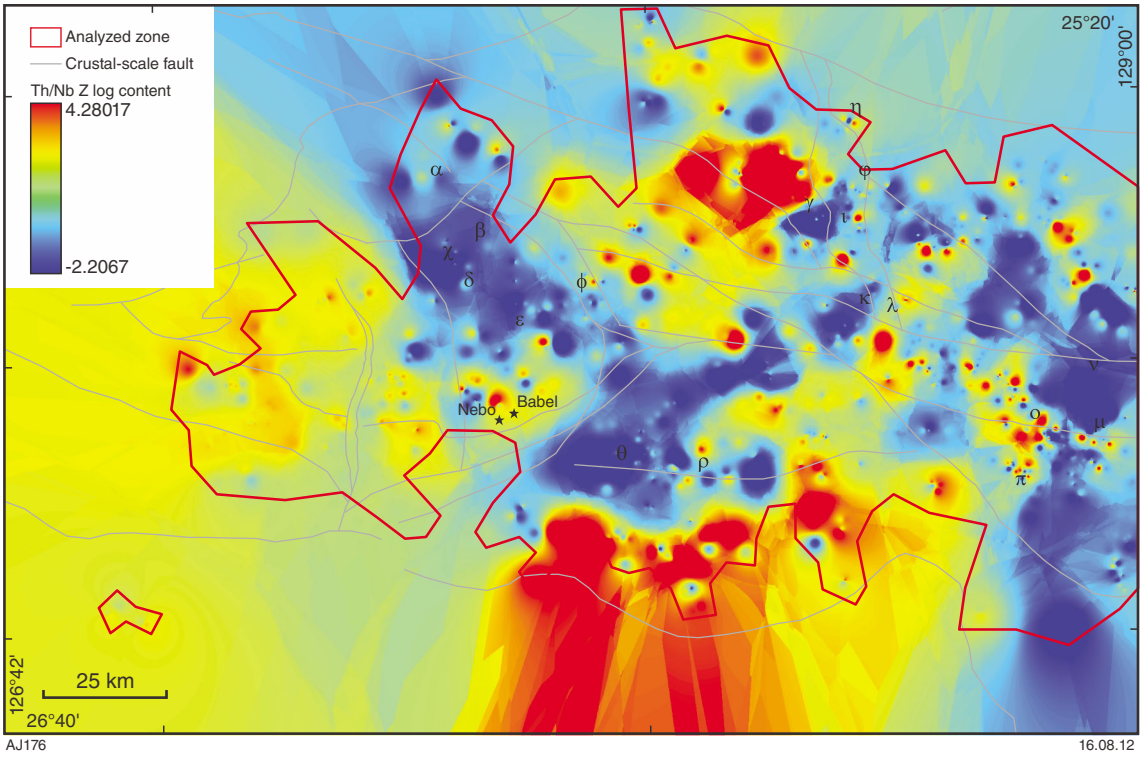

Figure A23. **Predictor map for Ni–Cu chemical trap: Th/Nb ratio (Z value, cf. text for explanation). Greek letters correspond to the Ni–Cu prospective zones (Fig. 15).**

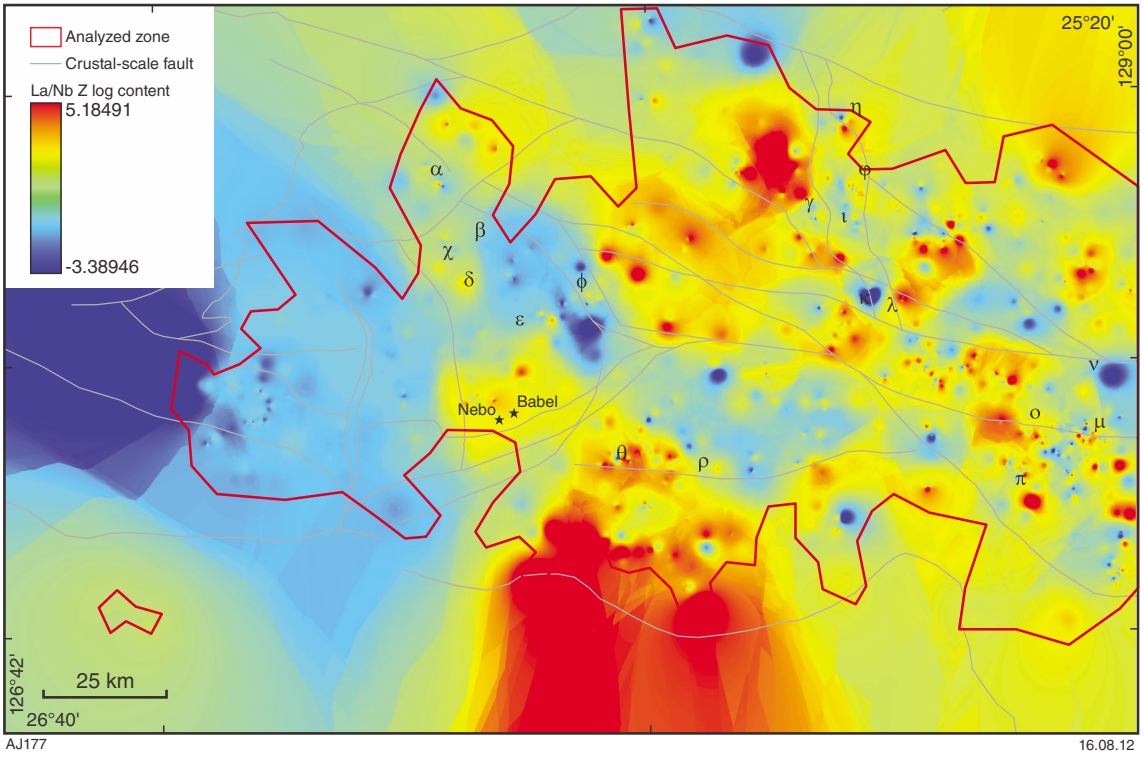

Figure A24. **Predictor map for Ni–Cu chemical trap: La/Nb ratio (Z value, cf. text for explanation). Greek letters correspond to the Ni–Cu prospective zones (Fig. 15).**

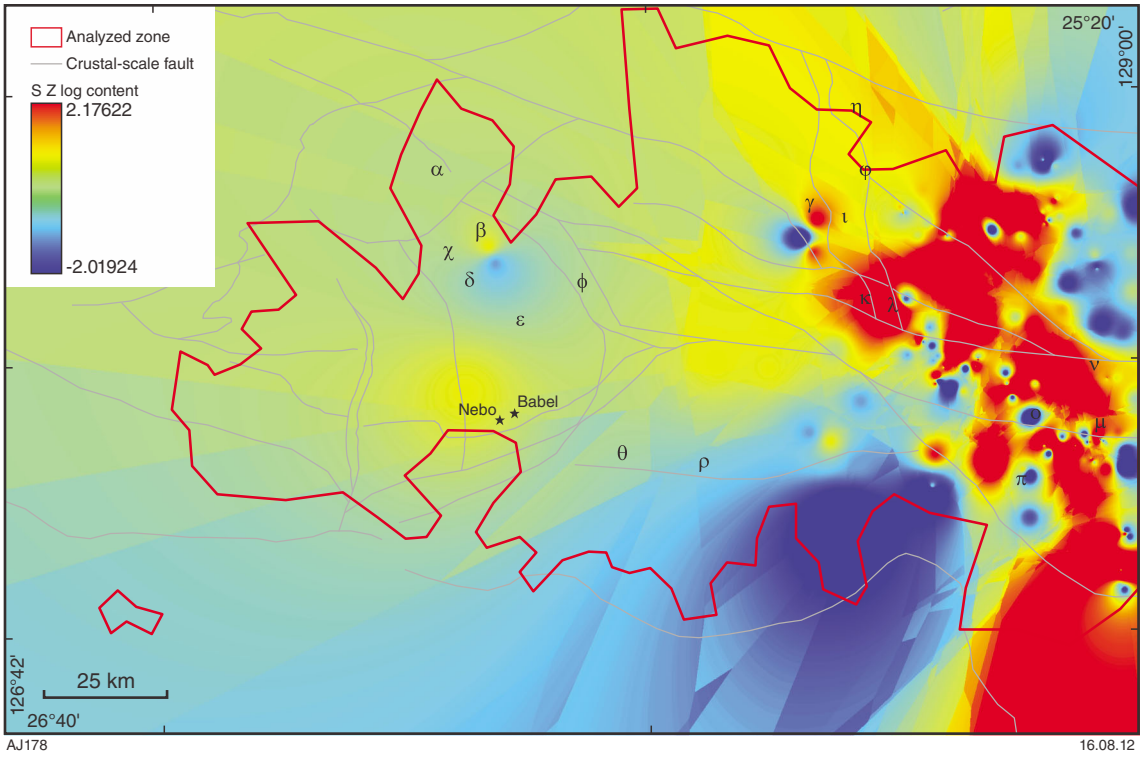

Figure A25. Predictor map for Ni–Cu chemical trap: S content (Z value, cf. text for explanation). Greek letters correspond to the Ni–Cu prospective zones (Fig. 15).

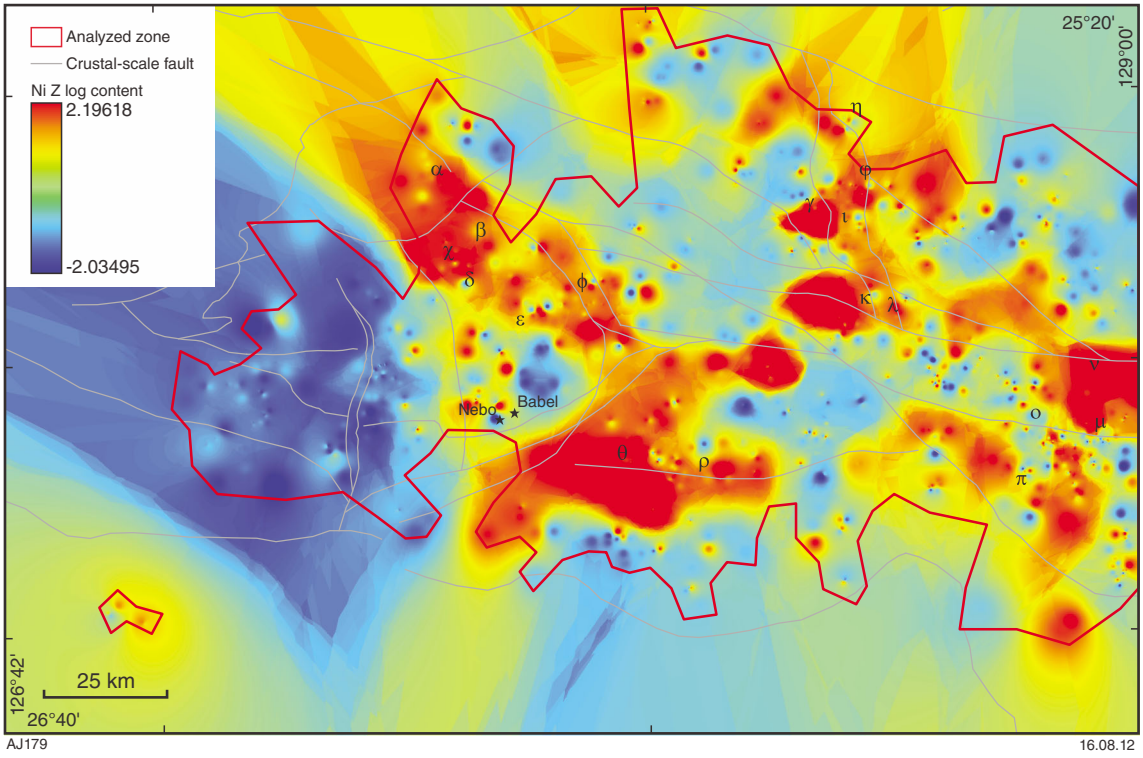

Figure A26. Predictor map for Ni–Cu and PGE chemical trap: Ni content (Z value, cf. text for explanation). Greek letters correspond to the Ni–Cu prospective zones (Fig. 15).

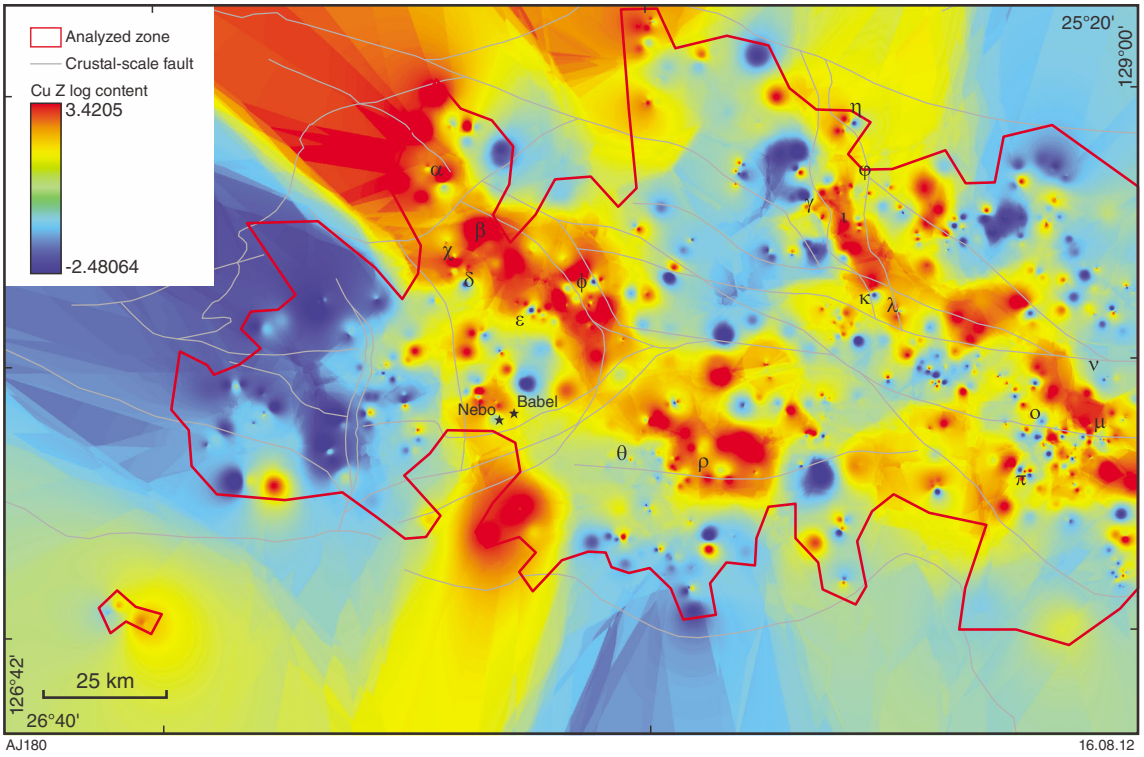

Figure A27. **Predictor map for Ni–Cu, PGE and IOCG chemical trap: Cu content (Z value, cf. text for explanation). Greek letters correspond to the Ni–Cu prospective zones (Fig. 15).**

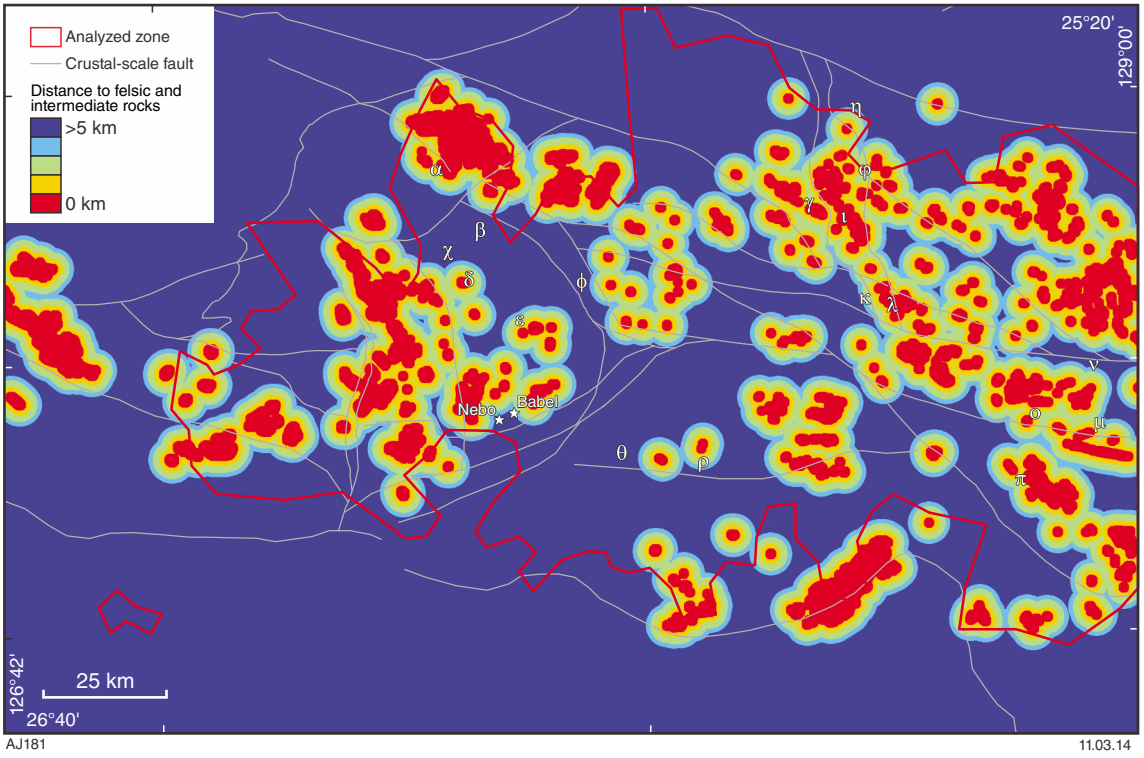

Figure A28. **Predictor map for Ni–Cu chemical trap: distance to felsic rocks with a 5 km buffer zone . Greek letters correspond to the Ni–Cu prospective zones (Fig. 15).**

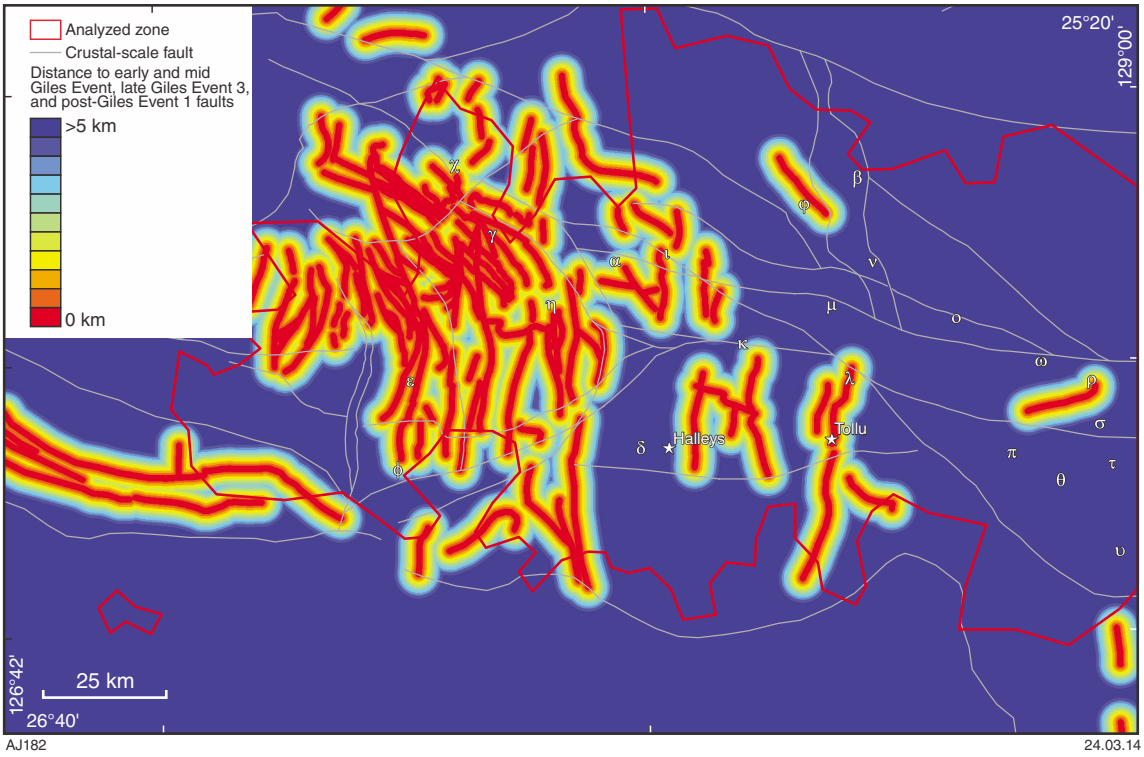

Figure A29. Predictor map for PGE pathway: proximity to early Giles 1, mid-Giles (syn-Giles 1), late Giles 3 and post-Giles 1 Event structures with 5 km buffer zone. Greek letters correspond to the PGE prospective zones (Fig. 18).

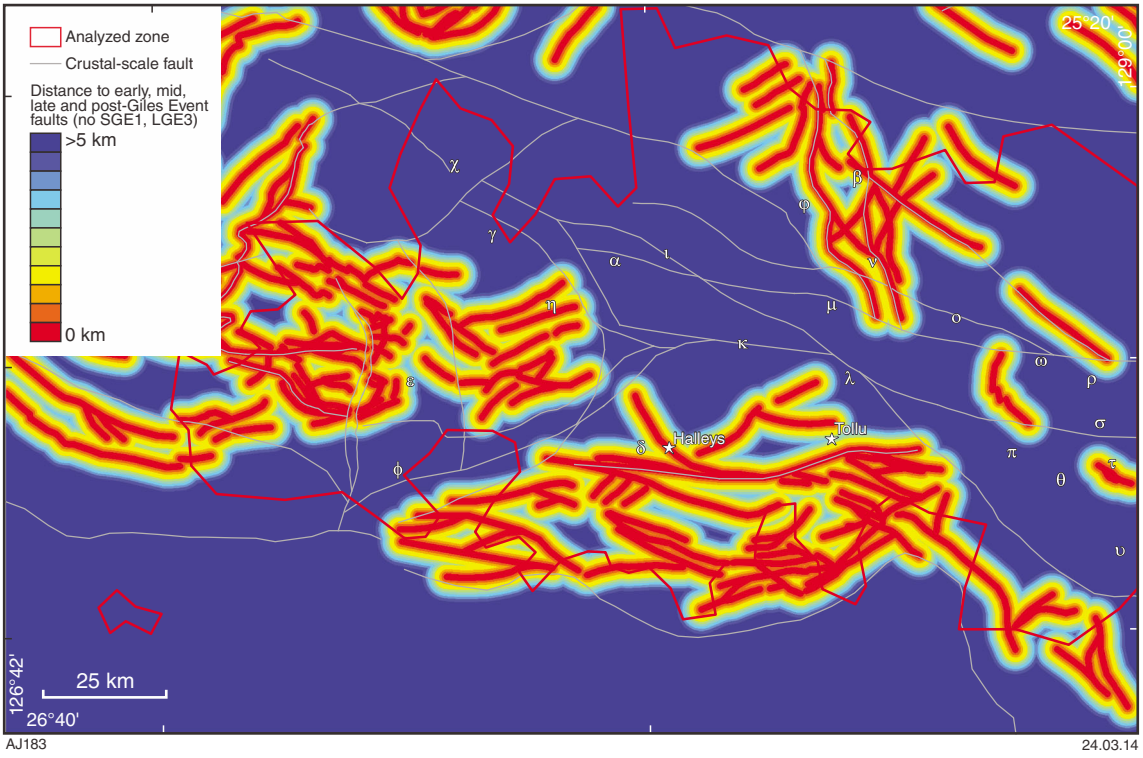

Figure A30. Predictor map for PGE pathway: proximity to early Giles 2, mid-Giles (other than syn-Giles 1) and late Giles Event structures (other than Late Giles 3 and post-Giles 1) with 5 km buffer zone. Greek letters correspond to the PGE prospective zones (Fig. 18).

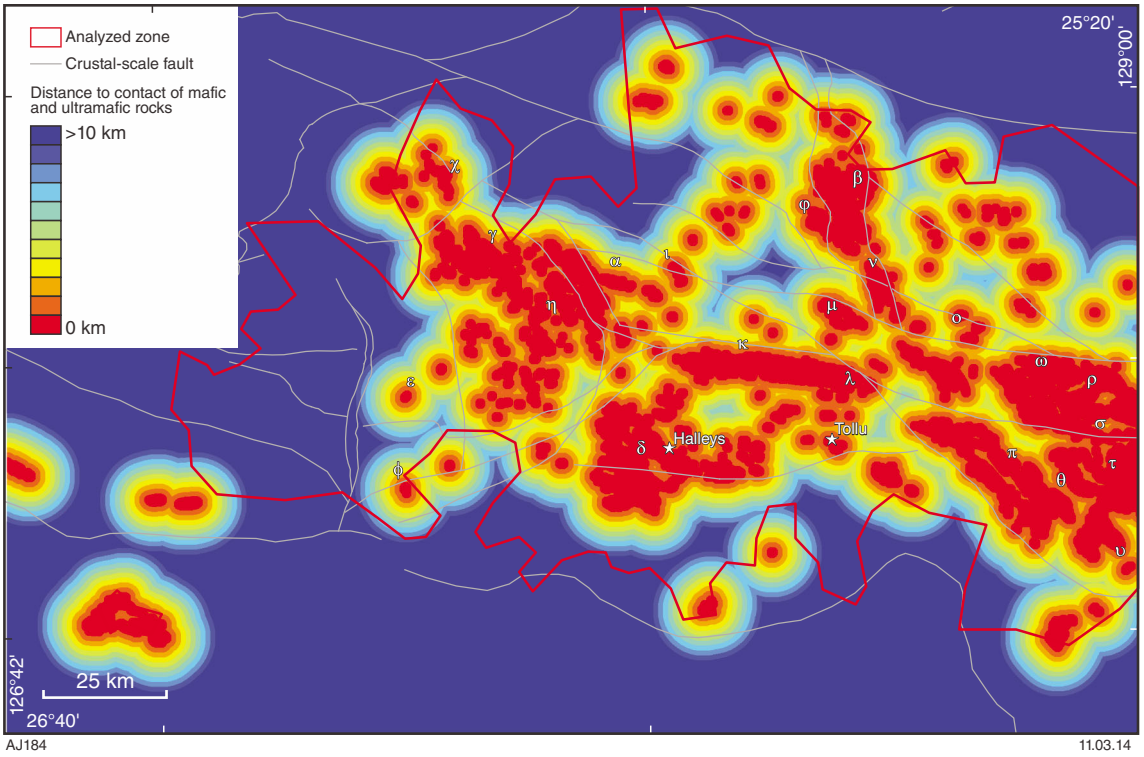

Figure A31. **Predictor map for PGE physical throttle: distance to contact of mafic and ultramafic rocks with a 10 km buffer zone. Greek letters correspond to the PGE prospective zones (Fig. 18).**

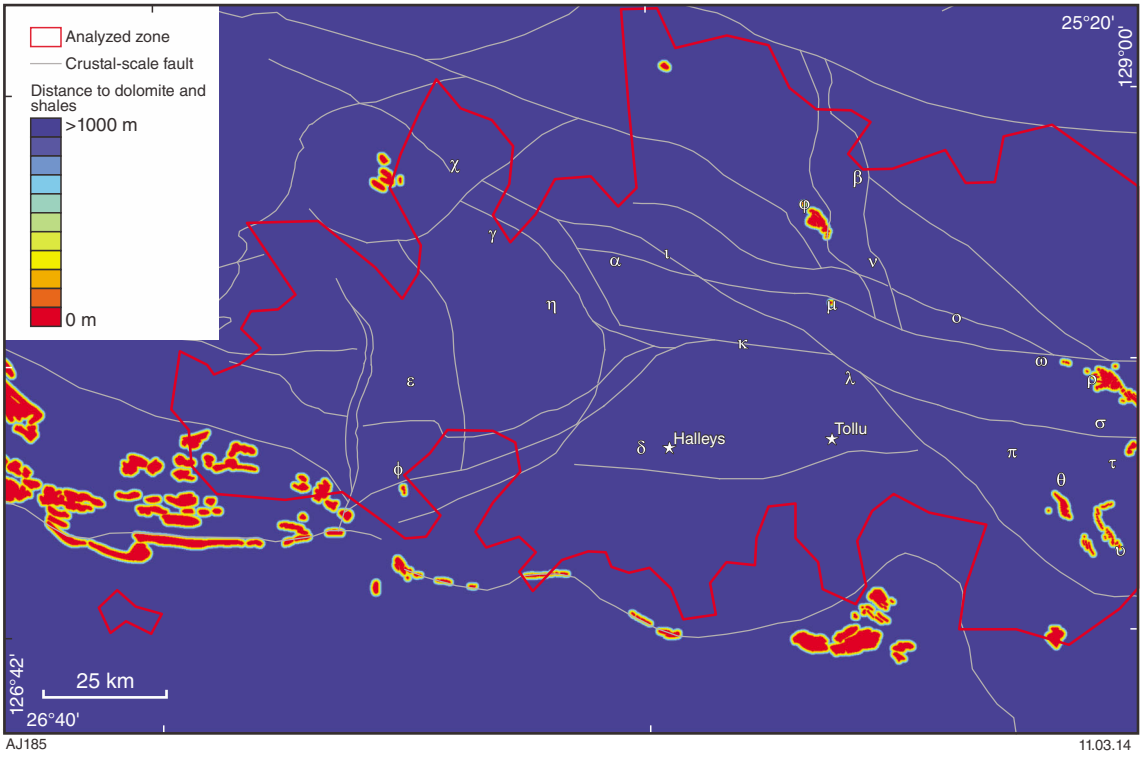

Figure A32. **Predictor map for PGE chemical trap: dolomites, and shales with a 1000 m buffer zone (considered as possible metasomatic alteration). Greek letters correspond to the PGE prospective zones (Fig. 18).**

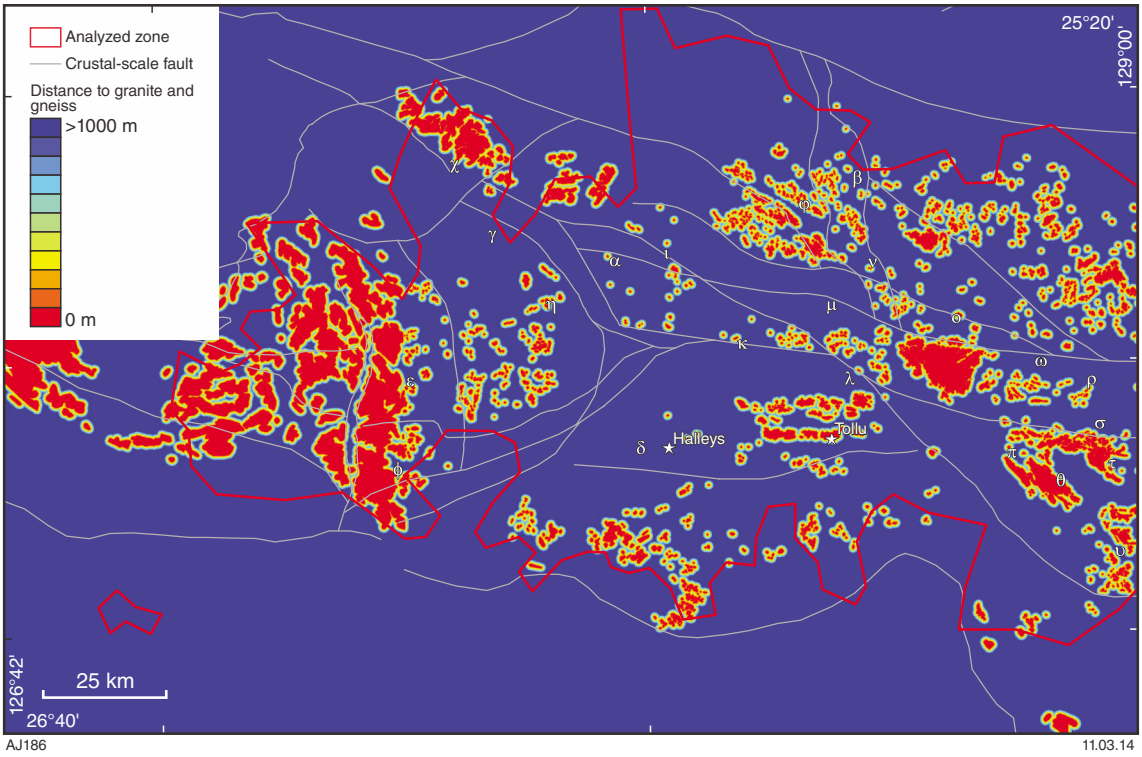

Figure A33. Predictor map for PGE chemical trap: granitic and gneissic rocks with a 1000 m buffer zone. Greek letters correspond to the PGE prospective zones (Fig. 18).

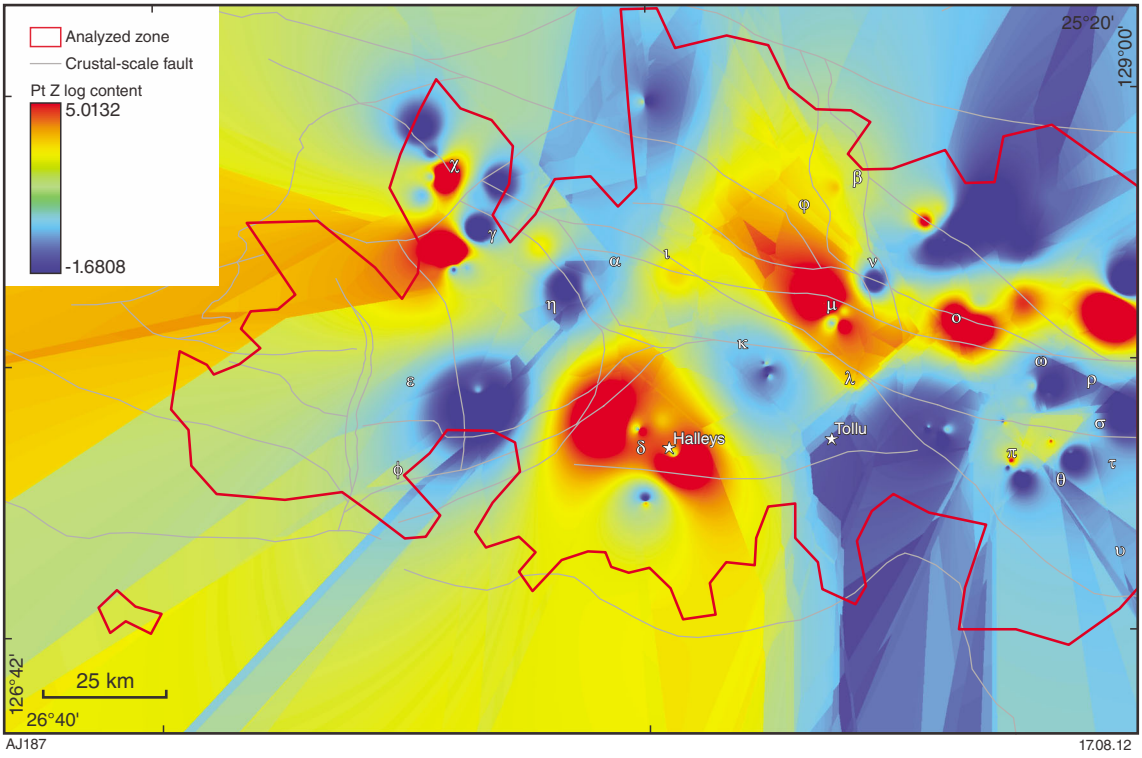

Figure A34. Predictor map for PGE chemical trap: Pt content (Z log value). Greek letters correspond to the PGE prospective zones (Fig. 18).

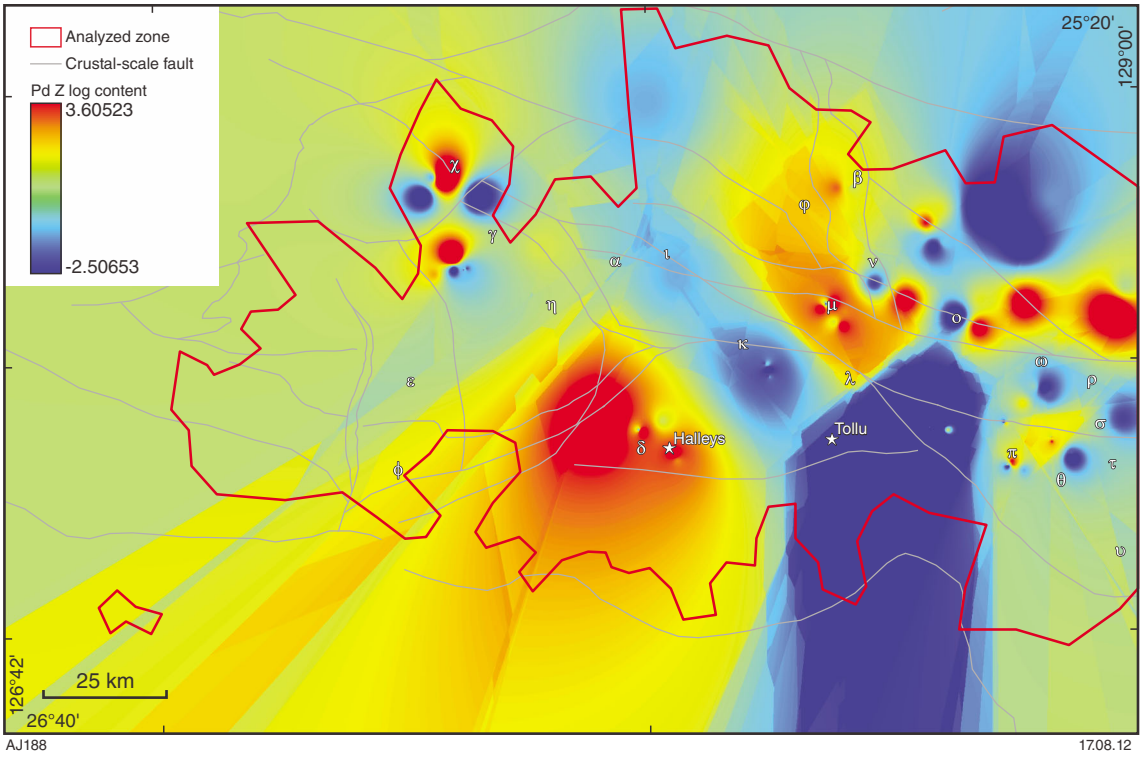

Figure A35. Predictor map for PGE chemical trap: Pd content (Z log value). Greek letters correspond to the PGE prospective zones (Fig. 18).

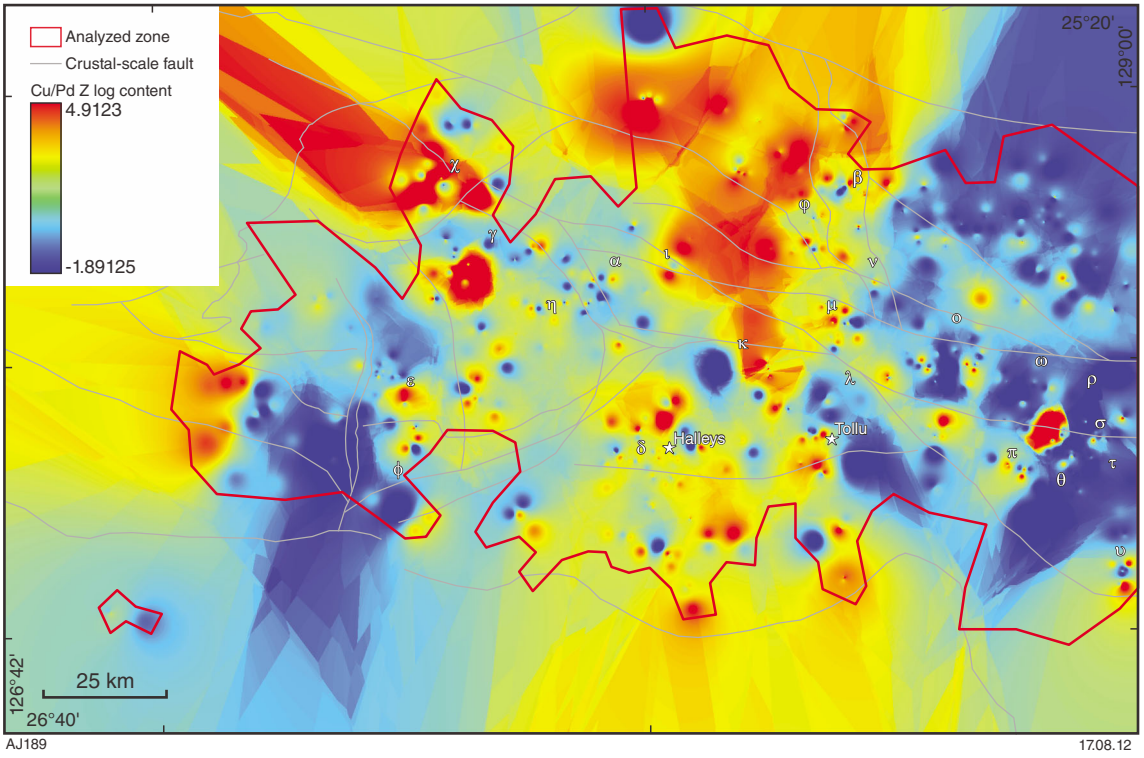

Figure A36. Predictor map for PGE chemical trap: Cu/Pd ratio (Z log value). Greek letters correspond to the PGE prospective zones (Fig. 18).

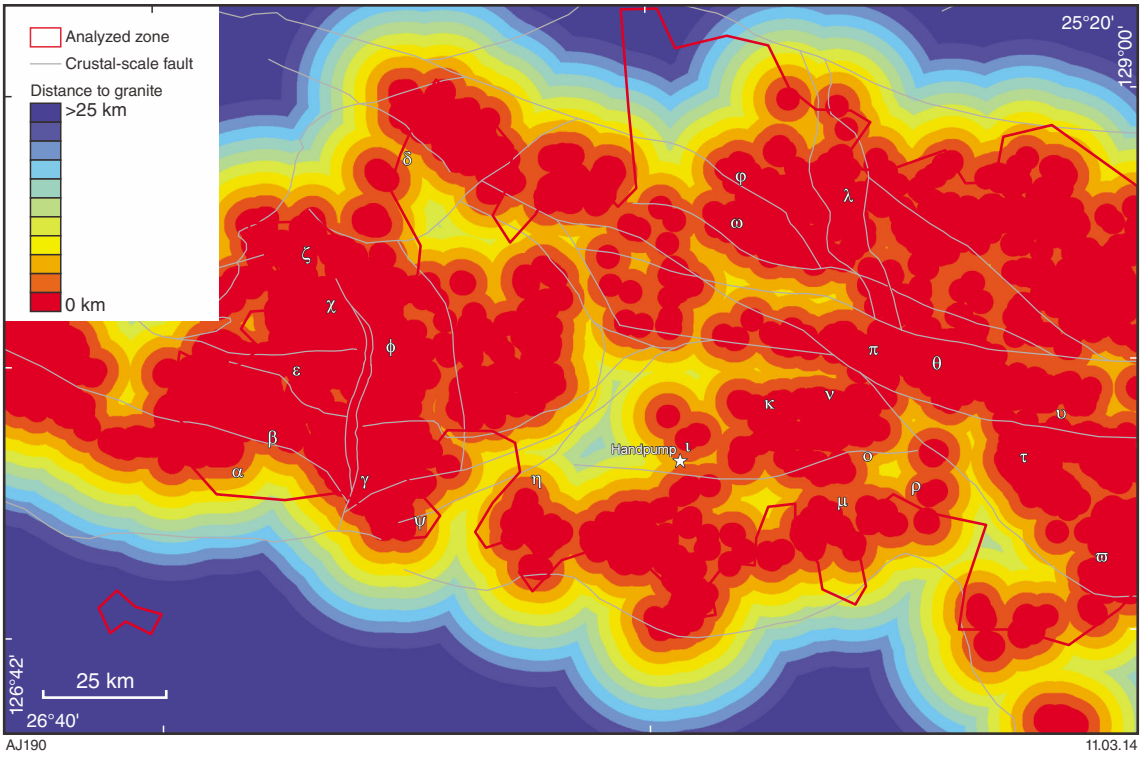

Figure A37. Predictor map for gold source: proximity to granitic rocks (up to 25 km). Greek letters correspond to the gold prospective zones (Fig. 20).

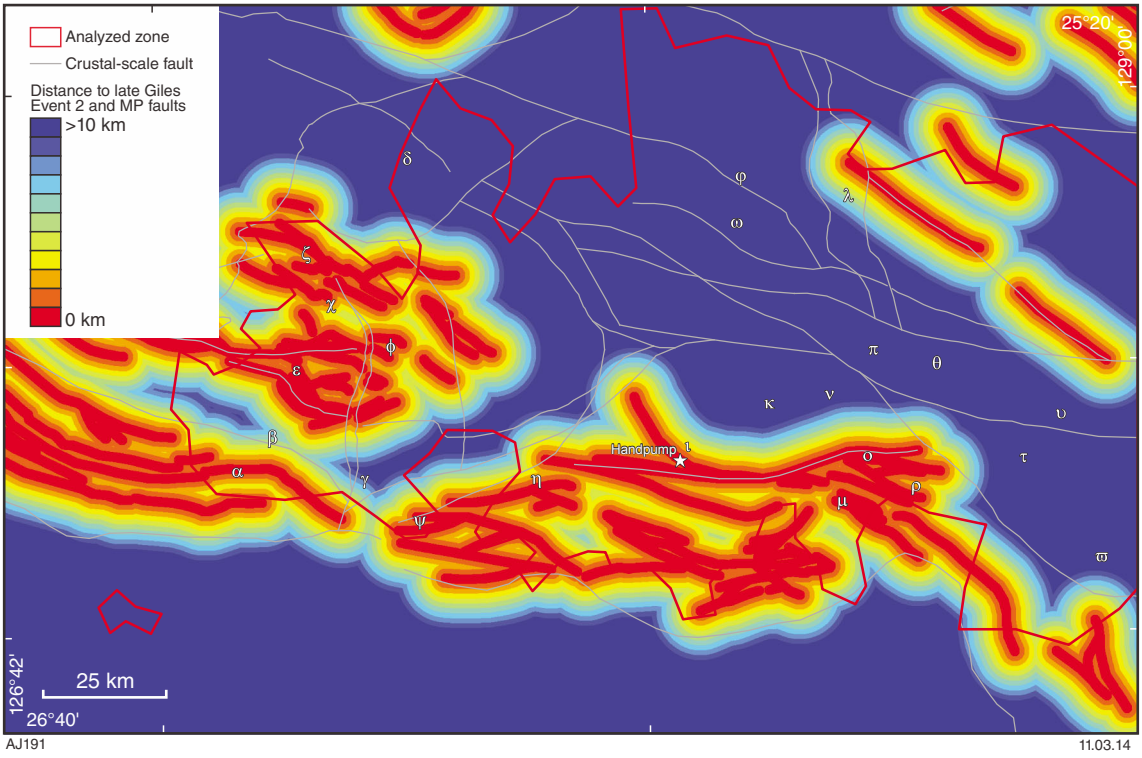

Figure A38. Predictor map for gold pathway: proximity to LGE2 and LGE2_MP structures with 5 km buffer zone. Greek letters correspond to the gold prospective zones (Fig. 20).

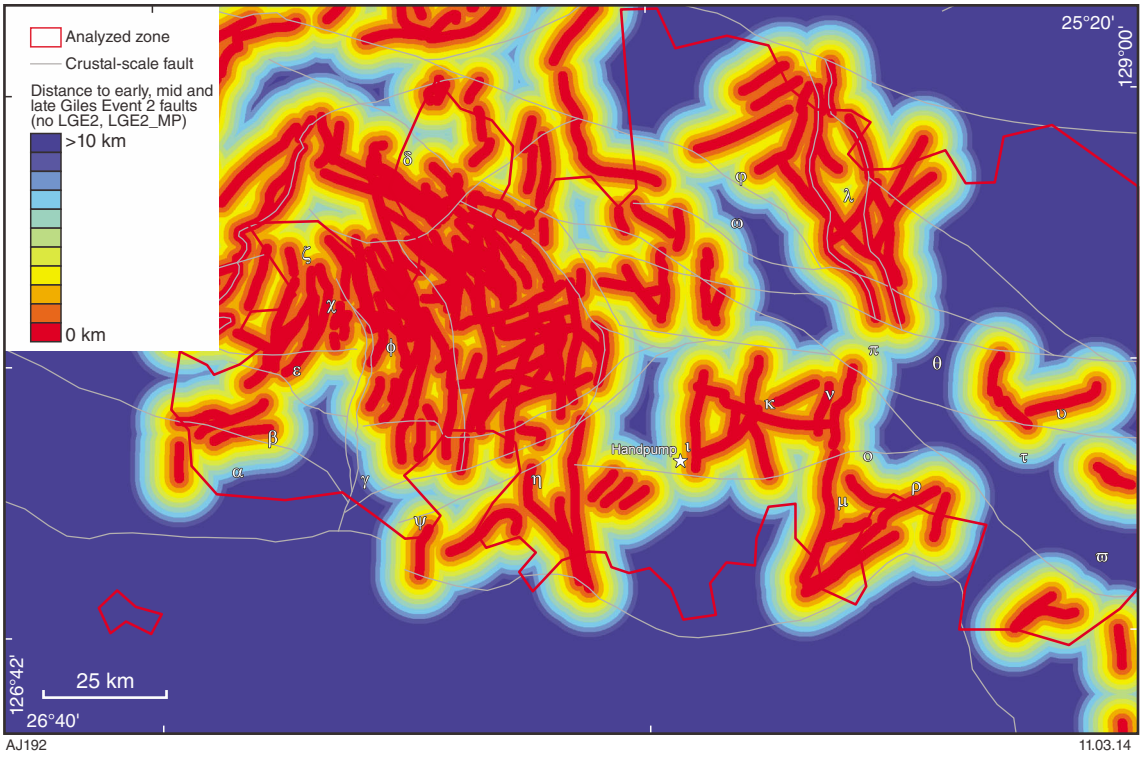

Figure A39. **Predictor map for gold pathway: proximity to early Giles (EGE), mid-Giles (MGE) and late Giles (LGE) Event faults (except for LGE2 and LGE2_MP) with 5 km buffer zone. Greek letters correspond to the gold prospective zones (Fig. 20).**

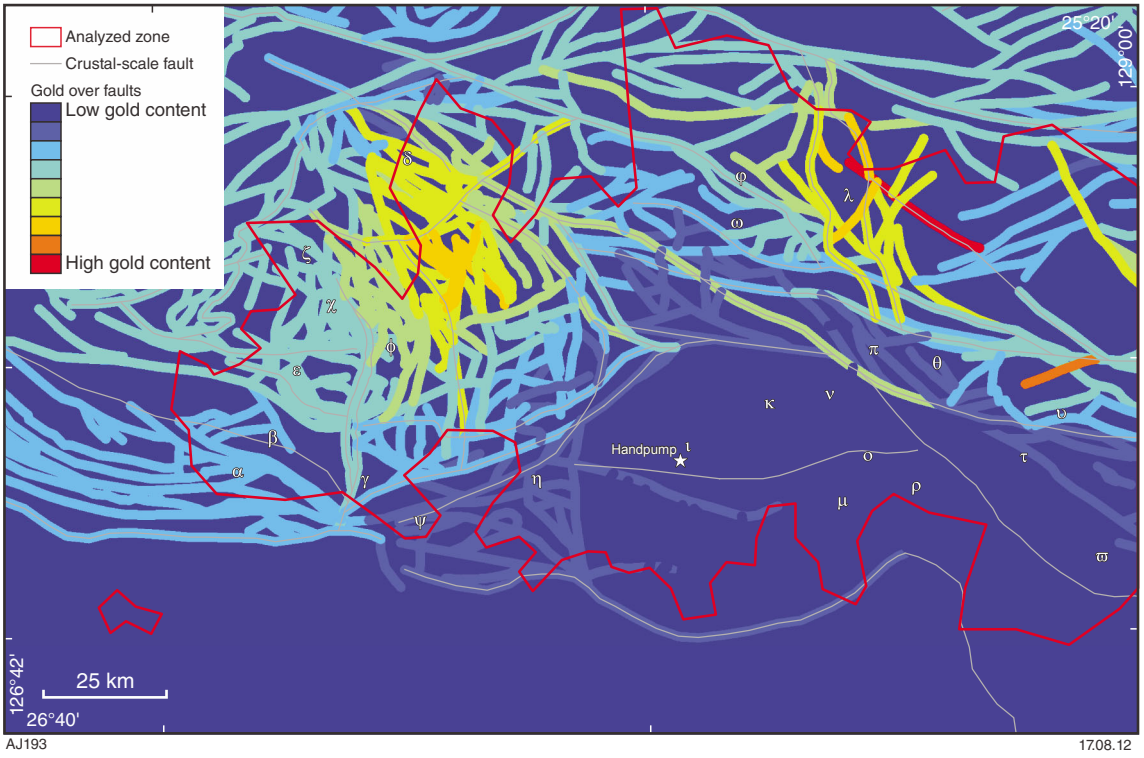

Figure A40. **Predictor map for gold pathway: gold contents over all faults. Zones shown in red indicate areas very close to faults that are linked to high gold contents; areas shown in blue correspond to the contrary. Greek letters correspond to the gold prospective zones (Fig. 20).**

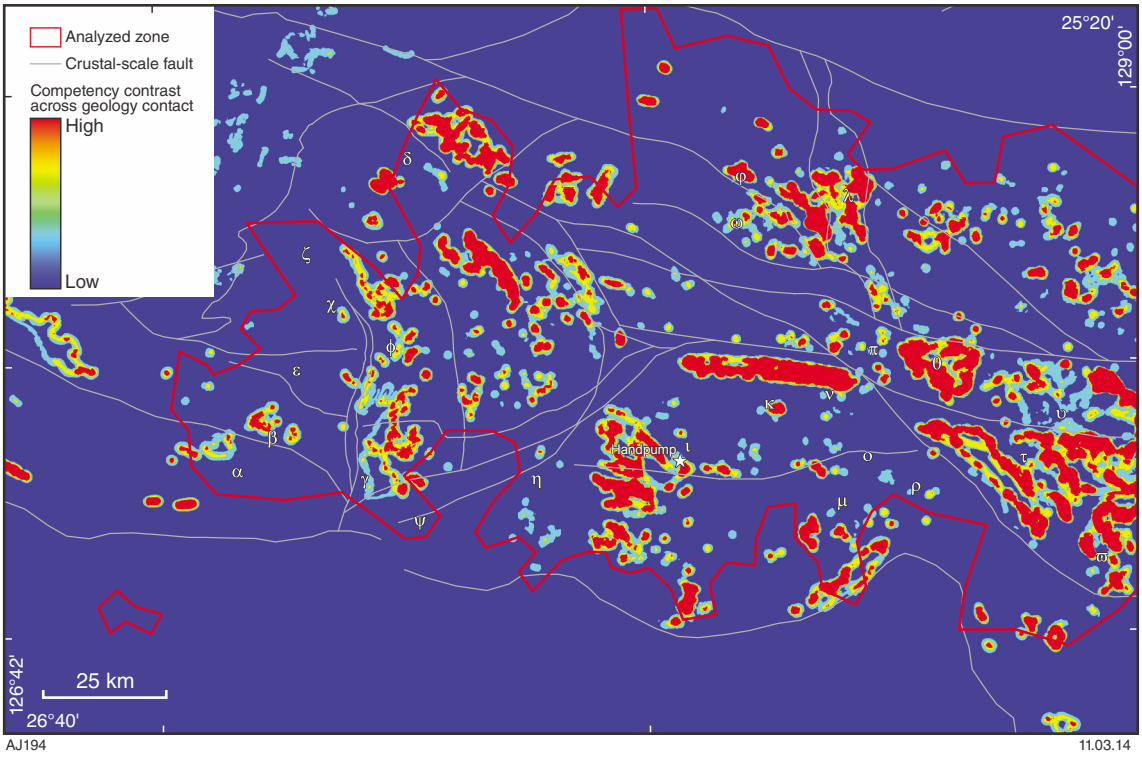

Figure A41. Predictor map for gold and IOCG physical trap: competency contrast across geological contacts. Greek letters correspond to the gold prospective zones (Fig. 20).

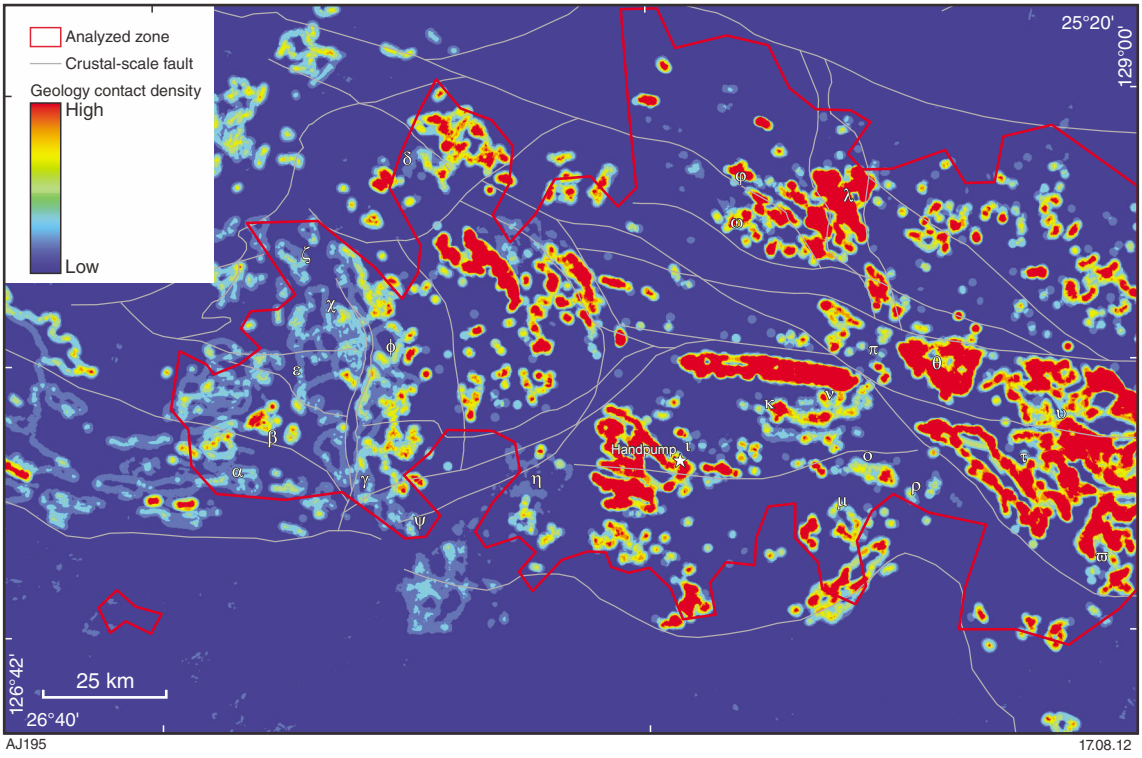

Figure A42. Predictor map for gold and IOCG physical trap: density of geological contacts. Red indicates areas of highest intensity of geological contacts; blue correspond to the contrary. Greek letters correspond to the gold prospective zones (Fig. 20).

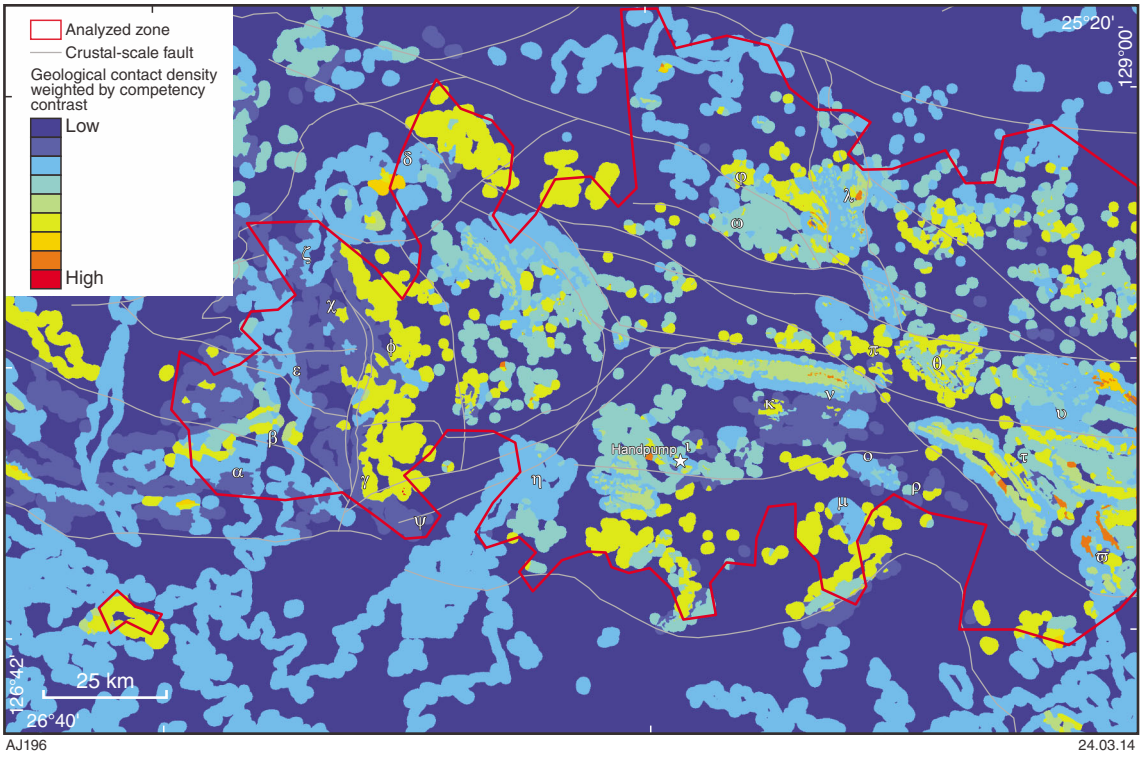

Figure A43. **Predictor map for gold and IOCG physical trap: geological contact density weighted by competency contrast. Red indicates areas with highest geological contact density weighted by geological contrast; blue corresponds to the contrary. Greek letters correspond to the gold prospective zones (Fig. 20).**

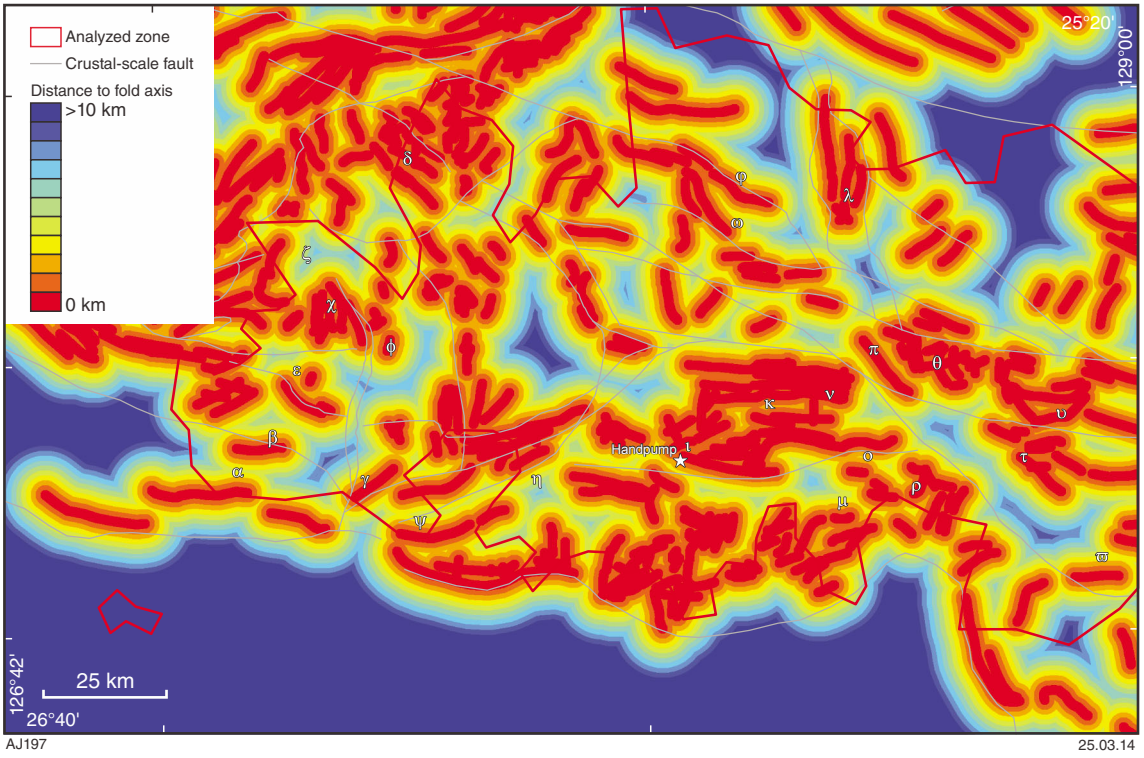

Figure A44. **Predictor map for gold physical trap: proximity to fold axes. For the analysis, only the first 10 km were taken into account. Greek letters correspond to the gold prospective zones (Fig. 20).**

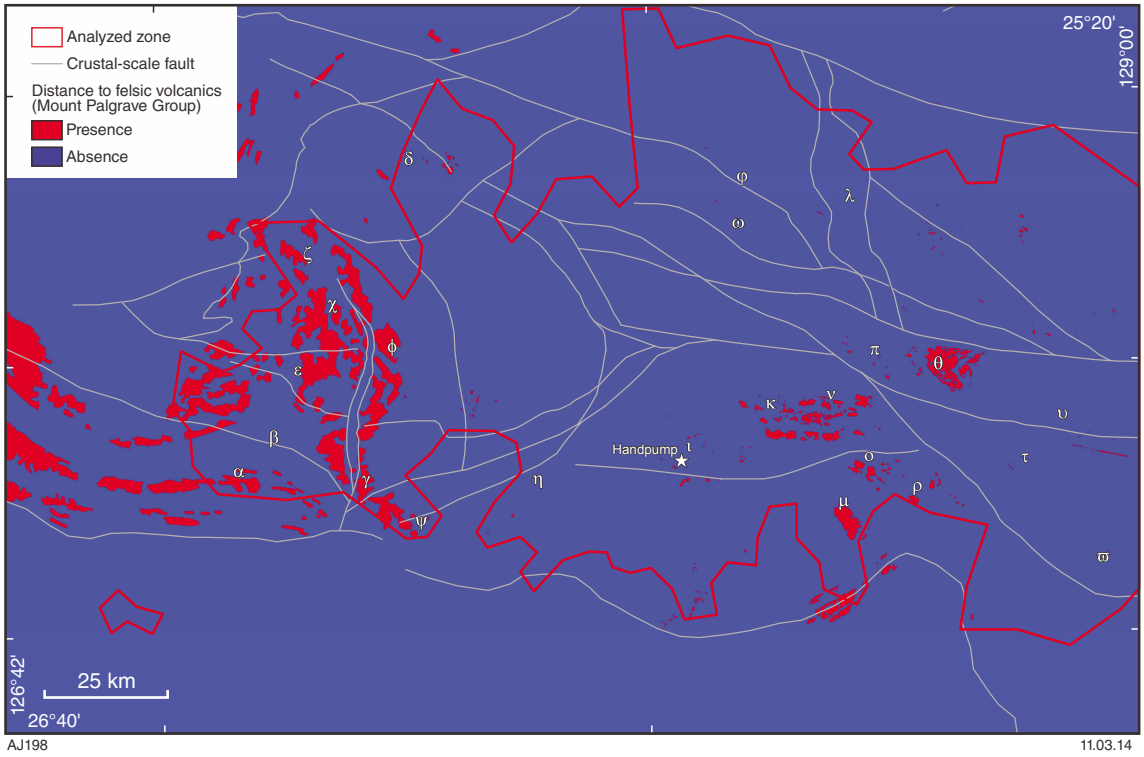

Figure A45. Predictor map for gold chemical trap: presence of gold host unit – felsic volcanic formation (including Palgrave Group). Greek letters correspond to the gold prospective zones (Fig. 20).

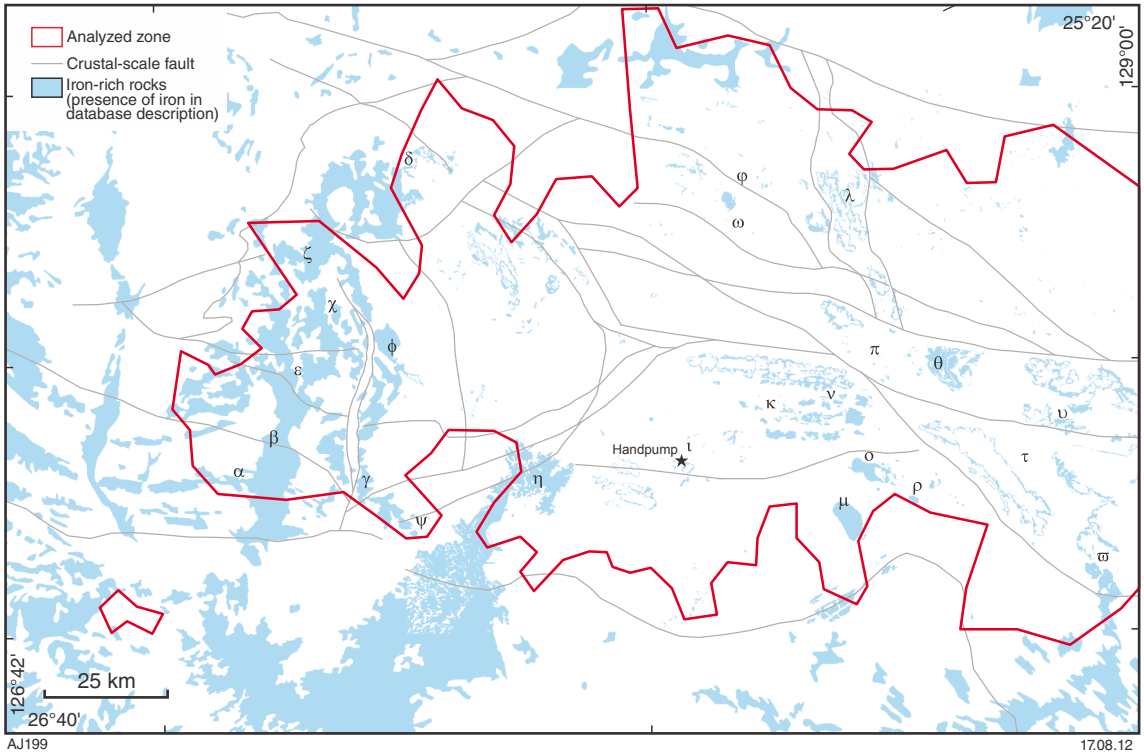

Figure A46. Predictor map for gold and IOCG chemical trap: presence of Fe-rich rocks. Greek letters correspond to the gold prospective zones (Fig. 20).

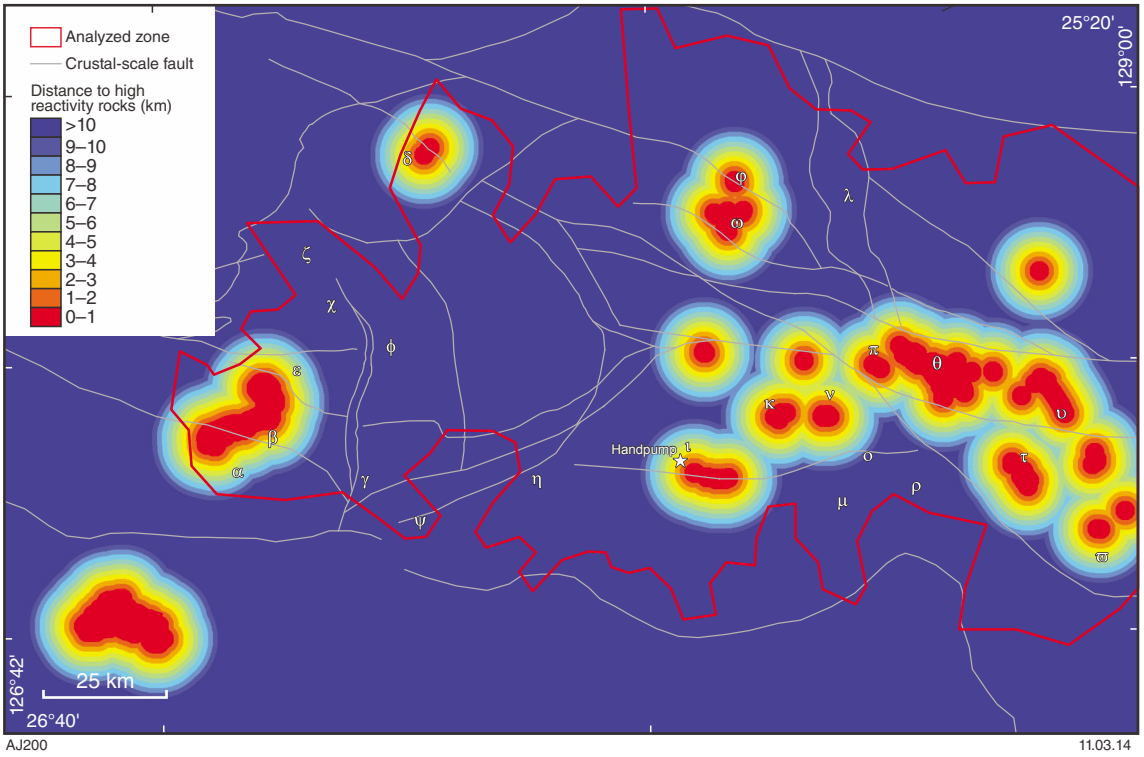

Figure A47. **Predictor map for gold chemical trap: distance to high reactivity rocks. Greek letters correspond to the gold prospective zones (Fig. 20).**

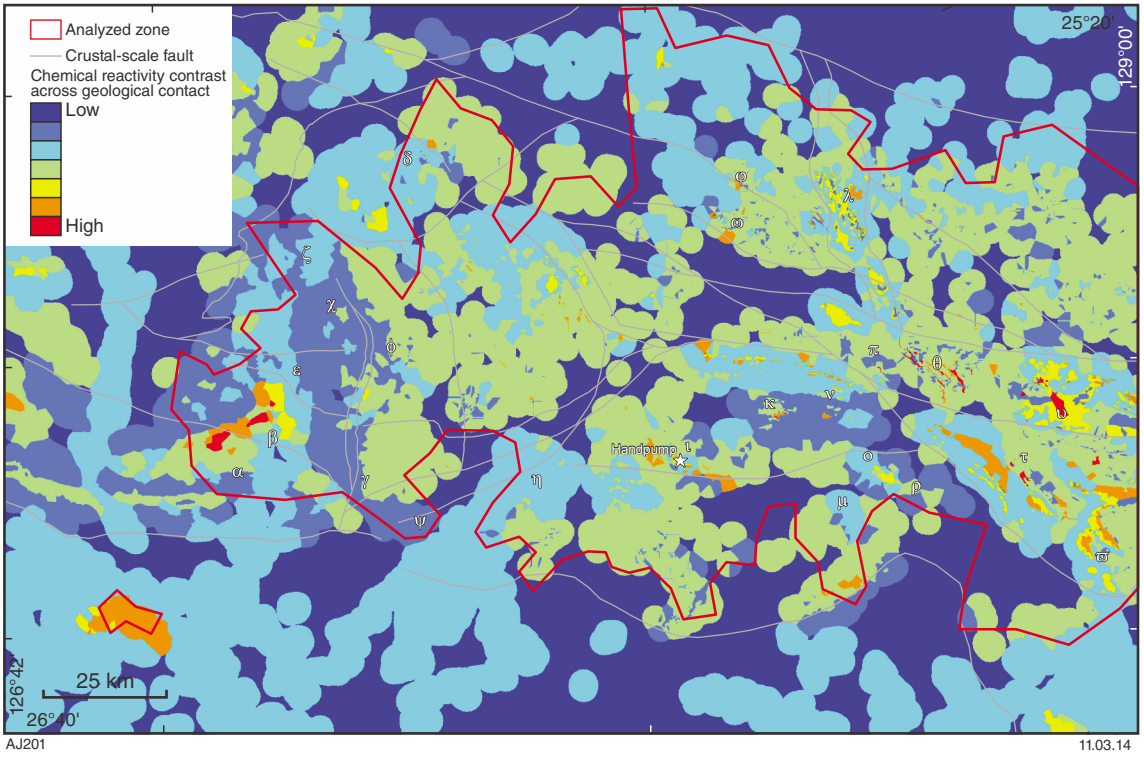

Figure A48. **Predictor map for gold chemical trap: chemical reactivity contrast across geological contact. Greek letters correspond to the gold prospective zones (Fig. 20).**

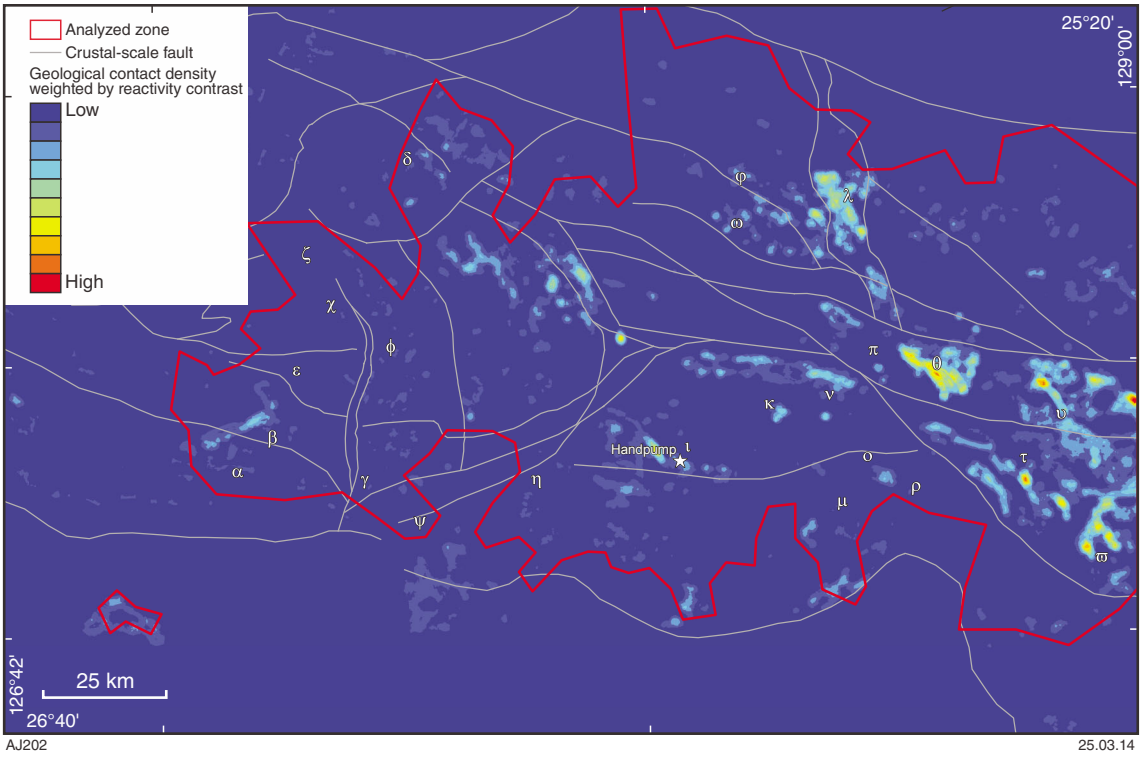

Figure A49. Predictor map for gold chemical trap: geological contact density weighted by chemical reactivity contrast. Red indicates areas with highest geological contact density weighted by reactivity contrast; blue corresponds to the contrary. Greek letters correspond to the gold prospective zones (Fig. 20).

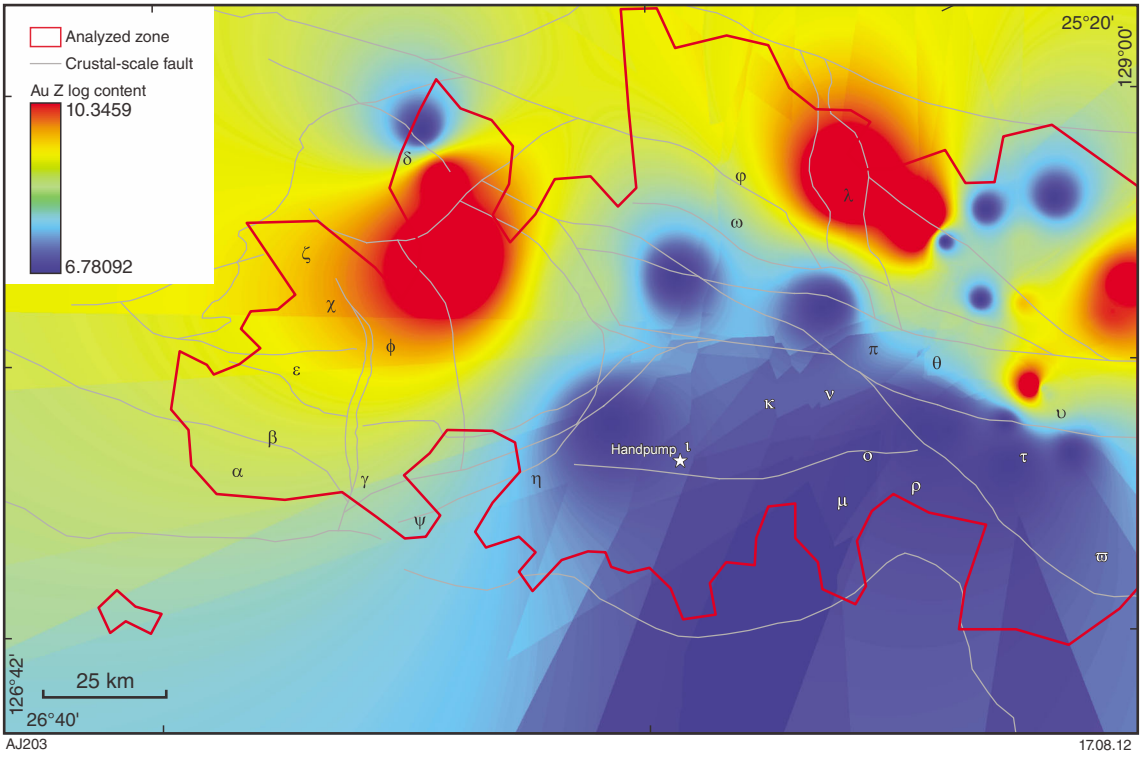

Figure A50. Predictor map for gold and IOCG chemical trap: gold content (Z log value). Greek letters correspond to the gold prospective zones (Fig. 20).

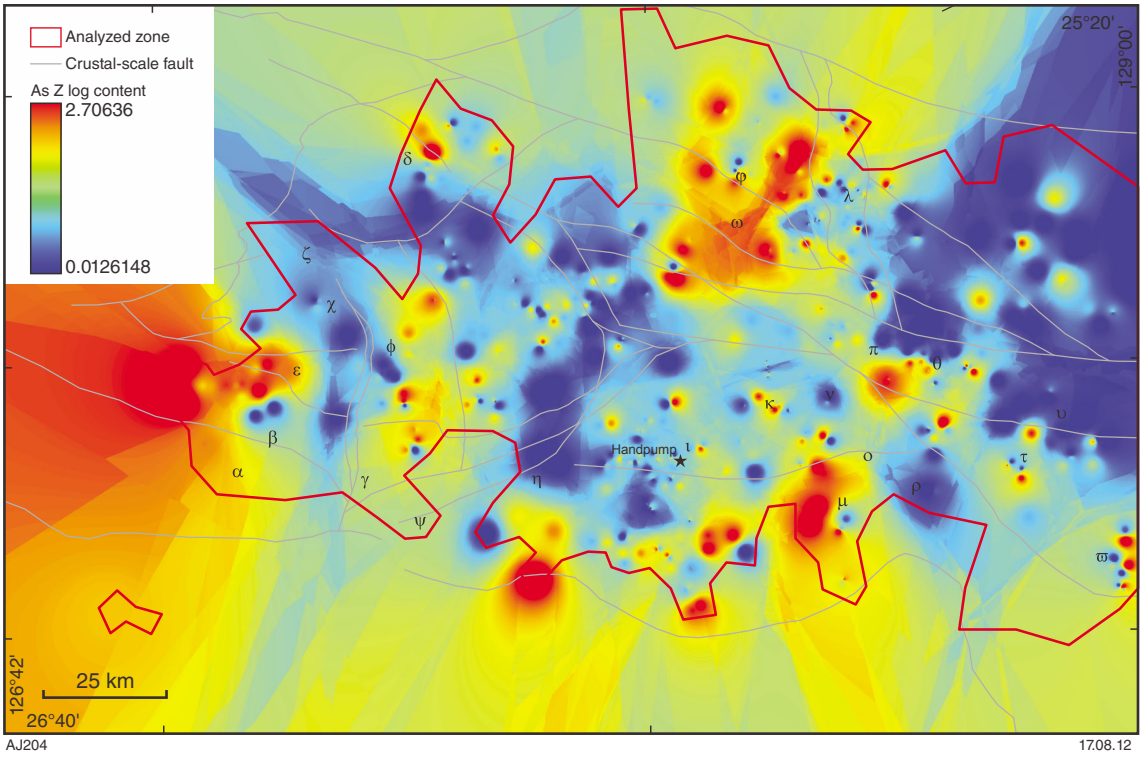

Figure A51. **Predictor map for gold chemical trap: arsenic content (Z log value). Greek letters correspond to the gold prospective zones (Fig. 20).**

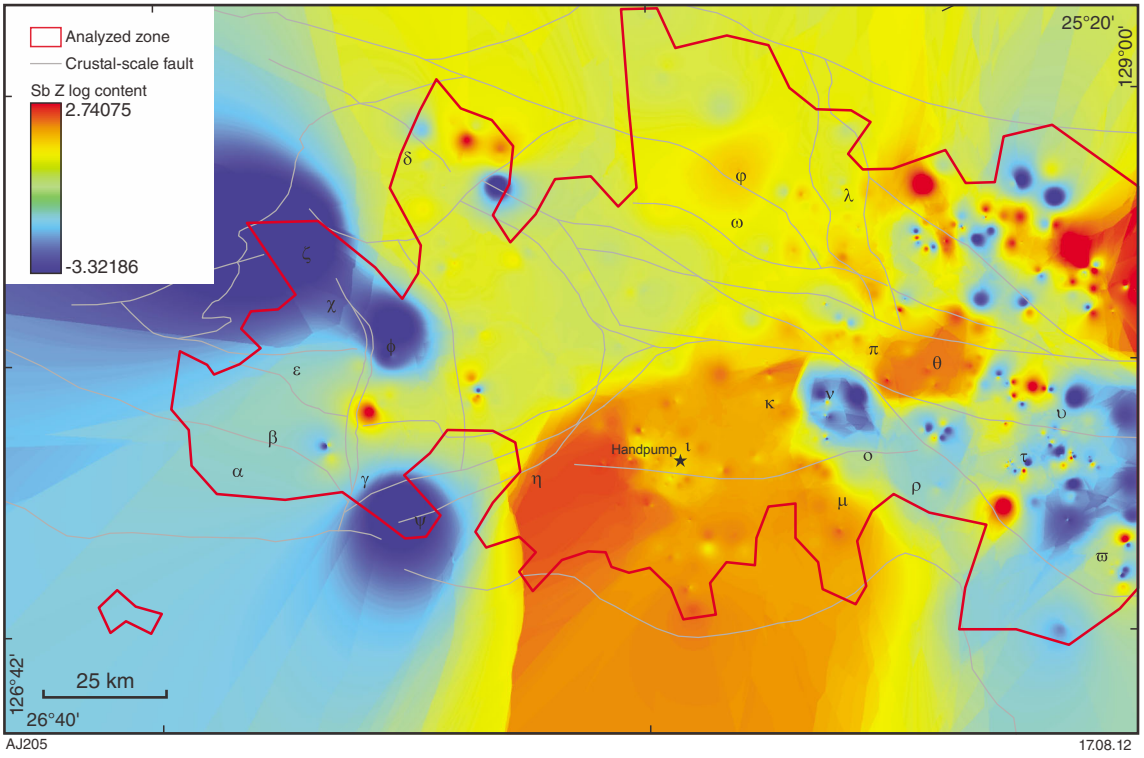

Figure A52. **Predictor map for gold chemical trap: antimony content (Z log value). Greek letters correspond to the gold prospective zones (Fig. 20).**

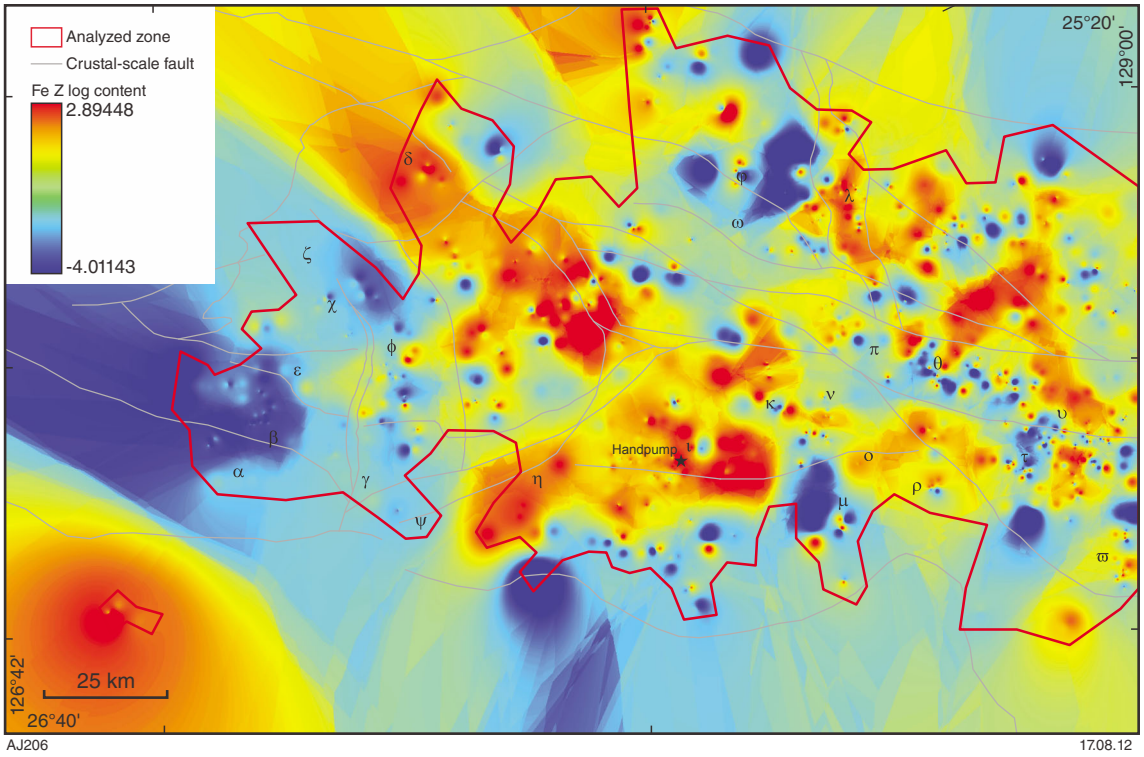

Figure A53. Predictor map for gold chemical trap: iron content (Z log value). Greek letters correspond to the gold prospective zones (Fig. 20).

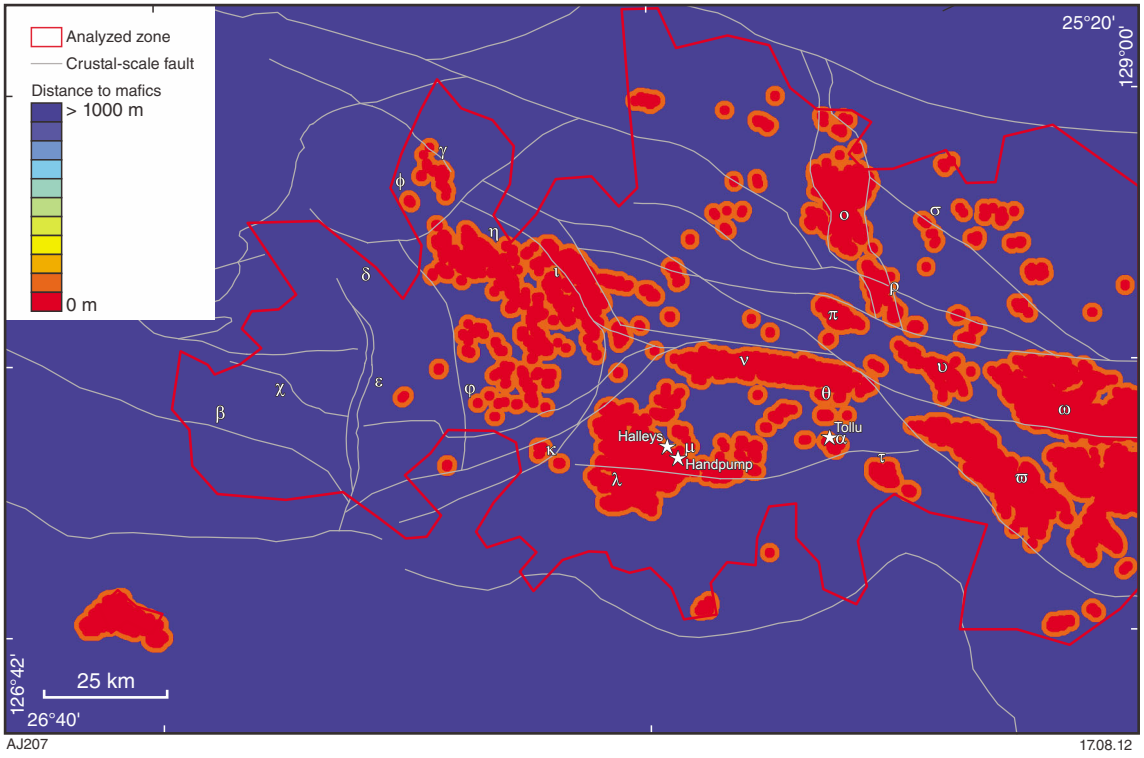

Figure A54. Predictor map for IOCG source: distance to mafic rocks (up to 1000 m). Greek letters correspond to the IOCG prospective zones (Fig. 24).

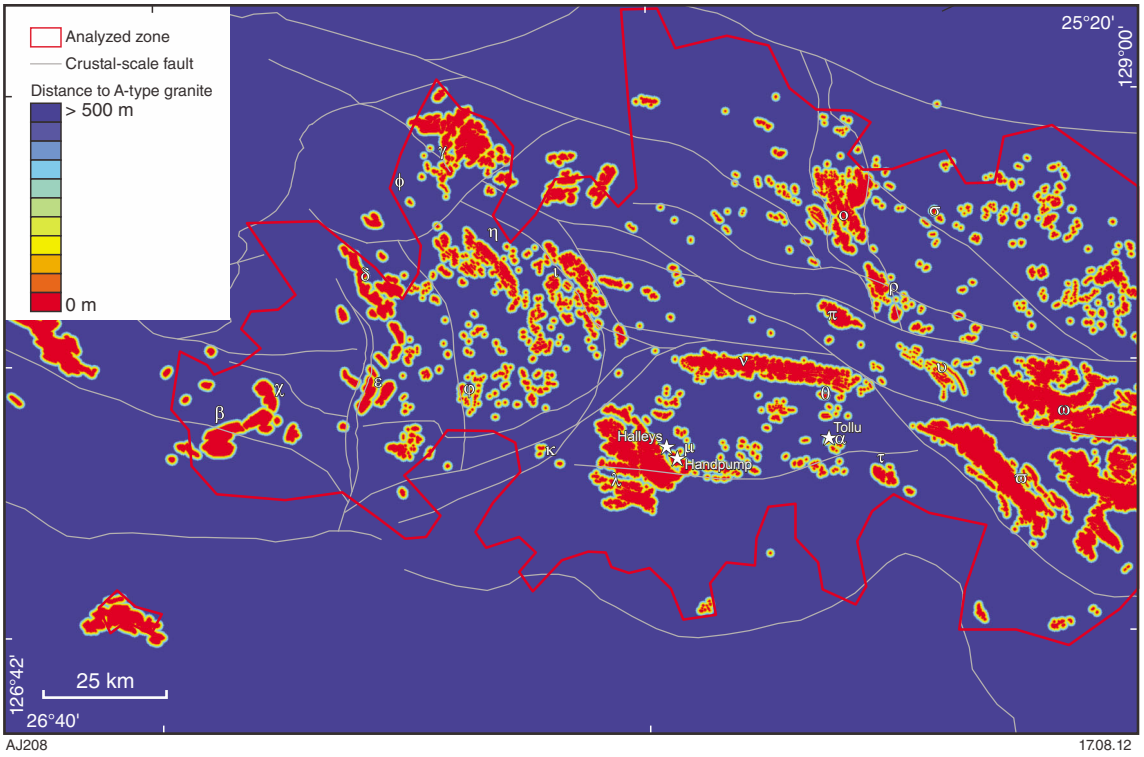

Figure A55. **Predictor map for IOCG source: distance to A-type granitic rocks (up to 500 m). Greek letters correspond to the IOCG prospective zones (Fig. 24).**

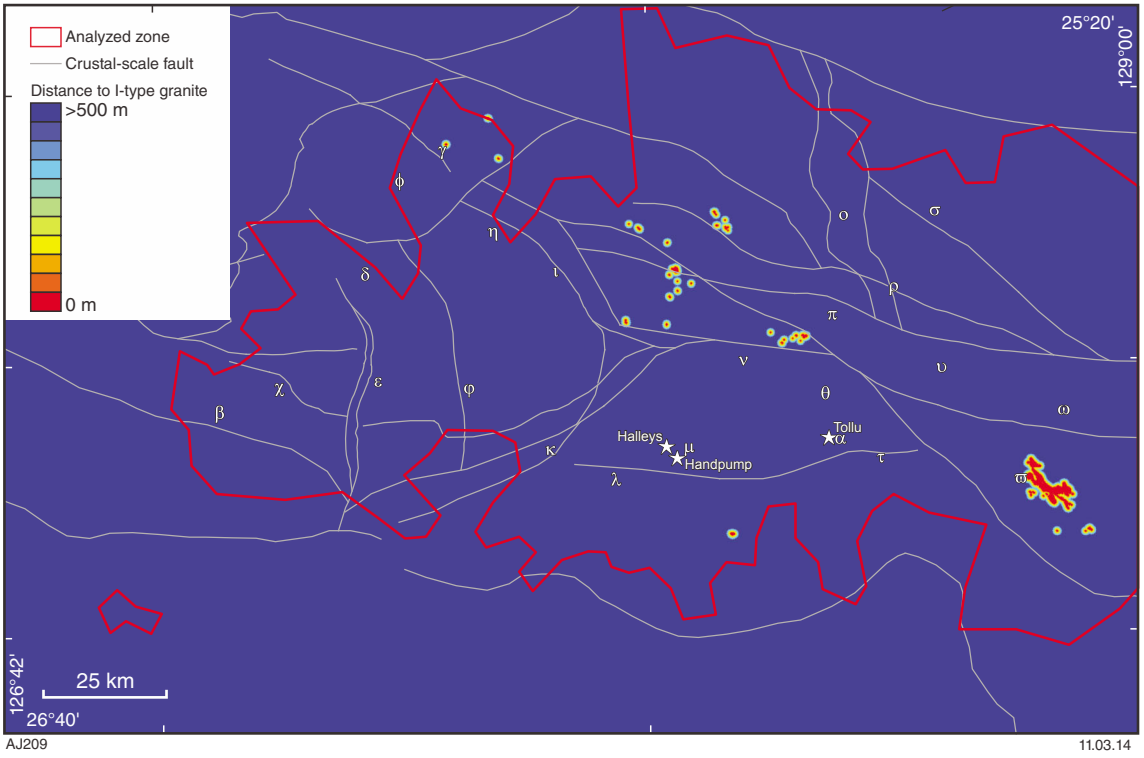

Figure A56. **Predictor map for IOCG source: distance to I-type granitic rocks (up to 500 m). Greek letters correspond to the IOCG prospective zones (Fig. 24).**

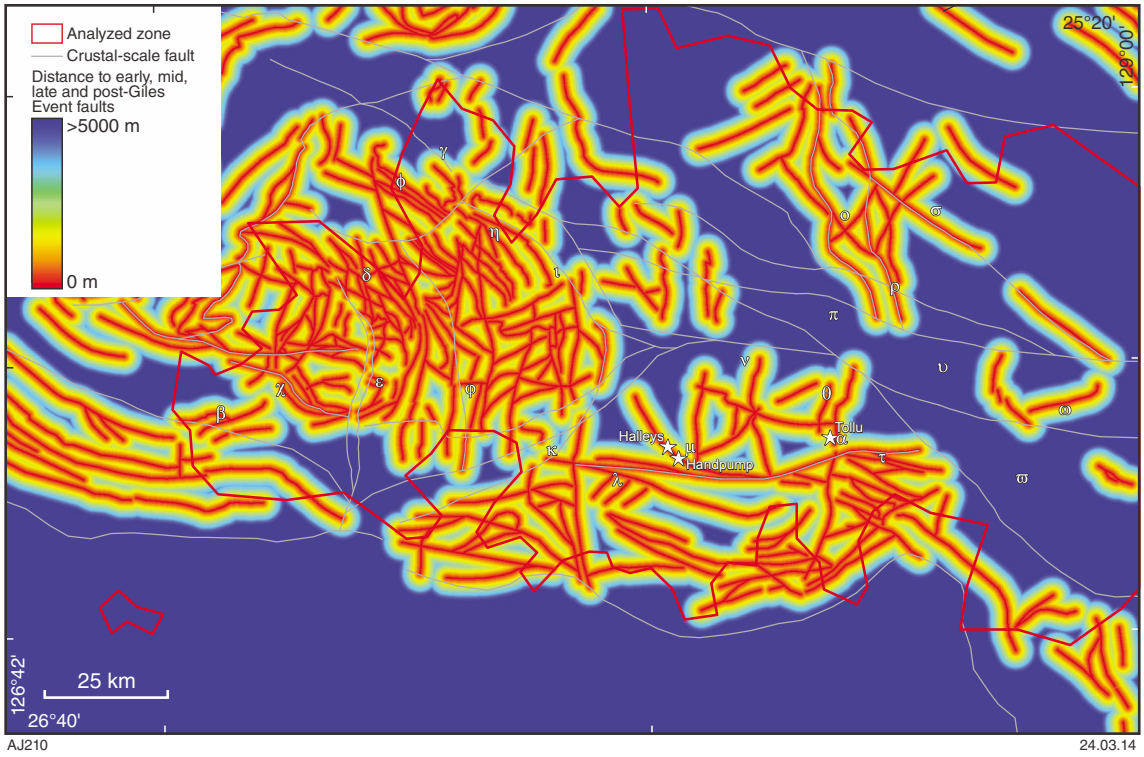

Figure A57. Predictor map for IOCG pathways: proximity to early Giles (EGE), mid-Giles (MGE) and late Giles (LGE) Event faults with 5 km buffer zone. Greek letters correspond to the IOCG prospective zones (Fig. 24).

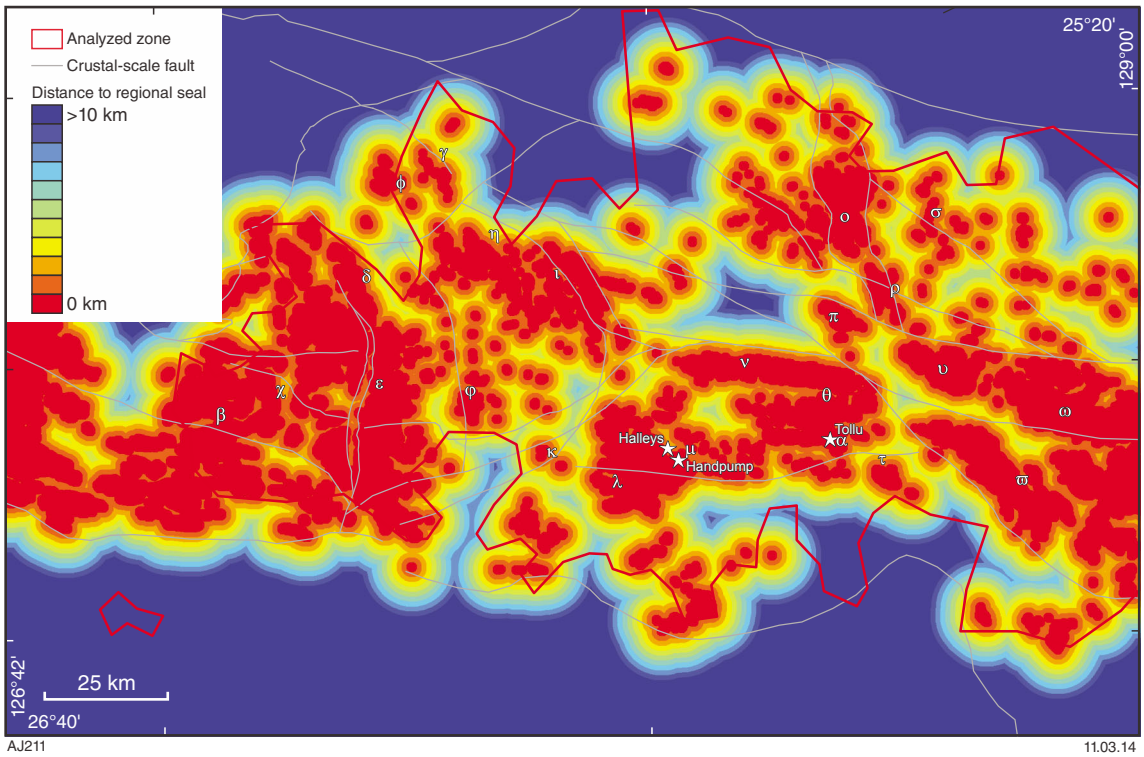

Figure A58. Predictor map for IOCG physical trap: proximity to regional seals. Greek letters correspond to the IOCG prospective zones (Fig. 24).

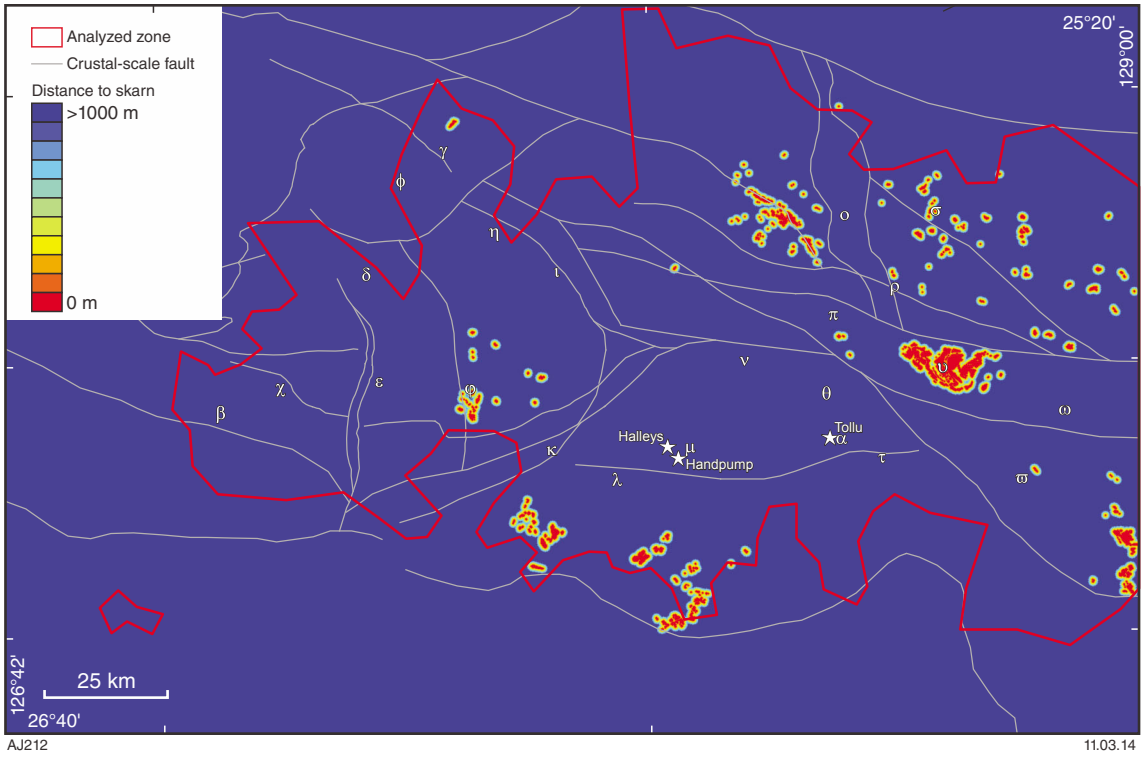

Figure A59. **Predictor map for IOCG chemical trap: proximity to skarn with a 1000 m buffer zone. Greek letters correspond to the IOCG prospective zones (Fig. 24).**

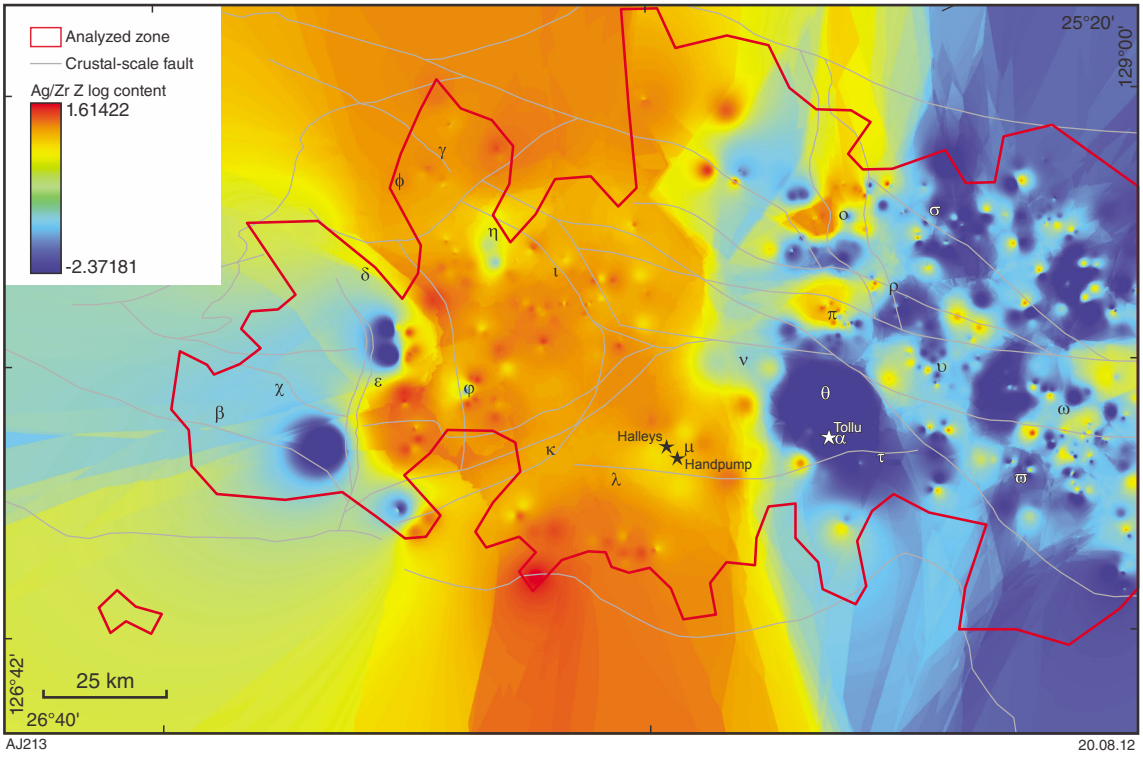

Figure A60. **Predictor map for IOCG chemical trap: Ag/Zr ratio (Z value). Greek letters correspond to the IOCG prospective zones (Fig. 24).**

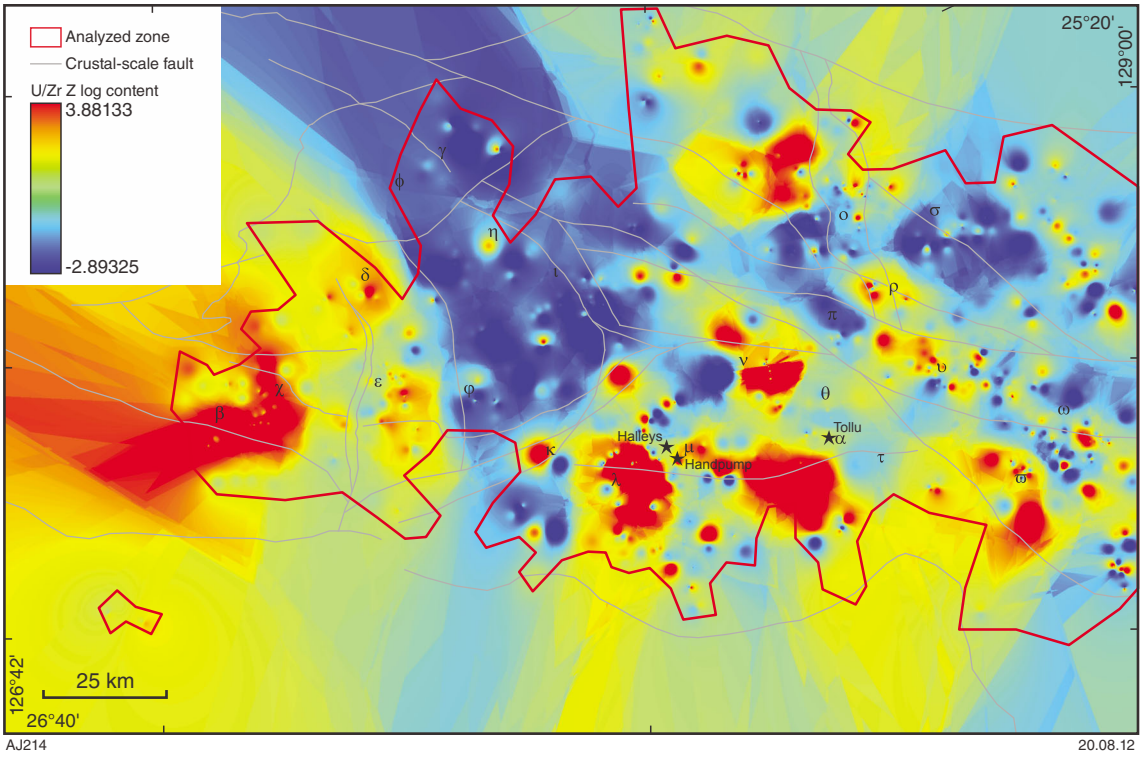

Figure A61. Predictor map for IOCG chemical trap: U/Zr ratio (Z value). Greek letters correspond to the IOCG prospective zones (Fig. 24).

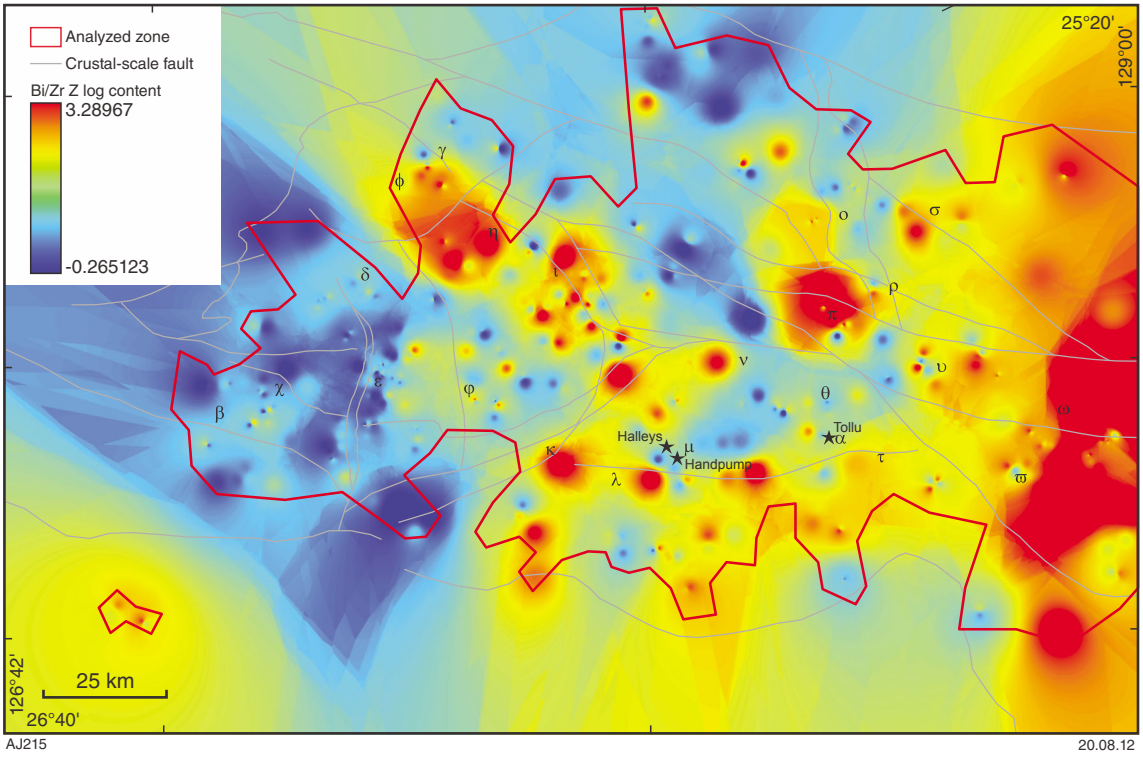

Figure A62. Predictor map for IOCG chemical trap: Bi/Zr ratio (Z value). Greek letters correspond to the IOCG prospective zones (Fig. 24).

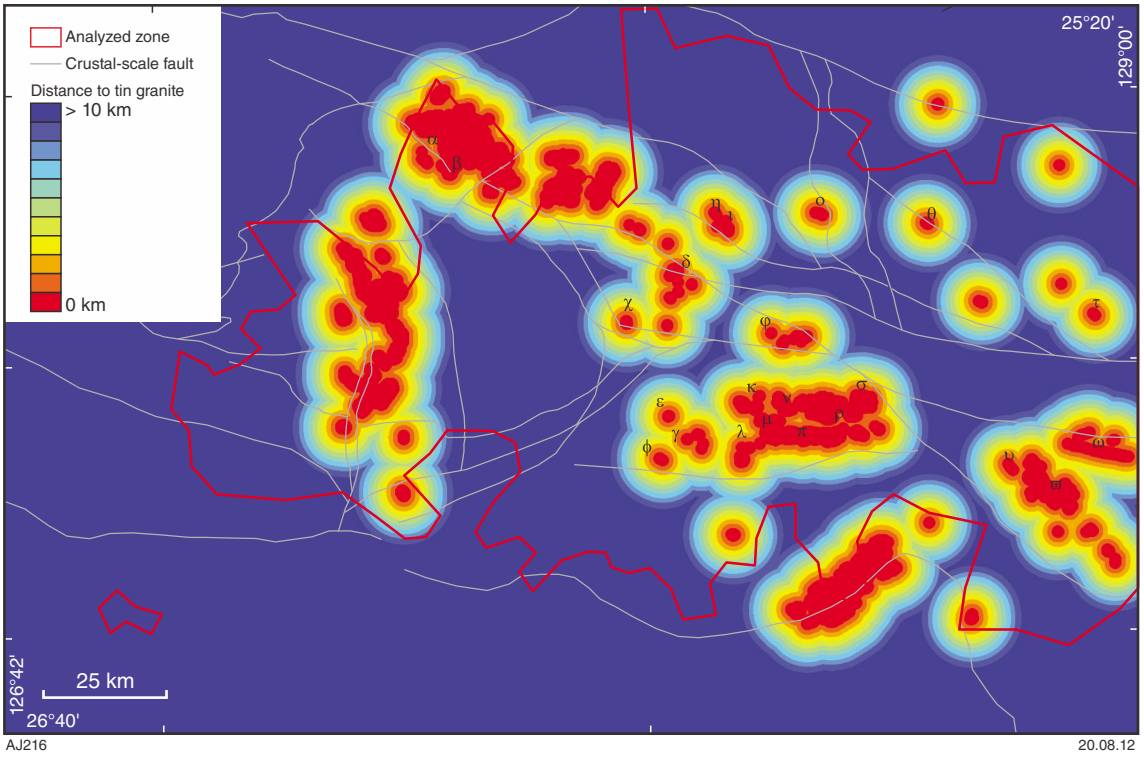

Figure A63. Predictor map for Sn–W source: proximity to tin granite (up to 25 km). Greek letters correspond to the Sn–W prospective zones (Fig. 27).

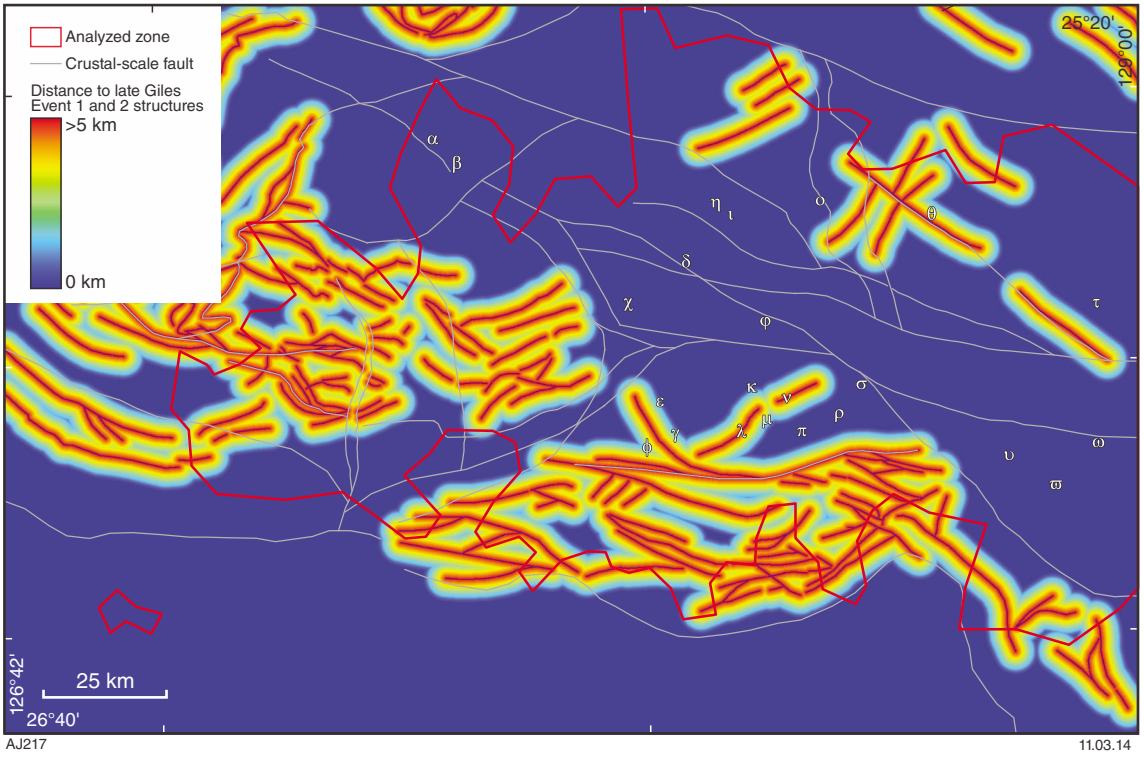

Figure A64. Predictor map for Sn–W pathway: proximity to late Giles Event 1 and 2 (LGE1 and LGE2) structures with 5 km buffer zone. Greek letters correspond to the Sn–W prospective zones (Fig. 27).

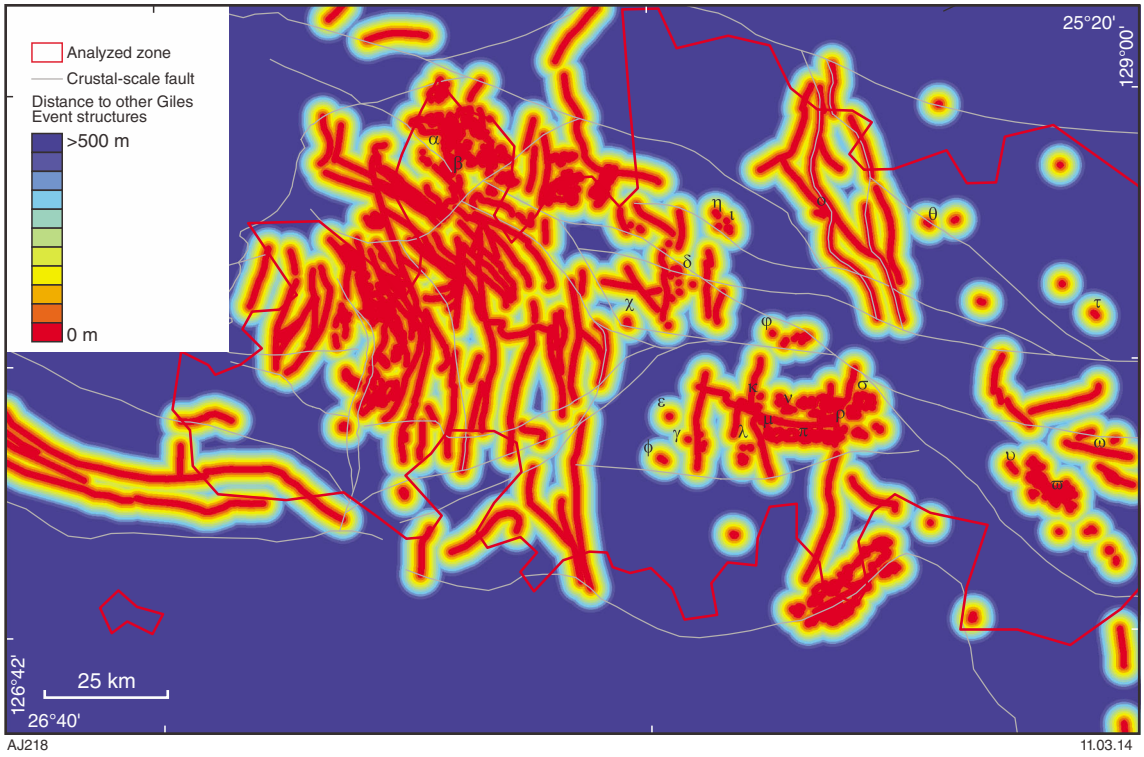

Figure A65. Predictor map for Sn–W pathway: proximity to early Giles (EGE), mid-Giles (MGE) and late Giles (LGE) faults (without LGE1 and LGE2) with 5 km buffer zone. Greek letters correspond to the Sn–W prospective zones (Fig. 27).

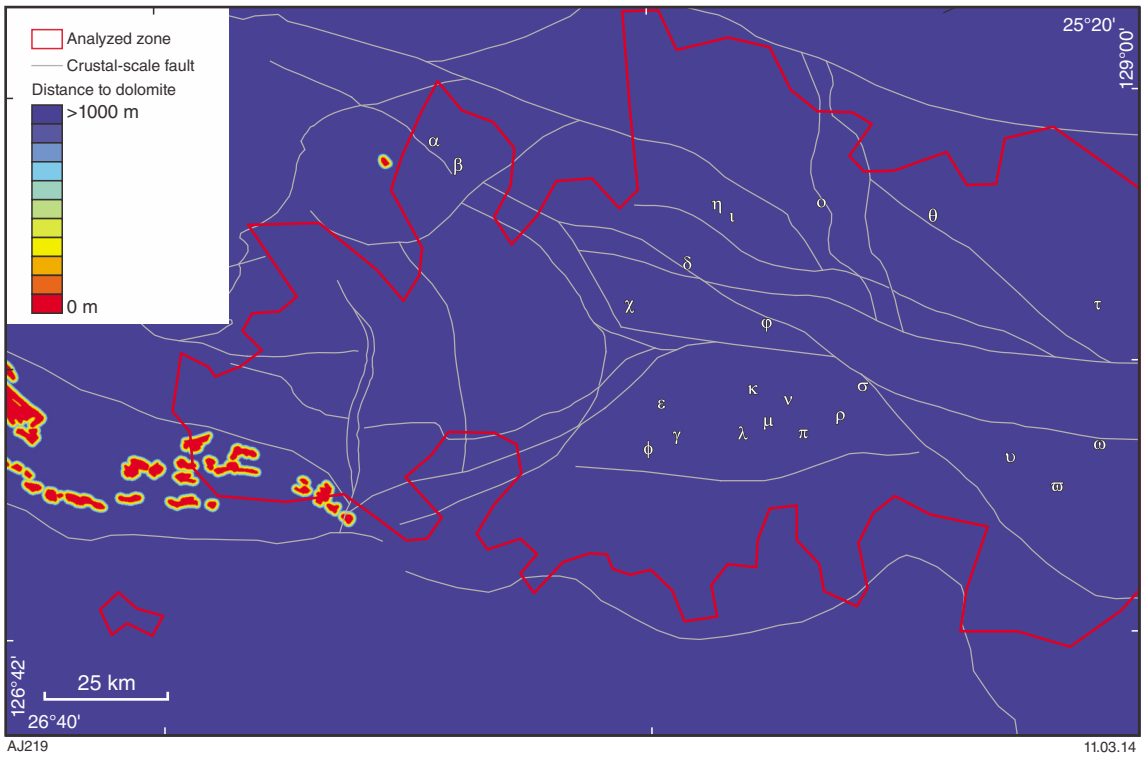

Figure A66. Predictor map for Sn–W chemical trap: distance to dolomite with a 1000 m buffer zone. Greek letters correspond to the Sn–W prospective zones (Fig. 27).

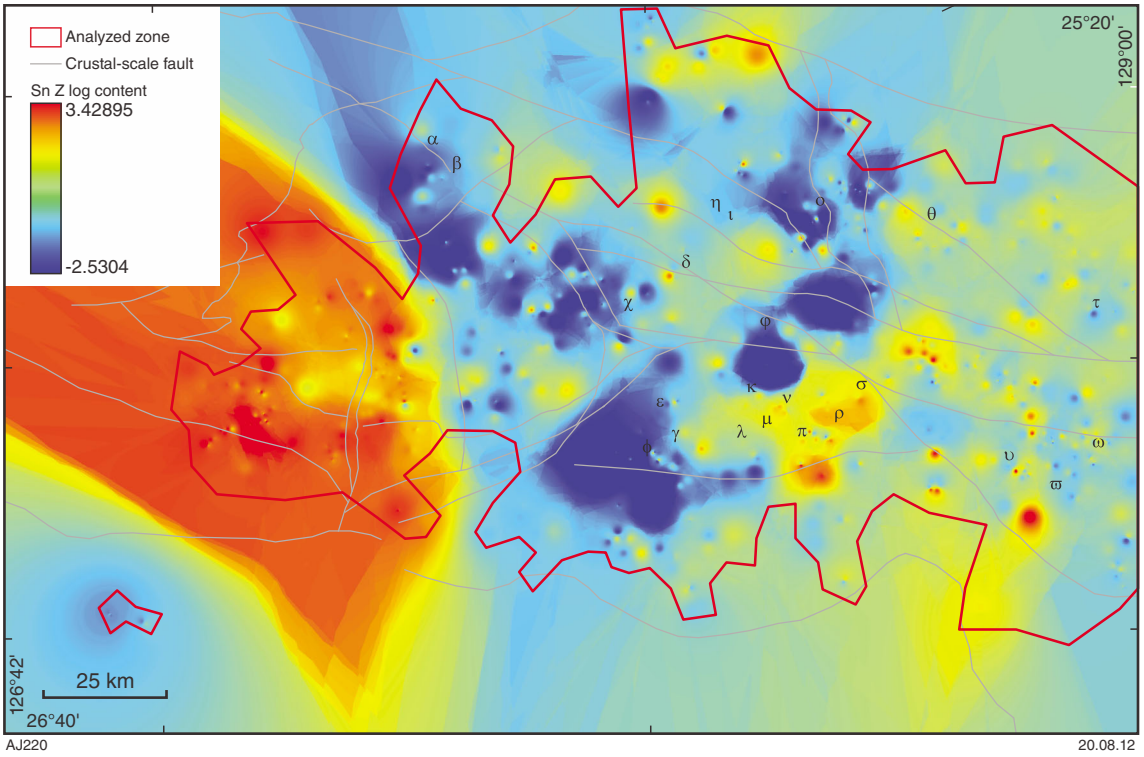

Figure A67. **Predictor map for Sn–W chemical trap: Sn content (Z value). Greek letters correspond to the Sn–W prospective zones (Fig. 27).**

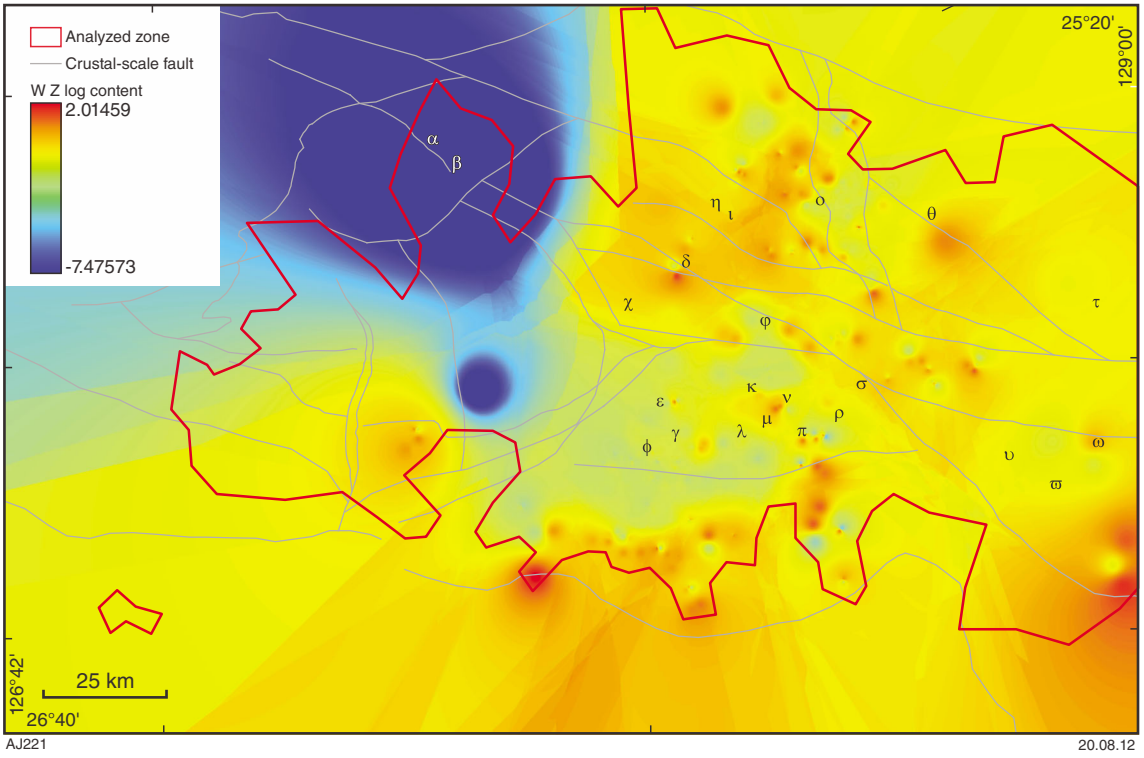

Figure A68. **Predictor map for Sn–W chemical trap: W content (Z value). Greek letters correspond to the Sn–W prospective zones (Fig. 27).**

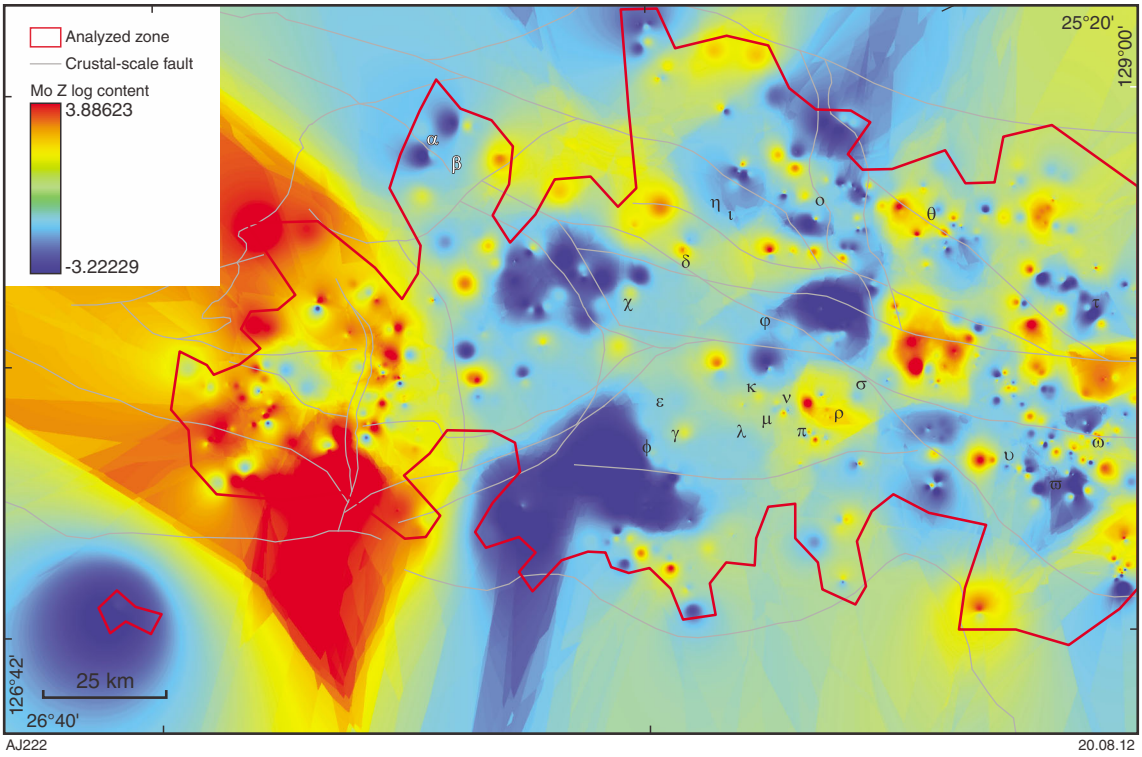

Figure A69. Predictor map for Sn–W chemical trap: Mo content (Z value). Greek letters correspond to the Sn–W prospective zones (Fig. 27).

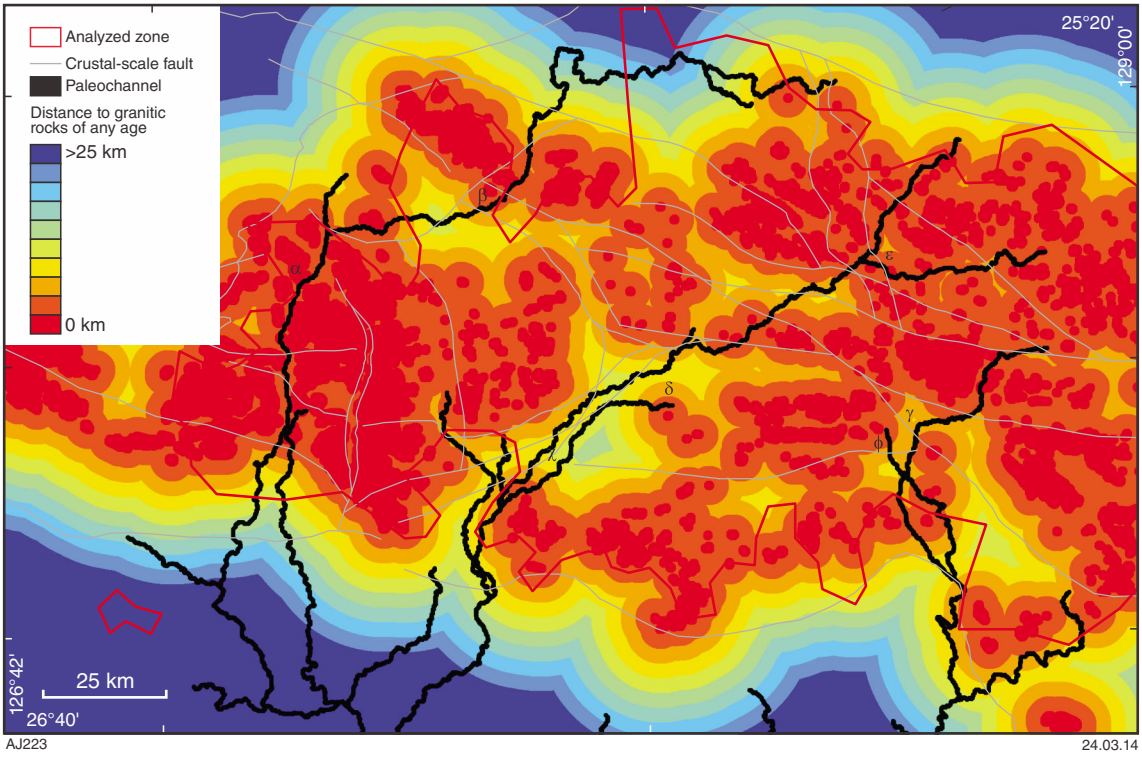

Figure A70. Predictor map for surficial uranium source: proximity to granitic rocks of any age (up to 25 km). Greek letters correspond to the surficial uranium prospective zones (Fig. 30).

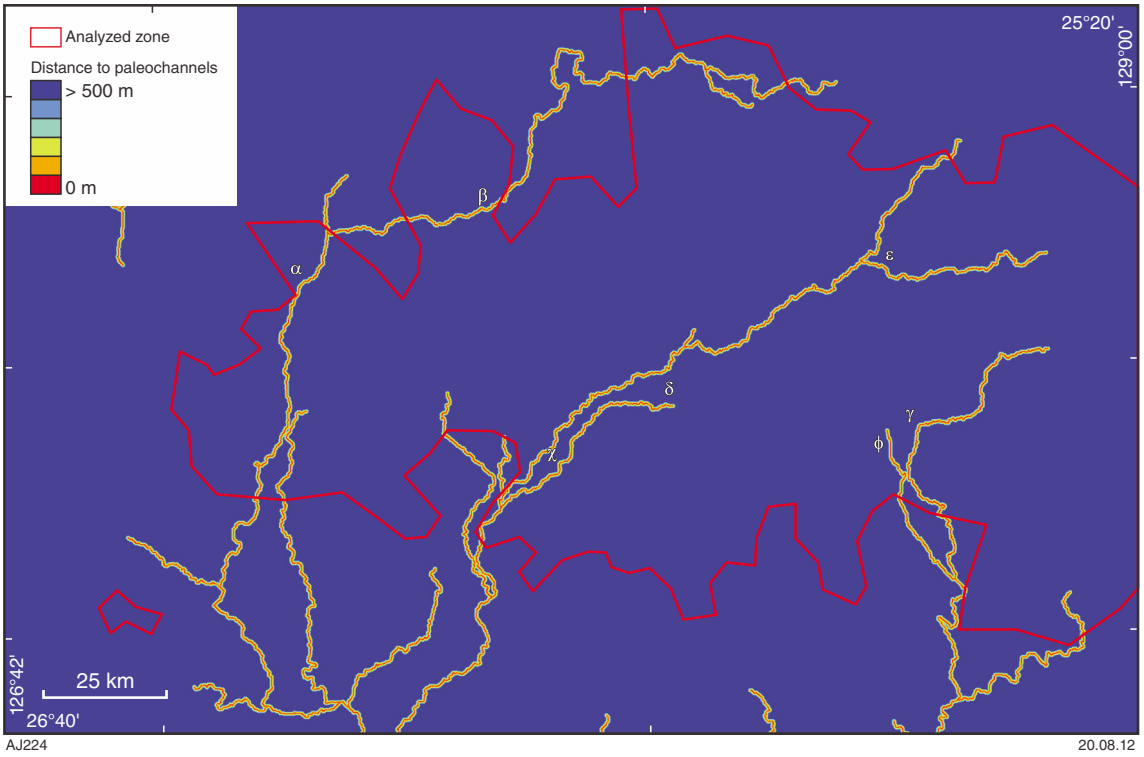

Figure A71. **Predictor map for surficial uranium pathway: proximity to paleochannels with a 5 km buffer zone. Greek letters correspond to the surficial uranium prospective zones (Fig. 30).**

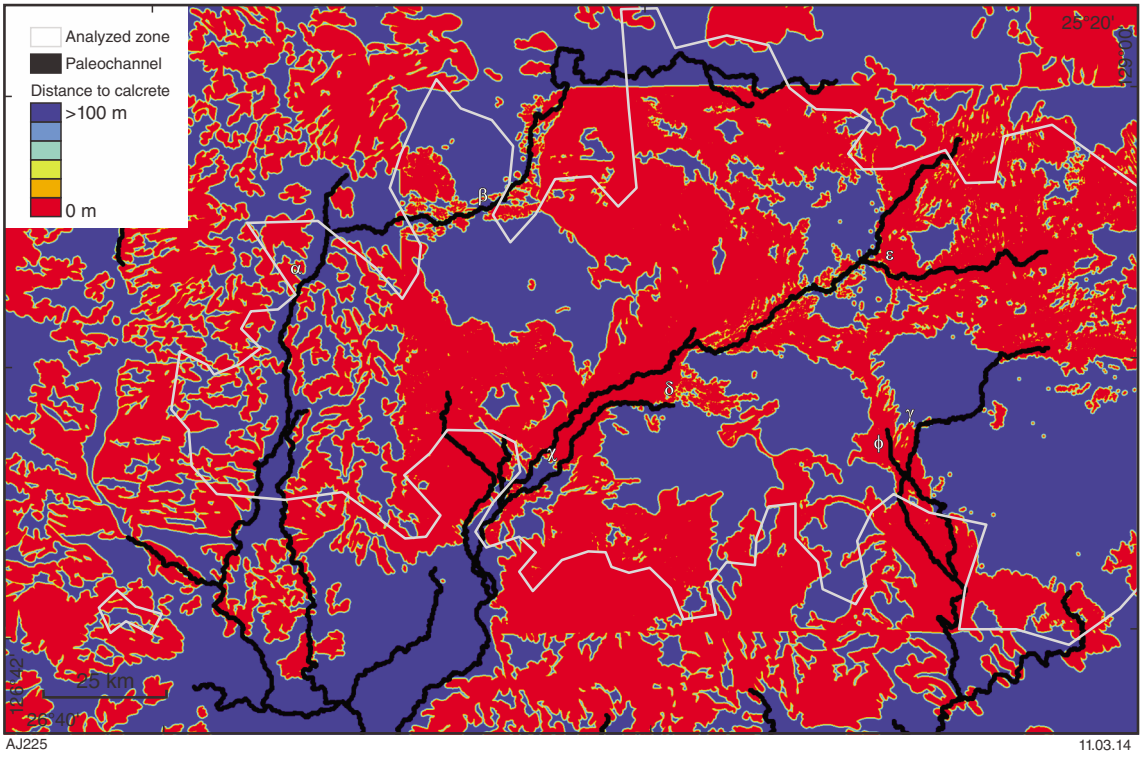

Figure A72. **Predictor map for surficial uranium physical trap: proximity to valley calcrete map. Red indicates the presence of valley calcrete; blue indicates its absence. Greek letters correspond to the surficial uranium prospective zones (Fig. 30).**

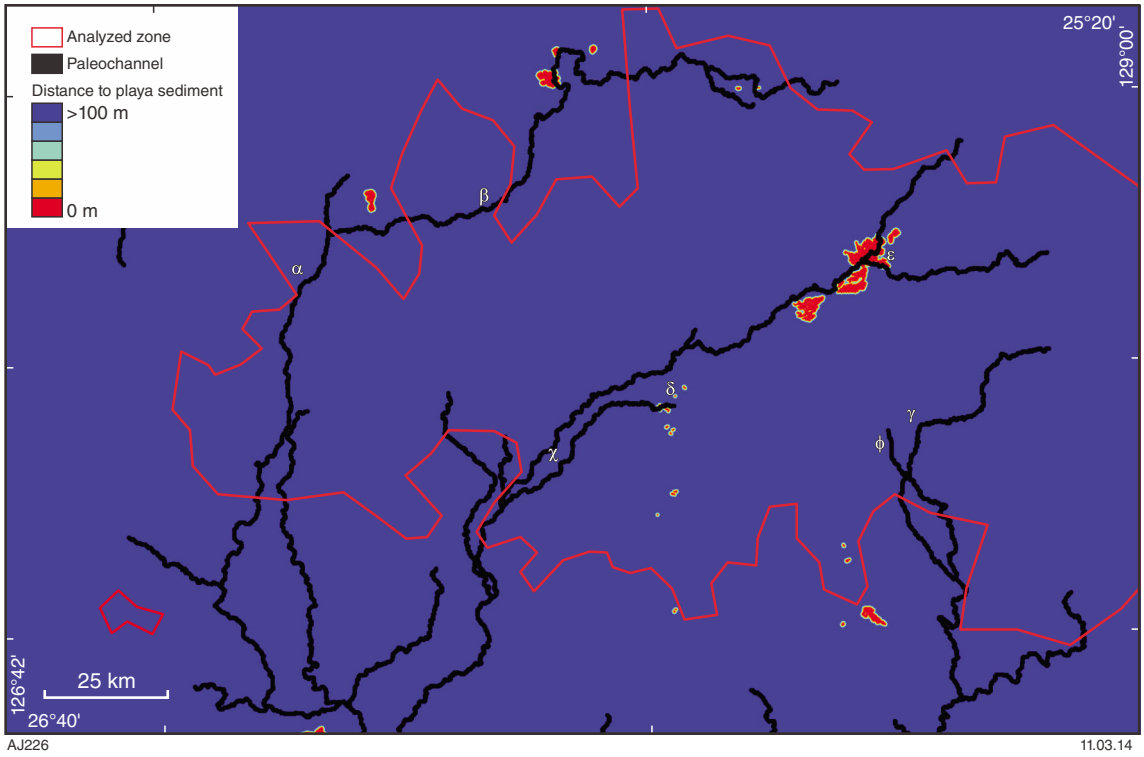

Figure A73. Predictor map for surficial uranium physical trap: proximity to playa sediments map. Red indicates the presence of playa sediments; blue corresponds to their absence; other colours make up the 100 m buffer zone. Greek letters correspond to the surficial uranium prospective zones (Fig. 30).

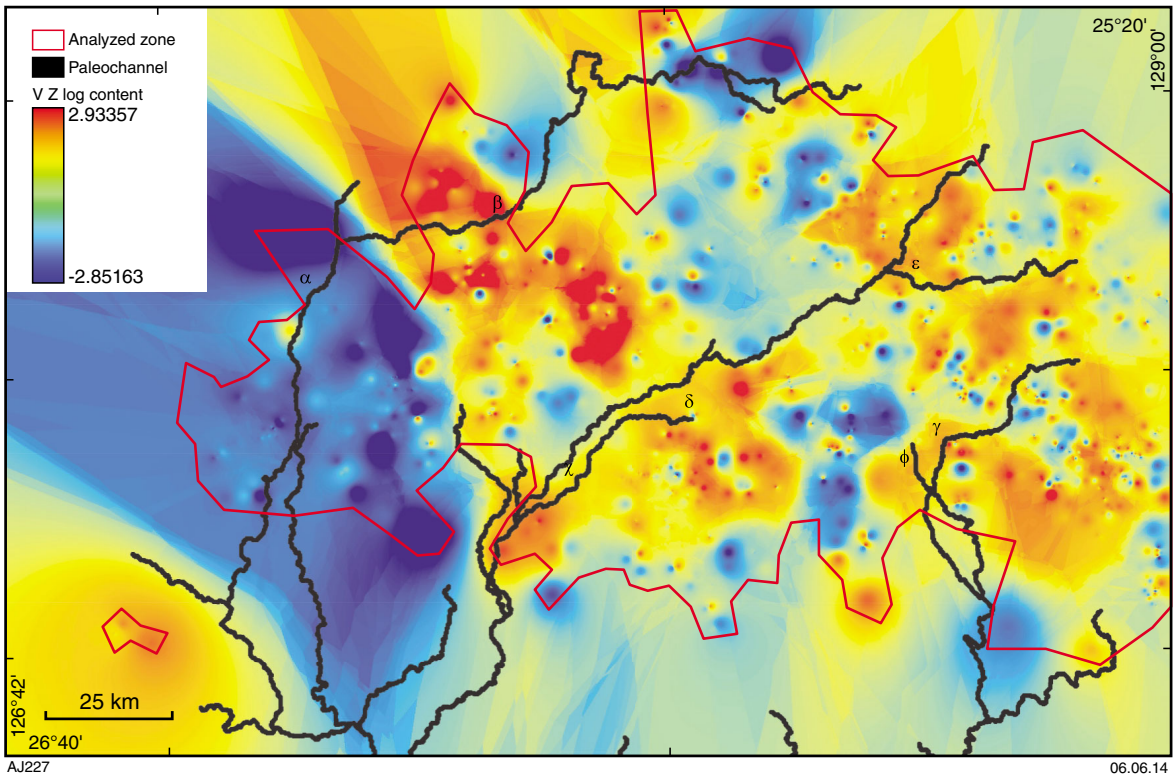

Figure A74. Predictor map for surficial uranium chemical trap: V content Greek letters correspond to the surficial uranium prospective zones (Fig. 30).

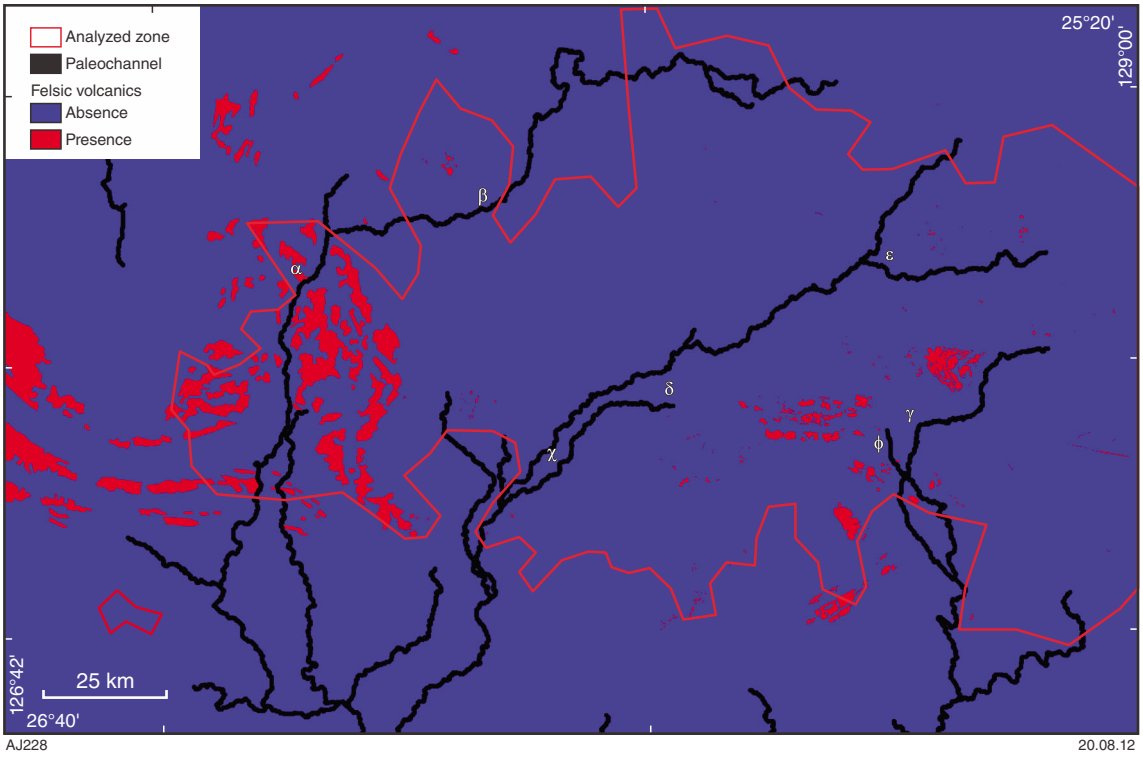

Figure A75. Predictor map for surficial uranium chemical trap: proximity to felsic volcanics

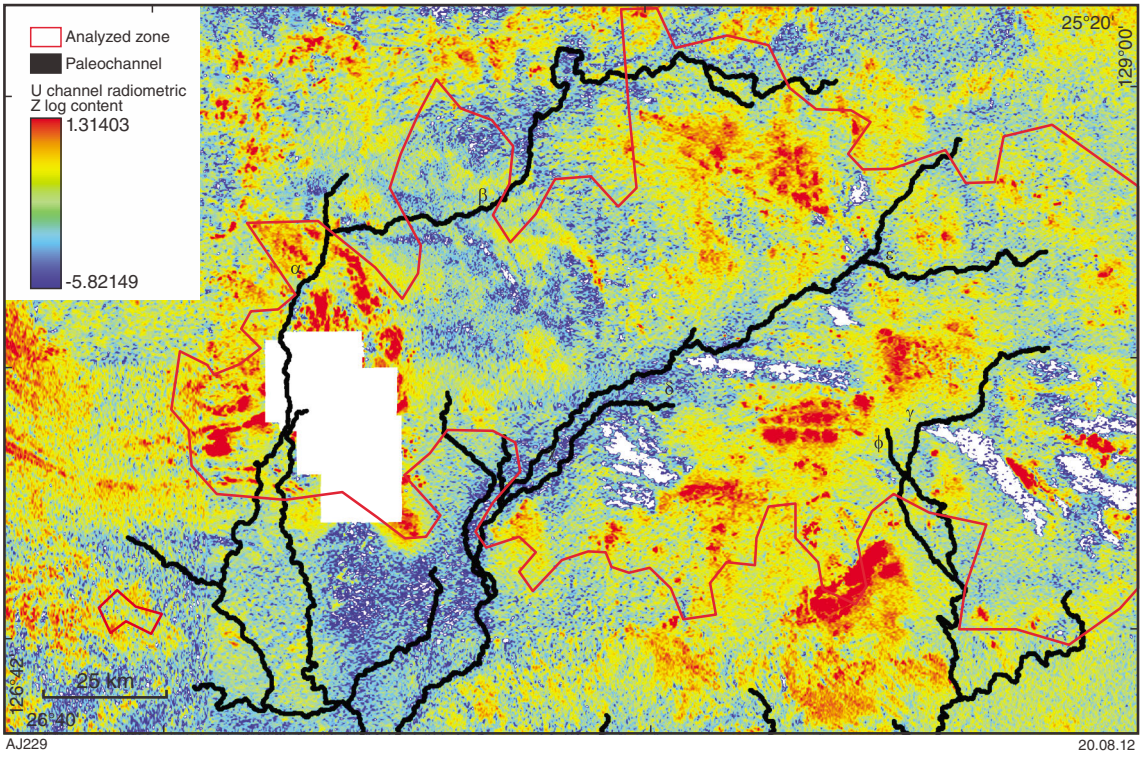

Figure A76. Predictor map for surficial uranium chemical trap: uranium content derived from the radiometric dataset (Z threshold value). Greek letters correspond to the surficial uranium prospective zones (Fig. 30).

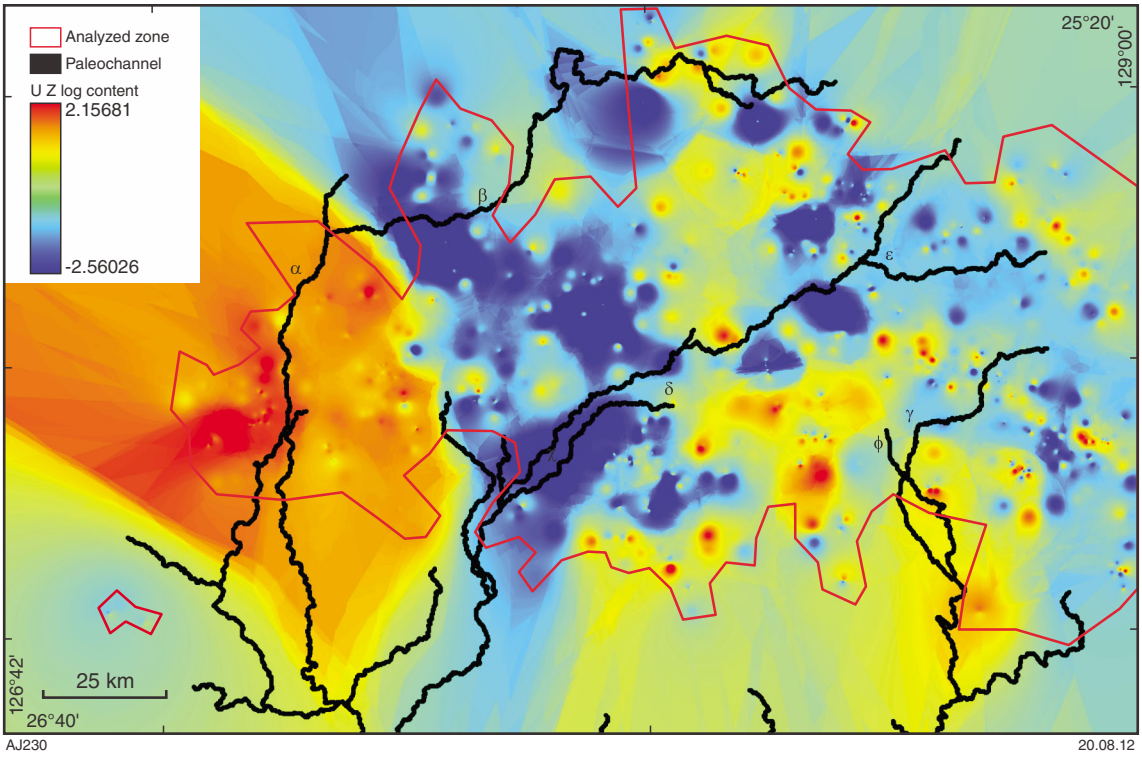

Figure A77. Predictor map for surficial uranium chemical trap: uranium content derived from the geochemistry dataset (Z value). Greek letters correspond to the surficial uranium prospective zones (Fig. 30).

This Report presents a multi-commodity prospectivity analysis of the west Musgrave Province, based on modelling by the Centre for Exploration Targeting (CET) at The University of Western Australia, based in turn on a new interpretation of the 3D geometry and timing of major structures and the architecture of subsurface stratigraphy in the west Musgrave Province. The majority of preserved major structures in the west Musgrave Province appear to have originated during the c. 1085–1040 Ma Giles Event or before, although many of these were subsequently reactivated during the Petermann and Alice Springs Orogenies. All primary and derived datasets were combined in a mineral system analysis using a knowledge-based, or 'fuzzy', logic framework to assess prospectivity. The mineral prospectivity analysis was carried out for magmatic nickel–copper, magmatic platinum group elements (PGE), orogenic and intrusion-related gold, iron oxide–copper–gold (IOCG), tin–tungsten, and surficial uranium mineral systems. Analyses of this type carry many uncertainties; however, our analyses map the most favourable areas for these deposit types on a conceptual basis. The results indicate several zones of relatively high prospectivity for each deposit type.

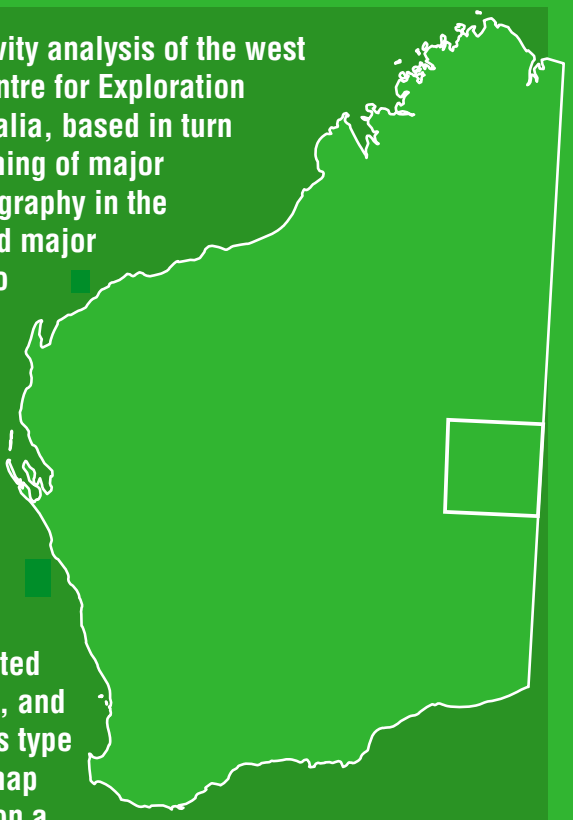

Further details of geological products and maps produced by the Geological Survey of Western Australia are available from:

Information Centre
Department of Mines and Petroleum
100 Plain Street
EAST PERTH WA 6004
Phone: (08) 9222 3459 Fax: (08) 9222 3444

www.dmp.wa.gov.au/GSWApublications

JOLY et al.

MINERAL SYSTEMS ANALYSIS OF THE WEST MUSGRAVE PROVINCE:
REGIONAL STRUCTURE AND PROSPECTIVITY MODELLING

REPORT 117